CHALMERS
UNIVERSITY OF TECHNOLOGY

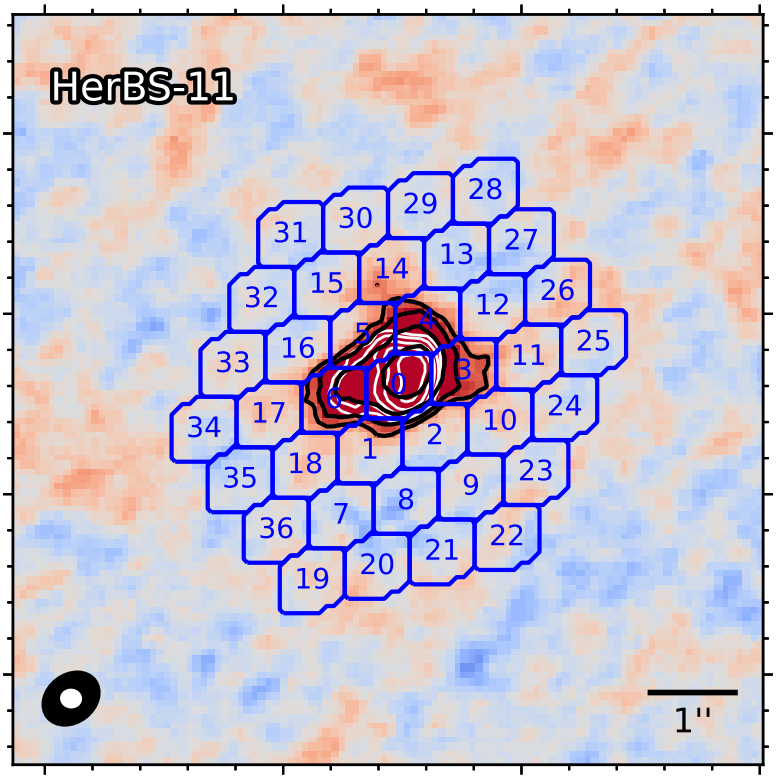

Dusty Star-Forming Galaxies at High-Redshift

A study on their star formation with dust and CO emission

Master's Thesis in Physics

PABLO ARRIAGADA TORRES

DEPARTMENT OF SPACE, EARTH AND ENVIRONMENT
CHALMERS UNIVERSITY OF TECHNOLOGY
Gothenburg, Sweden 2025
www.chalmers.se

Master's thesis 2025

Dusty Star-Forming Galaxies at High-Redshift

A study on their star formation with dust and CO emission

PABLO ARRIAGADA TORRES

CHALMERS
UNIVERSITY OF TECHNOLOGY

Department of Space, Earth and Environment
Division of Astronomy and Plasma Physics
Chalmers University of Technology
Gothenburg, Sweden 2025

Dusty Star-Forming Galaxies at High-Redshift
A study on their star formation with dust and CO emission
PABLO ARRIAGADA TORRES

Supervisor:	Prof. Kirsten Kraiberg Knudsen, Department of Space, Earth and Environment
Supervisor:	Dr. Tom Bakx, Department of Space, Earth and Environment
Examiner:	Assoc Prof. Magnus Thomasson, Department of Space, Earth and Environment

Master's Thesis 2025
Department of Space, Earth and Environment
Division of Astronomy and Plasma Physics
Chalmers University of Technology
SE-412 96 Gothenburg
Telephone +46 31 772 1000

Cover: Tessellation of beam-like apertures on the moment 0 map of the CO$(3-2)$ transition in the HerBS-11 galaxy.

Typeset in LaTeX
Printed by Chalmers Reproservice
Gothenburg, Sweden 2025

Dusty Star-Forming Galaxies at High-Redshift
A study on their star formation with dust and CO emission
PABLO ARRIAGADA TORRES
Department of Space, Earth and Environment
Chalmers University of Technology

Abstract

Dusty star-forming galaxies (DSFGs) are a population of galaxies found mostly at cosmic noon, the time of our Universe when star formation rate (SFR) density was at its peak, some 10 billion years ago. They are amongst the most intense starbursts in the Universe, reaching extreme SFRs up to thousands of solar masses per year. Despite being extreme galaxies placed at a critical time of our Universe, many aspects of their evolutionary path and star formation history are still a mystery. The aim of this thesis is to study the star formation of DSFGs at cosmic noon at resolved scales. To this end, high-resolution ALMA observations of Bands 3 through 8 are employed to test the Schmidt-Kennicutt (SK) relation in a sample of 23 DSFGs. An algorithm is developed to measure SFRs and molecular gas masses at kpc scales, in line with the high resolution of the observations. From these measurements, resolved SK diagrams were built for each galaxy. The slopes of these diagrams were obtained from two different fitting methodologies, yielding $N_1 = 1.51^{+0.89}_{-0.32}$ and $N_2 = 1.21^{+0.10}_{-0.22}$ across the entire sample. These results ($N > 1$) are consistent with a scenario where star formation is more efficient in high-density regions. This thesis provides unprecedented statistical significance to this claim, which had previously been described in individual objects. $N > 1$ represents an important difference between DSFGs at cosmic noon and local galaxies, where $N \approx 1$ is the consensus. The star formation scenario of DSFGs described in this thesis may have a significant impact in their evolutionary path until today, in ways that remain an open question.

Keywords: galaxies: evolution – galaxies: high-redshift – galaxies: star formation - submillimetre: galaxies

Acknowledgements

First and foremost I want to thank my supervisors, Kirsten and Tom. I have learned so much from you, more than I ever thought possible. Thank you for giving me the opportunity to do this project when I came knocking on your door, and for the constant support over the past four months. The time I have spent working with you has been the highlight of my university studies.

I want to thank my examiner Magnus for his insightful suggestions on early drafts of this thesis, and his encouragement. I would also like to thank Toshiki Saito for taking the time to meet me online all the way from Japan, and teaching me all those secrets about the Schmidt-Kennicutt relation. Cathy Horellou, thank you for your support and guidance during the time I have spent in Chalmers.

Becoming a Chalmerist was my dream long before I made it to Sweden. I want to thank the Adlerbert Foundations for making that dream possible. To the people I have shared this journey with, Björn, Jonathan, Arik, Anton, Martin, Lovisa, Patrick, Hampus, Vicente, Thiebaut, Charbel, Isak, and Johan, thank you for making these two years special.

I want to thank my partner, Jenny. I have put together a project I feel so proud of, and none of that would be possible without you. I don't know if it's much, but I do know it is as much yours as it is mine. Thank you for your encouragement, support, and for believing in me. Mamá, Marcela, gracias por estar acá hoy, en la culminación de algo grande que empezamos juntos. Papá, César, cada día intento parecerme más a ti. Oliver y Lucía, gracias por enseñarme día a día qué es lo realmente importante.

Pablo Arriagada Torres, Gothenburg, May 2025

List of Acronyms

Below is the list of acronyms that have been used throughout this thesis listed in alphabetical order:

AI	Artificial Intelligence
ACA	Atacama Compact Array
ALMA	Atacama Large Millimeter/submillimeter Array
BEARS	Bright Extragalactic ALMA Redshift Survey
CARTA	Cube Analysis and Rendering Tool for Astronomy
CASA	Common Astronomy Software Applications
CMB	Cosmic Microwave Background
Dec.	Declination
DSFG	Dusty Star-Forming Galaxy
ESA	European Space Agency
ESO	European Southern Observatory
FOV	Field Of View
FWHM	Full Width at Half Maximum
GAMA	Galaxy And Mass Assembly survey
GMC	Giant Molecular Cloud
H-ATLAS	*Herschel* Astrophysical Terahertz Large Area Survey
HPBW	Half-Power BeamWidth
HerBS	*Herschel* Bright Source
HyLIRG	Hyper-Luminous InfraRed Galaxy
ICRS	International Celestial Reference System
IMF	Initial Mass Function
IR	InfraRed
ISM	InterStellar Medium
JCMT	James Clerk Maxwell Telescope
LIRG	Luminous InfraRed Galaxy
LSB	Lower Side Band
MCMC	Markov Chain Monte Carlo
MS SFG	Main-Sequence Star-Forming Galaxy
NAOJ	National Astronomical Observatory of Japan
NGP	North Galactic Pole
NRAO	National Radio Astronomy Observatory
ODR	Orthogonal Distance Regression

PA	Position Angle
PDF/pdf	Probability Density Function
R.A.	Right Ascension
SCUBA	Submillimeter Common-User Bolometer Array
SCUBA-2	Submillimeter Common-User Bolometer Array 2
SED	Spectral Energy Distribution
SFR	Star Formation Rate
SFRD	Star Formation Rate Density
SGP	South Galactic Pole
SK	Schmidt-Kennicutt
SLED	Spectral Line Energy Distribution
SMG	Sub-Millimeter Galaxy
SNR	Signal-to-Noise Ratio
SPIRE	*Herschel*-Spectral and Photometric Imaging Receiver
ULIRG	UltraLuminous InfraRed Galaxy
USB	Upper Side Band
UV	UltraViolet
VLBI	Very Long Baseline Interferometry

Nomenclature

Below is the nomenclature of the most important parameters and variables that have been used throughout this thesis.

Parameters & Variables

$\alpha_{\rm CO}$	CO-to-H_2 conversion factor
A	Area
c	Speed of light
COV	Covariance matrix
D_L	Luminosity distance
ϵ	Intrinsic scatter
$f_{i,j}$	Fraction of overlapping pixels
$\theta_{\rm res}$	Angular resolution
$\theta_{\rm HPBW}$	Half-power beamwidth
J	Rotational quantum number
λ	Wavelength
$\mathcal{L}$	Likelihood
L	Luminosity
$L_{\rm IR}$	Infrared luminosity
$M_{\rm H_2}$	Molecular gas mass
ν	Frequency
N	Slope of Schmidt-Kennicutt diagram
$\Sigma_{\rm SFR}$	Star formation rate surface density
$\Sigma_{\rm H_2}$	Molecular gas mass surface density
σ	Noise/dispersion/error
S	Flux density
$S{\rm d}V$	Velocity-integrated flux

$\tau_{\rm dep}$	Depletion time
T	Temperature
$\mathcal{V}$	Complex visibility
ψ	Star formation rate density
$\Omega_{\rm A}$	Solid angle of Gaussian beam
z	Redshift

Contents

List of Figures

List of Tables

1
Introduction

One of the most fascinating puzzles in modern astronomy is how galaxies have evolved across time. Ever since they began forming, some 13.5 billion years ago, galaxies have evolved and changed in ways that remain only partially understood. With the advent of new technologies, we can now observe and simulate galaxies almost all the way back, but 13.5 billion years is a very long time and the pieces of the puzzle are not so easy to put together.

Galaxies are intrinsically very diverse and complex, both now and in the past. Furthermore, studying distant galaxies is challenging, as there are numerous limitations and biases to what we can observe from Earth or from space. Astronomers are actively trying to answer some fundamental questions about the evolution of galaxies, such as; how they first formed, what has driven the formation of stars, why some galaxies barely form any stars today, why some galaxies developed complex morphologies with disks and spiral arms (like our Milky Way), or what has been the role of mergers, gas accretion, or super massive black holes.

A crucial aspect of understanding the evolution of galaxies is describing the growth of stellar mass, and thus studying the formation of stars. A very significant fraction of the stars present in the Universe today was formed some 10 billion years ago, at a time that astronomers have named *cosmic noon*. Cosmic noon represents the peak of star formation density across the entire cosmic history. For this reason, the understanding of cosmic noon is paramount for a proper description of the evolution of galaxies.

This thesis aims to describe star formation at cosmic noon. In particular, it focuses on a population of galaxies named Dusty Star-Forming Galaxies (DSFGs), which played a key role during that time. DSFGs are known to form stars more actively than present-time galaxies. They are also candidates to be progenitors of modern-day ellipticals. However, there are many details about their star formation and evolution that astronomers are only starting to unravel.

This thesis studies DSFGs with the most widely used empirical relation to describe star formation in galaxies, the so-called Schmidt-Kennicutt relation. This relation lays its foundation in the very simple fact that stars form from molecular gas. More specifically, the Schmidt-Kennicutt relation compares the rate at which stars form against the presence of molecular gas, commonly showing a tight straight-line correlation. The Schmidt-Kennicutt relation has been studied extensively in galaxies in the local Universe, i.e., galaxies in the present time. Furthermore, it has been successfully tested across six orders of magnitude. In the case of cosmic noon, studies are scarce, often of individual galaxies and with methodologies that are inconsistent and introduce biases to any comparisons.

This thesis tests the Schmidt-Kennicutt relation in large number of DSFGs, using observations from the Atacama Large Millimeter/submillimeter Array (ALMA), the most powerful telescope on Earth to study the Universe at submm-mm wavelengths. The analysis is conducted with a consistent methodology, by which all galaxies can be compared fairly under good physical assumptions. Furthermore, it does so by taking full advantage of the high angular resolution achieved by ALMA, down to ~ 0.15 arcsec in the sky, or a few kpc. This resolution allows for galaxies to be *resolved*, i.e., for different parts within a galaxy to be studied independently.

A key parameter of the Schmidt-Kennicutt relation is the slope of the straight line. The slope can reveal how star formation is taking place at small scales in galaxies. The goal of this thesis is to constrain the resolved Schmidt-Kennicutt slope of DSFGs at scales of a few kpc, using a consistent methodology. Crucially, this will be done in a large sample (23 galaxies in total), which is unprecedented in the literature.

This thesis is organized as follows. In Chapter 2 the key background physics needed to understand the context and the content of the work are presented. Chapter 3 introduces the methods and resources employed to carry out the work. This includes a description of the specific sample of galaxies that was studied, the ALMA data, and how calculations were done. Chapter 4 (supported by Appendix G) presents the main results, namely the Schmidt-Kennicutt diagrams and the fitted slopes. Chapter 5 discusses the results in context with the literature. Limitations to the work are also included, together with improvement opportunities and future work. Lastly, in Chapter 6 the main contributions and findings of this thesis are summarized.

2

Theory

This chapter presents the relevant theory and background information to this thesis. A broad context of the history of the Universe is presented in Section 2.1. In Section 2.2 the term *redshift* is introduced. In Section 2.3, important properties and processes of galaxies are presented. Section 2.4 explains the Schmidt-Kennicutt relation, an empirical relation used describe star formation in galaxies. Lastly, Section 2.5 introduces dusty star-forming galaxies (DSFGs), the population of galaxies studied in this work.

2.1 Setting the cosmic stage

General reference of this section: The book Extragalactic Astronomy and Cosmology; An Introduction, by Schneider (2006).
Our Universe is 13.8 billion years old (Planck Collaboration et al., 2020). During this time it has gone through many important changes and stages, which have shaped it to become what it is today. This is studied by the branch of physics known as cosmology. In this section, a brief summary of the most relevant events across cosmic history is presented, as well as the most important questions still open.

Figure 2.1 shows a timeline of the Universe. At the earliest moment, it was in an extremely dense and hot state from which it began expanding, in what we know as the Big Bang. Immediatly after (some 10^{-34} seconds), it is believed to have suffered a dramatic increase in its size known as Cosmic Inflation (Guth, 1981). Following this, in the first three minutes the elements we know today were formed, in a process named Primordial Nucleosynthesis (Alpher et al., 1948). The result was an abundance of $\sim 75\%$ of Hydrogen (basically, protons) and $\sim 25\%$ Helium, with some Deuterium and Lithium.

After protons formed, temperatures were still too high for electrons to be able to combine with them. The Universe therefore remained ionized, in what is known as the primordial plasma. In this scenario, photons were constantly suffering Thomson scattering; they could not travel very far without interacting. This did not change until approximately 380,000 years later, when the Universe became cold enough ($T \sim$ 3000 K) for protons and electrons to combine. This is known as the Recombination of the Universe (Peebles, 1968). This name can be somewhat misleading, because it suggests that protons and electrons have been combined in the past, when they were actually combining for the very first time.

At this point, there was no longer a plasma that kept scattering photons; they could travel freely as the Universe became transparent. All these photons being

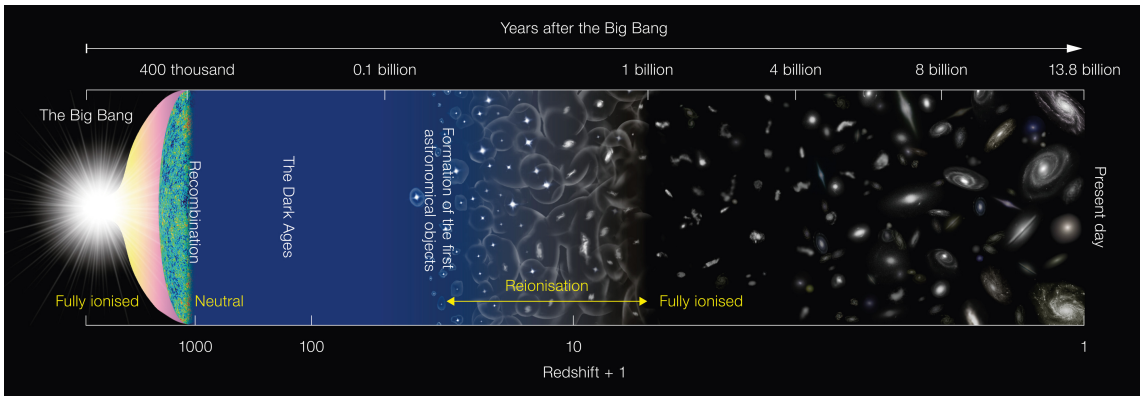

Figure 2.1: Timeline of the Universe, including most significant events such as the Big Bang, Recombination, and Reionization. Cosmic noon occurred at ages $\sim 3-4$ billion years, some ~ 10 billion years ago (e.g. Förster Schreiber & Wuyts 2020; also see Figure 2.3). The age of the Universe and redshift are shown in the x axes (for a more precise scale, see Figure 2.3). Image credit: NAOJ; available at `https://www.eso.org/public/australia/images/eso1620a/`.

released at Recombination, constitute the radiation known as the Cosmic Microwave Background (CMB; see Figure 2.2). This was first observed by Penzias & Wilson (1965), and is the most perfect black body ever detected to date. The CMB emission comes to Earth from all directions; interestingly, even from directions further apart than the distance that light could have covered in that time. Since nothing can travel faster than light, this makes it impossible for these components to share information. Yet, they do, as the CMB has (approximately) the same temperature in all directions at $T \approx 2.73$ K (Fixsen & Mather 2002; this temperature is cooler than the $T \sim 3000$ K mentioned before due to the expansion of the Universe). This paradox is known as the horizon problem, and it is solved by the introduction of the Cosmic Inflation earlier in the timeline.

The small temperature anisotropies shown in Figure 2.2 are related to very small density fluctuations present in the Early Universe. All structures existing in the Universe today, such as galaxies or clusters, have evolved from these tiny overdensities already present at such young age.

As shown in the timeline of Figure 2.1, after Recombination, there came the Dark Ages. This is a relatively unexplored time of the Universe, since (as the name suggests) there are no objects emitting light that astronomers can observe. There was only neutral Hydrogen, which slowly began to clump due to gravity. Eventually, between ages 100 and 150 million years, from the initial conditions set in the early Universe, the very first stars and galaxies began to form. Since this is the first starlight of the Universe, this period is often named cosmic dawn (e.g. Koopmans et al., 2015). The earliest galaxies astronomers have been able to detect are located around this time, when the Universe was only 300 million years old (e.g. see Carniani et al. 2024, two galaxies at redshift 14).

At this stage, the Universe became ionized again. This is believed to have happened via photoionization, i.e. due to energetic photons, which came from this newly-formed first generation of (presumably hot) stars. Another less likely scenario

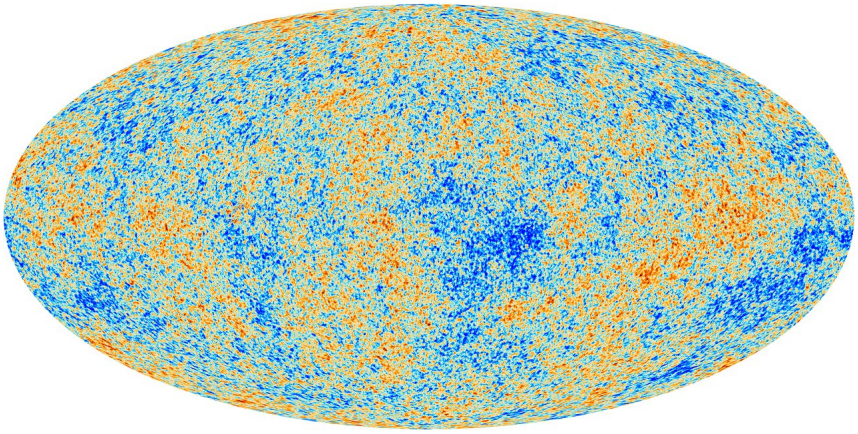

Figure 2.2: Cosmic Microwave Background radiation, as observed by *Planck* of the European Space Agency (ESA). Colors are anisotropies in the temperature. From some directions the radiation is slightly hotter than 2.73 K (in red), and from other slightly cooler (in blue). These differences in temperature are tiny, some five orders of magnitude smaller than 2.73 K. A more compact version of this image is shown in the timeline of Figure 2.1, at 400,000 years. Image credit: ESA and the Planck Collaboration; available at `https://supernova.eso.org/exhibition/images/1102_planck_cmb/`.

is that those photons were provided by super massive back holes. In either case, since the Universe became ionized again, astronomers have named this the Epoch of Reionization (e.g. Kannan et al., 2022).

The Epoch of Reionization was initially theorized by Gunn & Peterson (1965), and only first observed many decades later (e.g. Becker et al., 2001; Fan et al., 2002). Overall, there are decent constraints on when the Epoch of Reionization took place, between ages $\sim 300-900$ million years (see Figure 2.1). However, it is still not very well understood how the first stars formed, or how the Universe became ionized (e.g. Wise, 2019), which is how it has remained until today.

Following the Epoch of Reionization, over 12 billion years ago, the Universe began forming more and more stars, as quantified by the star formation rate density (SFRD; ψ). This is the stellar mass formed in a given time in a given comoving volume (i.e. a volume adjusted by the expansion of the Universe for a fair comparison).

Figure 2.3 shows the evolution of SFRD all the way to the present. As shown, star formation increased after the Epoch of Reionization. This cosmic build-up went on for $\sim$ 2 billion years, leading the Universe to a stage of peak SFRD, some 10 billion years ago. Astronomers have named this peak stage the cosmic noon (e.g. Förster Schreiber & Wuyts, 2020). After cosmic noon, SFRD has only declined.

Describing cosmic noon is crucial to get a full picture of how galaxies have evolved until today. The majority of stars in present galaxies were formed precisely during cosmic noon. As explained in the review by Förster Schreiber & Wuyts (2020), at cosmic noon galaxies already had clear relations between their properties, such as stellar mass, star formation rate, metallicity, gas content, structure, and kinematics.

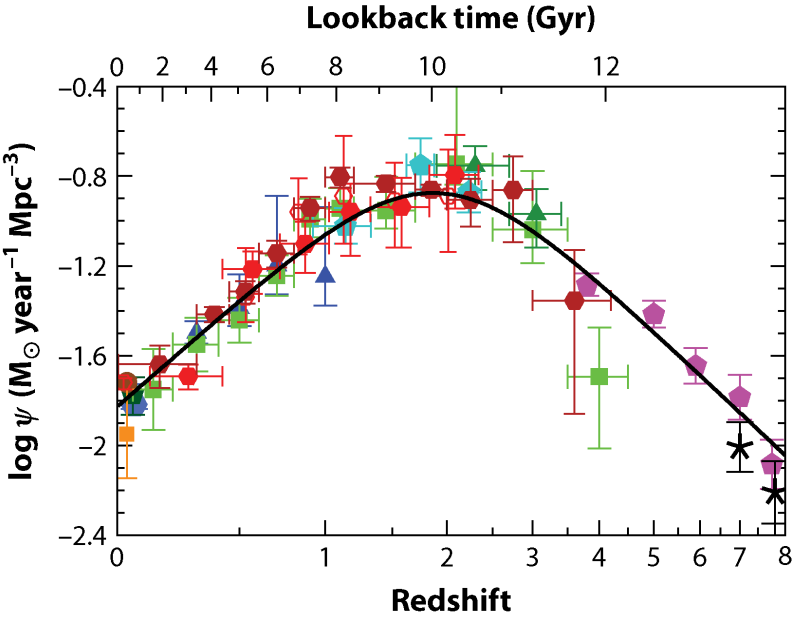

Figure 2.3: Evolution of star formation rate density (SFRD) across cosmic time. Lookback time refers to how long ago something happened, so the left hand-side of the graphic represents the present time. The right hand size represents the end of the Epoch of Reionization. A clear peak on the SFRD is reached 10 billion years ago ($z \approx 2$), which corresponds to cosmic noon. This Figure is taken from Madau & Dickinson (2014).

However, these relations have changed over the past 10 billion years. Galaxies have evolved, driven mainly by mergers, gas accretion from the intergalactic medium, or in-situ star formation (e.g. Conselice, 2014). Spiral and elliptical galaxies, as we observe today, appear very different from galaxies at cosmic noon, which appear far more messy or *peculiar*.

These mechanisms driving galaxy evolution remain still only partially understood. As mentioned earlier, astronomers are now able to observe galaxies all the way back to when the Universe was only 300 million years old, spanning many epochs of the Universe. This seems to imply that the evolution of galaxies can be studied directly, but is only true to a certain extent. Besides the intrinsic complexity of galaxies, there are observational biases and constraints that prevent astronomers from easily connecting the dots between different cosmic eras.

All these challenges make galaxy evolution a fundamental topic in modern astronomy, with intense ongoing research. There are active efforts in trying to understand how galaxies have evolved and formed across cosmic time, using both observations (e.g. Popesso et al., 2023; Finkelstein et al., 2023) and simulations (e.g. Agertz et al., 2020; Ishiyama et al., 2021). In this thesis I will study the star-forming galaxies at cosmic noon, a stage of paramount importance as the Universe was forming more stars than ever. This can shed some light on how galaxies 10 billion years ago have evolved into the galaxies we observe today.

2.2 Expansion of the Universe: redshift

One of the most remarkable aspects of the Universe is that it has been in constant expansion, ever since the Big Bang. This expansion was theorized and observed already some one hundred years ago (Friedmann, 1922; Hubble, 1929; Lemaître, 1931). Distant objects in space are moving away from each other at an apparent speed v that is proportional to their distance D, i.e.

$$v \propto D \ . \tag{2.1}$$

This is known as Hubble–Lemaître law. This relative motion between distant objects, effectively, means that the space between them is constantly being *stretched*. As a consequence, light also becomes stretched as it travels through space: its wavelength becomes longer. What this means is that an observer *sees* a longer wavelength ($\lambda_{\rm obs}$) than the intrinsic wavelength that was actually emitted ($\lambda_{\rm rest}$). This stretch or *shift* $\Delta\lambda \equiv \lambda_{\rm obs} - \lambda_{\rm rest}$ is quantified by the redshift z, defined by

$$z \equiv \frac{\Delta\lambda}{\lambda_{\rm rest}} \ . \tag{2.2}$$

Equation 2.2 includes shifts in the wavelength caused by any physical mechanism. The expansion of the Universe is not the only process that can contribute, others are relative movements (Doppler effect; Ives & Stilwell 1938) or gravity (Pound & Rebka, 1959). The redshift contribution from the expansion of the Universe alone is known as cosmological redshift $z_{\rm cosm}$. This is given by

$$1 + z_{\rm cosm} = \frac{a_0}{a(t_{\rm emit})} \ , \tag{2.3}$$

where a is the scale factor, a dimensionless parameters in the range $0 < a < 1$ which quantifies the size of the Universe. a_0 corresponds to the current size of the Universe, and $a(t_{\rm emit})$ corresponds to the size at the moment a radiation was emitted. Since the Universe has been in constant expansion, $a_0 \geq a(t_{\rm emit})$ is valid for any $t_{\rm emit}$. This means that

$$z_{\rm cosm} \geq 0 \ , \tag{2.4}$$

where $z_{\rm cosm} = 0$ corresponds to the present time. Following equation 2.3, an increasingly larger $z_{\rm cosm}$ traces back to times when the Universe was smaller and smaller. This is equivalent to tracing back to times closer and closer to the Big Bang. For this reason, astronomers commonly use the cosmological redshift as a way to measure the age of the Universe. This tight relation between redshift and age is very well reflected in Figures 2.1 and 2.3 (compare top and bottom x axes).

When using redshift to place an object in the timeline of the Universe, the contribution of relative movements and gravity are negligible. Therefore, astronomers commonly consider cosmological redshift the *total* redshift, or simply *the* redshift. Furthermore, the term *high-redshift* refers to a young Universe, whereas the terms *local* or *nearby* Universe basically refer to the present, $z \approx 0$. In this thesis the term *redshift* will refer the cosmological redshift, for which equation 2.2 is valid. Also, the term *high-redshift* will be used to refer to cosmic noon, as commonly done in

the relevant literature (e.g. Carilli & Walter, 2013; Casey et al., 2014; Hodge & da Cunha, 2020).

Equation 2.2 can be rewritten as

$$z = \frac{\lambda_{\text{obs}} - \lambda_{\text{rest}}}{\lambda_{\text{rest}}} \tag{2.5}$$

$$\implies \lambda_{\text{obs}} = (1+z)\lambda_{\text{rest}} \ . \tag{2.6}$$

Light waves follow the simply relation $c = \nu\lambda$, i.e. the wavelength and frequency ν are inversely proportional via the speed of light c. Therefore, equation 2.6 is equivalent to

$$\nu_{\text{obs}} = \frac{\nu_{\text{rest}}}{(1+z)} \ , \tag{2.7}$$

where ν_{obs} and ν_{rest} are the observed and rest frequencies, respectively.

Since the speed of light is finite, when astronomers observe objects in space, they are looking into the past. Equations 2.6 and 2.7 are therefore extremely useful to understand just how far back into the past they are looking. Rest wavelengths/frequencies of different types of radiation are commonly very well known. Consequently, when observing the light coming from an object (i.e. measuring λ_{obs} and ν_{obs}), the redshift z can be deduced. As previously explained, this is directly linked with the age of the Universe.

Our understanding of the expansion of the Universe has come a long way since the Hubble–Lemaître law was introduced in the 1920s. Several decades later, astronomers showed that the expansion is accelerating (Riess et al., 1998; Perlmutter et al., 1999). This is caused by a mysterious entity named dark energy, which has driven this acceleration for the past ~ 5 billion years (e.g. Frieman et al., 2008).

There are, however, still unresolved issues. The proportionality constant of the Hubble–Lemaître law in the present time is known as the Hubble constant, H_0. This is a crucial parameter of the cosmological model, since it basically quantifies how quickly the Universe is currently expanding. Considering the relation $v \propto D$, it has units of velocity divided by distance.

Different methods of estimating H_0 yield different results. Planck Collaboration et al. (2020) have calculated $H_0 = (67.4 \pm 0.5)$ km s^{-1} Mpc^{-1} with measurements of the CMB. On the other hand, Riess et al. (2022) have found $H_0 = (73.30 \pm 1.04)$ km s^{-1} Mpc^{-1} by studying nearby supernovae. These two results have a dramatic disagreement of over 5σ. This is a long-standing issue in cosmology, known as the Hubble tension (e.g. Di Valentino et al., 2021). In this thesis the results presented by Planck Collaboration et al. (2020) will be employed where needed, e.g. to estimate the distance to galaxy given its redshift.

Other than the Hubble tension, there are several aspects of the Universe that cosmology still cannot explain to the fullest. Some covered in this section and Section 2.1 are dark energy, inflation, the formation of the first stars, and galaxy evolution. Regardless, cosmology has come to predict with great success things like the abundance of Helium, relations between redshift and distance, the existence and properties of the CMB, or the number of neutrino families, amongst others. These accomplishments serve of great motivation and confidence that, despite the difficulties, the effort of scientists is pushing our understanding of the Universe in the right direction.

2.3 Galaxies today

General references of this section: The books Extragalactic Astronomy and Cosmology; An Introduction, by Schneider (2006); and Physics of the Interstellar and Intergalactic Medium, by Draine (2011).

Galaxies are of major importance in the description of the Universe. Interestingly, the insight that our Milky Way is only one of many galaxies in the Universe is only some one hundred years old. Over the past century, a great effort by astronomers has been centered around understanding the properties and evolution of galaxies. In this section, a brief summary of present-day galaxies is presented. Also, two relevant aspects of galaxies are described in Sections 2.3.1 and 2.3.2.

The galaxies we see today can be roughly separated in three groups according to their morphology: ellipticals, spirals and irregulars. This scheme was introduced by the astronomer Edwin Hubble in the 1920s (Hubble, 1926). Figure 2.4 shows the morphological classification commonly known as Hubble's sequence or turning fork.

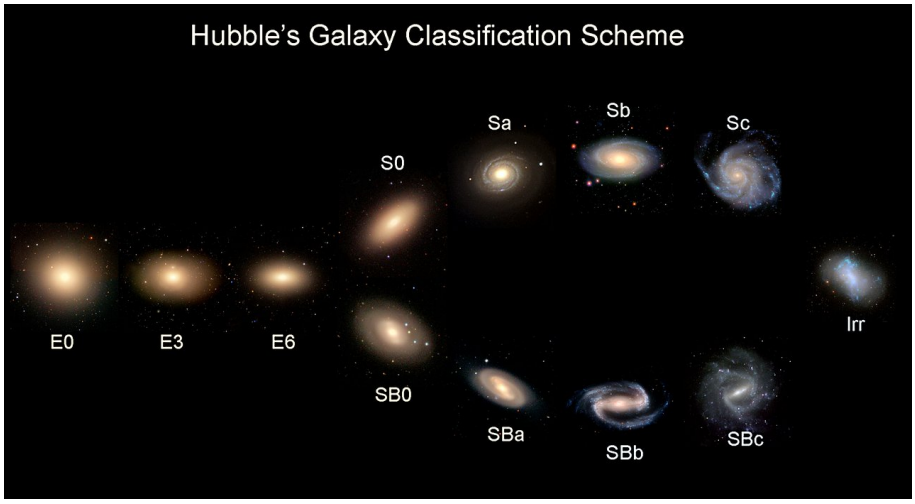

Figure 2.4: Hubble's "tuning fork" for galaxy classification (Hubble, 1926). Credit: Zooniverse; available at `https://supernova.eso.org/exhibition/images/1015_fork-1920/`.

On the left of Hubble's sequence, lie elliptical galaxies. These are shaped as ellipses, without any other clearly defined component. They range from E0 to E7, depending on their ellipticity (E0 are boxy, whereas E7 are the most elongated). On the right of Figure 2.4, lie spiral galaxies. They consist of a disk with spiral arms and a central bulge. Around $\sim 70\%$ of spirals have a stellar bar. The bar separates normal spirals (top right) from barred spirals (bottom right). They range as a, b, c, based on the properties of the disk (Sa/SBa have a bright disk with tight spiral arms and their brighteness distributed smoothly, whereas Sc/SBc have a fainter disk, with more open arms and brightness concentrated in knots of stars).

In the turning point of the fork, lie S0 galaxies (also named lenticulars). Their morphology can be described as a disk without spiral arms, resembling properties of both ellipticals and spirals. As outliers, outside the turning fork, lie irregular galaxies, whose morphology presents no regular structure.

Ellipticals and S0 galaxies are referred to as early-type galaxies, whereas spirals as late-type galaxies. These names obey historical reasons are should not be understood as an evolutionary track of a galaxy. The same can be said about Hubble's sequence. The word *sequence* does not mean that it presents stages in the life of a galaxy. There are other galaxies whose morphologies do not fit in Hubble's classification, but in practice this classification is considered a very good summary of the types of galaxies present in the local Universe.

The different morphology of elliptical and spirals is also related to their kinematic properties, such as the orbits described by their stars. Empirical studies have also shown that this is related to the luminosity of the galaxies. In ellipticals, whose morphology is less ordered than spirals, stars commonly describe random motion. The velocity dispersion of this motion (σ_0) is related to the luminosity L of the galaxy, as

$$L \propto \sigma_0^4 \ , \tag{2.8}$$

in what is known as the Faber-Jackson relation (Faber & Jackson, 1976).

On the contrary, in spiral galaxies stars tend to move orderly. They do so in the disk, with a maximum rotation velocity ($v_{\rm max}$) related to their luminosity as

$$L \propto v_{\rm max}^{\alpha} \ , \tag{2.9}$$

where $\alpha \sim 4$. This is known as the Tully-Fisher relation (Tully & Fisher, 1977).

The differences between ellipticals and spirals go way beyond just their morphology and kinematics. A key aspect which explains many differences is the presence of molecular gas (i.e. gas of H_2 molecules), the gas from which new stars form. Spirals commonly have massive reservoirs of molecular gas, whereas ellipticals do not.

As a consequence, spiral galaxies like the Milky Way are actively forming stars, whereas ellipticals form little to none. The active star formation in the arms of spirals makes it so that there are many massive young stars. Young stars usually have strong emission in ultraviolet (UV), which makes spirals appear blue when observed in the optical range. On the contrary, elliptical galaxies have mostly old stars, which tend to be low-mass and to appear more red.

Studying the properties of present-day spirals and ellipticals is crucial to get a full picture of the cosmic evolution. As explained in Section 2.1, astronomers are trying to understand the evolution from galaxies in the past (e.g. at cosmic noon) to galaxies today. For instance, spirals are tricky to describe since they have such a complex morphology, with bars, disks, arms and bulges. Current models suggest that continuous accretion of cold gas is crucial for spirals to form, and also to sustain their active star formation over long periods of time (e.g. Sancisi et al., 2008). Other authors argue the large inflows of gas might also occur via merger events (e.g. Robertson et al., 2006).

The case of elliptical galaxies could be different. Stars in ellipticals have a very high velocity dispersion σ_0, which suggests that the gas from which they formed did not have time to cool down into a disk. Following the Faber-Jackson relation (equation 2.8), they are very luminous too. Galaxies commonly have a tight relation between their luminosity in mass (e.g. Bell et al., 2003), which means that ellipticals can get very massive (at least in their stellar mass), significantly more than spirals (e.g. Vulcani et al., 2011).

Current models suggest that ellipticals may form from minor mergers of spiral galaxies (e.g. Bournaud et al., 2007; Taranu et al., 2015), where the cold gas is removed or heated, halting star formation. However, this evolutionary process, or how ellipticals came so have little molecular gas, remain to date not fully understood.

Another hypothesis is that ellipticals are an evolutionary stage of a population of galaxies with intense star formation shrouded in dust (e.g. Lilly et al., 1999; Hickox et al., 2012; Ma et al., 2015). These galaxies, named Dusty Star-Forming Galaxies, were most abundant at cosmic noon, playing an important role in the peak of SFRD. This thesis studies this population of galaxies, in particular trying to understand the star formation at small scales. This can add more evidence to the picture of what is the path by which elliptical galaxies have evolved until today.

2.3.1 Star formation at small scales

The gas and dust between the stars of a galaxy is known as the Interstellar Medium (ISM). The ISM can be in different phases, which are often defined by the state of the Hydrogen atoms, the most abundant element. In some regions of the ISM, H is ionized (HII), commonly due to photoionization of ultraviolet (UV) photons coming from young stars, which are hot and massive. In other parts, H is in a neutral state (HI).

In some regions of the ISM, Hydrogen atoms are able to bond and form H_2 molecules, commonly on the surface of dust grains. For this reason, this gas is known as molecular gas or H_2 gas. This phase of the ISM is very cool and dense. It reaches the most extreme values in the ISM, at temperatures as low as $\sim 10-50$ K, and H densities of high as $\sim 10^3-10^6$ cm^{-3}. Such dense molecular gas forms gigantic clouds that are gravitationally bound, which receive the name of Giant Molecular Clouds (GMCs). They can span sizes of dozens of pc and masses over 10^5 $M_\odot$.

It is in these clouds that star formation takes place. The importance of star formation could not be overstated, since stars are the fundamental objects in astronomy, and there are no galaxies without stars (e.g. Shu et al., 1987). In order for a star to form, clumps of this dense gas must be compressed even more, increasing the density dramatically by over 20 orders of magnitude. For this to happen, in the force balance gravity must be able to overcome opposing forces like thermal pressure or magnetic pressure. The gravitational collapse is therefore facilitated by the cool temperature of GMCs, which diminish thermal pressure. External factors like shock waves may also help compress the gas, as happens in the arms of spiral galaxies.

However, star formation is considered a very inefficient process. Only a small fraction of the H_2 gas ends up converted into stars (e.g. Evans et al., 2009). In the theoretical limit of having no forces opposing gravity, clouds would collapse at the fastest possible speed, in a time known as free-fall time (Spitzer, 1978; Draine, 2011). In reality, only $\sim 1\%$ of the gas forms stars in a free-fall time (e.g. Krumholz & Tan, 2007).

How a star is formed in a GMC is a process that remains to date not fully understood. There are great ongoing efforts by astronomers trying to expand the knowledge on star formation at these small scales, employing both observations (e.g. Yang et al., 2023; Li, 2024), and simulations (e.g. Jáquez-Domínguez et al., 2023;

Ragone-Figueroa et al., 2024). In this context, the mechanisms responsible for the inefficiency of star formation in GMCs are also very complex and only partially understood. Some of the more relevant factors are turbulence effects, magnetic fields or stellar feedback (e.g. Menon et al. 2022 and references therein).

In particular, stellar feedback plays one of the most crucial roles inside GMCs (e.g. reviews by Chevance et al. 2020, 2023). Stellar feedback refers to the effects of already-formed stars on the potential formation of new stars. The luminosity of galaxies is commonly dominated by the contribution of young massive stars (type O and B). These stars are very bright in the ultraviolet (UV) and optical parts of the electromagnetic spectrum. This emission is very energetic, and can very easily warm the molecular clouds, preventing them from cooling down. As mentioned before, gravity must overcome the force contributed by thermal pressure (amongst others). This force becomes stronger when temperature rises, which explains why stellar feedback can slow down star formation.

The growth of stellar mass is often quantified by the star formation rate (SFR). This has dimensions of mass divided by time, i.e. it quantifies the stellar mass formed in a given time. Commonly, the units of $M_\odot$ yr^{-1} are employed (see Figure 2.3). Given the dependence of star formation with molecular gas, the peak of star formation at cosmic noon is tightly related to the much larger molecular gas reservoirs in the ISM of galaxies.

2.3.2 Spectral lines

A common feature of galaxies is the presence of lines in their spectrum (see example in Figure 2.8). They exist due to the presence of atoms and molecules in the ISM of galaxies. Atoms and molecules have very specific discrete energy levels, as described by quantum mechanics. Figure 2.5 shows an example of the energy levels of two ions, singly ionized Nitrogen (NII) and doubly ionized Oxygen (OIII). The energy level represents various excitation levels.

An electron orbiting an atom can become excited, i.e. gain extra energy that makes it transition to a higher energy level. This can happen for a number of reasons, such as collisional excitations, absorption of photons, chemical reactions, or external magnetic field effects (e.g. Zeeman effect). Then, electrons in high-energy levels, have an associated probability of transitioning down to a lower energy level (see arrows in Figure 2.5). When this happens, they emit a photon whose energy (E) is the difference of energy between the two energy levels (basically, energy conservation). E is proportional to the frequency of the photon (ν) as

$$E = h\nu = h\frac{c}{\lambda} \, , \tag{2.10}$$

where h is Planck's constant. These extra photons emitted at specific frequencies are reflected in spiky peaks in the spectrum, which constitute emission lines. On the contrary, when atoms absorb photons at specific frequencies, they create absorption lines instead. In the examples of Figure 2.5, each transition (arrow) has written next to it the corresponding wavelength of the photon emitted.

The case of molecules is similar to atoms. Molecules commonly have more types of energy transitions, often unique to their structures. For instance, diatomic

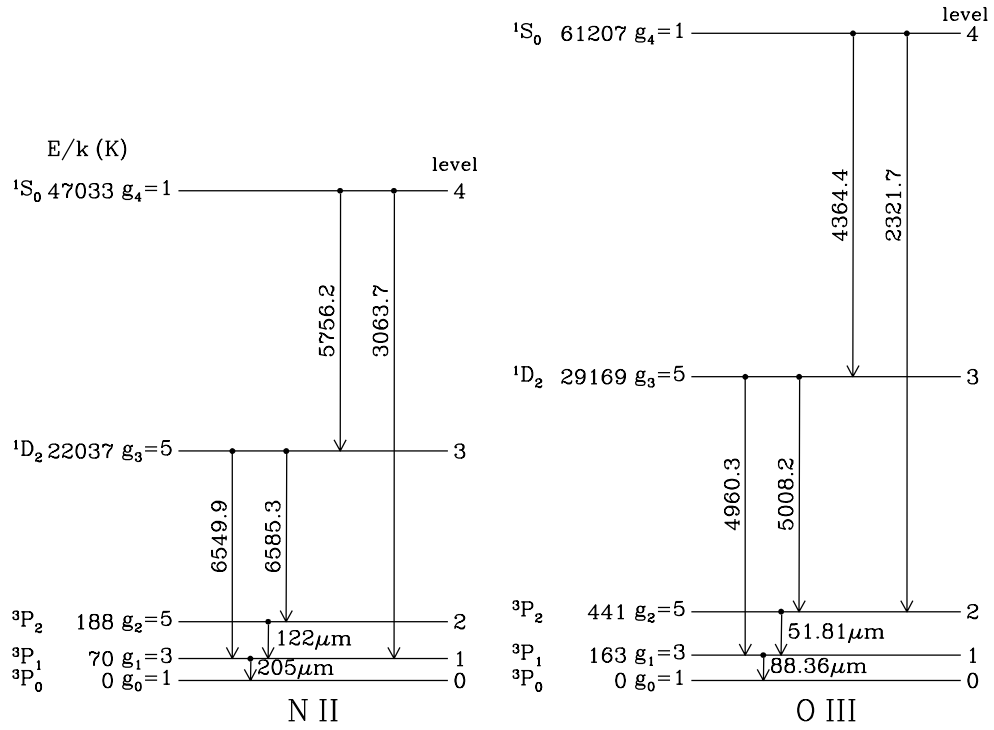

Figure 2.5: Examples of energy-level diagrams presented by Draine (2011) (their Figure 4.1); left for NII and right for OIII. They represent the excitation levels that electrons can have. Both have six electrons occupying several energy levels. The key feature is how energy levels are fixed at discrete positions (see energy E/k measured in K, where k is Boltzmann's constant). Any electron de-exciting from a higher energy level to a lower level, emits a photon in a wavelength specific to that atom, leaving thus a sort of *fingerprint*.

molecules can vibrate (stretch) along the internuclear axis, and can also rotate around an axis perpendicular to the internuclear axis. A relevant case in the study of galaxies is rotational transitions. The different ways in which a diatomic particle can rotate are quantified by the rotational quantum number J. Each rotation has a kinetic energy given by

$$E_{\text{rot}} = \frac{\hbar^2}{2m_r r_0^2} J(J+1) \ . \tag{2.11}$$

From the dependence of E_{rot} on J, it deduces that diatomic molecules rotate with increasingly more energy at higher J. In equation 2.11, $\hbar$ is the reduced Planck's constant, $m_r = m_1 m_2/(m_1 + m_2)$ the reduced mass of the molecule and r_0 the distance between the two atoms at equilibrium. The key take from this is that, similarly to the atoms shown in Figure 2.5, in molecules the energy levels are also unique to each molecule. In the case of diatomic molecules, it depends on the mass of each atom m_1, m_2, and their separation r_0.

Molecules can become excited by similar mechanisms as atoms. They can also transition to lower energy levels (e.g. a transition $J \to J-1$), emitting a photon whose energy matches the shift in energy. For a rotational transition, following

equation 2.11

$$\Delta E = E_{\text{rot, J}} - E_{\text{rot, J-1}} = \frac{\hbar^2}{2m_r r_0^2} J(J+1) - \frac{\hbar^2}{2m_r r_0^2}(J-1)J \tag{2.12}$$

$$= \frac{\hbar^2}{2m_r r_0^2}\left(J^2 + J - J^2 + J\right) \tag{2.13}$$

$$= 2B_0 J \ . \tag{2.14}$$

where the constant $B_0 \equiv \hbar^2/(2m_r r_0^2)$ contains the information of specific molecule. As shown, the energy of the photon in a given molecule depends solely on the rotational energy of the transition (given by J). The frequency of the photon is tied to the energy via equation 2.10 (i.e. $\Delta E = h\nu$).

The transitions of the H_2 molecule can rarely be observed in molecular clouds, because the temperatures it requires to become excited are too high ($\gtrsim 100$ K). In order to trace molecular gas, astronomer commonly used the next most abundant molecule, carbon monoxide (CO; Bolatto et al. e.g. 2013). The reduced mass of CO is ~ 6.9 amu. The triple bond between the C and O atoms is extremely strong, which makes them be very close to each other (i.e. r_0 is small). Following equation 2.14 and $E = h\nu$, the frequency of the photons emitted in the first five rotational transitions of CO are presented in Table 2.1.

Table 2.1: Frequency and wavelengths of the first five rotational transitions of CO. These two relate via the equation $c = \nu\lambda$.

$J \to J-1$	ν [GHz]	λ [mm]
$1 \to 0$	115.271	2.60
$2 \to 1$	230.538	1.30
$3 \to 2$	345.796	0.867
$4 \to 3$	461.041	0.650
$5 \to 4$	576.268	0.520

Given that the transitions of atoms and molecules are so well known, they are often referred to as their *fingerprints*. Spectral lines at those frequencies are evidence of their presence in a given environment. This is very useful, for instance, to estimate redshifts of distant galaxies. By observing the wavelength at which lines are emitted, astronomers can compare against tabulated values and calculate the redshift via equation 2.6. This is known as the *spectroscopic* redshift.

2.4 Schmidt-Kennicutt relation

Astronomers have historically tried to find a quantifiable relation between the star formation in a galaxy and the properties of the Interstellar Medium (ISM). An empirical relation was first proposed by Maarten Schmidt (Schmidt, 1959, 1963) focusing on the Milky Way. He theorized that the SFR density of a galaxy (ψ) is proportional to the total interstellar gas density (ρ_{gas}), with an exponent N, as

$$\psi \propto \rho_{\text{gas}}^N \ .$$

The first studies where this relation was extended to major surveys of galaxies were carried out by Robert C. Kennicutt Jr (Kennicutt, 1989, 1998). Here, the SFR and gas mass are considered in the form of their surface densities ($\Sigma_{\rm SFR}$ and $\Sigma_{\rm gas}$, respectively), rather than volume densities, i.e. SFR and gas mass are calculated in a given surface rather than volume. This is done since areas in the sky can be calculated directly from observations, whereas measuring the third spatial dimension is usually more challenging. The equation proposed by Kennicutt (1989) is therefore

$$\Sigma_{\rm SFR} = A \left(\Sigma_{\rm gas}\right)^N \ , \tag{2.15}$$

where A is some constant. In a log-log scale, equation 2.15 becomes

$$\log \Sigma_{\rm SFR} = N \log \Sigma_{\rm gas} + A' \ , \tag{2.16}$$

where the constant A was redefined $A' \equiv \log A$. In Kennicutt (1998), equation 2.16 was empirically tested in a sample of 61 spiral galaxies, and 36 starburst galaxies (i.e. galaxies with high SFR), obtaining the plot shown in Figure 2.6. This showed a striking straight-line with a slope $N \approx 1.4$.

Figure 2.6 and equation 2.16 consider the total gas in the ISM, which is mostly HI (neutral Hydrogen) and H_2 (molecular Hydrogen), i.e. $\Sigma_{\rm gas} = \Sigma_{\rm HI} + \Sigma_{\rm H_2}$. As discussed in Section 2.3.1, it is now known that stars form from H_2 (molecular gas) and not HI. More specifically, Wong & Blitz (2002) have shown that the correlation between $\Sigma_{\rm SFR}$ and $\Sigma_{\rm H_2}$ is strong across many orders of magnitude, whereas the correlation with $\Sigma_{\rm HI}$ is much weaker and only found in a very small range (below 10 $M_\odot$ pc^{-2}). For this reason, it is common to neglect the HI contribution and study the relation

$$\Sigma_{\rm SFR} = A \left(\Sigma_{\rm H_2}\right)^N \ , \tag{2.17}$$

or alternatively

$$\log \Sigma_{\rm SFR} = N \log \Sigma_{\rm H_2} + A' \ . \tag{2.18}$$

Equation 2.17 is known as the "Schmidt-Kennicutt (SK) relation", in honor of the astronomers who pioneered this work. The SK relation has become one of the best ways to describe star formation in galaxies, to the point where it is often referred to as *the* "star formation law" (e.g. Casey et al., 2014).

One important caveat about the SK relation, comes from the fact that the mass of molecular gas and the star formation rate are calculated in a surface area. This assumes that $\Sigma_{\rm SFR}$ and $\Sigma_{\rm H_2}$ are co-spatial, i.e., that stars form in the same regions where there is H_2. The correlation shown in Figure 2.6 is so strong because this assumption is mostly correct across many environments, but situations where this is violated could make the SK relation inadequate to describe the star formation.

The two constants in the SK relation (A and N, see equation 2.17), are tightly related to several physical mechanisms. As explained in the review by Casey et al. (2014), the normalization constant A can be understood as the star formation efficiency, i.e. how easily stars form out of a parcel of gas. For instance, a starburst galaxy is expected to have a larger A than a *normal* galaxy, which means that it can form many more stars (higher $\Sigma_{\rm SFR}$) from the same amount of molecular gas (same $\Sigma_{\rm H_2}$). It moves a galaxy up or down the plot of Figure 2.6. The star formation efficiency can be affected by several factors such as turbulence in the ISM or feedback from stars.

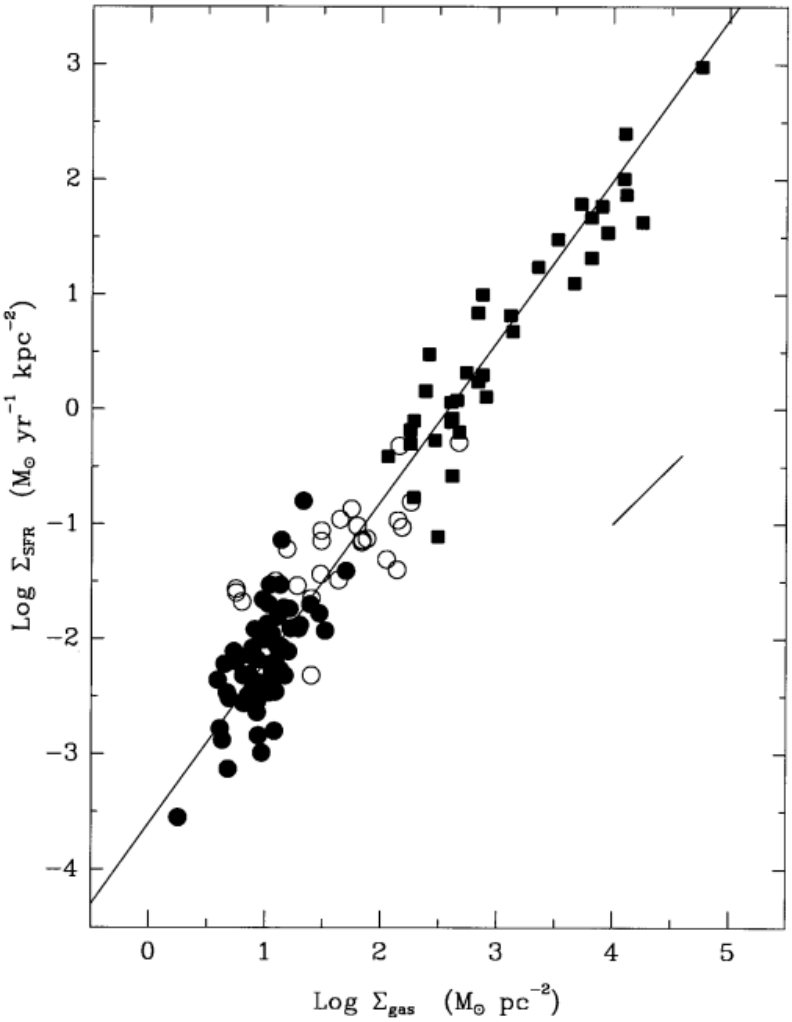

Figure 2.6: Star formation relation for spiral and starburst galaxies (circles and squares, respectively), presented in the original work by Kennicutt (1998). The quantities in the axes are divided by an area (pc^2 and kpc^2), since they represent surface densities (as introduced in equation 2.15). The relation is a straight line as predicted by equation 2.16, with $N \approx 1.4$. One remarkable aspect reflected in the graphic is that, since the axes are in log, the correlation is consistent across several orders of magnitudes. The gas in the x-axis includes both HI and H_2.

N, the slope in log-log SK relation as shown in equation 2.18, is a much more critical parameter. It reveals insights of the small scale physics of star formation. For instance, a unity slope (i.e. $N = 1$) implies $\Sigma_{\mathrm{SFR}} \propto \Sigma_{\mathrm{H_2}}$, i.e. with more molecular gas, star formation increases at the same rate. This implies that GMCs are basically identical to each other: counting two instead of one doubles the mass as it also doubles the formation of stars. For this reason, this is often referred to *universal star formation*. A slope of $N = 1.5$ is consistent with the free-fall time of GMCs, which is the fastest they can collapse in theory (see Section 2.3.1). A slope $N < 1$ can point at a large presence of diffusive molecular gas in the ISM (e.g. Shetty et al., 2014), which is not as dense or cold as the dense molecular gas where stars more commonly form (Draine, 2011).

In Figure 2.6 each data point comes from a different galaxy. Another common way of studying the SK relation is in *resolved* studies, i.e., comparing different parts of the same galaxy instead of comparing different galaxies. This is challenging because it requires observing with better spatial resolution that allows to tell apart different regions of a galaxy (i.e. to *resolve* a galaxy), instead of just observing it as one whole. Regardless, this has been done extensively in the nearby Universe (e.g. Bigiel et al., 2008, 2011; Leroy et al., 2013; Bolatto et al., 2017; Pessa et al., 2022; Leroy et al., 2025). One recent example is the work by Sun et al. (2023), who used resolved measurements across 80 nearby galaxies to produce the SK diagram presented in Figure 2.7.

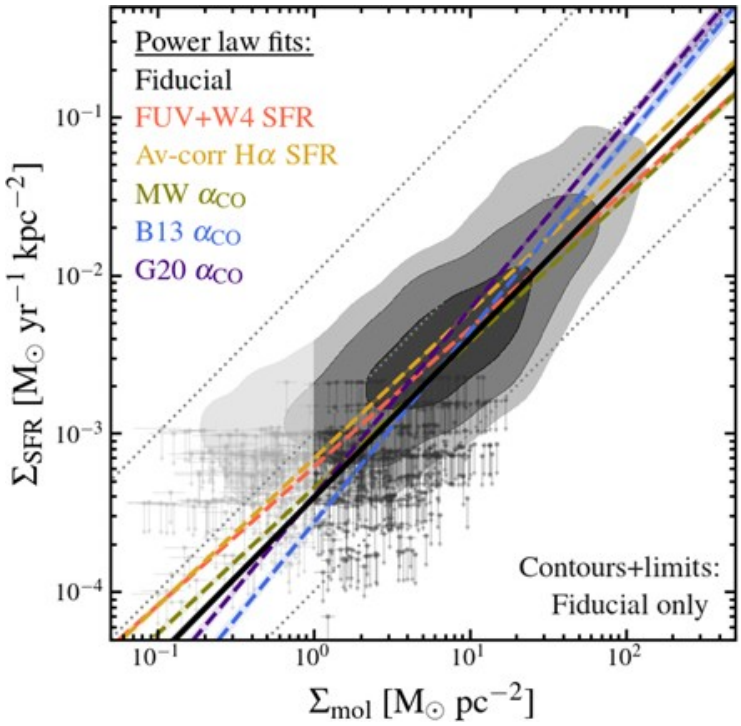

Figure 2.7: Resolved Schmidt-Kennicutt relation for 80 nearby galaxies, presented by Sun et al. (2023). The resolved measurements are at a scale of $\sim$ 1.5 kpc. Contours show 40%, 80% and 95% density levels of all measurements. The dashed colored lines are fits obtained with different methods; they are consistent with a unity slope ($N = 0.88 - 1.21$). Grey dotted lines represent depletion times of 100 Myr, 1 Gr and 10 Gyr (from top left to bottom right).

Figure 2.7 reveals several relevant aspects of the (resolved) Schmidt-Kennicutt relation. One is the diagonal depletion time lines $\tau_{\rm dep}$, shown in grey dots. The depletion time is how long it would take for a galaxy to use up all the available molecular gas at a given star formation rate. For instance, a total H_2 mass of 10^9 $M_\odot$, where stars are forming at a rate of 1 $M_\odot$ yr^{-1}, would be used up it a time of

$$\tau_{\rm dep,\ example} = \frac{10^9\ M_\odot}{1\ M_\odot\ yr^{-1}} = 10^9\ yr\ , \tag{2.19}$$

i.e. the depletion time is 1 Gyr. In the SK diagram, values across a diagonal with slope 1 have the same depletion time. The depletion time can also be understood

as the opposite of the star formation efficiency (A in equation 2.17); how easily stars form from a parcel of gas (i.e. A) is inversely proportional to how quickly the molecular gas is used up (i.e. $\tau_{\rm dep}$).

A slope of $N = 1$ in the SK diagram implies a constant depletion time. This is the consensus in the literature amongst resolved observations of galaxies in the nearby Universe (e.g. the already mentioned Bigiel et al. 2011; Leroy et al. 2013; Pessa et al. 2022; Sun et al. 2023), as reflected in Figure 2.7. The corresponding depletion time is commonly in the range $\tau_{\rm dep} \approx 2 - 2.5$ Gyr.

Another interesting aspect of Figure 2.7 is that the fitted slope can change when employing different methods. This could lead to astronomers drawing different conclusions from the same set of observations. Furthermore, different ways of calculating $\Sigma_{\rm SFR}$ and $\Sigma_{\rm H_2}$ also introduce significant uncertainties to the SK relation. The work presented in this thesis is obviously no exception to this, as will be discussed in Chapter 5.

Figures 2.6 and 2.7 reflect how the SK relation can change at different resolutions (unresolved and resolved galaxies). When astronomers zoom-in even more, to scales well below 1 kpc (e.g. < 100 pc), the SK relation commonly breaks completely (e.g. Pan et al., 2022). This is because at such scales molecular clouds and star-forming regions are more clearly separated, which violates the key assumption behind the SK relation (i.e. formation of stars and molecular gas are co-spatial).

The SK relation has also been tested at high-redshift (e.g. Daddi et al., 2010; Genzel et al., 2010), although less extensively than in the nearby Universe. Since objects are much further away, a much better spatial resolution is needed to make resolved studies. Modern telescopes like the Atacama Large Millimeter/submillimeter Array (ALMA) have recently allowed astronomers to achieve this, although it has commonly been done only in individual objects with no consistent approach amongst different authors (e.g. Hodge et al., 2015; Thomson et al., 2015; Hatsukade et al., 2015; Chen et al., 2017; Vallini et al., 2023; Arriagada-Neira et al., 2025).

For the first time ever in the literature, this thesis will study the N parameter of the SK relation in a large sample of galaxies at high-redshift. Unlike the various studies cited above, this work will approach all galaxies systematically with the same algorithm. This will allow for a fair comparison free of biases introduced by different methodologies.

2.5 Dusty Star-Forming Galaxies

General reference of this Section: The comprehensive review by Casey et al. (2014).
A significant discovery in the study of the high-redshift Universe is a population of galaxies that are extremely bright at far-infrared (IR) and submillimeter (submm) parts of the electromagnetic spectrum, but almost invisible in the optical or ultraviolet (UV) ranges. These galaxies were first detected in the 1990s by Smail et al. (1997) using measurements at 0.85 mm of the Submillimeter Common-User Bolometer Array (SCUBA; Cunningham et al. 1994), on the James Clerk Maxwell Telescope (JCMT) in Hawaii. Since they are detected in the submm range, they are often referred to as Sub-Millimeter Galaxies (SMGs).

The optical, near-IR and UV wavelengths are where most of the luminosity produced by stars is expected (e.g. Driver et al., 2008); with UV and blue light mainly coming from young stars. The little emission of SMGs in these ranges is due to the presence of significant amounts of dust grains in their interstellar medium (ISM). Dust absorbs the starlight radiation, effectively hiding it away. Dust then gets heated and re-emits via thermal emission at far-IR ($\sim 15 - 1000\ \mu$m). This finding was very important for astronomers as it showed that star formation (SF) cannot only be studied in the optical and UV ranges as it was commonly done; doing so would miss about half of the star formation activity in the Universe.

The IR luminosity of SMGs coming from dust is very extreme. It can very easily reach the ranges $L_{\rm IR} > 10^{11-12}$ L$_\odot$, which places SMGs in the category of (ultra) luminous infrared galaxies ((U)-LIRGs; Sanders & Mirabel 1996). (U)LIRGs are galaxies defined by this high IR luminosity ($L_{\rm IR} > 10^{11}$ L$_\odot$ for LIRGs and $L_{\rm IR} > 10^{12}$ L$_\odot$ for ULIRGs). (U)LIRGs are rich in molecular gas and commonly triggered by strong interactions or merger between spiral galaxies. They are rare in the local Universe but become dominant from $z \sim 0.3$. SMGs can even reach $L_{\rm IR} > 10^{13}$ L$_\odot$ (Hyper-luminous infrared galaxies; HyLIRGs), which puts them close to the most luminous galaxies ever detected in the Universe (e.g. Tsai et al., 2015).

Such high IR luminosity emitted by the dust grains can only be explained if they are hit by an extreme amount of radiation coming from the stars, particularly young O and B stars. Since these stars are so short-lived, a high SFR is needed to maintain this radiation. In fact, SMGs are considered the most intense starbursts in the Universe, with SFRs up to a few 1000 M$_\odot$ yr^{-1} (i.e. they can form stars with a total mass equivalent to over 1000 time our Sun, in just one year). This is close to the maximum that a galaxy can sustain (e.g. Barger et al., 2014). As a comparison, the SFR of the Milky Way is only $\sim 1 - 4$ M$_\odot$ yr^{-1} (e.g. Chomiuk & Povich, 2011). This is even more impressive considering how compact SMGs are; their typical effective radius (i.e. the radius containing half of the total luminosity) is $r_{\rm eff} \sim 1.8$ kpc (e.g. Hodge et al., 2016), compared to the Milky Way's $r_{\rm eff} \sim 4 - 4.5$ kpc (e.g. Zhou et al., 2023).

Due to their physics, i.e. having a high SFR which is almost entirely shrouded by dust, SMGs are also refereed to as Dusty Star-Forming Galaxies (DSFGs). This term will be employed from now on in this work to refer to this population of galaxies. DSFGs have a median redshift of $2.4 - 2.6$ (e.g. Chapman et al., 2003; Dudzevičiūtė et al., 2020). Following equation 2.6, at this redshift an intrinsic far-IR emission is observed at a wavelength of a few $\sim$0.1 mm, which explains why DSFGs are detected in the submm range.

Furthermore, a redshift of ~ 2.5 places DSFGs right at cosmic noon, i.e. in the peak of SFRD as shown in Figure 2.3, some 10 to 11 billion years ago. In this context DSFGs were key, as star formation at cosmic noon was dominated by the dust-obscured component (e.g. Zavala et al., 2021; Algera et al., 2023). DSFGs have also been detected well into the Epoch of Reionization (e.g. Strandet et al., 2017; Jarugula et al., 2021) though this is rare, since at this stage it has been too little time after the Big Bang for them to form their large amounts of dust.

In Schmidt-Kennicutt relation, DSFGs have been shown to lie in the high $\Sigma_{\rm H_2}$ end of the relation (e.g. Hagimoto et al., 2023), with larger reservoirs of molecular gas

and higher star formation rates than local galaxies. Given their starburst nature, they also have much shorter depletion times, often close to 100 Myr. Tentative resolved studies show that, opposite to local galaxies, DSFGs do not have constant depletion times, they rather have a resolved slope $N > 1$ (e.g. Hodge et al., 2015; Thomson et al., 2015; Hatsukade et al., 2015; Chen et al., 2017). This thesis will further constrain the slope of DSFGs in the resolved SK relation, which has never been done in large samples.

All things considered, studying DSFGs is pivotal for astronomer to get a full picture of cosmic history. Not only did they play a crucial role in the time of the Universe where the majority of the stars were formed, but they are also outstanding candidates to be ancestors of modern-day elliptical galaxies (e.g. Lilly et al., 1999; Hickox et al., 2012; Ma et al., 2015). As mentioned in Section 2.3, ellipticals are very massive, and barely form stars since there is almost no H_2 available. The short depletion time of DSFGs could be the reason they evolved into galaxies with so little H_2 available. Furthermore, their large H_2 reservoirs could explain why ellipticals have such high stellar masses.

In Figure 2.8 a typical spectrum of a DSFG is presented. The continuum emission is significant between the mm and far-IR ranges ($\sim 200 - 2200$ GHz), due the the dust thermal emission as described above. There is also a wealth of spectral lines, from molecules like CO, H_2O, CH^+, or OH^+, to atoms like C, N, or O. These lines reveal the presence of a wealth of atoms and molecules in the ISM of DSFGs, as explained in Section 2.3.2.

There are a number of features which help astronomers observe DSFGs at high-redshift. One of them is the negative k-correction, visualized in Figure 2.9. Objects, naturally, appear dimmer the further away they are. This is the case for DSFGs at increasingly higher redshift. However, since the spectrum is shifted to longer wavelengths, the window observed by ALMA captures parts closer to the peak of the spectrum. As reflected in Figure 2.9, this means that ALMA can observe DSFGs across a large range of redshifts at a similar flux density.

Another recurring feature is gravitational lensing. This occurs when an object lies in the line-of-sight between us, the observers, and a galaxy. Due to effects predicted by the theory of general relativity, the light coming from the background galaxy is bent and magnified by the object in the line of sight (Einstein, 1936; Hewitt et al., 1988), as depicted in Figure 2.10. This results in an image resembling a ring, commonly named Einstein Ring. Since the light is magnified, this effect allows for studies of galaxies that would otherwise be too faint to even detect.

It has been shown that gravitational lensing is very common amongst DSFGs in the literature (e.g. Bakx et al., 2018). This is clearly an observational bias; unlensed galaxies are far more difficult to even detect. Lensing events preserve surface density brightness (i.e. radiation and projected size are equally amplified), which means that such effects will not be taken into account in the Schmidt-Kennicutt analysis. Modeling gravitational lenses, in DSFGs or any other type of galaxy, is an extremely complex problem which requires sophisticated tools and is beyond the scope of this project (e.g. Atek et al., 2018; Gururajan et al., 2022).

Lastly, it must be said that much of our understanding on DSFGs comes from past decade, thanks to the development of modern telescopes such as the Atacama

Large Millimeter/submillimeter Array (ALMA; see the comprehensive review by Hodge & da Cunha 2020). ALMA has allowed for observations at much better angular resolution and sensitivity than previously possible. Also, the frequency coverage of ALMA (see Section 3.2.2) captures key features of these galaxies, such as the dust emission and a number of emission lines. This observational improvement is even more important in the study of DSFGs when considering that theoretical approaches have been largely unsuccessful. Models and simulations have struggled to predict the origin, characteristics, fate or number density of these extreme objects (e.g. Hayward et al., 2013). This thesis will employ ALMA observations of DSFGs at high-angular resolution (see Section 3.2.3), which means that this work would not be possible without the advent of such technology.

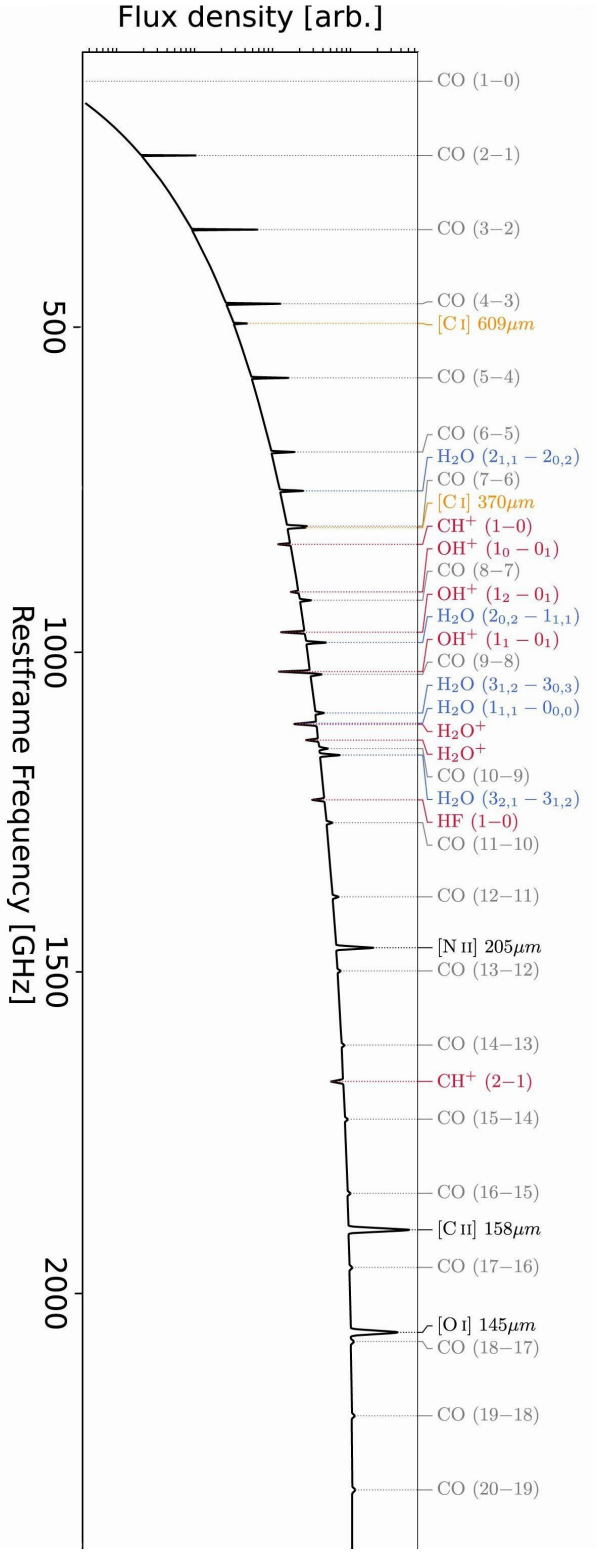

Figure 2.8: Typical spectrum of a dusty galaxy, as presented by Bakx et al. (2024) (this is a modified version of their figure). The most prominent features are the continuum emission, coming from the dust, based on a two-body model by Pearson et al. (2013), and the spectral lines of a local ULIRG as presented by Rangwala et al. (2011). The first five emission lines of CO are at the frequencies shown in Table 2.1. In terms of wavelength, the frequency range shown covers from far-IR to mm.

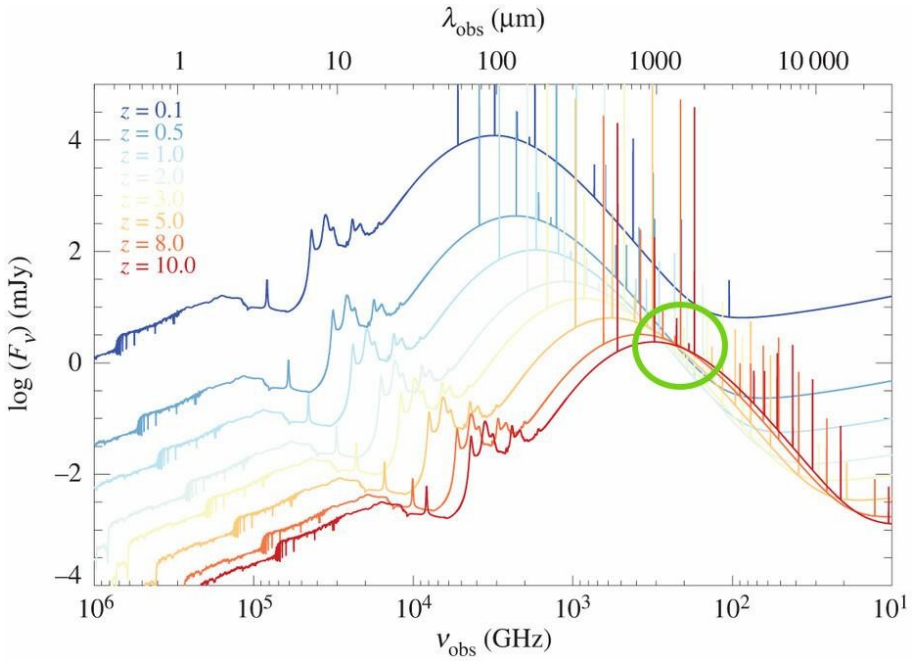

Figure 2.9: Visualization of the negative k-correction, as presented by Hodge & da Cunha (2020). Each spectrum is the observed flux density of an example ULIRG at different redshift. The spectrum becomes dimmer (i.e. moves further down) at higher redshifts, but it is also shifted to longer frequencies (i.e. moves to the right, following equation 2.6). These two effects offset each other almost perfectly at around $\lambda \sim 1$mm (marked in a green circle) where there is a similar flux for galaxies from $z = 0.5$ through $z = 10$, a range spanning from ~ 5 to over ~ 13 billion years ago. This allows for DSFGs to be studied across a large redshift range by ALMA.

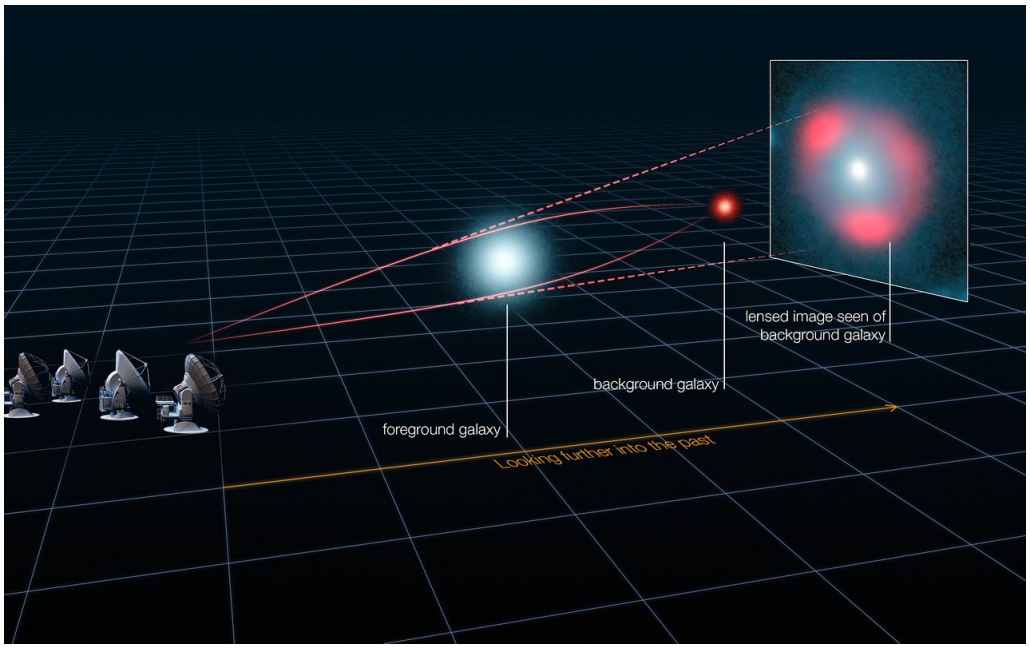

Figure 2.10: Schematic of gravitational lensing. ALMA (antennas) is observing a dusty star-forming galaxy (background galaxy), where a foreground galaxy (or cluster) in the line-of-sight is magnifying the light coming from the DSFG. This results in the DSFG showing a ring-like structure, commonly named Einstein Ring. This structure can show multiple images of the same region of the galaxy. Image credit: ALMA (ESO/NRAO/NAOJ), L. Calçada (ESO), Y. Hezaveh et al.; available at `https://www.eso.org/public/australia/images/eso1313b/?lang`.

3
Methodology

In this chapter, the parent sample of the galaxies studied is described in Section 3.1. The basics of radioastronomy, ALMA, and the data employed is presented in Section 3.2. Lastly, how the data is processed is described in Sections 3.3, 3.4, 3.5, 3.6 and 3.7.

3.1 Parent sample: HerBS

The Dusty Star-Forming Galaxies (DSFGs) studied in this work are a sub-sample of the *Herschel* Bright Sources sample (HerBS). The HerBS sample was first defined by Bakx et al. (2018), based on existing observations of the *Herschel* Astrophysical Terahertz Large Area Survey (H-ATLAS; Eales et al. 2010). This a survey in which the *Herschel* Space Observatory observed over 600 deg^2 of the sky, more than four times the total area of all previous *Herschel* extragalactic surveys combined. This was done for a remarkable observing time of $\sim$ 600 hours, which allowed for great sensitivity to fainter objects, across five photometric bands (100, 160, 250, 350 and 500 μm, Valiante et al. 2016).

H-ATLAS observed a total five fields in the sky (see Figure 3.1); one close to the North Galactic Pole (NGP), three equatorial fields previously observed in the Galaxy And Mass Assembly survey (GAMA-9, GAMA-12, GAMA-15; Driver et al. 2009), and one close to the South Galactic Pole (SGP). It detected close to half a million sources. Following the first major data release of H-ATLAS (Valiante et al., 2016), Bakx et al. (2018) defined the HerBS-sample based on the flux density at 500 μm (S_{500}; flux density is the power per unit area per unit frequency, commonly measured in Jansky, Jy) and photometric redshift ($z_{\rm phot}$) of the sources, as

1. $S_{500} > 80$ mJy, and
2. $z_{\rm phot} > 2$.

After removing all nearby galaxies and blazars, the HerBS sample consists of 209 sources across the NGP, GAMA-9, GAMA-12, GAMA-15 and SGP fields. These were labeled HerBS-1 through HerBS-209 in descending order of S_{500} (i.e. the brightest galaxies are at the beginning of the catalogue). The positions in the sky of the entire sample are shown in Figure 3.1.

The coordinates, densities flux measurement, estimated redshift and luminosity of all 209 sources are presented in Table A1 of Bakx et al. (2018) (later corrected in Bakx et al. 2020a). These were calculated with observations by the Spectral and Photometric Imaging Receiver (SPIRE; Griffin et al. 2005) and Submillimeter Common-User Bolometer Array 2 (SCUBA-2; Holland et al. 2013). The former was

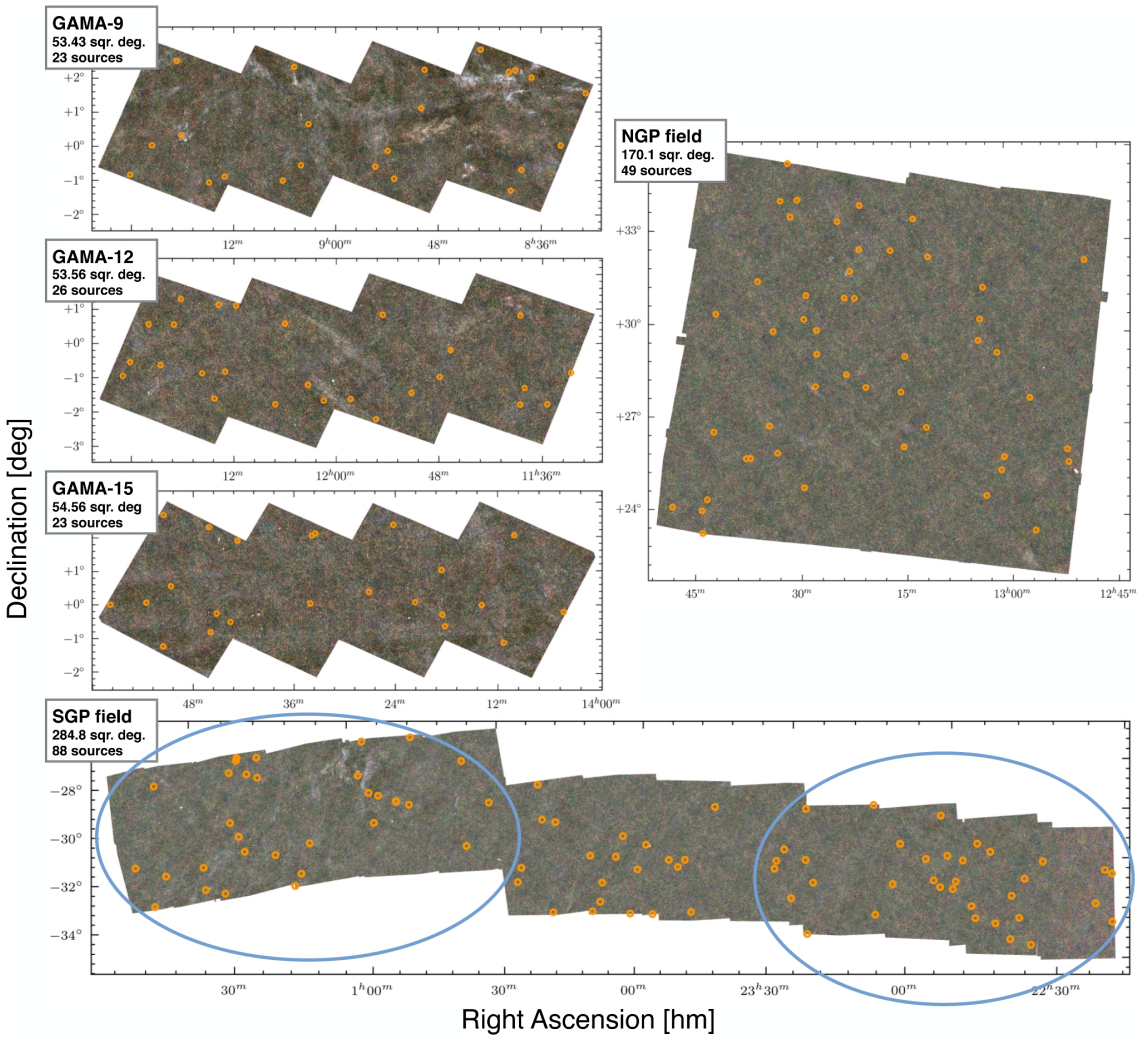

Figure 3.1: All sources 209 of the HerBS sample (in orange), across five fields in the sky observed by H-ATLAS (Eales et al., 2010). The x and y axes correspond to Right Ascension (R.A.) and declination (Dec.) coordinates in the International Celestial Reference System (ICRS; see Appendix A for a brief description of celestial coordinates). Inside blue ellipses, the 67 sources that are a part of my work. Upon observations at higher angular resolution, many of these sources have been resolved into multiple DSFGs. This figure is taken from Bakx et al. 2018 (Figure 1).

in *Herschel*, and the latter is in the James Clarke Maxwell Telescope (JCMT), as the modern replacement of SCUBA mentioned in Section 2.5.

The selection criteria of the HerBS sample potentially introduce an important bias: only the brightest DSFGs are taken into account; it might miss the physics taking place on fainter DSFGs. This is a common compromise since fainter objects are difficult to observe and detect. However, as Bakx et al. (2018) point out, a significant fraction of the sources are gravitationally lensed (around 76%). This means that many of the sources might not be so luminous intrinsically, but appear brighter to us due to the presence of an object in the line-of-sight magnifying their light (see Section 2.5). As a consequence, the HerBS sample can probe the properties

DSFGs across a wide range of luminosities, from luminous infrared galaxies (LIRGs) to hyper-luminous infrared galaxies (HyLIRGS). This has actually been shown more recently by Bakx et al. (2024). Considering this and the redshift criterion, the HerBS sample is a great window to explore a variety of DSFGs at cosmic noon.

In H-ATLAS, the observations achieved a resolution of $\sim 36''$ at 500 μm (Eales et al., 2010). This is significantly larger than the typical angular size of a DSFG at $2 < z < 3$ (often $\sim 1''$ or less). For this reason, this sources observed by *Herschel* can be understood as unresolved *blobs*. Upon observations with higher angular resolution, many of the initial sources were resolved into multiple galaxies, labeled A, B, C, and so on.

The sources located in the SGP field have been the subject of the Bright Extragalactic ALMA Redshift Survey (BEARS) science programme. In a first study by Urquhart et al. (2022), they targeted 85 sources which were resolved into 142 galaxies. They obtained accurate spectroscopic redshift measurements of 71 galaxies, following an analysis of spectral lines as outlined by Bakx et al. (2020b). They employed observations of ALMA and the Atacama Compact Array (ACA). In a second BEARS study (Bendo et al., 2023), ALMA continuum images for those 85 sources are presented, with a thorough photometric study.

The most recent BEARS work (Hagimoto et al., 2023) studied the emission lines of 71 HerBS sources at great depth, which included a study on their star formation with the Schmidt-Kennicutt relation, similarly to the aim of my thesis. They employed ALMA observations at resolution $\sim 2-3$ arcsec. This allowed for a good global description of the galaxies, but it was insufficient for a resolved study. Bakx et al. (2024) improved on this SK study on 16 sources, using high-resolution ALMA observations ($\sim 0.1-0.5$ arcsec). They targeted only the sources close to the center of the SGP field (in Figure 3.1, the sources excluded from the blue ellipses), in order to make their ALMA observations more efficient.

The sample of DSFGs used in my thesis corresponds to the 67 sources in the SGP field inside the blue ellipses. These sources have observations with a spatial resolution comparable to that of Bakx et al. (2024), which will allow me to improve on the SK analysis done by Hagimoto et al. (2023). The 67 sources of my sample have been resolved into 122 different DSFGs. For a full description of my sample see Section 4.1.

3.2 Radioastronomy

General reference of this section: The book Essential Radio Astronomy by Condon & Ransom (2016).

Observing the Universe from Earth is challenging. Thanks to the advent of new technologies, scientists have been able to develop ever more sophisticated telescopes throughout the past century. These have certainly helped, but there are some obstacles intrinsic to the nature of our Earth which no amount of technological progress can overcome.

Figure 3.2 presents a description of the Earth's atmosphere's transparency to radiation. Its transmission level is plotted against the electromagnetic spectrum. The atmosphere blocks radiation in a large part of the spectrum. It absorbs incoming

light in the gamma-ray wavelengths, X-ray, ultraviolet (UV), and most infrared (IR). This shielding has been crucial for life on Earth to develop as we know it, as it protects humans and animals from dangerous radiation. There are, however, two major windows which the atmosphere does not block. One of them is in the visible or optical range ($\lambda \approx 380$ nm $-$ 780 nm), including some near-IR. This is the part of the spectrum that the human eye has evolved to see, precisely because the atmosphere let's that radiation through (hence the name visible/optical). Astronomical objects are actively studied from Earth in this range, e.g. with the Very Large Telescope in Chile.

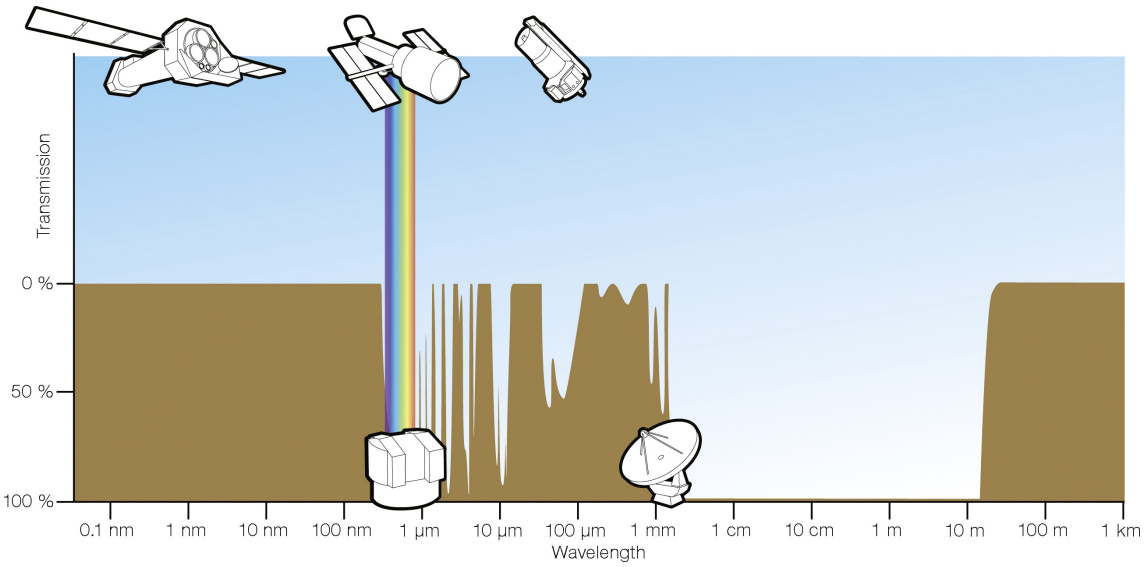

Figure 3.2: Atmosphere transmission across the electromagnetic spectrum. Brown represents the atmosphere blocking the radiation. The main two windows, at ∼100% transparency, are in the optical/visible (with the rainbow), and the radio window (across five orders of magnitude in λ). A few examples of telescopes are included; in the ground for the optical and radio windows, and in space for the other ranges. This plot is taken from Condon & Ransom 2016 (Figure 1.1).

The other range of the electromagnetic spectrum where the atmosphere is transparent is in the radio waves. This is a very broad window, spanning up to five orders of magnitude in the range $\lambda \approx 0.3$ mm $-$ 30 m ($\nu \approx 10$ MHz $-$ 1 THz in frequencies). This is known as the radio window. Together with the optical window, these are the two parts of the spectrum that astronomers can observe from the ground. All others require space telescopes to be studied (e.g. Fermi for gamma-rays, Chandra for X-rays, Galaxy Evolution Explorer for UV, or James Webb for IR).

Radioastronomy is therefore the study of radio emission from sources in space. It was pioneered by Jansky (1933), who first detected radio noise from the Milky Way. Radioastronomy has been crucial in pushing our understanding of the Universe ever since. Nearly all objects emit radio waves at some level. Since the radio window is so broad, almost all objects and radiation mechanisms can be observed at radio wavelengths. Even if the energies of the waves are low (due to their low frequencies), the processes they describe are not necessarily low-energy. Some objects studied with

radioastronomy, such as quasars, supernovae or pulsar, are commonly explosive and powerful.

A distinctive feature of radio telescopes is how large they are. In astronomy, the angular resolution (θ_{res}) is the smallest angle in the sky that a telescope can distinguish, i.e. *resolve*. Smaller angles than this are not distinguished reliably. Then, in order to study the fine details of an object, a good resolution is needed (i.e. a high-resolution, which means small θ_{res}). The resolution of a telescope in radians is approximately proportional to

$$\theta_{\text{res}} \propto \frac{\lambda}{D} \, , \tag{3.1}$$

where λ is the wavelength of the radiation, and D the diameter of the telescope. Since radioastronomy studies the longest wavelengths of the electromagnetic spectrum (see Figure 3.2), large telescopes needed to lower θ_{res} and get a good resolution. Therefore, radioastronomy employs big antennas, capable of capturing the radio waves coming from space. These single antenna are commonly known as single dish. Some of the most iconic ones are the Large Millimeter Telescope in Mexico ($D = 50$ m), the Green Bank Telescope in the United States ($D = 100$ m), and the Five-hundred-meter Aperture Spherical Telescope in China ($D = 500$ m, largest in the world).

The resolution of a radio telescope is commonly indicated by its the beam. The beam is the region in the sky in which radiation can be detected by the radio telescope. It basically measures the area in the sky that the telescope is sensitive to, reflecting the angular sensitivity pattern (Marr et al., 2015; Snell & Kurtz, 2019). Figure 3.3 shows the typical beam of a radio telescope.

Beams are often approximated as Gaussian. This means that the sensitivity of the radio telescope peaks at the center (straight-on direction at $\theta = 0$), and for longer angles it decays following the curve shown in Figure 3.3. If the beam was instead a rectangle unit or top-hat, the response would be uniform across a given angle (e.g. θ_{TH}), and then drop to zero. In such case, the telescope would have totally independent responses in regions in the sky separated by a distance of θ_{TH}. In reality, given the beam shown in Figure 3.3, the responses are not fully independent at any angular separation when observing an object with a radio telescope.

The total area of the nearly Gaussian beam can be calculated directly from the half-power beamwidth angle θ_{HPBW}, following equation 3.118 of Condon & Ransom (2016)

$$\Omega_{\text{A}} = \left(\frac{\pi}{4 \ln 2} \right) \theta^2_{\text{HPBW}} \approx 1.133 \; \theta^2_{\text{HPBW}}. \tag{3.2}$$

This is known as the *solid angle* of the Gaussian beam.

3.2.1 Interferometry

In order to improve angular resolution significantly, a number of radio telescope antennas can operate together. Such array is known as an interferometer. When multiple antennas observe together, the distance between two antennas is called baseline. Following equation 3.1, the resolution of an interferometer is calculated

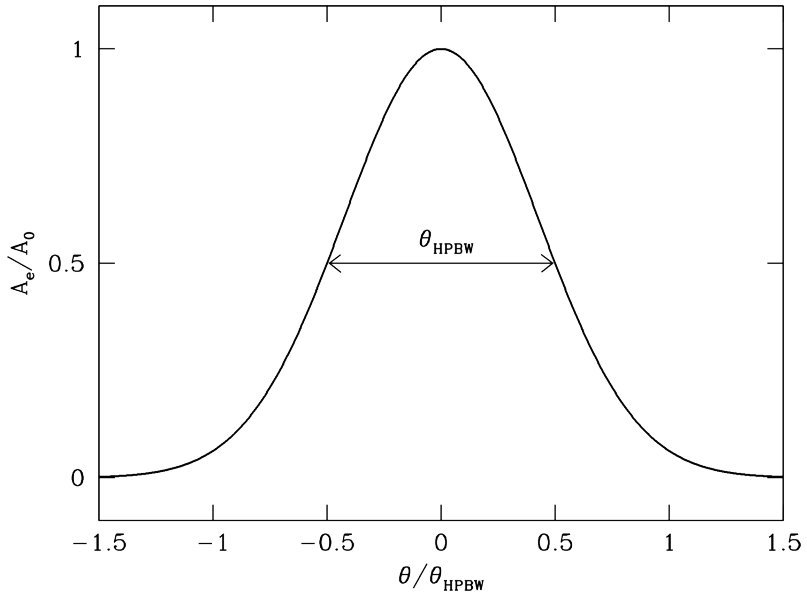

Figure 3.3: Typical beam of a radio telescope. The effective antenna aperture is plotted against offset angle (both in normalized units). The distribution is characterized by θ_{HPBW}, the half-power beamwidth (HPBW; the width angle at half the peak). The distribution is nearly Gaussian, meaning that at the center the antennas response is maximized, and then it decays at lower angles. Crucially, this decay is neither sharp nor all the way down to zero (it is not a rectangle or top-hat distribution). This plot is taken from Condon & Ransom 2016 (Figure 3.15).

with D being equal to the longest baseline of the array. An array of antennas located kilometers apart from each other can therefore achieve angular resolutions that are beyond the reach of single dishes.

The simplest interferometer has two antennas. In Figure 3.4, a schematic of such situation is presented. The interferometer works not by directly studying the signal from the source, but rather from measuring the different responses of each antenna (Jolly, 2021). Both antennas produce the same signals V_1 and V_2, only delayed in time,

$$V_1 = V\cos[\omega(t-\tau_g)]\ , \tag{3.3}$$
$$V_2 = V\cos(\omega t)\ , \tag{3.4}$$

where the delay $\tau_g = \vec{b}\cdot\hat{s}/c$ is known as the *geometric delay* (see Figure 3.4). The voltages are amplified, multiplied, and averaged in time by a correlator. This yields the correlator response

$$R = \langle V_1 V_2\rangle\cos(\omega\tau_g). \tag{3.5}$$

Equation 3.5 is valid for a point source. A source extended in the sky with brightness distribution $I_\nu(\hat{s})$ can be treated as a continuous sum of independent

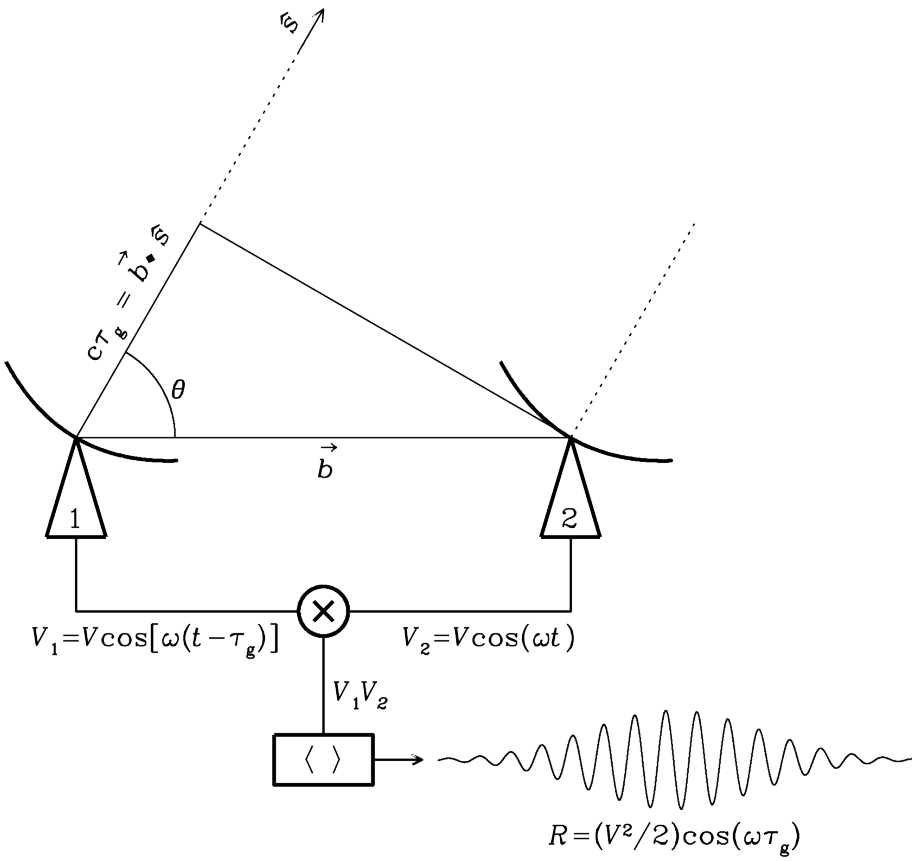

Figure 3.4: Schematic of a two-element interferometer (antennas 1 and 2), observing a point source at a very narrow frequency range centered at $\nu = \omega/(2\pi)$. Unit vector $\hat{s}$ points towards the source. $\vec{b}$ is the baseline vector pointing from one antenna to the other. The antennas do not receive the signal from the source simultaneously; there is a tiny time delay (τ_g) due to the finite speed of light (c). V_1 and V_2 are the outputs voltages of each antenna. They are the same since they are observing the same object, but V_1 is delayed a time of $\tau_g = \vec{b} \cdot \hat{s}/c$. The box in the bottom is the correlator, which multiplies and averages the voltages. This plot is taken from Condon & Ransom 2016 (Figure 3.41).

point sources. In that case, equation 3.5 can be generalized as

$$R_{\rm c} = \int I_\nu(\hat{s}) \cos(\omega\tau_g) d\Omega \tag{3.6}$$

$$= \int I_\nu(\hat{s}) \cos(2\pi\nu\vec{b} \cdot \hat{s}/c) d\Omega \tag{3.7}$$

$$= \int I_\nu(\hat{s}) \cos(2\pi\vec{b} \cdot \hat{s}/\lambda) d\Omega \ , \tag{3.8}$$

where ω, τ_g, and $c = \nu\lambda$ were introduced. Equation 3.8 reflects the even (symmetric) part of I_ν. The odd (antisymmetric) part of I_ν is captured by a second correlator with a phase delay of 90°. The resulting equation ($R_{\rm s}$) is identical to 3.8, only with sin() instead of cos().

The complex visibility $\mathcal{V}$ is defined as

$$\mathcal{V} \equiv R_{\rm c} - iR_{\rm s} \ , \tag{3.9}$$

from where

$$\mathcal{V} = \int I_\nu(\hat{s}) e^{-i2\pi\ \vec{b}\cdot\hat{s}/\lambda} d\Omega \ , \tag{3.10}$$

after introducing equation 3.8 and the R_s equivalent with sin(). The exponential appears from combining cos() and $i\sin()$. The visibility $\mathcal{V}$ is a crucial quantity in interferometry, because it represents what is actually being measured by the antennas. From equation 3.10, it deduces that they observe the Fourier transform of the true brightness of the source (I_ν). In order to retrieve I_ν, the quantity of interest, astronomers must therefore perform an inverse Fourier transform.

A useful way of visualizing this is by introducing the *uv*-plane. This comes from assigning (u, v) coordinates to the visibility space, i.e. to the Fourier space. Equation 3.10 can be rewritten (approximately) as

$$\mathcal{V}(u, v) = \int I_\nu(l, m) e^{-i2\pi(ul+um)} dl dm \ , \tag{3.11}$$

where l and m represent coordinates in the sky.

An interferometer with more than two antennas, is simply a set of several two-element interferometers. Figure 3.5 shows how astronomers can build a scientific image from a set of interferometric visibilities.

Following equation 3.11, with a finite number of antennas only a finite number of (u, v) positions can be sampled (these positions are shown at the top center of Figure 3.5, it is the *uv* sampling). These are determined by the distribution of the antennas, i.e. by the baselines vectors. Antennas measure $\mathcal{V}$ in those positions, as shown in the top right of Figure 3.5. However, the total Fourier transform of the source covers the entire *uv*-plane (top left in Figure 3.5), including positions inaccessible to the antennas.

When astronomers perform the inverse Fourier transform on the measured visibilities, they get what is known as the dirty image (bottom right of Figure 3.5). It is an image of the object, but it is contaminated due to the scarce sampling of the *uv*-plane. Since the positions of the antennas are known, astronomers can *clean* this dirty image by making an educated guess of what the true image looks like. This involves using the dirty beam (bottom center of Figure 3.5), which is the inverse Fourier transform of the (u, v) sampling.

The most popular algorithm used for doing this is `CLEAN`, first developed by Högbom (1974). It is important to notice that there is not one single image that can be created from a set of observations. At the end, there is always some *guessing* that must be done due to the limited coverage of the *uv*-plane. Having many antennas is helpful in this regard, because the *uv*-plane is more sampled. The `CLEAN` algorithm has many parameters that astronomers can tune, and is considered a great tool to obtain good images from interferometric observations.

As mentioned before, setting antennas very fart apart can improve the resolution significantly, which is great for studying the fine details of objects. In high-redshift galaxies this is even more important than in local galaxies, since they are further away and appear smaller in the sky. However, having only antennas far apart means that there are big unsampled gaps in the *uv*-plane. This results in capturing the extended emission very poorly. The ideal scenario is to have antennas distributed far apart, to achieve good spatial resolution, but also others closer together, to capture

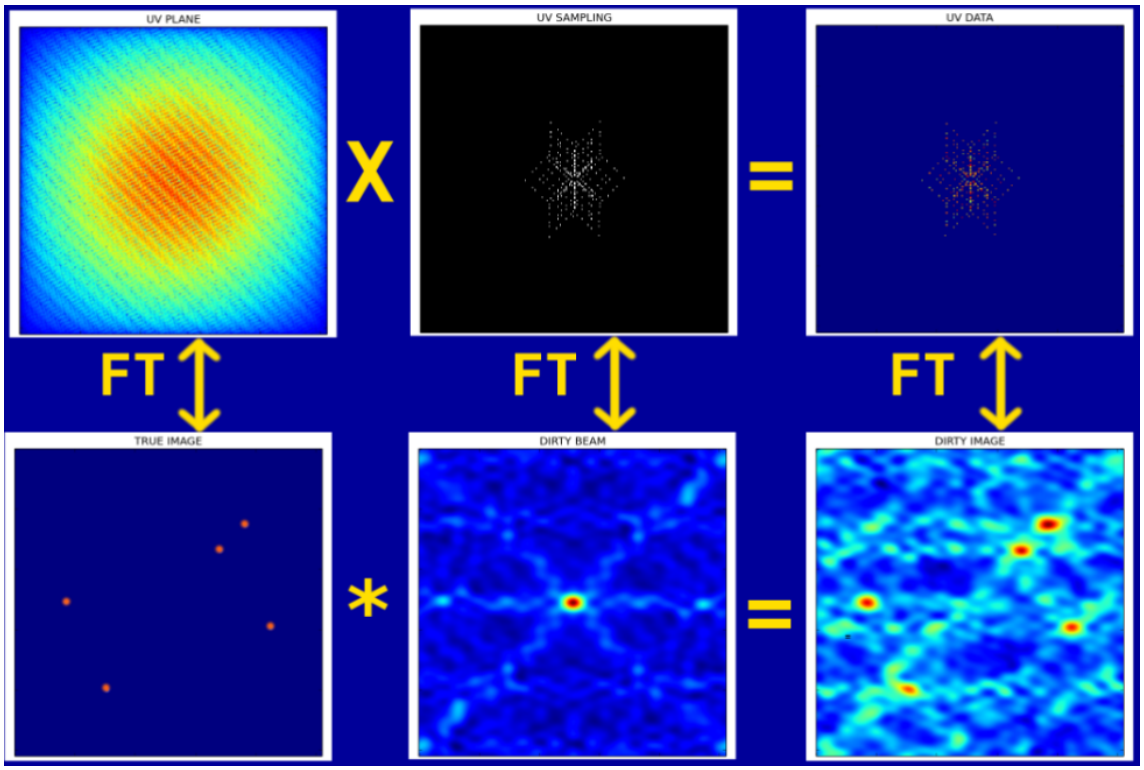

Figure 3.5: Process to create a science image with an interferometer. Top row is in the Fourier domain (u, v); bottom row in the real domain (l, m). Bottom: from left to right, the true image of the object that astronomers want to retrieve; image sampled by antennas when observing *nothing*, equivalent to observing a perfect point source (the dirty beam is equivalent to a point spread function); image of the object directly from the antennas visibilities (dirty image). Top: from left to right, true Fourier transform of the object (inaccessible to antennas); positions in the uv-plane that antennas can sample given their distribution; the actual data coming from the antennas. See how, from left to right, each pair of images connect via a Fourier or inverse Fourier transform. Image credit: Martí-Vidal (2016).

the extended emission. In practice astronomers must always compromise. Aiming for a great resolution hinders the extended emission (as in this work), and vice versa.

3.2.2 ALMA

This thesis employs observations obtained with the Atacama Large Millimeter/submillimiter Array (ALMA). ALMA is the biggest and most powerful telescope on Earth to observe the radio window. Furthermore, it is the largest ground-based astronomical project in existence, at any wavelength. It is located in one of the driest places on Earth; the Chajnantor plateau in northern Chile at 5000 meters of altitude (see Figure 3.6). It consists of fifty-four 12-m antennas and twelve 7 m antennas, which together they can observe the Universe as one powerful interferometer.

Since the early 2010s, ALMA has provided astronomers with a remarkable win-

Figure 3.6: ALMA observing the night sky. Credit: ESO/Y. Beletsky; available at `https://www.eso.org/public/unitedkingdom/images/uhd_beletsky_alma_16/`.

dow to study the Universe like never before[1]. In particular, regarding Dusty Star-Forming Galaxies (DSFGs), it has allowed astronomers to study this population of galaxies at unprecedented angular resolution (ALMA has baselines up to 16 km long), sensitivity (ALMA can detect much fainter objects than its predecessors), and frequency coverage. All this progress has recently been reviewed by Hodge & da Cunha (2020), though it is worth knowing that astronomers were already looking forward to this several years before ALMA was realized (e.g. Blain, 1999).

Regarding the frequency coverage, ALMA observes the radio window with ten different bands (Band 1 through 10). Each band specializes on a specific frequency range. They go from low frequencies (Band 1, $\nu \sim 35$ GHz or $\lambda \sim 6$ mm) to high frequencies (Band 10, $\nu \sim 950$ GHz or $\lambda \sim 0.3$ mm), and many more frequencies in between[2].

3.2.3 Data

This work employs Bands 3 through 8 ALMA observations of the HerBS galaxies in the SGP field (see Figure 3.1). These were carried out between October 2022 and April 2023 (Program ID: 2022.1.00432.S; Principal Investigator: T. Bakx). The ALMA antennas formed long baselines which allowed for a high angular resolution, down to $\sim 0.15''$.

The observations were performed following a very efficient method developed by Bakx et al. (2024). As explained by the authors, the idea is to target as many

[1]The interested reader can check ALMA's latest contributions at `https://www.almaobservatory.org/en/home/`

[2]See `https://www.eso.org/public/unitedkingdom/teles-instr/alma/receiver-bands/` for full coverage of each band.

spectral lines as possible without the need of re-calibrating the configuration of ALMA, which is very costly in time. The SGP field was divided in five sub-fields from left to right, as shown in Figure 3.7. Each of these can be observed without the need of any re-calibration. Bakx et al. (2024) study the galaxies in the center field, which they name *pilot*. The galaxies in the remaining four are the subject of this thesis (SGP-1, -2, -3 and -4), as explained in Section 3.1.

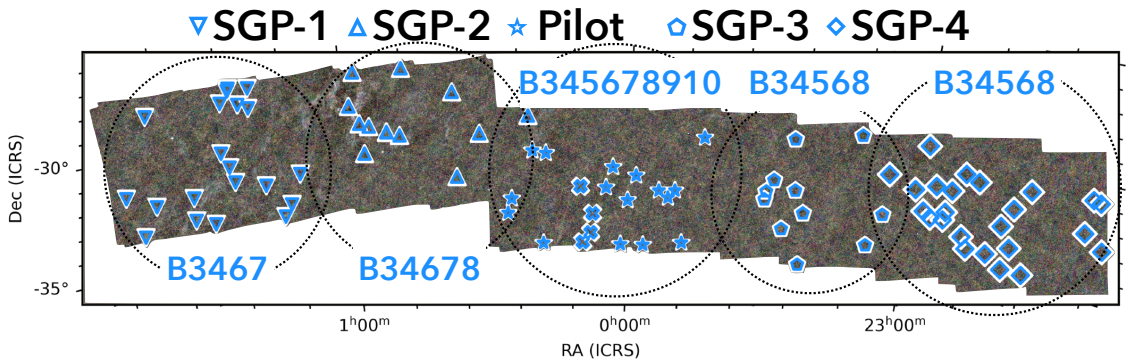

Figure 3.7: South Galactic Pole (SGP) field, divided into five sub-fields (from left to right, SGP-1, SGP-2, Pilot, SGP-3 and SGP-4). The galaxies in each of these (in blue) can be observed by ALMA without the need of any recalibration. Blue numbers indicate the ALMA bands used for observation.

With one single calibration, ALMA can target the positions of all sources in one sub-field. Their specific coordinates in the sky are known from the definition of the HerBS sample (Bakx et al., 2018). As mentioned in Section 3.1, many of these initial sources have been resolved into multiple galaxies upon observations at higher angular resolution. For this reason, the celestial coordinates targeted by ALMA can be understood as a *field* it observed, where there might be multiple *sources* or *galaxies*. For instance, ALMA observed the field HerBS-69 in SGP-1, which contains two sources/galaxies: HerBS-69A and HerBS-69B. Each field was observed for ~ 2 minutes.

Table 3.1 summarizes the key aspects of the observations. It includes the bands that observed each sub-field, with their frequency range and resolution. Each band has two frequency ranges, the lower side band (LSB) and the upper side band (USB). Each of these spans 3.65 GHz, and the two sides are separated by ~ 8.35 GHz. As described in Section 3.2.2, higher bands cover higher frequencies, which results in better resolution (following equation 3.1).

There are two types of data used in this work: continuum maps and data cubes. For each field (e.g. HerBS-69), a 2D image is produced in each band by averaging across the frequency range. By considering the entire spectral window, the continuum emission in that range is captured. This continuum emission traces the dust, which is emitting (approximately) as a black-body. Since spectral lines are narrow, they are commonly filtered out. The units are Jy/beam.

Besides these 2D continuum maps, ALMA also produced data in 3D. Figure 3.8 presents a schematic of this type of data, known as data cubes. The extra dimension is the spectral axis. Data cubes do not average across the frequency,

Table 3.1: ALMA observations across all four sub-fields (SGP-1, -2, -3 and -4). Bands, frequency ranges and spatial resolution are included.

Band	Bandwidth [GHz]	Resolution [arcsec × arcsec]
SGP-1:	HerBS-75 -178 -69 -14 -107 -160 -73 -200 -101 -55 -151 -120 -186 -23 -40 -114 -11 -138 -145 -27	
3	92.30 ... 95.95 & 104.30 ... 107.95	- × -
4	136.41 ... 140.06 & 148.41 ... 152.06	0.34 × 0.26
6	250.24 ... 253.89 & 264.74 ... 268.39	0.23 × 0.22
7	291.97 ... 295.61 & 303.97 ... 307.61	0.16 × 0.14
SGP-2:	HerBS-90 -63 -24 -45 -57 -181 -77 -174 -56 -60 -122 -207	
3	95.11 ... 98.75 & 96.88 ... 98.75	0.60 × 0.49
4	147.10 ... 150.74 & 159.10 ... 62.74	0.43 × 0.35
6	252.32 ... 255.96 & 266.82 ... 270.46	0.21 × 0.16
7	286.59 ... 290.24 & 298.59 ... 302.24	0.17 × 0.14
8	402.11 ... 405.75 & 414.11 ... 417.75	0.14 × 0.13
SGP-3	HerBS-37 -18 -118 -146 -102 -39 -17 -28 -132 -49 -123	
3	93.45 ... 97.10 & 105.45 ... 109.10	0.57 × 0.47
4	140.12 ... 143.76 & 152.12 ... 155.76	0.40 × 0.30
5	190.66 ... 194.31 & 202.66 ... 206.31	0.23 × 0.19
6	214.92 ... 218.56 & 229.42 ... 233.06	0.26 × 0.22
8	391.99 ... 395.64 & 403.99 ... 407.64	0.15 × 0.14
SGP-4	HerBS-135 -168 -84 -103 -47 -68 -97 -144 -26 -111 -67 -166 -182 -192 -209 -33 -208 -141 -148 -121 -131 -198 -80 -189	
3	86.15 ... 89.79 & 98.15 ... 101.79	0.71 × 0.57
4	131.88 ... 135.53 & 143.88 ... 147.53	0.35 × 0.27
5	191.23 ... 194.87 & 203.23 ... 206.87	0.30 × 0.26
6	230.44 ... 234.08 & 244.93 ... 248.58	0.27 × 0.25
8	416.86 ... 420.50 & 428.86 ... 432.50	0.16 × 0.14

but rather include a measurement (Jy/beam units) at each frequency channel. This type of data allows astronomers to study spectral lines in detail. For instance, given good enough spatial resolution, data cubes can show how an emission line changes in different parts of a galaxy (e.g. it becomes more bright, shifted or wide). Such changes may reveal important physical processes of the galaxy.

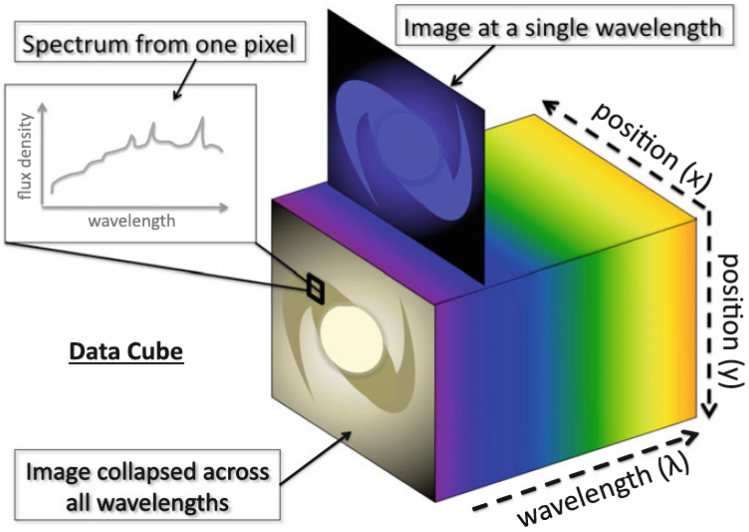

Figure 3.8: Schematic diagram of a data cube, as presented by Harrison (2014). The three axes of the cube are spatial (x), spatial (y) and spectral (ν or λ). Each pixel contains an entire spectrum, instead of just one value as in the 2D continuum maps. Just like the spatial axes are binned in pixels, the spectral axis is binned in channels.

The spectral axis of data cubes can be measured in ν or λ (these two are tied by $c = \nu\lambda$), or also as a radial velocity v_{radio}. For a spectral line centered at ν_0, the entire frequency axis can be converted into radial velocity with the equation

$$v_{\text{radio}} = c\left(1 - \frac{\nu}{\nu_0}\right) \ . \tag{3.12}$$

In particular, this work will employ the spectral axis of data cubes in velocities, as will be described in Section 3.5.

The last type of data is the primary beam correction (PBC). These are values between 0 and 1 that correct the fact that ALMA is more sensitive towards the center of the field of view than the edges (primary beam), so emission from the edges may look artificially fainter.

The data was reduced and imaged with the software Common Astronomy Software Applications (CASA; CASA Team et al. 2022), one of the most used software for processing ALMA observations. It was done following the same outline as Bakx et al. (2024). CASA can implement the `CLEAN` algorithm mentioned in Section 3.2.1, with the task `TCLEAN`. For the continuum images, CASA version 6.2.1 was employed, where `TCLEAN` was run with natural weighting. In the data cubes, CASA 6.4.1 was used. `TCLEAN` was run with Briggs weighting and robust factor 2, which is best for

detecting faint emission. The resolutions reported in Table 3.1 are obtained after running `TCLEAN`.

Throughout this work, the data were analyzed entirely in python. The ALMA data (continuum maps and data cubes) were processed with the SpectralCube package (Robitaille et al., 2016). For plots, the Matplotlib (Hunter, 2007) and APLpy libraries were employed (Robitaille & Bressert, 2012).

3.3 Calculation of Σ_{H_2}

The surface density of the molecular gas mass (Σ_{H_2}) must be calculated for the x-axis of the SK relation. Despite being the most abundant molecule in the Universe, detecting molecular hydrogen (H_2) directly is extremely difficult. The two atoms of the molecule are identical. This symmetry causes that the molecule has no dipolar rotational transitions. Furthermore, its purely rotational quadrupole transitions are weak due to long decay lifetimes. However, the most important difficulty in detecting H_2 in emission, is that this molecule requires temperatures of $T \gtrsim 100$ K to become excited (Bolatto et al., 2013). These are significantly higher than common temperatures in diffusive or dense H_2 environments, which are typically below ~ 50 K (Draine, 2011). All things considered, it is much easier for astronomers to study the molecular gas with different tracers rather than with H_2 directly (even if detecting H_2 is not impossible, mainly with space telescopes, e.g. Habart et al. 2005).

I will study the molecular gas using carbon monoxide (CO) as a tracer. This is the second most abundant molecule in the Universe. CO is easily formed in molecular clouds, and very stable. It also becomes easily excited, mainly through collisions with H_2 molecules, which outnumber the CO molecules by a few 1,000. CO has a low dipole moment and low excitation energy of ≈ 5.53 K (e.g. Solomon & Vanden Bout, 2005; Bolatto et al., 2013). This is so low that CO can be found even in the coldest molecular clouds. Furthermore, the rotational transitions of CO are found in wavelengths between mm and sub-mm (see Section 2.3.2), which makes them a perfect target for ALMA. CO is therefore, by far, the most popular molecule used by astronomers to study the molecular gas in the ISM of our Galaxy and other galaxies (e.g. Glover & Mac Low, 2011).

Ideally the ground-state transition of CO is used, i.e. CO$(1-0)$. However, already at $z > 1$, its rest wavelength ($\lambda = 2.6$ mm) is redshifted beyond the range covered in the ALMA observations employed in this work. I will therefore use transitions at higher $J \rightarrow J-1$, up to $5 \rightarrow 4$. Higher transitions no longer trace the cool gas but rather denser or warmer environments (e.g. Yang et al., 2017; Gururajan et al., 2022). This component of the ISM can also be of great interest but is not in the scope of this thesis.

Using the ALMA observations, the velocity-integrated flux of the CO line $S\mathrm{d}V$ is calculated for a given aperture in a galaxy (see Section 3.5 for full description of how this is done). From this flux the H_2 gas mass is obtained in three steps: calculating the luminosity of the line (Section 3.3.1), converting this to ground-state luminosity (Section 3.3.2) and converting luminosity to H_2 mass (Section 3.3.3). Finally, the surface density Σ_{H_2} is obtained by dividing the H_2 mass by the physical

area in which the measurement is done (e.g. the size of the aperture in pc^2).

3.3.1 Line luminosity

In general, the flux F is a way of measuring how bright a source in the sky appears to us. As the energy of the source travels across space, its intrinsic power (luminosity L) is distributed in a sphere of surface area $4\pi D_L^2$, where D_L is the luminosity distance. F is therefore mathematically expressed as

$$F = \frac{L}{4\pi D_L^2} \ . \tag{3.13}$$

From this equation, it shows that F is the total power received per unit area. It also shows that D_L is the distance to a source that can be deduced by comparing its intrinsic to observed brightness.

Since objects are commonly studied at specific wavelengths, it is more practical to use their monochromatic counterparts, which are the flux density S and monochromatic luminosity L_ν (power per unit frequency). Equation 3.13 can therefore be rewritten as

$$\nu_{\rm obs} S(\nu_{\rm obs}) = \frac{\nu_{\rm rest} L_\nu(\nu_{\rm rest})}{4\pi D_L^2} \ , \tag{3.14}$$

where $\nu_{\rm obs}$ and $\nu_{\rm rest}$ are the observed and rest frequencies, respectively (they relate via the redshift $\nu_{\rm rest} = (1+z)\nu_{\rm obs}$ as shown in equation 2.7). They help to further illustrate the point that S is measured and is L_ν intrinsic. From equation 3.14, the luminosity at a given frequency is

$$L_\nu(\nu_{\rm rest}) = 4\pi D_L^2 \frac{\nu_{\rm obs}}{\nu_{\rm rest}} S(\nu_{\rm obs}) \ . \tag{3.15}$$

Following Solomon et al. (1992), in the case of a CO transition, equation 3.15 can be rewritten to obtain the line luminosity as

$$\frac{L_{\rm CO}}{\rm L_\odot} = 1.04 \times 10^{-3} \frac{S{\rm d}V}{[\text{Jy km s}^{-1}]} \frac{\nu_{\rm rest}}{(1+z)} D_L^2 \left[\frac{1}{\text{GHz Mpc}^2}\right] \ , \tag{3.16}$$

where $S{\rm d}V$ is the velocity-integrated flux of the CO line, z the redshift, and the factor 1.04×10^{-3} accounts for the units that have been introduced. Commonly, the CO line luminosity can be expressed as an areal-integrated source brightness temperature (e.g. Carilli & Walter, 2013; Casey et al., 2014), where equation 3.16 is rewritten as

$$\frac{L'_{\rm CO}}{[\text{K km s}^{-1}\ \text{pc}^2]} = 3.25 \times 10^7 \times \frac{S{\rm d}V}{[\text{Jy km s}^{-1}]} \times \frac{D_L^2}{(1+z)^3 \nu_{\rm obs}^2} \left[\frac{\text{GHz}^2}{\text{Mpc}^2}\right] \ . \tag{3.17}$$

This equation will be used to estimate the luminosity of the CO line. For the galaxies of my sample, z is already known, $\nu_{\rm obs}$ is calculated via equation 2.7, $S{\rm d}V$ is measured from the ALMA data (see Section 3.5), and D_L is estimated for a given redshift using `cosmology` of AstroPy (Astropy Collaboration et al. 2013; in Section 2.2 I presented the cosmology chosen for this work).

3.3.2 Ground state

The line luminosity obtained in Section 3.3.1 must be converted to ground state line luminosity, $L'_{\mathrm{CO}(1\to0)}$. This is done based on the excitation of the CO molecule, i.e. the relative strengths of the transitions, sometimes referred to as CO spectral line energy distribution (CO SLED) or simply CO ladder (e.g. reviews by Carilli & Walter, 2013; Casey et al., 2014). Effectively, a fixed ratio $r_{J,1}$ between the CO luminosity of a given J level, $L'_{\mathrm{CO}(J\to J-1)}$, and the ground state, is assumed as

$$r_{J,1} \equiv \frac{L'_{\mathrm{CO}(J\to J-1)}}{L'_{\mathrm{CO}(1\to0)}} \ . \tag{3.18}$$

Several studies have attempted to constrain these ratios. A relevant example is Rosenberg et al. (2015), who also studied (U)LIRGs detected with *Herschel*, although locally. They showed that these galaxies can have up to three different classes of ladders, depending on the gas excitation conditions. More recently, Kirkpatrick et al. (2019) made a comprehensive analysis including all high-redshift CO detections available (over four hundred in total). This reduced uncertainties significantly, which is a common issue in these types of studies, since all the available information on the molecular gas was accounted for. The downside is that this may include a variety of galaxies whose physical properties differ from DSFGs due to different selection criteria.

I will employ the values presented by the more recent work of Harrington et al. (2021). They study a sample of 24 DSFGs at $z \sim 1-4$, selected with the *Planck* satellite, based on their sub-mm continuum emission. This is similar to the HerBS sample which was selected based on the flux at 0.5 mm. Eight of these *Planck* sources have a cross-match in *Herschel* detections. Also, eight of them have been identified independently by Cañameras et al. (2015). They measure the velocity-integrated flux for several CO transitions, ranging from $J = 1$ to 12. They use a sophisticated model that describes the molecular ISM with nine free parameters where the gas density is driven by turbulence. In Table 3.2 the mean ratios derived from their 24 sources are presented. Only the transitions relevant to my work are included (up to $J = 5$). The authors argue that these ratios are fully consistent with a wealth of studies available in the literature, including the already mentioned Rosenberg et al. (2015); Kirkpatrick et al. (2019), and also the estimations on DSFGs by Carilli & Walter (2013).

Table 3.2: CO luminosity ratios that will be used to convert from a given J transition to the ground-state. Values are taken from Table 4 of Harrington et al. (2021). Error bars represent a 1σ uncertainty.

J	$r_{J,1}$
2	0.88 ± 0.07
3	0.69 ± 0.12
4	0.52 ± 0.14
5	0.37 ± 0.15

This study by Harrington et al. (2021) is chosen under the reasonable assumption

that those DSFGs are similar to the ones included in my thesis. I will employ the values in Table 3.2, but it must be taken into account that DSFGs can have a variety of CO ladders, and this subject is an active topic of research (e.g. Taylor et al., 2025). This variety has even been shown for galaxies of the HerBS sample by Hagimoto et al. (2023) or Bakx et al. (2024). These uncertainties are reflected in the important error-bars of Table 3.2, which will contribute to the uncertainty in my measurements.

3.3.3 CO-to-H_2

The CO ground-state luminosity $L'_{\mathrm{CO}(1\to0)}$, estimated in Section 3.3.2, is converted to H_2 mass via a single factor α_{CO}, as

$$M_{\mathrm{H_2}} = \alpha_{\mathrm{CO}}\, L'_{\mathrm{CO}(1\to0)} \ , \tag{3.19}$$

where α_{CO} has units $\mathrm{M_\odot(K\ km\ s^{-1}pc^2)^{-1}}$. This factor is, effectively, simply a mass-to-luminosity ratio, which are studied in galaxies in other contexts too (e.g. Bell et al., 2003). As shown in the comprehensive review on α_{CO} by Bolatto et al. (2013), this factor comes from considering the virial theorem on a Giant Molecular Cloud (GMC), i.e.

$$2K + U = 0 \ , \tag{3.20}$$

where K is total kinetic energy and U the total gravitational potential energy. This is valid for systems that are gravitationally bound and in dynamical equilibrium, over long time averages (Goldstein et al., 2002). From this theorem, the mass of the GMC can be deduced to the following expression (equation 8 of Bolatto et al., 2013)

$$M_{\mathrm{vir}} = \frac{3(5-2k)}{G(3-k)} R\, \sigma^2 \ , \tag{3.21}$$

where R is the projected radius of the cloud, σ the 1D velocity dispersion, G the gravitational constant and k the index of the spherical volume distribution $\rho(r) \propto r^{-k}$. This mass is labeled as *virial mass* since it is deduced from the virial theorem, and is considered a good measure of the H_2 mass, i.e. $M_{\mathrm{vir}} \approx M_{\mathrm{H_2}}$. k can be considered roughly constant at $k \approx 1$ (e.g. MacLaren et al., 1988), so that the mass has a more simple relation

$$M_{\mathrm{vir}} = M_{\mathrm{H_2}} \propto R\, \sigma^2 \ . \tag{3.22}$$

Empirically, it has been shown that σ and R follow the relation (e.g. Heyer et al., 2009)

$$\sigma \propto R^{0.5} \ , \tag{3.23}$$

which is often referred to as the size-line width relation. Inserted in equation 3.22, it yields

$$M_{\mathrm{H_2}} \propto (\sigma^2)\sigma^2 = \sigma^4 \ . \tag{3.24}$$

Now, in Section 3.3.1 L'_{CO} was defined as the areal (πR^2) integrated source brightness temperature ($T_{\mathrm{B}}\sqrt{2\pi}\,\sigma$), so that

$$L'_{\mathrm{CO}} = \pi R^2 T_{\mathrm{B}} \sqrt{2\pi}\,\sigma = \pi(\sigma^2)^2 T_{\mathrm{B}} \sqrt{2\pi}\,\sigma \propto T_{\mathrm{B}}\sigma^5 \ , \tag{3.25}$$

where equation 3.23 was introduced. Combining equations 3.24 and 3.25,

$$M_{\mathrm{H_2}} \propto \sigma^4 \propto \left(\frac{L'_{\mathrm{CO}}}{T_{\mathrm{B}}}\right)^{4/5} = (L'_{\mathrm{CO}})^{0.8}\,(T_{\mathrm{B}})^{-0.8} \ . \tag{3.26}$$

From this, the factor α_{CO} is directly defined as

$$\alpha_{\mathrm{CO}} \equiv \frac{M_{\mathrm{H_2}}}{L'_{\mathrm{CO}}} \propto \frac{(L'_{\mathrm{CO}})^{0.8}\,(T_{\mathrm{B}})^{-0.8}}{L'_{\mathrm{CO}}} \tag{3.27}$$

$$\implies \alpha_{\mathrm{CO}} = K\,(L'_{\mathrm{CO}})^{-0.2}\,(T_{\mathrm{B}})^{-0.8} \ , \tag{3.28}$$

where K is a proportionality constant. From equation 3.28 is clear that α_{CO} is constant under the assumptions that the brightness temperature is approximately constant. Also, there is a weak dependence on the CO luminosity ($\propto (L'_{\mathrm{CO}})^{-0.2}$), which means that α_{CO} increases for the more massive GMCs, but it is assumed that this is not significant. This method of using α_{CO} also relies on the assumption that clouds are virialized. Whether they actually are has been a matter of debate with conflicting evidence (e.g. review by McKee & Ostriker 2007), but over large samples this assumption, though flawed, is a fair way of modeling the clouds. Further assumptions are that the mass is dominated by H_2 (although the contribution of He is accounted for), and the size-line width relation.

I will adopt the value calibrated by the recent work of Dunne et al. (2022), of $\alpha_{\mathrm{CO}} = (4.0\pm0.1)\ \mathrm{M_\odot(K\ km\ s^{-1}pc^2)^{-1}}$. They suggest this factor based on an analysis of a large sample of over 400 galaxies, ranging from local spirals to DSFGs at $z \approx 6$. Their methodology is very robust, as they cross-calibrate three of the most popular traces of molecular gas: CO (used in this thesis), [CI], and dust. Remarkably, they find one single value of α_{CO} to adequately describe their extremely diverse sample. This value has been already used by Bakx et al. (2024) to study the SK relation in the HerBS sample.

3.4 Calculation of Σ_{SFR}

The surface density of the SFR (Σ_{SFR}) must be calculated for the y-axis of the SK relation. There are several tracers of the SFR discussed in the literature. SFR can be traced in different parts of the electromagnetic spectrum, such as the ultraviolet (UV), infrared (IR), radio, X-ray, or even counting stars (Kennicutt & Evans, 2012). Due to the strong IR emission of DSFGs (see Section 2.5), this it the preferred part of the spectrum to estimate the SFR in this type of sources.

I will calculate the Σ_{SFR} under the reasonable assumption that SFR is traced by dust emission. Since dust emission is reflected in the ALMA continuum, I therefore assume

$$\mathrm{SFR} \propto L_{\mathrm{IR}} \propto \text{dust emission} \propto \text{ALMA continuum} \ , \tag{3.29}$$

where L_{IR} is the infrared (IR) luminosity, i.e. the luminosity in the range $\lambda_{\mathrm{rest}} = (8 - 1000)\ \mu$m. As explained in the review by Calzetti (2013), the shape of the thermal IR spectral energy distribution (SED) of a galaxy, i.e. the spectrum in the range $(8 - 1000)\ \mu$m, depends on the SED of the starlight. Young O and B stars,

luminous in UV, heat the dust to higher temperatures than older stars that are faint in the UV. The hotter the dust, the higher the emissivity in the IR and the more luminous the IR SED. Then, $L_{\rm IR}$ reflects the importance of O and B stars in the galaxy, which live much shorter than old or low-mass stars (e.g. a G star like the Sun). It therefore reveals how actively new stars are being formed, i.e. it traces the SFR.

$L_{\rm IR}$ can be converted into SFR via a single conversion factor IR-to-SFR. The choice of IR-to-SFR underlies several assumptions about the physics of the galaxy. In extremely dusty environments such as DSFGs, it is commonly assumed that the dust can absorb practically all the starlight. This is not the case in other galaxies where on average it is only around 50% (Kennicutt & Evans, 2012). For instance, using Starburst99 models for star formation (Leitherer et al., 1999), and assuming stellar solar-metallicity where dust can absorb and re-emit the entire starlight emission, Calzetti (2013) propose a factor of

$$\text{IR-to-SFR}_{\,\text{Calz13}} = 2.8 \times 10^{-44} \frac{\mathrm{M_\odot\ yr^{-1}}}{\mathrm{erg/s}} \tag{3.30}$$

$$\approx 1.1 \times 10^{-10} \mathrm{M_\odot\ yr^{-1}} \left(\mathrm{L_\odot^{-1}}\right) \ . \tag{3.31}$$

For the HerBS sample, Hagimoto et al. (2023) build their SK relation considering a factor larger than above, at

$$\text{IR-to-SFR}_{\,\text{Hagi23}} = 1.47 \times 10^{-10} \mathrm{M_\odot\ yr^{-1}} \left(\mathrm{L_\odot^{-1}}\right) \ . \tag{3.32}$$

As explained by Murphy et al. (2011), this comes from using the Starburst99 model with a Kroupa Initial Mass Function (IMF; Kroupa 2001). Further assumptions involved are that the dust absorbs and re-radiates the entire continuum emission (key assumption to separate DSFGs from other galaxies), and that this dust emission is optically thin. For my study I will adopt the same factor as Bakx et al. (2024), the most recent study on the HerBS sample at resolution similar to my data. They consider a factor of

$$\text{IR-to-SFR}_{\,\text{Bakx24}} = 1.73 \times 10^{-10} \mathrm{M_\odot\ yr^{-1}} \left(\mathrm{L_\odot^{-1}}\right) \ , \tag{3.33}$$

which is valid for a Salpeter 1-100 $\mathrm{M_\odot}$ IMF (Salpeter, 1955) under the same assumptions explained above.

The total IR luminosities of the HerBS sample are reported in table A1 of Bakx et al. (2020a); they all lie in the range $10^{13} < L_{\rm IR}/\mathrm{L_\odot} < 10^{14}$. I will employ these values directly, although it is worth describing briefly how they were obtained. The HerBS sample was observed by Bakx et al. (2018) with SCUBA-2 at 850 μm, and SPIRE at 250-, 300- and 500 μm. A galaxy SED template for the entire HerBS sample was derived using the subset of sources with known robust spectroscopic redshift $z_{\rm spec}$ (at that time, 22 of them, none of which is a part of my work). The measured flux densities of the galaxies S_ν are modeled assuming two dust components (hot and cold), as

$$S_\nu = A_{\rm off} \left[B_\nu(T_{\rm h}) \nu^\beta + \alpha B_\nu(T_{\rm c}) \nu^\beta \right] \ , \tag{3.34}$$

where ν is the rest frequency at which the flux density was measured (this can only be known with robust redshift measurements), $A_{\rm off}$ a normalization factor, B_ν the

Planck blackbody function, β the dust emissivity, $T_{\rm h}$ and $T_{\rm c}$ the temperatures of the hot and cold dust components, and α the mass ratio of the cold to hot dust components. The fit aimed to minimize the chi-square estimate

$$\chi^2 = \sum_{i=1}^{n} \sum^{\lambda} \left[\frac{A_i S_{\rm model,i} - S_{\rm meas,i}}{\sigma_{\rm meas,i}} \right]^2 , \tag{3.35}$$

where the first sum indicates all the sources, and the second sum all the available wavelengths where S_ν was measured. The numerator is the residual (modeled flux minus measured flux) and the denominator the measured noise. They tested three templates, one with all free parameters ($T_{\rm h}$ and $T_{\rm c}$, α and β), one with fixed $\beta = 2$, and one from the literature (Pearson et al., 2013). The first of these was considered best based on its lower χ^2. From this fit, photometric redshifts $z_{\rm phot}$ of all sources of the sample were estimated. For each source, given the estimate of $z_{\rm phot}$, they integrated the best template in the range $\lambda_{\rm rest} = (8 - 1000)\ \mu$m to obtain the IR luminosity. In Figure 3.9 the models fitted by Bakx et al. (2018) are shown.

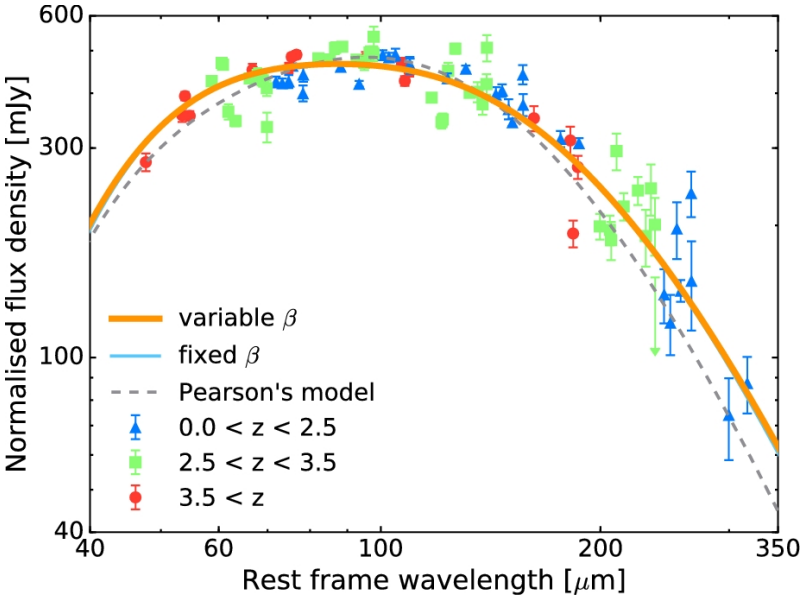

Figure 3.9: The three models fitted by Bakx et al. 2018 (this figure is taken from that paper; Figure 7), following equation 3.34 (flux density against rest frequency/wavelength). The models with variable β, free β and one from the literature (Pearson et al., 2013) are shown. The preferred model is the one in orange, which was used to estimate $L_{\rm IR}$ in the entire sample. The data points, coming from 22 sources, are split in three redshift ranges for easier readability.

Assuming $L_{\rm IR}$ known and proportional to the dust emission, which is proportional to the ALMA continuum (see equation 3.29), I can consider the following ratio

$$\frac{L_{\rm IR,\ total}}{\rm continuum_{total}} = \frac{L_{\rm IR,\ A}}{\rm continuum_A} , \tag{3.36}$$

which compares the total $L_{\rm IR}$ and continuum emission of a galaxy to those in a smaller region A. From equation 3.36, it follows

$$L_{\rm IR,\ A} = \left(\frac{\rm continuum_A}{\rm continuum_{total}}\right) L_{\rm IR,\ total} \tag{3.37}$$

$$= f_{\rm A} \times L_{\rm IR,\ total}\ . \tag{3.38}$$

This means that the IR luminosity of a region A in a galaxy can be estimated with the fraction of the total continuum included in that region, $f_{\rm A}$, multiplied by the total IR luminosity of the galaxy (available at Bakx et al. 2020a). In this work, $f_{\rm A}$ is obtained from the ALMA Band 6 dust continuum measurements. The IR luminosity of the region is converted to SFR simply via the factor $1.73 \times 10^{-10} {\rm M_\odot\ yr^{-1}(L_\odot^{-1})}$ as discussed before. Lastly, this SFR ($\rm M_\odot\ yr^{-1}$ units) is divided by the size of the aperture to obtain the desired SFR surface density $\Sigma_{\rm SFR}$ (similarly to the the H_2 mass as explained in Section 3.3). In fields where there are multiple galaxies, the IR luminosity reported by Bakx et al. (2020a) is split in the same fraction as their respective continuum emissions (e.g. galaxies HerBS-69A and HerBS-69B contain $\sim 73.5\%$ and $\sim 26.5\%$ of the total continuum emission in field HerBS-69, respectively).

3.5 Total flux measurements

An important part of characterizing the sample is measuring the velocity-integrated flux $S{\rm d}V$ (units Jy km $\rm s^{-1}$) of the emission and absorption lines detected. This was done for the low CO transitions, relevant to this work. In this section I present the method employed to make this calculation, which can be used for the lines of other molecules or atoms as well. The procedure can be divided in three steps: creating a moment 0 map (Section 3.5.1), creating an aperture (Section 3.5.2) and extracting the flux from the line profile (Section 3.5.3).

3.5.1 Moment 0 map

The first step is to create a moment 0 map of the CO line. The moment 0 map is the total integrated intensity of a line, across all frequency channels where the line is present. In general, this is a great way of gaining an initial basic understanding of the molecular gas in a galaxy, since it shows the regions where gas *is*.

For a given galaxy whose redshift z is known, the observed frequency of a line can be estimated with equation 2.7. For instance, the emission line CO$(3-2)$ (rest frequency $\nu_{\rm rest} \approx 345.796$ GHz), in the galaxy HerBS-11 ($z = 2.631$) is found at

$$\nu_{\rm obs} = \frac{345.796\ {\rm GHz}}{2.631 + 1} \approx 95.234\ {\rm GHz}\ , \tag{3.39}$$

where $\nu_{\rm obs}$ is the observed frequency. I therefore employ data cubes centered at 92.2 GHz and 95.0 GHz, which, correspond to lower side band of Band 3.

The frequencies of the data cubes are converted into velocities with equation 3.12. The spectral axes are down-sampled to the range $(-4000, 4000)$ km $\rm s^{-1}$. A

crucial step to cheapen computational cost significantly is considering only the small patch of the sky where the galaxy is, and ignoring the rest. This is handled with the World Coordinate System subroutine `WCS` of AstroPy, for given (RA, dec) coordinates and a size of the sky patch.

The continuum is subtracted considering the median value along the spectral axis. This is a fairly simple subtraction, more sophisticated methods could involve fitting a polynomial function to the regions of the spectrum free of emission (e.g. Cornwell et al., 1992). Regardless, it produces good line spectra where the line does start from the 0 level.

The moment 0 of each cube is created with `moment(order=0)` of SpectralCube, for a slab between a chosen minimum and maximal velocity $v_{\rm min}$ and $v_{\rm max}$. For each line an initial $v_{\rm min} = -600$ km s^{-1} and $v_{\rm max} = 600$ km s^{-1} was assumed. These values are then refined iteratively upon inspection of the line profile.

If multiple cubes are used for a line, the two respective moment 0 maps are combined with a scheme that assigns proportional weight to the relative contribution of each cube. In Figure 3.10 an example of the moment 0 map of CO$(3-2)$ in HerBS-11 is presented (all 9 plots show the same map).

3.5.2 Aperture

An aperture from which to extract a spectrum must be created. Creating (effectively, *drawing*) an aperture is a common theme in astronomy. There is not one obvious best way of doing this. Several studies in the literature have explored different methods and software (e.g. Laher et al., 2012; Merlin et al., 2019; Kaur & Joshi, 2021). The ultimate goal is to select all and only the pixels with real emission. In practice there are always compromises, but strategies can be used to get a line profile which includes as much real signal as possible and as little noise at possible.

One option is to *manually* draw an aperture containing the line emission as seen in the moment 0 map, using interactive user-friendly software such as Cube Analysis and Rendering Tool for Astronomy (CARTA; Comrie et al. 2021) or CASA. This can produce a good line profile, but it has a significant drawback: its lack of reproducibility. There would probably be as many different apertures as astronomers trying to make one.

In order to have a more consistent and reproducible approach, I select the apertures based on signal-to-noise ratios (SNRs). Considering the noise (i.e. standard deviation) σ of a map, I set the following criterion: only pixels whose signal is above a threshold of a number of σ (1σ, 2σ, 3σ, etc) are included in the aperture. Such an approach is employed e.g. by Stanley et al. (2023), also on DSFGs at high-redshift. They draw their aperture considering the pixels in the moment 0 map with $> 2\sigma$. There are mainly two potential problems with this approach: (i) including false positives at high signal (especially if the line emission is not so bright), and (ii) excluding real emission at low signal.

To counter these issues, I follow a similar strategy to Bakx et al. (2024). Firstly, to avoid including false emission, a threshold in the continuum emission can also be set. This assumes that the star formation (traced by dust continuum) is co-spatial with molecular gas (traced by CO line emission). This is a common assumption

in the Schmidt-Kennicutt relation, as explained in Section 2.4. With this criterion, all emission that is too far from the continuum is considered to be false. With `radio_beam` of AstroPy, the resolution of the continuum map is smoothed down (effectively, worsened) to match the resolution of the CO data cube. This way, both data have the same beam size.

In python, the pixels that fulfill the criteria in the moment 0 and continuum maps are registered in 2D masks of booleans. These two masks are combined, to include only the pixels that fulfill both criteria. Effectively, the *edge* of this mask is the preliminary aperture. After this, in order to include the real emission at low signal, this aperture is smoothed, i.e. enlarged, by a number of beam sizes. This undoubtedly adds more noise, but it is a fair compromise to capture all the emission, and avoid false positive artificially increasing the flux estimate. This is done assuming that the beam is circular rather than the common ellipsoid shape. Since ALMA beams are usually fairly circular (due to the clever spacing of the antennas) this is not a very worrying assumption.

In order to get a better understanding on how the measurement of the flux changes when tuning these three parameters (i.e. moment 0 threshold, continuum threshold and beams to smooth), I took the CO$(3-2)$ line in HerBS-11 as an example. In Table 3.3 I present the fluxes measured when trying different combinations of parameters, which are obtained with Gaussian fits (see Section 3.5.3). Furthermore, in Figure 3.10 I show different apertures drawn on the moment 0 map of the line.

Table 3.3: Values of the velocity-integrated flux $S\mathrm{d}V$ obtained for different combinations of line moment 0 threshold, continuum threshold, and number of beams to smooth, for the CO$(3-2)$ transition of HerBS-11. All values in Jy km s^{-1}. With *, the calculations whose apertures are shown in Figure 3.10.

Continuum threshold:	**Line moment 0 threshold:**			
	-99σ	1σ	2σ	3σ
	Beams smoothing = 1			
-99σ	9.48 ± 1.16	10.16 ± 0.83	9.35 ± 0.69	8.57 ± 0.60
1σ	$8.90 \pm 0.64^*$	8.90 ± 0.64	8.88 ± 0.64	8.52 ± 0.59
2σ	$8.24 \pm 0.57^*$	8.24 ± 0.57	8.24 ± 0.57	8.20 ± 0.56
3σ	$7.05 \pm 0.49^*$	7.05 ± 0.49	7.05 ± 0.49	7.05 ± 0.49
	Beams smoothing = 2			
-99σ	9.48 ± 1.16	10.16 ± 1.01	10.10 ± 0.89	9.95 ± 0.82
1σ	$10.01 \pm 0.85^*$	10.01 ± 0.85	10.02 ± 0.85	9.92 ± 0.81
2σ	$9.87 \pm 0.80^*$	9.87 ± 0.80	9.87 ± 0.80	9.85 ± 0.79
3σ	$9.33 \pm 0.73^*$	9.33 ± 0.73	9.33 ± 0.73	9.33 ± 0.73
	Beams smoothing = 3			
-99σ	9.48 ± 1.16	9.60 ± 1.09	9.95 ± 1.05	10.10 ± 1.01
1σ	$10.00 \pm 1.04^*$	10.00 ± 1.04	10.04 ± 1.04	10.09 ± 1.00
2σ	$10.18 \pm 1.00^*$	10.18 ± 1.00	10.18 ± 1.00	10.18 ± 0.99
3σ	$10.07 \pm 0.92^*$	10.07 ± 0.92	10.07 ± 0.92	10.07 ± 0.92

Table 3.3 includes a threshold equal to -99σ. This basically means no constraint. In particular, the calculation where both the line moment 0 and continuum threshold

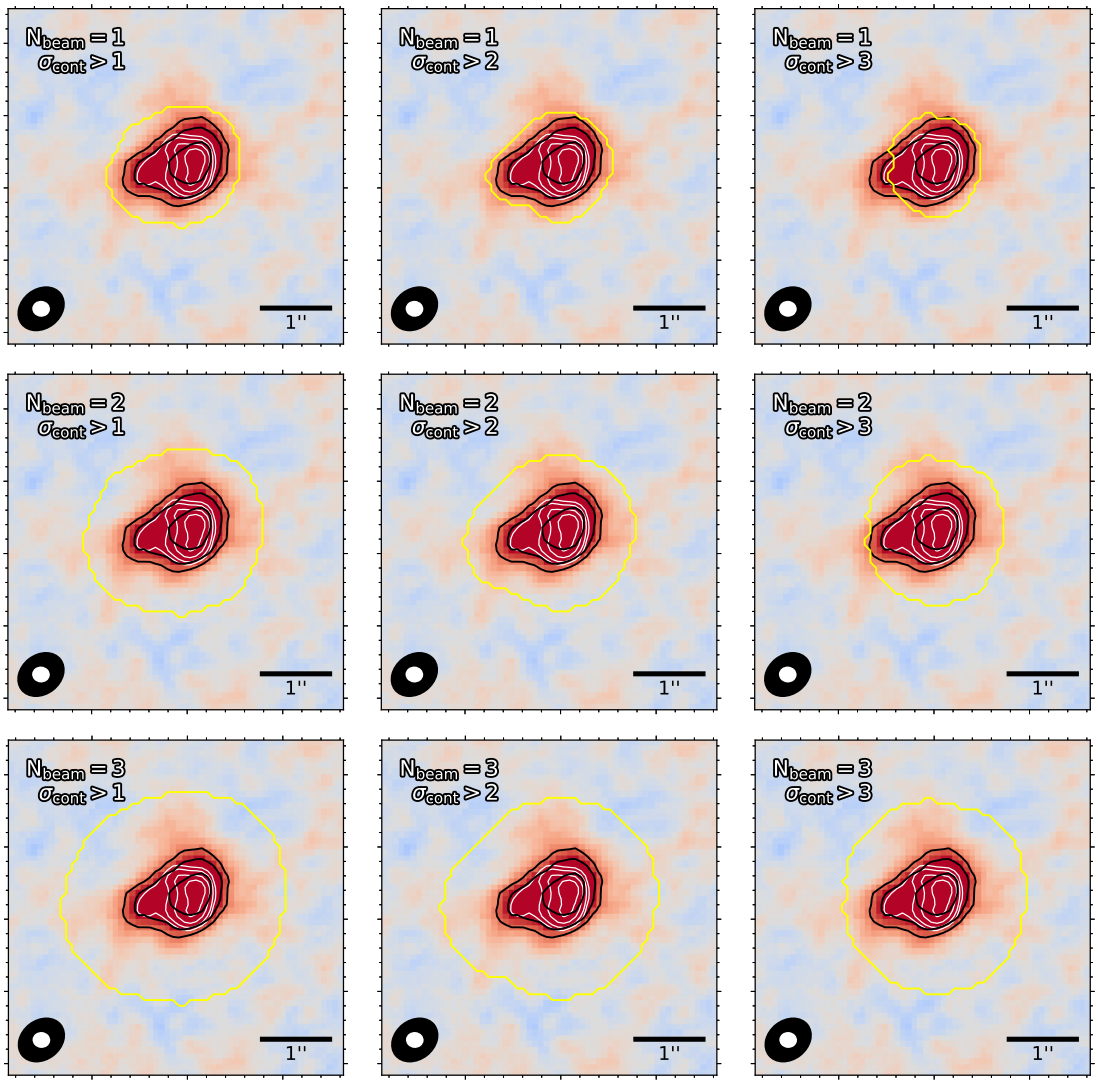

Figure 3.10: Comparison of nine candidate apertures to extract a line profile. The map corresponds to the moment 0 of the CO$(3-2)$ emission line in HerBS-11. In black lines, the $2\sigma, 3\sigma, 5\sigma$ contours of the map. In white lines, the $2\sigma, 3\sigma, 5\sigma, 8\sigma$ contours of the Band 6 continuum map. In the bottom left of each sub-figure, the ALMA beam sizes of the data cubes (in black) and the continuum (in white). In a yellow line, the aperture created with the parameters shown in the sub-figures. No threshold is set for the moment 0 map, since effectively the main constraint is given by the continuum, due to its much larger SNR. The measured fluxes from these nine apertures are signaled with * in Table 3.3. The aperture in the center-left panel is ultimately chosen.

are set to -99σ (i.e. aperture includes entire region) is the only true representation of reality. Working with no constraints at all is not possible in practice, since there is too much noise to make a proper calculation of $S\mathrm{d}V$.

Table 3.3 reflects that for any continuum constraint (i.e. any continuum threshold that is not -99σ), the threshold in the line moment 0 does not have a significant impact in the flux that is measured; this is seen in the fact that the numbers in a

row barely change in any number of beams smoothing. This happens because the continuum emission is much brighter that the line moment 0 (see contour lines in Figure 3.10). This is true of CO$(3-2)$ in HerBS-11, which is relatively bright, so in fainter lines it will be even more convincing. As a consequence, when creating the aperture is more useful to constrain the continuum rather than the moment 0 map. Regardless, these nuances will change from line to line, so the criteria will be assessed individually for each line.

Figure 3.10 includes no constraints in the moment 0 map for the same reason. From a purely visual inspection, smoothing the aperture with 1 beam is too tight around the emission; there is surely flux missing. On the contrary, smoothing with 3 beams seems to capture all the emission, but also adds a lot of unnecessary noise. This gradual increase in noise for bigger apertures is also reflected in Table 3.3 (bigger error bars when smoothing with more beams).

The two apertures in Figure 3.10 which seem to best capture all the emission and very little extra noise are the first and second of the middle row. These were created with 2 beams of smoothing and continuum thresholds of 1σ and 2σ. Table 3.3 shows that the fluxes measured in these cases are

$$S\mathrm{d}V(\mathrm{N_{beam}}=2;\sigma_{\mathrm{cont}}>1)=(10.01\pm0.85)\ \mathrm{Jy\ km\ s^{-1}}\ , \tag{3.40}$$

$$S\mathrm{d}V(\mathrm{N_{beam}}=2;\sigma_{\mathrm{cont}}>2)=(9.87\pm0.80)\ \mathrm{Jy\ km\ s^{-1}}\ . \tag{3.41}$$

Regardless of coming from a different set of parameters, these two results are clearly fully consistent within their uncertainties. This goes to show that, despite the creation of the aperture being subjective to my choice of parameters, as long as the aperture looks reasonable the integrated flux will be consistent. As explained in Section 2.4, the error bars of this value $S\mathrm{d}V$ will increase significantly when converted to H_2 mass, which makes small discrepancies such as the one presented in equations 3.40 and 3.41 even less worrying. In general, I aim for larger apertures in order to include all the flux despite the extra noise. For the line presented as the example, $S\mathrm{d}V(\mathrm{N_{beam}}=2;\sigma_{\mathrm{cont}}>1)=(10.01\pm0.85)$ Jy km s^{-1} is chosen.

3.5.3 Flux extraction

Once the aperture is chosen, the spectrum is extracted from the cube(s), in units Jy/beam. It is corrected by the primary beam, considering the value of the pixel in the center of the galaxy. Effectively, each spectrum is divided by a number between 0 and 1. Since most galaxies are well-centered in their fields of views, the correction is usually very small. Also, the units are converted to Jy by dividing by the area of the beam measured in pixels. This factor comes from equation 3.2, and is commonly around 40-70 (i.e. there are 40 to 70 pixels inside the ALMA beam; see second column of Table 3.5 for some examples).

In Figure 3.11 there are two examples of line profiles extracted with this method; for HerBS-11 and HerBS-17 (the first two galaxies of my sample with a low CO line, see Table 4.1). The total velocity-integrated flux $S\mathrm{d}V$ is estimated from these line profiles in two ways. First, a Gaussian fit is performed with the lmfit library (Newville et al., 2025). A second way is to measure the geometric sum of the line, i.e. simply the summing the area of each rectangle in yellow in Figure 3.11. In Table

3.4 a comparison of the calculations extracted with these two methods is presented for several lines. The methods are largely consistent within their error-bars. In the Gaussian fit, this error is provided directly by lmfit, whereas in the geometric sum it comes from propagating the standard deviation across all relevant velocity channels.

The Gaussian fit is preferred when measuring the total line flux in galaxies, since it provides useful measurements of the width and center velocity of the line, and the lines are commonly fairly Gaussian. There are, however, exceptions to this, e.g. the double-peaked CO(5 − 4) line in HerBS-27 shown in Section 4.1. These cases are not improved further, but the bad fit is reflected in a large error bar. Regardless, in all cases the measurement of this fit is consistent with the geometric sum. When measuring the line flux in smaller regions of a galaxy (this will be done to build resolved SK diagrams, see Section 3.6 and specifically Section 3.6.3), the geometric sum is preferred, since it is more common to get line profiles which are not Gaussian (e.g. asymmetric or double-peaked), and the information of the width and position of the line is not relevant in the SK relation.

Table 3.4: Comparison of the velocity-integrated flux obtained for CO lines across the first galaxies of the sample (see Table 4.1), with two different methods. All values in Jy km s^{-1}. The two methods are clearly fully consistent within their error-bars. The first two lines, CO(3 − 2) in HerBS-11 and HerBS-17, correspond to the examples shown in Figure 3.11.

Galaxy	Line	$S\mathrm{d}V$ via Gaussian fit	$S\mathrm{d}V$ via Geometric sum
HerBS-11	CO(3 − 2)	10.01 ± 0.85	10.20 ± 1.25
HerBS-17	CO(3 − 2)	7.32 ± 1.44	6.97 ± 1.05
HerBS-18	CO(3 − 2)	6.87 ± 0.90	7.07 ± 1.01
HerBS-23A	CO(5 − 4)	3.30 ± 0.85	3.49 ± 0.68
HerBS-27	CO(5 − 4)	6.08 ± 1.21	5.75 ± 0.81
HerBS-28	CO(4 − 3)	5.66 ± 1.96	5.17 ± 1.01
HerBS-33A	CO(3 − 2)	2.85 ± 1.15	3.00 ± 0.75
HerBS-37	CO(3 − 2)	6.41 ± 1.98	6.11 ± 0.90

3.6 Resolved Schmidt-Kennicutt algorithm

In order to make use of the great resolution achieved by ALMA, I create resolved diagrams of the SK relation, i.e., for each galaxy I calculate Σ_{SFR} and $\Sigma_{\mathrm{H_2}}$ in different regions in a ∼kpc scale. This will allow me to study how the star formation varies within a galaxy, instead of making one single global description (i.e. an unresolved description). The calculations are done in a beam-per-beam basis, i.e. with apertures resembling the size and shape of the CO data cube beam. This is chosen because the beam represents the smallest region in the sky in which measurements can be (approximately) independent; two different beams in the sky are considered to be uncorrelated. The resolution of the CO data cubes is at a physical scale of a few kpc.

The goal is to create an algorithm that can be applied to a large number of

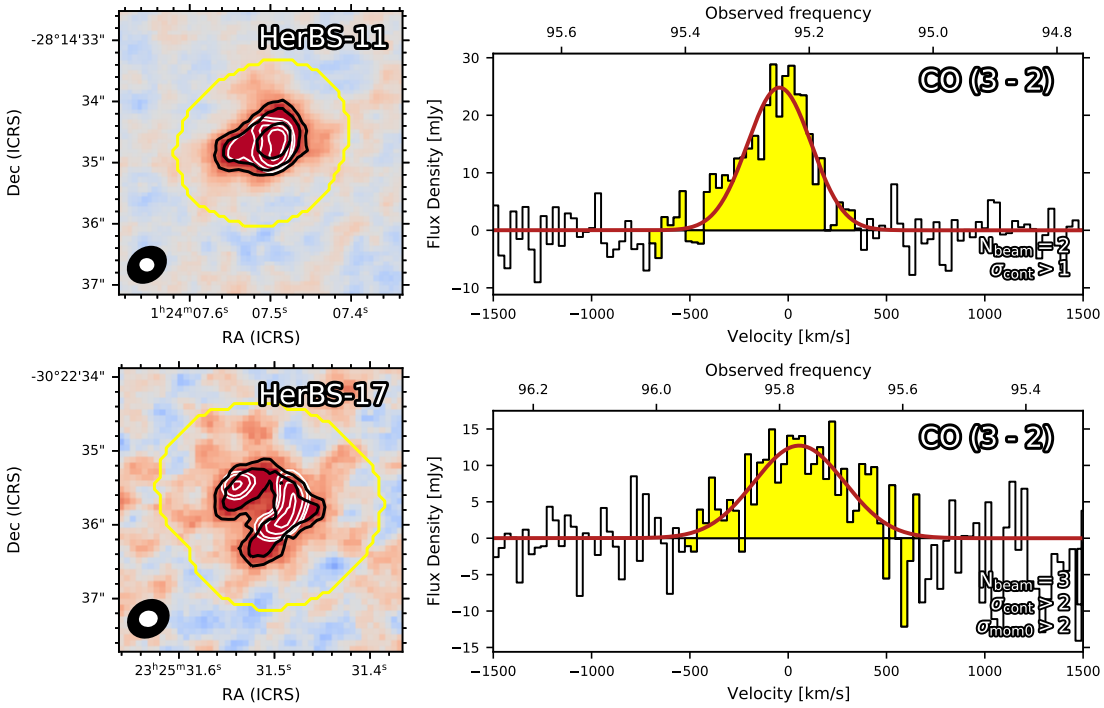

Figure 3.11: For the CO(3 − 2) line in HerBS-11 and HerBS-17, the moment 0 map on the left (colors same as Figure 3.10, i.e. color map and black contours are moment 0 map, while white contours are continuum map), and the spectrum extracted from the yellow aperture on the right. Each spectrum shows the gaussian fit in red; and in yellow the velocity range used to create the moment 0 map and to estimate the geometric sum of Table 3.4. The selection criteria for the aperture is noted in the bottom right of the respective spectrum. The line profiles are clearly well described by the Gaussian fit.

galaxies systematically, regardless of their specific morphology. This will allow for a fair comparison, where they are all studied by the same methodology. The algorithm does the following. For a galaxy of the sample, given the moment 0 and continuum maps:

1. Create an aperture that resembles the beam of the CO line.
2. Populate the sky with this aperture until enough space has been covered.
3. Extract SdV flux and continuum emissions in each aperture.
4. Repeat steps 2-3 centering the apertures in all possible locations.
5. Calculate error-bars for SdV flux and continuum from the background noise.
6. Calculate $\Sigma_{\rm SFR}$ and $\Sigma_{\rm H_2}$ in apertures where a detection is made.

Now each step is explained in detail.

3.6.1 Creating a basic aperture

An aperture which resembles the ALMA beam of the CO line must be created. Effectively, this means selecting the group of pixels that best represents the size and shape of the beam. In python terms, the aperture is a 2D mask of booleans of the same size as the moment 0 and continuum maps. In general, ALMA beams are tilted

ellipses, whose relevant parameters are stored in the data. As explained in Section 3.2, ALMA beams follow a distribution that can be approximated as a Gaussian. The data reports the Full Width at Half Maximum (FWHM) in the directions of the major and minor axes (FWHM_1 and FWHM_2), in degrees. The area of the beam can be estimated as

$$A = \frac{\pi}{4\ln 2} \times \mathrm{FWHM}_1 \times \mathrm{FWHM}_2 \ \ [\mathrm{degrees}^2] \ , \tag{3.42}$$

which simply follows equation 3.2 (in each axis, FWHM represents θ_{HPBW}). This area is equivalent to the area of an ellipse whose semi-major and semi-minor axes a and b are

$$a = \frac{\mathrm{FWHM}_1}{2\sqrt{\ln 2}} [\mathrm{degrees}] \ , \tag{3.43}$$

$$b = \frac{\mathrm{FWHM}_2}{2\sqrt{\ln 2}} [\mathrm{degrees}] \ . \tag{3.44}$$

The data files include factors to directly convert a and b from degrees to pixels, which is needed.

Now, the ellipse is rotated with a modified rotation matrix. The usual rotation matrix is

$$\mathcal{R}(\theta) = \begin{bmatrix} \cos\theta & -\sin\theta \\ \sin\theta & \cos\theta \end{bmatrix} \ , \tag{3.45}$$

for a counterclockwise rotation where θ is measured from the positive x semi-axis. The data files include the beam position angle α (PA; the inclination of the beam). This is measured counterclockwise from the north (positive y semi-axis), so that $\theta = \alpha + \pi/2$. Then, for a point in the pixel space (x, y) centered at (x_0, y_0), I make the conversion

$$x' = (x - x_0)\cos(\alpha + \pi/2) + (y - y_0)\sin(\alpha + \pi/2) \ , \tag{3.46}$$

$$y' = -(x - x_0)\sin(\alpha + \pi/2) + (y - y_0)\cos(\alpha + \pi/2) \ , \tag{3.47}$$

which includes a translation to (x_0, y_0) and a rotation by $\alpha + \pi/2$. Furthermore, the signs of the sin() terms are reversed from equation 3.45 because astronomical images have the x-axis (R.A.) pointing to the left. Lastly, all pixels considered for the aperture are the ones inside the ellipse equation:

$$\frac{x'^2}{a^2} + \frac{y'^2}{b^2} \leq 1 \ , \tag{3.48}$$

where all quantities are defined in 3.43, 3.44, 3.46 and 3.47; with FWHM_1, FWHM_2 and α reported in the data file. In Figure 3.12 an example of the resulting aperture for HerBS-11 is presented.

The basic aperture will be used to extract fluxes from different regions of a galaxy. It will therefore be placed in different parts of the pixel space. It must not leave any gaps and not cover any pixel twice, in order to properly measure all regions of the galaxy independently without any flux loss. Effectively, this means that the aperture must tessellate the pixel space. This tessellation is done assuming that the

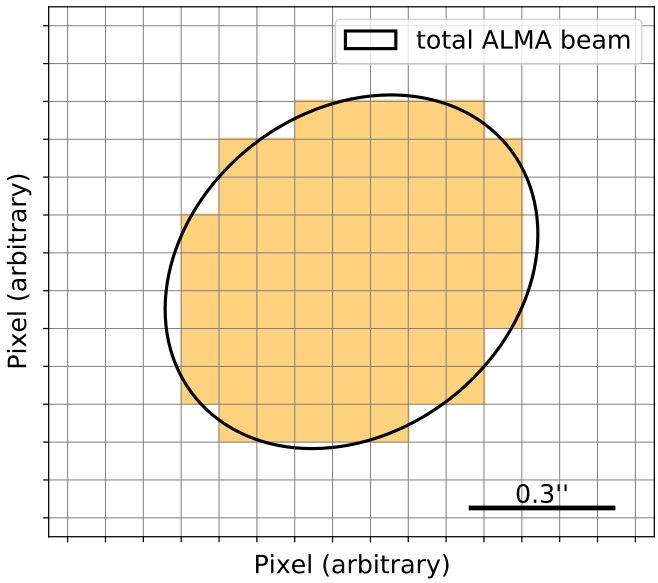

Figure 3.12: Basic aperture created for the HerBS-11 galaxy with equation 3.48, centered in an arbitrary pixel, compared against the ALMA beam of the CO$(3-2)$ line. The ellipse has dimensions $a \approx 0.42'' \approx 5.30$ pixels, $b \approx 0.33'' \approx 4.24$ pixels (a and b defined in equations 3.43, 3.44) and $\alpha \approx -52°$.

shape of the aperture resembles a hexagon, so that each aperture has 6 apertures around it. In a tessellation of hexagons, the relative position of three hexagons is enough information to do the entire tessellation, since all other hexagons are placed scaling and combining of distances between the first three.

In order to ensure that the chosen aperture tessellates correctly, and to find the relative position of two other apertures, I do as follows: The basic aperture created with equation 3.48 is repeated directly above and to the right (as shown in the top left panel of Figure 3.13). Then, these two new apertures are shifted closer to the top right corner of the first aperture, one pixel at a time, until they can no longer get any closer (as shown in subsequent panels of Figure 3.13). This is done so that they leave as few pixel gaps as possible in between.

Each gap pixel must be appended to the aperture in order for the tessellation to work. The difficulty lies in deciding where in the aperture is best to add the pixel. For each gap pixel, the algorithm searches which of the three apertures it touches the most times in all 8 direction (up, down, left, right and diagonally). In the example of Figure 3.13, there are two pixels in the gap (see bottom right panel). The left one touches the blue and light-blue apertures in three directions, and the orange in one. Then, it is added to the blue aperture (in a tie, the blue aperture is always favored). The right pixel touches the blue aperture in one direction, the light-blue in two and the orange in four, so it is added to the orange aperture. In each case, a mirror pixel is also added to the respective aperture. Figure 3.14 reflects how this process is done.

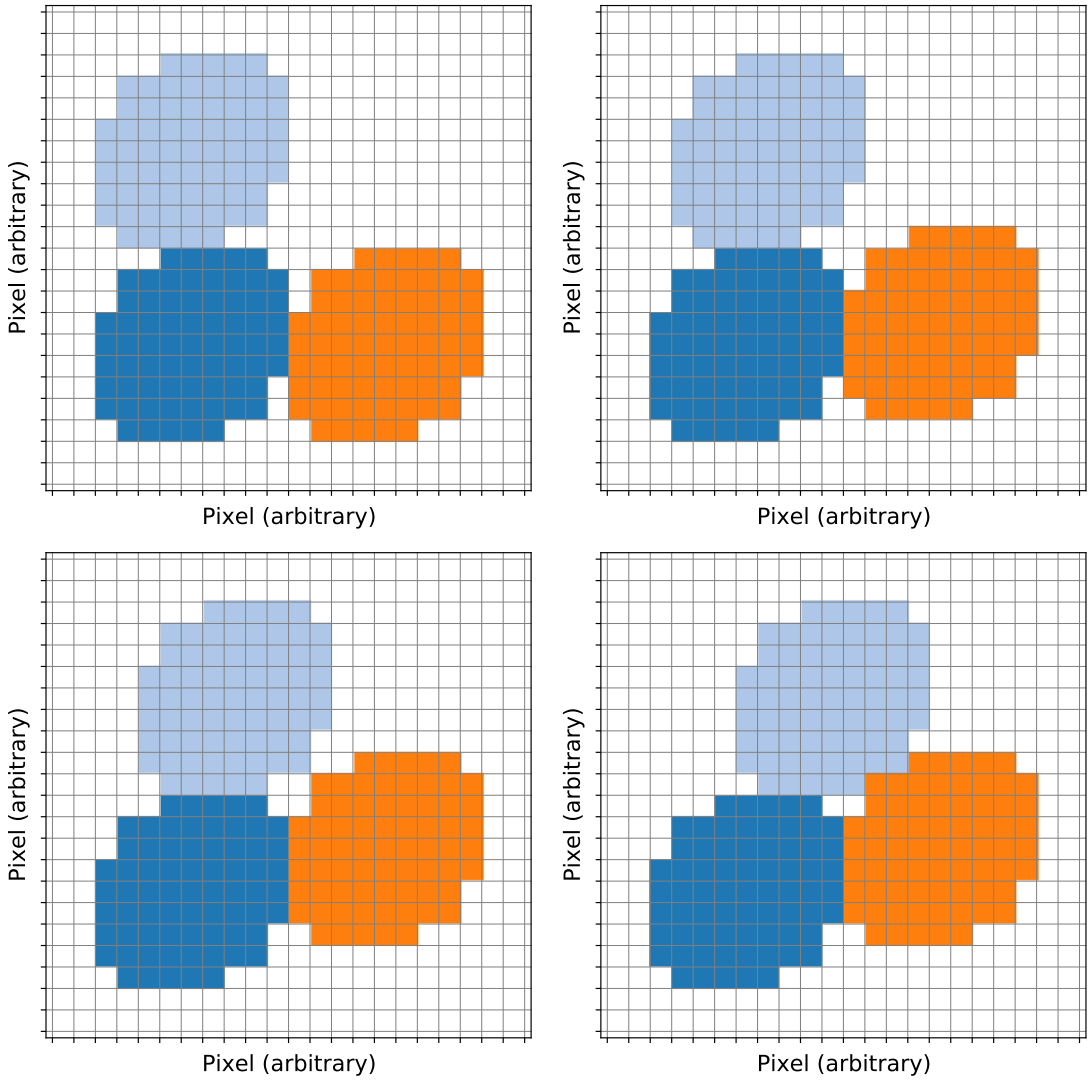

Figure 3.13: Step-by-step procedure to find correct tessellation of apertures and possible gaps in between. In the top left panel, the basic aperture (blue) is repeated directly above (light-blue) and to the right (orange). In each subsequent panel (left to right), the light-blue and orange apertures are shifted right and up, respectively, one pixel at a time. This stops when they can no longer get any closer, leaving as few gaps as possible in between. Some simplifications must be made. E.g. before the last step, only one of the two apertures can continue moving. Either the light-blue moves two pixels to the right or the orange moves two pixels up. In both cases the number of gap pixels would be the same (2). The light-blue aperture is chosen to move. From this procedure the relative distance (in pixels) of the apertures is also obtained. Pixel to arcsec scale is the same as shown in Figure 3.12.

Finally, the three apertures are overlaid on top of each other and their combination of pixels becomes the final aperture used for the galaxy. In Figure 3.15 the aperture used for HerBS-11 is shown. This is basically the same as in Figure 3.12, only with those extra pixels to ensure that the tessellation works.

The success of the tessellation depends heavily on the first aperture created with

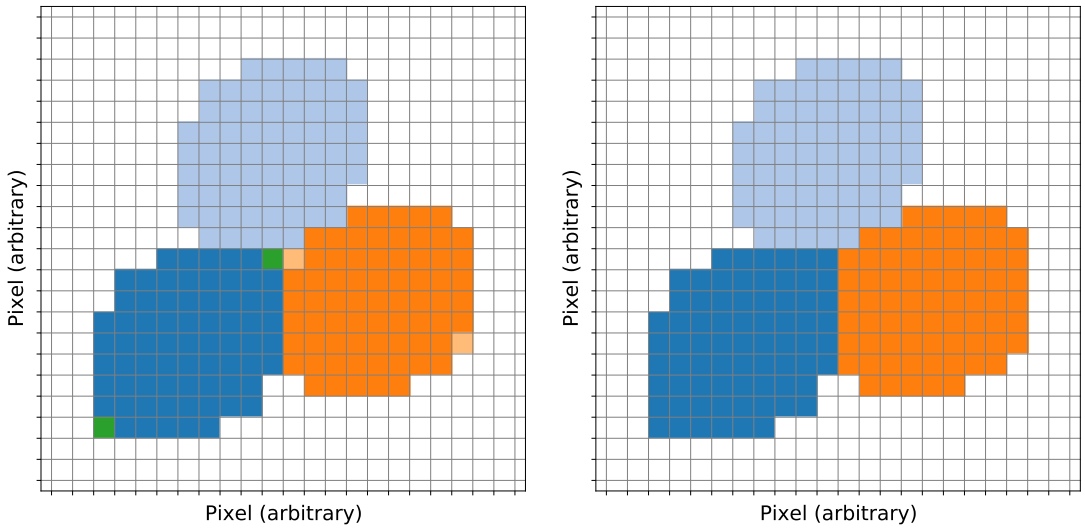

Figure 3.14: Modification of aperture in order to fill gaps in tessellation. In the algorithm, this is the continuation of the steps shown in Figure 3.13 (same example for HerBS-11). Gap pixels are colored in green and beige. They will be added to the blue and orange apertures, respectively, as shown on the right panel. In green and beige also the mirror pixels added to the respective aperture.

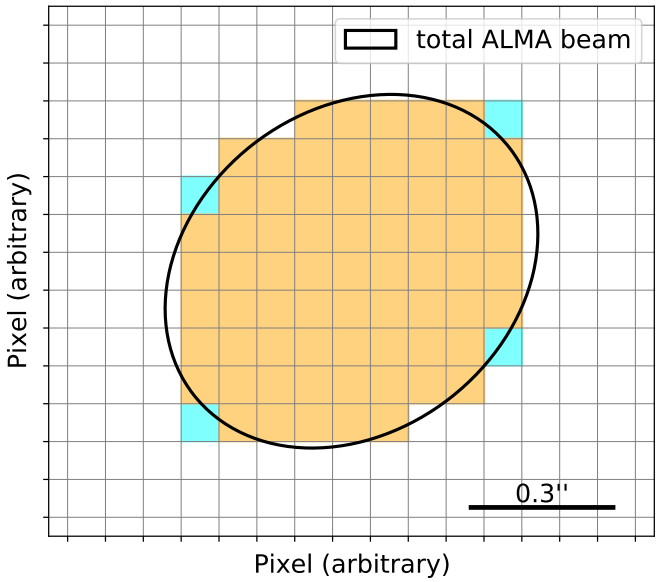

Figure 3.15: Basic aperture created for the HerBS-11, after correcting for gap pixels, compared against the ALMA beam of the CO$(3-2)$ line. In beige, the same as in Figure 3.12, i.e. the pixels that result from using the ellipse equation 3.48. In cyan the extra pixels added to ensure tessellation. Dimensions are the same as in Figure 3.12.

equation 3.48. If this equation yields an aperture with sharp edges (e.g. one single pixel sticking out from an otherwise straight edge), the I perform a Gaussian blur to the mask in order to soften the edge, using `gaussian_filter` of SciPy (Virtanen et al., 2020). This yields slightly smaller apertures, but which can be tessellated more easily and whose size might anyway increase as shown in Figure 3.15.

In Table 3.5, the size of the ALMA beam (from equation 3.42 converted to pixels^2) is compared against the size of the aperture (i.e. number of pixels) for several galaxies. This comparison shows that the apertures produced by the algorithm have a good size. The aperture should preferably be bigger than smaller than the beam (it's better to assume a worse resolution than a better one). This is the case in most galaxies, altough there are exceptions such as HerBS-28 or HerBS-33A which occur due to the Gaussian blurring. Furthermore, in Figure 3.16 the basic apertures of four galaxies are shown tessellating the pixel space, with ALMA beams overlaid in them. It's clear that the apertures resemble the ALMA beams both in size and shape. The algorithm is considered successful in building adequate apertures for the galaxies of the sample.

Table 3.5: Areas of the ALMA beam and the basic aperture for several galaxies included in this work. In the last column, the effective size of the aperture in beams (simply the ratio between columns 3 and 2).

Galaxy	Beam [pixels^2]	Aperture [pixels^2]	N_{beams}
HerBS-11	70.60	73	1.03
HerBS-17	54.18	55	1.02
HerBS-18	41.44	43	1.04
HerBS-28	54.60	53	0.97
HerBS-33A	85.64	81	0.95
HerBS-47A	53.74	55	1.02
HerBS-160	72.48	73	1.01

3.6.2 Placing rings of apertures

I now have a good aperture which resembles the ALMA beam and which I can tessellate in order to study different parts of a galaxy. How to use it? Since I want an approach that can be used systematically for any galaxy, I do not place this aperture *by hand* in parts of the sky based on a specific CO moment 0 map. Instead, for any galaxy of my sample, my idea is to place the first aperture close to the center (in Section 3.6.4 this is elaborated), and then place more in concentric rings until sufficient space of the sky is covered to properly capture the galaxy.

From the procedure shown in Figure 3.13, the relative positions $(\Delta x_1, \Delta y_1)$ and $(\Delta x_2, \Delta y_2)$ between the first aperture and two other are obtained (in terms of pixels). Placing an entire ring of apertures around the center aperture, as shown in Figure 3.16, is relatively straightforward. A third aperture can be placed by considering $(\Delta x_3, \Delta y_3) = (\Delta x_2 - \Delta x_1, \Delta y_2 - \Delta y_1)$ (this is the dark green aperture in Figure 3.16), and the ring is completed by mirroring the first half of the ring, i.e. with

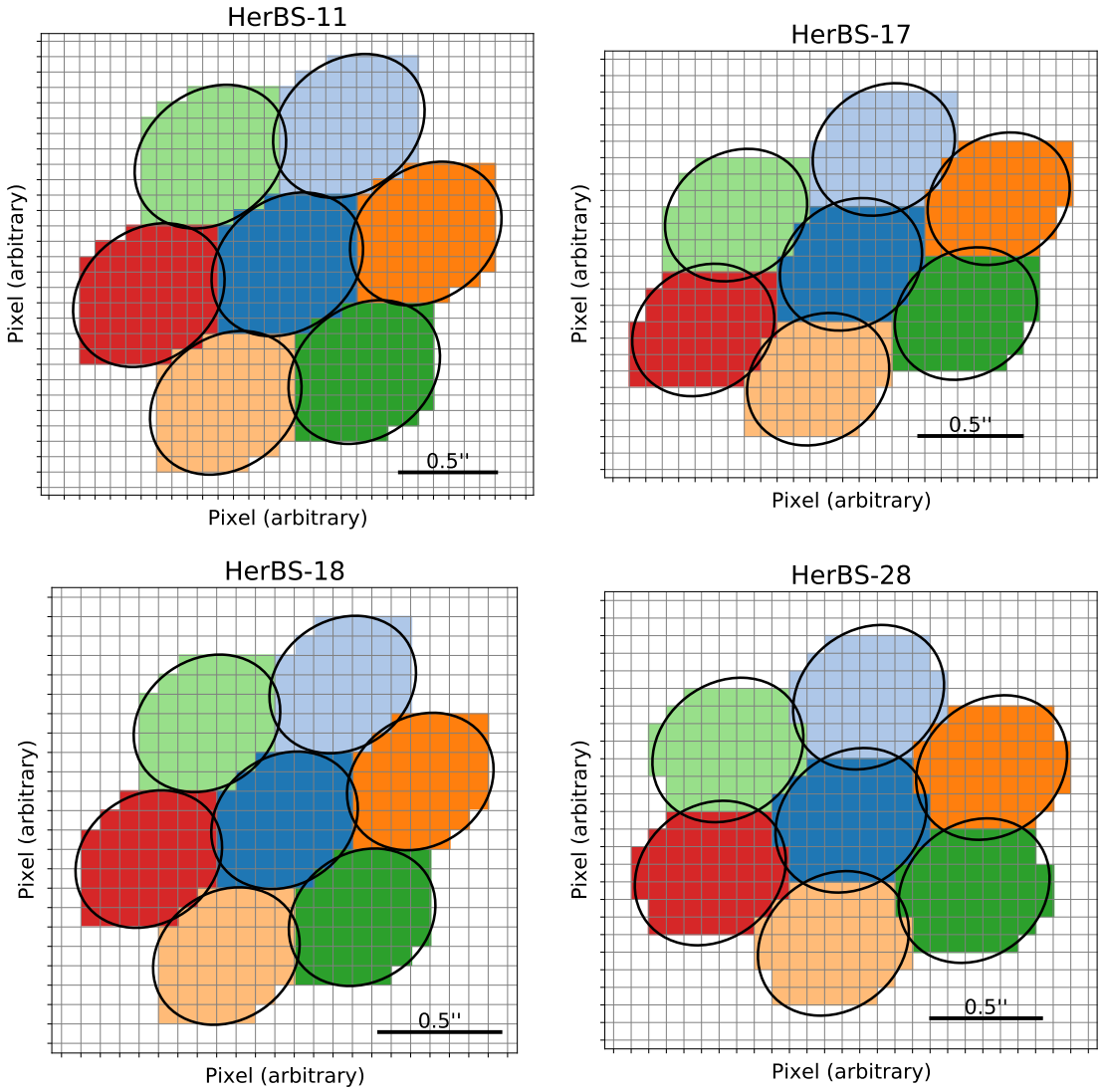

Figure 3.16: For four galaxies (HerBS-11, 17, 18 and 28), in blue is shown the basic aperture, with an entire ring of apertures tessellated around it. As a comparison, in black ellipses, the corresponding ALMA beam that each aperture is modeling.

apertures shifted by $(-\Delta x_1, -\Delta y_1)$, $(-\Delta x_2, -\Delta y_2)$ and $(-\Delta x_3, -\Delta y_3)$ with respect to the center one.

In Figure 3.17 three entire rings of apertures are shown on the CO(3−2) moment 0 map of HerBS-11 and HerBS-17. This approach with rings ensures that I can capture the relevant parts of the galaxy regardless of what direction is favored; e.g. if a galaxy has more emission to the north or the south, I do not need to place apertures there specifically, but rather just build more rings until that emission is covered. All apertures where no emission is detected (e.g. apertures 19-36 in Figure 3.17 are clearly just background) can simply be discarded later due to their low SNR (in Section 3.6.6 this is further explained).

After the first ring of apertures, the next rings can also be created by linearly combining $(\Delta x_1, \Delta y_1)$ and $(\Delta x_2, \Delta y_2)$, but it gets more tricky, since each ring has

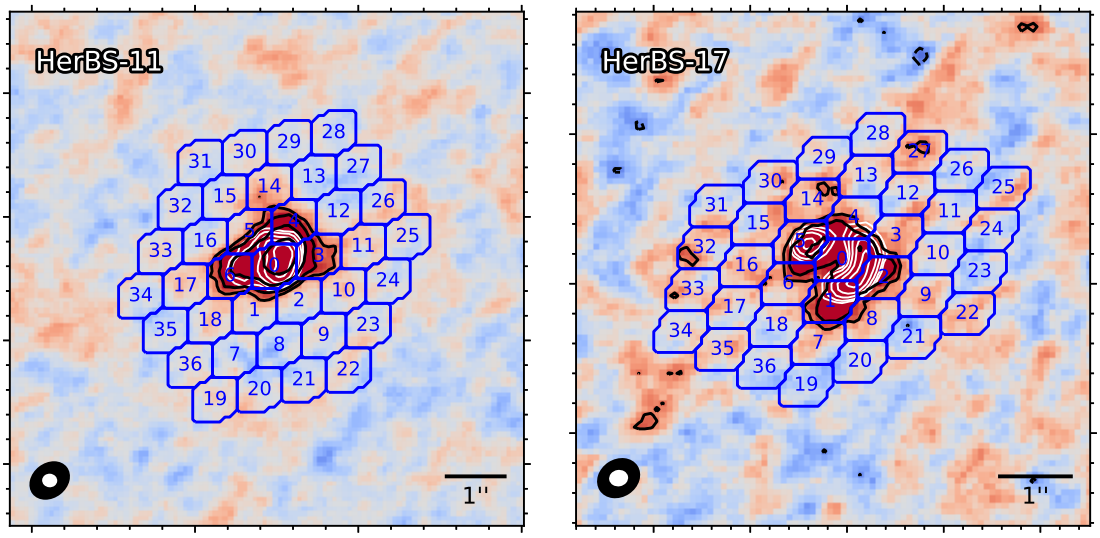

Figure 3.17: Tessellation of the basic apertures of HerBS-11 (left) and HerBS-17 (right), overlaid in the respective moment 0 maps of the CO(3 − 2) line. These maps are analogous to those in Figure 3.10 (i.e. color map and black contours are moment 0 map, while white contours are continuum map), only more zoomed-out. The 0th aperture is at the center, then the first ring of apertures ($k = 1$) corresponds to apertures 1-6, the second ring ($k = 2$) to apertures 7-18, and the third one ($k = 3$) to 19-36.

more apertures than the previous one. The kth ring has $6k$ apertures, so the first one has 6, the next 12, then 18 and so on. The best approach to create rings of apertures is using axial coordinates, which are appropriate for hexagonal geometry. In Figure 3.18 the basic grid for this system is presented. Each hexagon (or in my case, aperture), can be represented by a point in the (q, r) space. Two adjacent points in the axial coordinate system (q_1, r_1) and (q_2, r_2) can be connected via six different unit vectors, which are the directions $\mathcal{D}$

$$\mathcal{D} = \{(+1, 0), (+1, -1), (0, -1), (-1, 0), (-1, +1), (0, +1)\} \ . \tag{3.49}$$

The center aperture corresponds to the position $(q, r) = (0, 0)$. For each kth ring, the (q, r) coordinate of a new aperture is obtained as follows

1. The first aperture of the ring has coordinates $(-k, k)$. E.g., for the second ring ($k = 2$), it's simply $(-2, 2)$.
2. The next k apertures come from adding the first direction in equation 3.49, subsequently, k times. E.g. For the second ring ($k = 2$), the next two apertures have coordinates $(-1, 2)$ and $(0, 2)$, which come from adding the vector $(+1, 0)$ to $(-2, 2)$ once and then again.
3. Repeat step 2 for the next direction in equation 3.49, until all 6 directions have been completed. This will yield the total of $6k$ apertures. E.g. For the second ring ($k = 2$), the next two apertures have coordinates $(1, 1)$ and $(2, 0)$, which come from adding the vector $(+1, -1)$ to $(0, 2)$ once and then again.

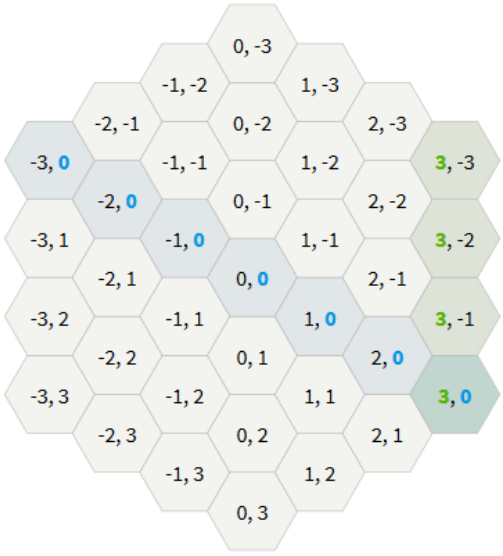

Figure 3.18: Axial coordinates commonly used to tessellate hexagons; in this work they are used to tessellate the basic aperture of a galaxy. Each point is defined by the coordinates (q, r). Credit: Abdel5; available at `https://gamedev.stackexchange.com/questions/109232/hex-axial-coordinates-to-table-coordinates-conversion`.

In the pixel space, where apertures are effectively placed, the position of each aperture is deduced from its (q, r) position as

$$\Delta x = q \times \Delta x_2 + r \times \Delta x_3 \ , \tag{3.50}$$

$$\Delta y = q \times \Delta y_2 + r \times \Delta y_3 \ , \tag{3.51}$$

where $(\Delta x, \Delta y)$ is the shift with respect to the center aperture, and $(\Delta x_2, \Delta y_2)$, $(\Delta x_3, \Delta y_3)$ are known from Figure 3.16 as already explained. In Figure 3.17 is shown inside each aperture the order in which they are created. In summary, with this strategy, $6k$ new apertures can be placed for any new ring that is desired. The number of rings is decided based on a visual inspection of the apertures on the moment 0 map. In the cases of HerBS-11 and HerBS-17 (Figure 3.17), three rings were clearly good enough to cover the total area of the sky with potential continuum or CO emission.

3.6.3 Extracting flux and continuum measurements

Having the apertures, I can directly extract the necessary measurements: continuum and CO flux. Since the continuum is a 2D map, I simply add the values of all pixels inside the aperture. I use the map that has been convolved to match the resolution of the CO data cube (as explained in Section 3.5.2). The conversion Jy/beam to Jy is done in the same manner as was explained in Section 3.5.3 (i.e. divide by the area of the beam in pixels).

For the CO line, the spectrum inside an aperture is extracted as explained in Section 3.5.3, and the velocity-integrated flux $S\mathrm{d}V$ is calculated with the geometric

sum. In Figure 3.19 I present the line spectra of apertures 0-7 in HerBS-11, as seen in the left panel of Figure 3.17. From Figure 3.17 is clear that apertures 0, 3, 4, 5 and 6 are well inside the emission, apertures 1 and 2 only partially, and aperture 7 should be only noise. This is reflected very well in the line profiles of Figure 3.19.

3.6.4 Exploring all cases

In Figure 3.17 was shown an example of how the aperture can be used to study different parts of a galaxy. If these apertures had been placed slightly differently, e.g. move the entire tessellation a few pixels to the left or to the right, the same goal would be achieved: extract measurements from different parts of the galaxy in regions according to the ALMA resolution. The measurements would be different from the first example, but both would capture the same phenomenon. Since there is no one preferred way of placing the apertures, the algorithm explores all possibilities. This reflects the scatter that the resolved SK relation can have.

The center position of the galaxy (RA, dec) is estimated with the continuum snapshots (see Section 4.1). This is converted into (x, y) pixels, considering the moment 0 map of the CO line. In Figure 3.17, aperture 0 is centered around this pixel for HerBS-11 (as a consequence, the entire tessellation is centered around this pixel too). Any pixel inside that aperture 0 could be used to center a new tessellation, and all these tessellations would be different, i.e. there would be no two apertures capturing the same set of pixels. Since aperture 0 contains 73 pixels (as shown in Table 3.5), there are 73 different ways to make the tessellation for HerBS-11, which means that 73 different resolved SK diagrams can be built. In Figure 3.20, three examples of different tessellations are presented, for both HerBS-11 and HerBS-17.

For each case, the measurements of velocity-integrated flux $S\mathrm{d}V$ and continuum are extracted. A resolved SK diagram can be obtained from each case, all of them being equally representative of the galaxy.

3.6.5 Calculating error bars

The measurement errors for the velocity-integrated fluxes $S\mathrm{d}V$ and continuums must be estimated. The standard deviation σ in a velocity channel can be extracted directly from the data cubes. The region of the sky used for this is the background. In Figure 3.17, the zoomed-out moment 0 map of the CO$(3-2)$ line of two galaxies were presented. The entire region included in these maps which is outside the grid of apertures, is considered to calculate σ. This region needs to be large, in order to get good statistics and a good measurement of true noise of the sky. By pure visual inspection, using regions like shown in Figure 3.17 yields good measurements, as larger regions produce no different values for σ in any galaxy.

The standard deviation extracted for a channel is measured in Jy/beam. I assume the noise is uncorrelated and Gaussian, so that I convert to Jy by simple error propagation, i.e. multiplying by $\sqrt{\mathrm{N_{beams}}}$. In this case, $\mathrm{N_{beams}}$ is the number of beams inside the basic aperture, which correspond to the number of independent measurements. Since these apertures are designed to match the size of the beam, $\mathrm{N_{beams}}$ is always a number close to 1. In Table 3.5 this value is shown for a few

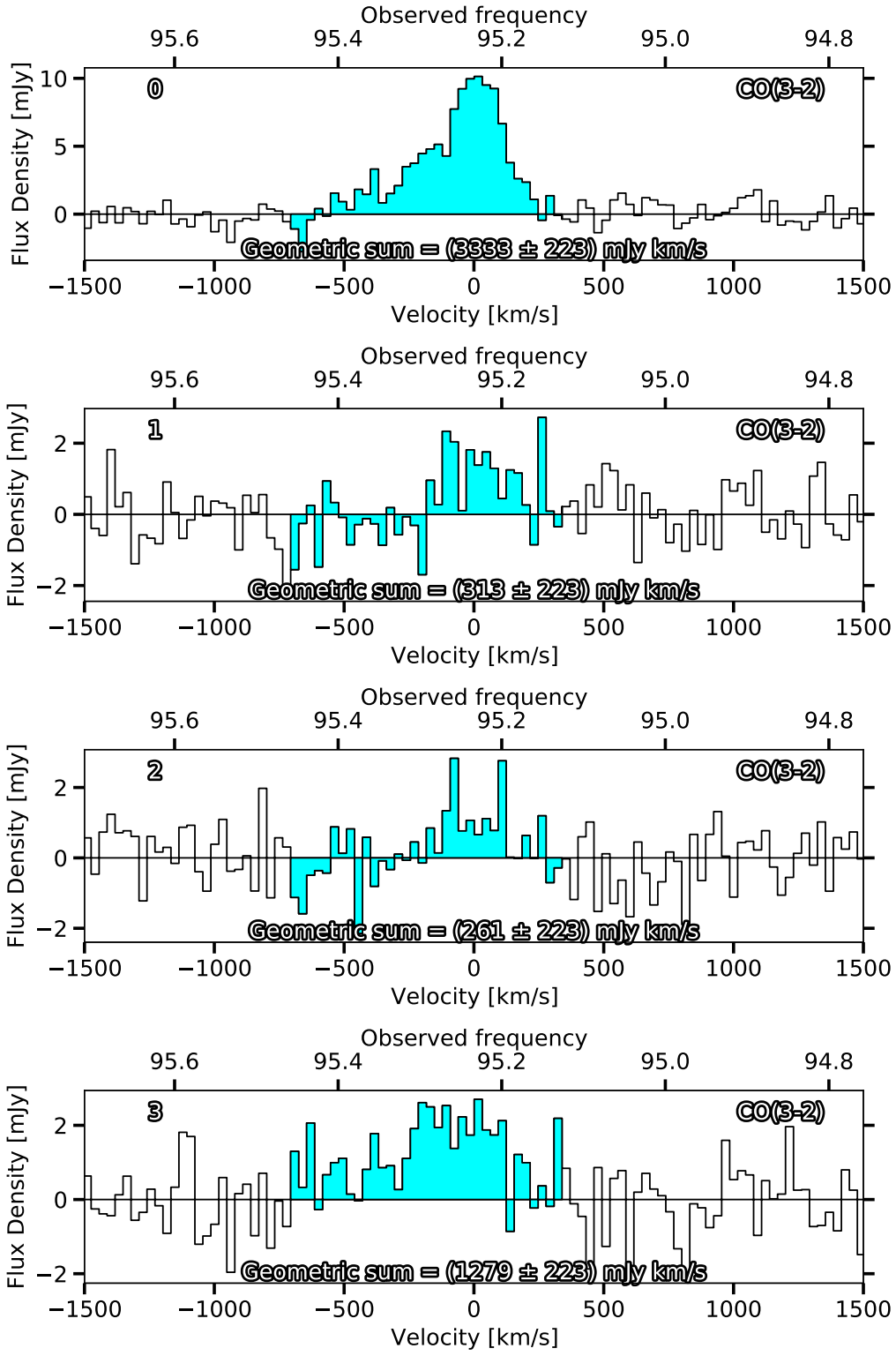

Figure 3.19: CO(3 − 2) line profiles of the first eight apertures of HerBS-11, as shown in Figure 3.17. In each panel, the aperture that the spectrum corresponds to is labeled in the top left. The velocity-integrated flux $S\mathrm{d}V$ is also shown, obtained with the geometric sum in the velocity range shown in cyan (same range for all profiles). The error bars are estimated as described in Section 3.6.5.

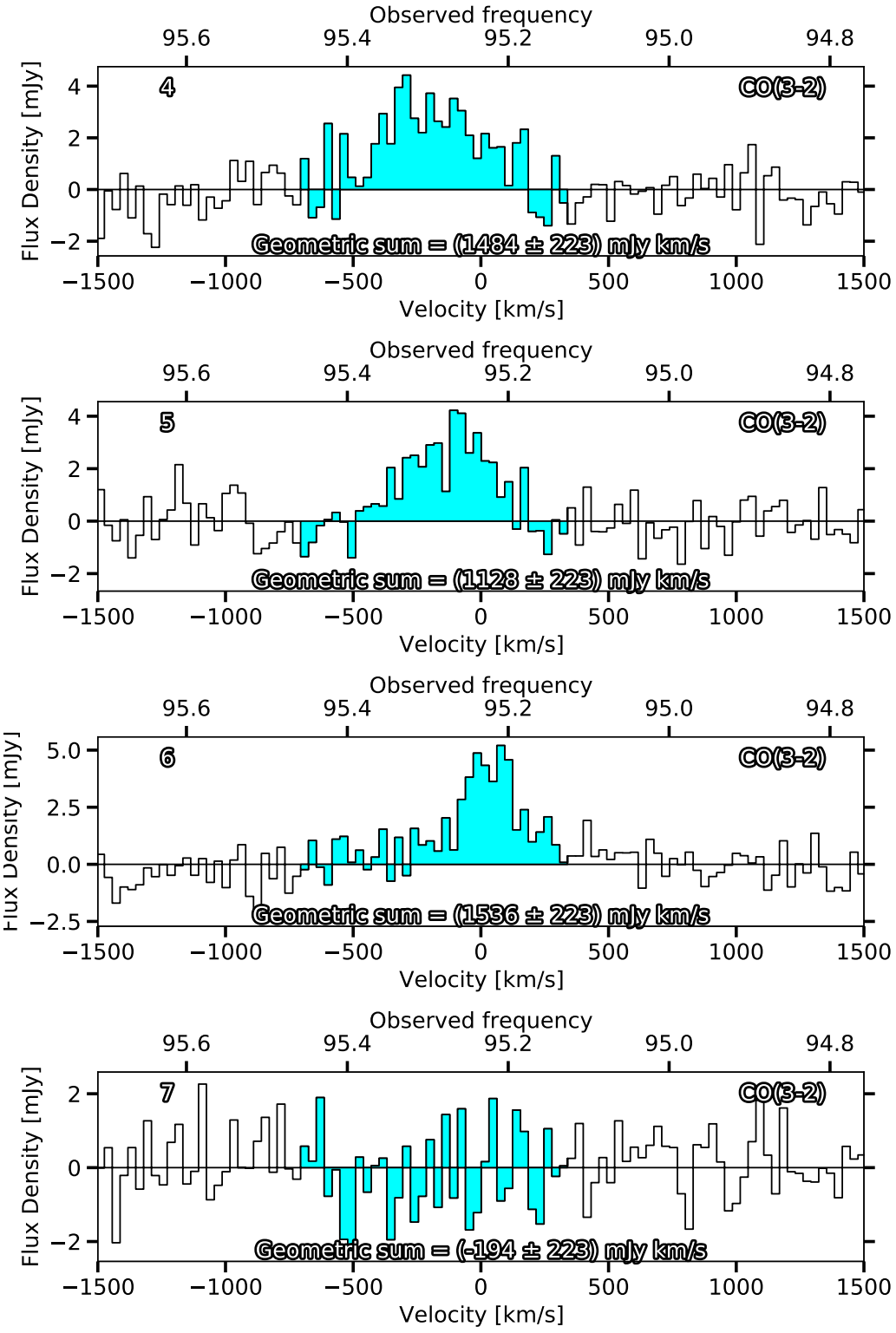

Figure 3.19: (continuation). Apertures 0-6 are all considered for building the corresponding SK diagram, since they pass the detection criteria: SNR > 3 (apertures 0, 3, 4, 5 and 6), or at least SNR > 1 while the continuum is SNR > 3 (apertures 1 and 2). Aperture 7 is only noise, which can also be seen from the left panel of Figure 3.17 (apertures 0-6 are all in the source, and 7 is not).

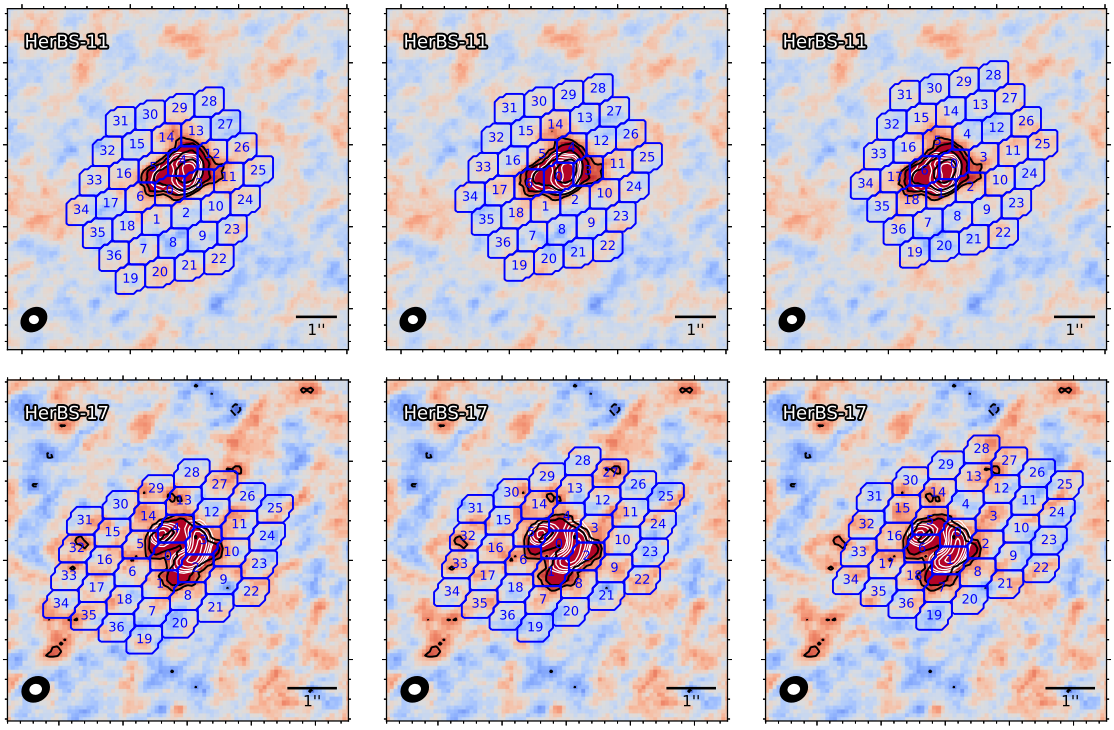

Figure 3.20: Examples of aperture tessellations for HerBS-11 (top) and HerBS-17 (bottom). The respective apertures (blue) are plotted on the moment 0 maps of the CO(3 – 2) line, similarly to Figure 3.17. Color map and black contours are moment 0 map, while white contours are continuum map. For each galaxy there is a grid of 37 apertures, which is clearly shifted in each of the three panels. Only three examples are presented, but for HerBS-11 and HerBS-17 there 73 and 55 examples of this tessellation in total, one for each pixel inside their basic aperture (see Table 3.5 for the size of these apertures).

galaxies. In Figure 3.21, the errors across different velocity channels are presented for HerBS-11 and HerBS-17. In red is shown the frequencies where the CO transition is. The errors in this range are added in quadrature, and then propagated by multiplying by the width of the velocity channel (commonly $\Delta v \approx 30$ km s^{-1}). With this, the 1σ error-bar for $S\mathrm{d}V$ in mJy km s^{-1} is finally obtained.

For the continuum the process is analogous, only there is no need to sum in quadrature since it is only one channel, and also no need to propagate since no velocity term is involved. The error-bars estimated in this section are also used to calculate the SNR.

3.6.6 Calculating surface densities

Using the measurements obtained in Section 3.6.3, the molecular gas mass (in $\mathrm{M}_\odot$) and SFR (in $\mathrm{M}_\odot$ yr^{-1}) are obtained as explained in Sections 3.3 and 3.4. These calculations are performed only in the apertures where a detection is found. The criteria set for a detection is that the SNR of either the continuum or $S\mathrm{d}V$ of the CO line must be above 3, while for the other must be at least above 1. The

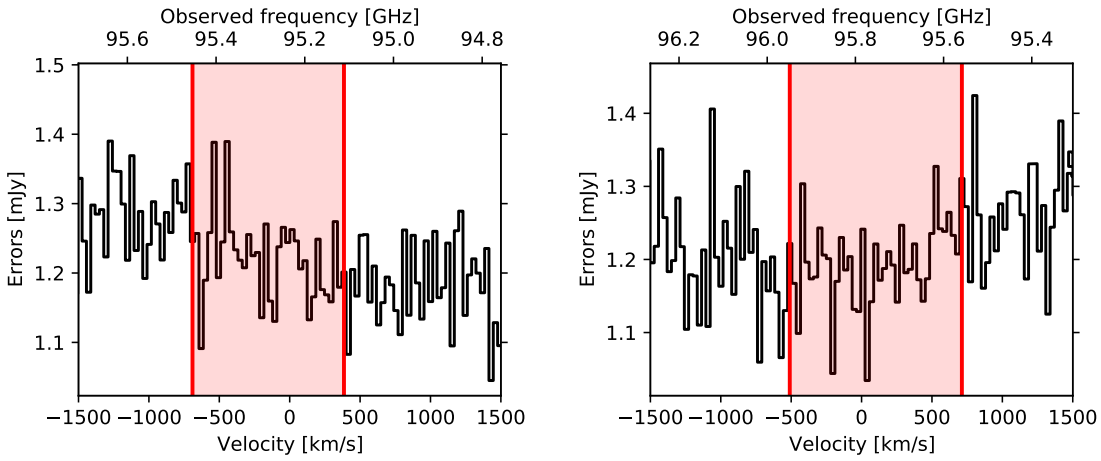

Figure 3.21: Errors (standard deviations) across different channels in HerBS-11 (left) and HerBS-17 (right). These have already been corrected by $\sqrt{\mathrm{N_{beams}}}$ (by design, a value close to $\sqrt{1}$). The errors are obtained from the regions of Figure 3.17 outside the 37 apertures. In red, the frequencies where the CO transition is located. This is the range used to estimate the error-bar of $S\mathrm{d}V$.

rare cases where both continuum and $S\mathrm{d}V$ have $2 < \mathrm{SNR} < 3$ are also considered. These criteria, which demand overlapping continuum and line emission, rest in the assumption that dust (traced by the continuum) is co-spatial with the molecular gas (traced by the low J CO line), as has been discussed in Section 2.4. In the examples in Figure 3.17, the criteria are met in apertures 0-6 for HerBS-11 (as discussed in Figure 3.19), and 0-6 and 14 for HerBS-17.

In case the continuum has $\mathrm{SNR} > 3$ but the velocity-integrated flux has $\mathrm{SNR} < 1$, the SFR is estimated as usual, while an upper limit is estimated for the molecular gas mass using the value corresponding to 1σ (i.e. the error-bar). These regions in galaxies are of great interest since they contain intense star formation while little to no molecular gas. The opposite scenario ($\mathrm{SNR} > 3$ for $S\mathrm{d}V$ and $\mathrm{SNR} < 1$ for the continuum) did not come up in any aperture in any galaxy since the continuum maps are much brighter than the CO line in terms of SNR. The total continuum emission, which is needed in equation 3.37, is obtained from all apertures where continuum has $\mathrm{SNR} > 2$.

The SFRs and molecular gas masses are converted into surface densities (Σ) dividing by the surface area of the basic aperture in kpc^2 and pc^2, respectively. This surface area is obtained from a conversion of angular size to physical size (arcsec to kpc), given the cosmology detailed in Section 2.2 (approximately 0.127 arcsec/kpc at $z = 3$). Following equation 3.42, the area of the beam in kpc^2 can be obtained, which is then converted into the area of the aperture via the $\mathrm{N_{beams}}$ factors shown in Table 3.5.

3.7 Line fitting

One of the most important aspects of the SK relation, as discussed in Section 2.4, is the slope. In order to get an estimation of the slope in the resolved SK diagrams, two methods are employed: one for each resolved SK diagram separately and one considering all measurements together.

3.7.1 Direct fits

A line is fitted to each of the resolved SK diagrams via an orthogonal distance regression (ODR) with `odr` of SciPy. This regression works by minimizing the orthogonal distance from the data-points to the model (Boggs et al., 1987). This is a common strategy when there are error-bars in both x and y axes, which is not the case in more simple methods like ordinary least squares which considers only errors in the y-axis. Also, ODR is a more general method than the total least squares.

In Figure 3.22 I present two examples of resolved SK diagrams with their respective fits obtained via ODR. The asymmetric error-bars are averaged to the same length when fitting. The upper limits were included in the fit with a simplistic approach: in the y-axis they were taken as their actual measurement, whereas in the x-axis they were weighted by 0.75, i.e. a measurement equal to 0.75 times the noise level. In the log scale, this meant adding $\log(0.75) \approx -0.124$ to the upper limit. This weight made for a *reasonable* accounting of these measurements, without biasing the fit too significantly. For their error-bars in the x-axis, the largest error-bar of any other datapoint in the diagram is considered.

3.7.2 Fit of combined data

As explained in Section 3.6.4, for each galaxy there exist multiple resolved SK diagrams (Section 4.2 introduces several examples). In order to make use of all these measurements, a line is fitted using the data of all SK diagrams combined. I perform a Bayesian analysis with Markov chain Monte Carlo (MCMC) sampling (e.g. Hogg & Foreman-Mackey, 2018). I assume a multivariate Gaussian distribution for the likelihood, which is the most general (or least restrictive) distribution in statistics. This can be explained with the central limit theorem or the principle of maximum entropy (Barron, 1986). I consider a simple model

$$y = Nx + b \ . \tag{3.52}$$

The total likelihood for all n data points (x_i, y_i) is therefore

$$\mathcal{L} = \frac{1}{(2\pi)^{n/2}(\det(\mathrm{COV}))^{1/2}} \exp\left(-\frac{1}{2}\vec{r}^{\mathrm{T}}\mathrm{COV}^{-1}\vec{r}\right) \ , \tag{3.53}$$

and the log-likelihood

$$\ln\mathcal{L} = -\frac{1}{2}\left(n\ln(2\pi) + \ln|\mathrm{COV}| + \vec{r}^{\mathrm{T}}\mathrm{COV}^{-1}\vec{r}\right) \ , \tag{3.54}$$

where ln is the natural logarithm. This version of the multivariate normal distribution is adequate for measurements that are not independent, as in this case (e.g.

Hogg et al., 2010). $\vec{r} \equiv \vec{y} - \vec{\mu}$ is the residual vector (measurements minus model), where each element is given by

$$r_i \equiv y_i - \mu_i = y_i - (Nx_i + b) \ , \tag{3.55}$$

i.e. the y-axis y_i of the ith data point, minus the is the mean prediction of the model given its x-axis x_i, $\mu_i = Nx_i + b$. The transpose of the residual vector is $\vec{r}^{\mathrm{T}}$.

As shown in Figure 3.20, when considering all tessellations together, there are apertures which overlap with each other, i.e. they measure fluxes from pixels in common. This means that their measurements are are not totally independent. In equation 3.54, the term COV corresponds to the covariance matrix, which quantifies this dependence (in the literature, the letter Σ is commonly used for the covariance matrix, but here it is not employed since that letter is assigned to surface densities). For two given apertures i, j, I quantify this with a factor $f_{i,j}$ which is the fraction of overlapping pixels. This factor has the range

$$0 \leq f_{i,j} < 1 \ , \tag{3.56}$$

i.e. two apertures could have no overlap at all ($f_{i,j} = 0$, no correlation since they share no pixels) or a strong correlation ($f_{i,j}$ close to 1 since they share the majority of their pixels), but never $f_{i,j} = 1$ since the algorithm is designed so that no two apertures ever measure the same set of pixels. Considering that a data point i has an error-bar (standard deviation) in the x- and y-axis ($\sigma_{x,i}, \sigma_{y,i}$), its total variance is

$$\sigma_i^2 = (\sigma_{i,y})^2 + (N\sigma_{i,x})^2 \ . \tag{3.57}$$

This comes from propagating the error via the model. Commonly, authors include an extra term which accounts for intrinsic dispersion of the data (e.g. Pessa et al., 2022), i.e. the physics in the galaxies also causes deviations from the straight-line in the SK relation; not all deviations are due to a bad model or flawed measurement. This is omitted from my model for simplicity, as will be discussed in Section 5.2.5. Following equation 3.57, the covariance matrix COV is built as

$$\mathrm{COV}_{i,j} = f_{i,j}\sqrt{\sigma_i^2 \sigma_j^2} = f_{i,j}\sigma_i\sigma_j \ , \tag{3.58}$$

i.e. the covariance of two data points i and j (position i, j of the matrix) comes from the product of their respective total standard deviations, with the $f_{i,j}$ factor. This matrix is symmetrical, i.e. $\mathrm{COV}_{i,j} = \mathrm{COV}_{j,i}$, and the diagonal is simply the variance of each data point, i.e. $\mathrm{COV}_{i,i} = \sigma_i^2$.

At this point, there is one important compromise. As shown in equation 3.54, this matrix must be inverted, and the determinant calculated. This is done with `linalg` of NumPy (Harris et al., 2020). Cholesky decompositions are also used to easy up the calculations (e.g. Golub & Van Loan, 2013). Since the covariance matrix has a size of few hundreds $\times$ few hundreds (there are that many data points), this operation is fairly expensive.

For this reason, the covariance matrix is calculated only once, using best slope estimated from the direct fits via ODR (see Section 3.7.1). This way, the correlation between measurements is not updated in each step a walker takes; one single approximation is made and this is used in the entire sampling.

The upper limits are handled the same way as the direct fits (see Section 3.7.1), i.e. by weighting them by 0.75, considering the largest error-bar in x available for σ_x, and then treating them like a *normal* measurement.

For the prior of the slope N, I set a normal distribution centered at 1.5 with standard deviation 0.3. This is chosen since slopes larger than 1 are expected for high-redshift DSFGs (as discussed in Section 2.4), but lower values could also be properly explored. For the intercept b I set an uninformative flat prior between -10 and 10. 10 walkers with 5000 steps each (300 warm-up) are enough to properly sample the parameter space, which is relatively small (only two parameters). Their initial positions are chosen randomly in the ranges $N \in [0.5, 2]$ and $b \in [-4, 1]$.

The MCMC sampling of the log-posterior is done with the emcee library (Foreman-Mackey et al., 2013). In Figure 3.23 I present two examples of the line fits performed on all the data together, again of HerBS-11 and HerBS-17. In Appendix B I present a few examples of cornerplots showing the log-posterior distributions sampled by the walkers. The convergence of the walkers was assessed by inspecting their traces, as well as their autocorrelation time.

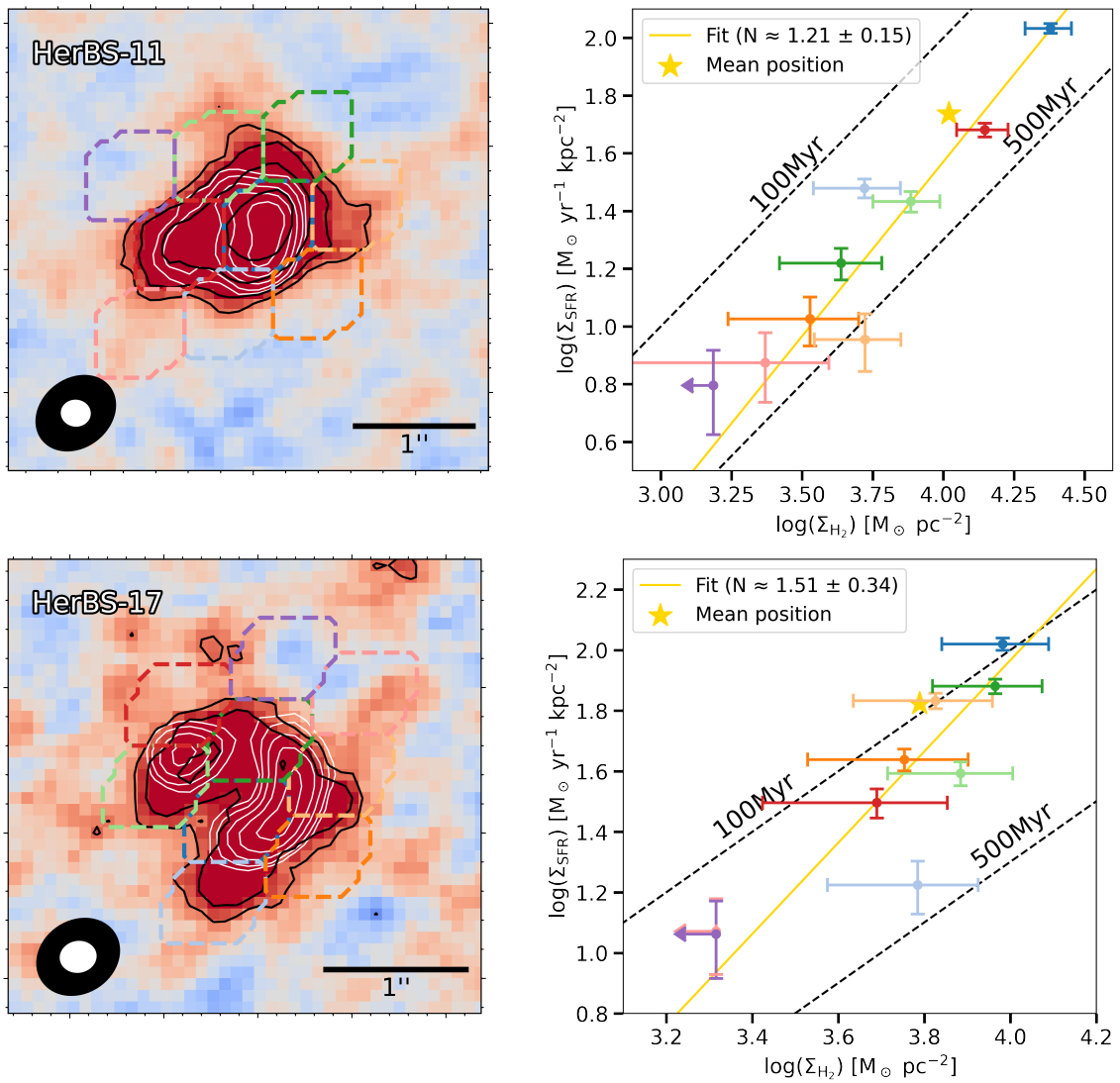

Figure 3.22: Resolved SK diagrams produced with the algorithm described in Section 3.6; one of HerBS-11 (top), and one of HerBS-17 (bottom). Left: Moment 0 maps (zoomed-in compared to Figure 3.17), with the apertures where a detection was found. Color map and black contours are moment 0 map, while white contours are continuum map. Right: Corresponding SK diagrams, where the dots are color-coded accordingly to the apertures. Error-bars are symmetrical in a linear scale, so they become asymmetrical in log scale. Diagrams include the ODR fit with the corresponding slope N, and the averaged mean position of all data points. The error of N is also given by the ODR fitting routine. In dashed lines, constant depletion times. Like these plots, there are 73 in total for HerBS-11 and 55 for HerBS-17 (since their basic apertures have 73 and 55 pixels, as shown in Table 3.5). Out of those, these two examples in particular were chosen for this figure to illustrate the situation of upper limits. These come from apertures where the continuum map has SNR > 3 and the moment 0 map has SNR < 1, i.e. there is detection in the continuum and no detection in the line. This allows for a proper calculation in the y-axis and only an upper limit in the x-axis, set at 1σ (noise level).

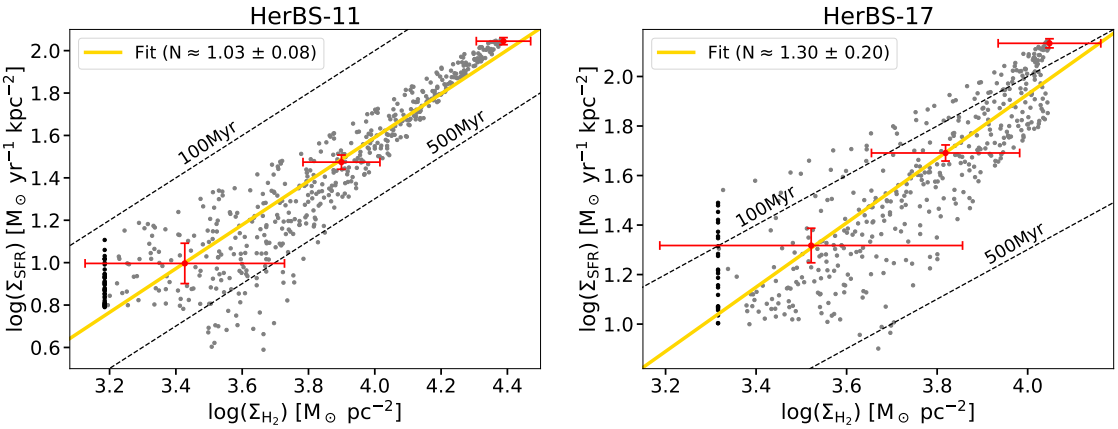

Figure 3.23: Resolved SK diagrams which include the measurements of all individual SK diagrams. In grey the proper measurements, and in black the upper limits in the x-axis at 1σ. The fit obtained with MCMC sampling is included in yellow, with the corresponding fitted slope. Error-bars of the data points are omitted for easier visualization, but typical error-bars are included for three example points in red. The error-bars are originally asymmetric (see Figure 3.22), but were averaged for the fits to simplify the calculations.

4

Results

In this chapter, the entire sample of galaxies in the sub-fields SGP-1, -2, -3 and -4 is presented in Section 4.1. For the 23 galaxies studied with the Schmidt-Kennicutt (SK) relation, Section 4.2 introduces the resolved SK diagrams. This includes their slope N, a key parameter studied in the thesis.

4.1 Sample

The entire sample of 122 galaxies considered in this work is presented in Table 4.1. The spectroscopic redshift (where available) and celestial coordinates are included. The majority of the sources in this table are already presented by Bendo et al. (2023). However, since the angular resolution of my data is significantly higher ($2'' \rightarrow 0.15''$), the exact coordinates of each galaxy are now much better constrained. Also, as described in the footnotes of the table, now more galaxies and redshift measurements are included.

Table 4.1: Sample of 122 galaxies included in this work. They are divided in groups of 8 similarly to the dust continuum emission maps in Appendix C. First column: name of the galaxy, which is the field and an extra letter in case there are multiple galaxies. Second column: spectroscopic redshift where available (69 galaxies in total). Third and fourth columns: celestial coordinates R.A and Dec. (in ICRS), which were determined by inspecting the continuum maps in Appendix C with the software CARTA. Fifth column: lowest CO line available (if any; only up to transition $5 \rightarrow 4$). Sixth column: galaxies that were ultimately used to create resolved SK diagrams.

Galaxy	$z_{\mathrm{spec}}{}^{a}$	R.A. (ICRS)	Dec. (ICRS)	Low CO line	SK
HerBS-11	2.631	01:24:07.503	−28:14:34.76	$\mathrm{CO}(3-2)$	✓
HerBS-14	3.782	01:38:40.417	−28:18:57.43		
HerBS-17	2.6101^{b}	23:25:31.507	−30:22:35.68	$\mathrm{CO}(3-2)$	✓
HerBS-18	2.182	23:24:19.814	−32:39:26.57	$\mathrm{CO}(3-2)$	✓
HerBS-23A	4.39^{b}	01:20:46.569	−28:24:04.25	$\mathrm{CO}(5-4)$	✓
HerBS-23B	-	01:20:46.053	−28:23:56.87		
HerBS-24	2.198	00:47:36.089	−27:29:51.88		
HerBS-26A	3.157^{b}	22:58:44.876	−29:51:25.41		
HerBS-26B	-	22:58:44.815	−29:51:21.65		
HerBS-27	4.509	01:14:23.995	−33:36:16.51	$\mathrm{CO}(5-4)$	✓
HerBS-28	3.925	23:08:15.722	−34:38:00.92	$\mathrm{CO}(4-3)$	✓

Table 4.1: (continuation).

Source	$z_{\rm spec}$[a]	R.A. (ICRS)	Dec. (ICRS)	Low CO line	SK
HerBS-33A‡	2.9951[b]	22:48:05.174	−33:58:21.05	CO(3 − 2)	✓
HerBS-33B‡	-	22:48:05.511	−33:58:19.53		
HerBS-37	2.619	23:26:23.055	−34:26:44.04	CO(3 − 2)	✓
HerBS-39	3.229	23:29:00.813	−32:17:45.24	CO(4 − 3)	
HerBS-40	1.971	01:32:40.288	−33:09:07.98		
HerBS-45A	2.434	00:51:32.942	−30:18:49.61		
HerBS-45B	-	00:51:32.471	−30:18:48.82		
HerBS-45C*	-	00:51:33.082	−30:18:49.39		
HerBS-45D*	-	00:51:32.836	−30:18:51.79		
HerBS-45E*	-	00:51:32.628	−30:18:45.06		
HerBS-47A	2.433	22:52:50.733	−31:37:00.11	CO(3 − 2)	✓
HerBS-47B*	-	22:52:50.697	−31:36:50.14		
HerBS-49A	2.724	23:05:46.378	−33:10:38.07	CO(5 − 4)	
HerBS-49B	2.730	23:05:46.585	−33:10:42.93	CO(5 − 4)	
HerBS-55	2.656	01:39:52.090	−32:14:45.28	CO(3 − 2)	✓
HerBS-56A	-	00:32:07.160	−30:37:13.11		
HerBS-56B	-	00:32:08.594	−30:37:30.89		
HerBS-56C	2.561	00:32:07.590	−30:37:35.12	CO(3 − 2)	
HerBS-56D	-	00:32:07.931	−30:37:32.43		
HerBS-57	3.265	00:48:53.341	−30:31:09.86		
HerBS-60	3.261	00:57:24.322	−27:31:23.37		
HerBS-63A‡	2.432	00:51:31.700	−30:20:20.54		
HerBS-63B‡	-	00:51:31.848	−30:20:04.45		
HerBS-67	3.71[b]	22:42:07.200	−32:42:02.01		
HerBS-68	2.719	22:37:53.870	−30:58:28.60		
HerBS-69A	2.075	01:24:16.151	−31:04:59.34	CO(4 − 3)	✓
HerBS-69B	2.073	01:24:15.874	−31:05:04.72	CO(4 − 3)	✓
HerBS-73	3.026	01:28:53.086	−33:27:19.06		
HerBS-75A	-	01:18:23.622	−27:44:11.48		
HerBS-75B	-	01:18:24.235	−27:44:02.72		
HerBS-75C	-	01:18:23.820	−27:44:14.93		
HerBS-75D*	-	01:18:23.550	−27:44:02.27		
HerBS-77A	2.228	00:56:29.252	−31:12:07.42		
HerBS-77B	-	00:56:30.489	−31:12:15.66		
HerBS-77C*	-	00:56:29.428	−31:12:06.56		
HerBS-80A	2.231	23:00:02.542	−31:50:08.81		
HerBS-80B	1.968	23:00:02.859	−31:50:07.78	CO(5 − 4)	
HerBS-80C	-	23:00:02.943	−31:50:01.95		
HerBS-84A	2.5178[b]	22:44:01.091	−34:00:32.58	CO(3 − 2)	
HerBS-84B*	-	22:44:00.527	−34:00:28.47		
HerBS-90A	3.992	00:56:59.285	−29:50:39.50		
HerBS-90B†	-	00:57:00.310	−29:50:40.70		
HerBS-97A	-	22:40:28.503	−34:31:33.44		

Table 4.1: (continuation).

Source	$z_{\rm spec}$[a]	R.A. (ICRS)	Dec. (ICRS)	Low CO line	SK
HerBS-97B	-	22:40:27.732	−34:31:38.16		
HerBS-101A	2.02690[c]	01:12:46.522	−33:06:10.45		
HerBS-101B	2.02690[c]	01:12:46.100	−33:06:12.53		
HerBS-102A	3.287	23:30:24.432	−32:50:32.33	$CO(4-3)$	✓
HerBS-102B	-	23:30:23.513	−32:50:43.27		
HerBS-103	2.942	22:53:24.232	−32:35:04.31	$CO(3-2)$	✓
HerBS-107	2.553	01:45:20.067	−31:38:32.20		
HerBS-111	2.371	22:39:42.337	−33:33:04.29		
HerBS-114	2.3017[b]	01:22:09.378	−27:38:25.40	$CO(3-2)$	
HerBS-118A‡	4.0923[c]	23:21:59.428	−35:56:21.05		
HerBS-120A	3.125	01:22:22.444	−27:44:53.77	$CO(5-4)$	
HerBS-120B	3.124	01:22:22.132	−27:44:58.94	$CO(5-4)$	
HerBS-121A	3.741	22:36:15.329	−34:33:02.57		
HerBS-121B	-	22:36:14.998	−34:32:56.70		
HerBS-122A	2.883	00:37:16.705	−32:32:57.41	$CO(5-4)$	✓
HerBS-122B	-	00:37:16.867	−32:33:09.34		
HerBS-123	2.170	23:30:37.484	−33:12:17.52	$CO(3-2)$	
HerBS-131A	-	22:53:38.410	−32:55:49.15		
HerBS-131B	2.197	22:53:39.488	−32:55:52.36	$CO(4-3)$	
HerBS-132A	2.473	23:12:05.323	−29:50:26.53		
HerBS-132B*	-	23:12:04.932	−29:50:31.34		
HerBS-132C*	-	23:12:05.269	−29:50:32.31		
HerBS-135A	2.401	22:56:11.796	−32:56:51.85	$CO(3-2)$	
HerBS-135B	-	22:56:11.405	−32:56:52.49		
HerBS-138A	-	01:17:30.564	−32:07:20.79		
HerBS-138B*	1.407	01:17:30.434	−32:07:22.41	$CO(2-1)$	
HerBS-141	2.085	22:47:59.746	−31:01:34.87		
HerBS-144A	2.42[b]	22:26:28.637	−32:11:08.25	$CO(3-2)$	✓
HerBS-144B	-	22:26:30.273	−32:11:10.57		
HerBS-145A	2.730	01:23:34.638	−31:46:23.63	$CO(3-2)$	
HerBS-145B	-	01:23:35.760	−31:46:24.93		
HerBS-146A	-	23:22:10.953	−33:37:48.89		
HerBS-146B	2.003	23:22:10.573	−33:37:58.47	$CO(4-3)$	✓
HerBS-148	3.0876[b]	22:40:26.557	−31:51:54.13		
HerBS-151A	-	01:25:30.765	−30:25:12.05		
HerBS-151B	-	01:25:29.819	−30:24:55.71		
HerBS-160	3.955	01:10:14.480	−31:48:16.02	$CO(4-3)$	✓
HerBS-166A‡	-	22:25:03.538	−30:48:48.25		
HerBS-166C‡*	-	22:25:03.747	−30:48:46.77		
HerBS-168A	2.583	22:50:45.476	−30:47:19.85		
HerBS-168B	-	22:50:45.759	−30:47:13.22		
HerBS-174A	1.6669[c]	00:37:29.010	−28:41:28.58		
HerBS-174B	1.6669[c]	00:37:28.374	−28:41:25.66		

Table 4.1: (continuation).

Source	$z_{\rm spec}$[a]	R.A. (ICRS)	Dec. (ICRS)	Low CO line	SK
HerBS-178A	2.658	01:18:50.259	−28:36:43.93	CO(3 − 2)	
HerBS-178B	2.655	01:18:50.109	−28:36:40.70	CO(3 − 2)	
HerBS-178C	2.656	01:18:49.969	−28:36:43.34	CO(3 − 2)	
HerBS-178D†	-	01:18:50.177	−28:36:43.01		
HerBS-181A†	1.524[c]	00:58:49.747	−29:01:18.29		
HerBS-181B	1.524[c]	00:58:50.644	−29:01:14.04		
HerBS-181C*	1.524[c]	00:58:49.961	−29:01:23.21		
HerBS-181D*	1.524[c]	00:58:49.359	−29:01:22.78		
HerBS-182A	2.227	23:05:38.797	−31:22:05.39		
HerBS-182B	-	23:05:38.182	−31:22:02.23		
HerBS-182C	-	23:05:38.536	−31:22:04.91		
HerBS-182D	-	23:05:38.140	−31:22:04.73		
HerBS-186A‡	3.1701[c]	01:32:17.229	−32:09:55.33	CO(5 − 4)	
HerBS-186C‡*	3.1701[c]	01:32:16.720	−32:09:53.36	CO(5 − 4)	
HerBS-189	3.300	22:56:00.773	−31:32:32.62	CO(5 − 4)	
HerBS-192	2.4037[b]	22:26:28.940	−30:44:23.27	CO(3 − 2)	
HerBS-198A	-	22:22:35.901	−32:45:23.82		
HerBS-198B*	-	22:22:35.840	−32:45:25.49		
HerBS-200	2.151	01:43:13.303	−33:26:33.12		
HerBS-207	1.569	00:55:06.513	−30:00:28.32		
HerBS-208A	2.478	22:57:44.575	−32:42:33.15	CO(3 − 2)	✓
HerBS-208B	2.483	22:57:44.832	−32:42:32.75	CO(3 − 2)	
HerBS-209A	2.272	22:49:21.053	−33:29:41.95		
HerBS-209B	-	22:49:20.517	−33:29:41.17		
HerBS-209C*	-	22:49:20.609	−33:29:37.95		

Notes on Table 4.1.

[a] Unless otherwise specified, these spectroscopic redshifts are from Urquhart et al. (2022).

[b] These redshift are from Bakx et al. (2025) (in prep.) via private communication.

[c] These redshift are also from Bakx et al. (2025) (in prep.) via private communication. The measurements were done with observations whose angular resolution is not high enough to identify which component corresponds to this redshift.

† These galaxies are reported by by Bendo et al. (2023), who detected them at 2 mm. However, in the data employed in this work they are not detected. They are listed here for completeness.

‡ These galaxies have one more galaxy in their field: HerBS-33C, -63C, -118B, -166B and -186B, which are reported by Bendo et al. (2023). They are excluded since they are outside the field of view (FOV) of the dust continuum observations presented in Appendix C.

∗ These galaxies are newly detected in this work, without prior mention in Bendo et al. (2023). In the case of HerBS-138, the authors report that A and B are

two different galaxies but do not provide the coordinates for HerBS-138B.

The entire sample is further presented in Appendix C, where the dust continuum emission across ALMA Bands 3 through 8 are shown. These plots reveal a rich diversity in the morphology of the galaxies. Some exhibit a fairly circular emission of one single component (similar to a 2D Gaussian distribution; e.g. HerBS-11, -24, -73, -84A, -102A, -103, -111, -135A or -200). Other galaxies present strong gravitational lensing, reflected in a partial Einstein ring (e.g. HerBS-23A, -28, -60, -69A or -168A). Some galaxies have multiple poles of emission which do not quite resemble a ring, (e.g. HerBS-23B, -49A, -55, -57, -114, -123 or -141), while others have one single elongated component (e.g. HerBS-26A, -27, -120B or -160).

This richness in the morphologies of Dusty Star Forming Galaxies (DSFGs) has been observed previously in the literature (e.g. Bakx et al., 2024). Given that lensing events preserve surface brightness, galaxies with ring-like structures and those with single components are approached equally when creating resolved SK diagrams in this work.

From Figure C.1 it can also be seen that a few Band 7 images have potential issues in the image reconstruction process. This can be seen in HerBS-17, -18, -57, -90A, and -132A, where white *spots* are seen by the emission. This might be due to excessive cleaning with the `TCLEAN` algorithm mentioned in Section 3.2.3.

Bands 7 and 8 of the continuum have the highest angular resolution across the bands used in this work (3 through 8). Since these are not available across all galaxies, and Band 7 has reconstruction issues, Band 6 is chosen to estimate SFR (see Section 3.4). This is the band with next highest angular resolution, and is available for all galaxies.

In Figure 4.1 a histogram with all available spectroscopic redshifts is presented. The redshifts range from $z_{\rm spec} = 1.407$ to $z_{\rm spec} = 4.509$, (the corresponding age of the Universe is between ~ 1.33 Gyr to ~ 4.51 Gyr), while the majority of the galaxies lie between $z_{\rm spec} \approx 2$ to $z_{\rm spec} \approx 3.5$ (age of the Universe between ~ 1.80 Gyr to ~ 3.28 Gyr). The median redshift ~ 2.58 is expected considering the typical median redshift of DSFGs, as discussed in Section 2.5.

Given the redshifts in Table 4.1, with equation 2.7 I calculate the frequencies at which the relevant lines lie in each galaxy (in Figure 2.8 these lines were presented). With the frequency ranges of the ALMA observations (see Table 3.1), the lines potentially covered in each galaxy can be obtained. These are detailed in Appendix D. This information is key because it reveals what galaxies can potentially be used to build SK diagrams; the minimum requirement is that a low CO($J \rightarrow J-1$) transition can be found in them ($J \leq 5$). The last two columns of Table 4.1 summarize this information. A total of 40 galaxies have a low CO transition, out of which 19 are ultimately employed for the SK analysis.

In Figure 3.11 the first two galaxies included in the Schmidt-Kennicutt (SK) analysis were presented (HerBS-11 and HerBS-17). Now in Figure 4.2 the next three are shown: HerBS-18, HerBS-23A and HerBS-27. Similarly to HerBS-11 and HerBS-17, the line emission is prominent reaching regions with SNR up to 5. Also, in these five galaxies the emission can be considered extended, as it is several times bigger in the sky than the ALMA beam (black ellipse in the bottom left of the moment 0 maps). This is crucial to make a proper resolved study with SK diagrams, because

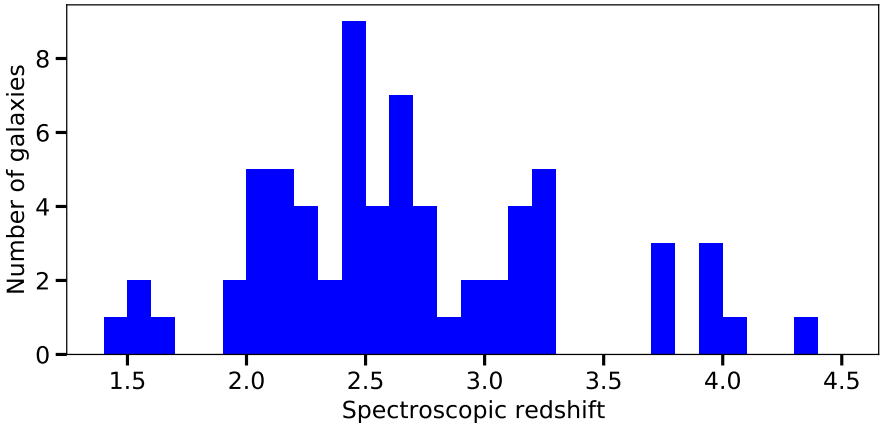

Figure 4.1: Histogram with the known spectroscopic redshifts of sample of DSFGs. In total, 69 out of 122 have this information available (see Table 4.1). Redshifts with source-confusion are also included in this histogram.

it allows for several independent measurements. The remaining galaxies used for the SK analysis are shown in Appendix E. This includes four extra galaxies which were not a part of my initial sample (HerBS-21, HerBS-25, HerBS-36 and HerBS-41A).

21 out of 40 galaxies with potential CO emission were not used for the SK analysis (see Table 4.1). They are considered to be either too faint (i.e. barely any CO emission detected), too compact (i.e. the resolution is not high enough to resolve the galaxies into many beams), or insufficiently covered by the frequency ALMA range (i.e. the CO line lies at the end of the frequency window). In Appendix F some examples of these cases are presented. In the case of faint galaxies, they are commonly B or C sources in fields where there is a brighter galaxy dominating the total emission.

4.2 Resolved SK diagrams

For each galaxy, dozens of different resolved SK diagrams were built, as explained in Section 3.6.4. Three examples for each galaxy are presented in Appendix G. From each resolved SK diagram a different slope N is extracted. The values of N are presented as histograms in Figure 4.3 as probability density functions (PDFs). Figure 4.3 also includes the *best* N for each galaxy. The median value is chosen for this, with percentiles 16 and 84 as the error-bars (approximately $\pm 1\sigma$).

Figure 4.4 presents the fits performed to all measurements together, via MCMC. HerBS-11 and HerBS-17 are omitted since those are already shown in Figure 3.23. The best value for N is included. This is chosen as the median value sampled by the walkers, with the error-bar being the standard deviation.

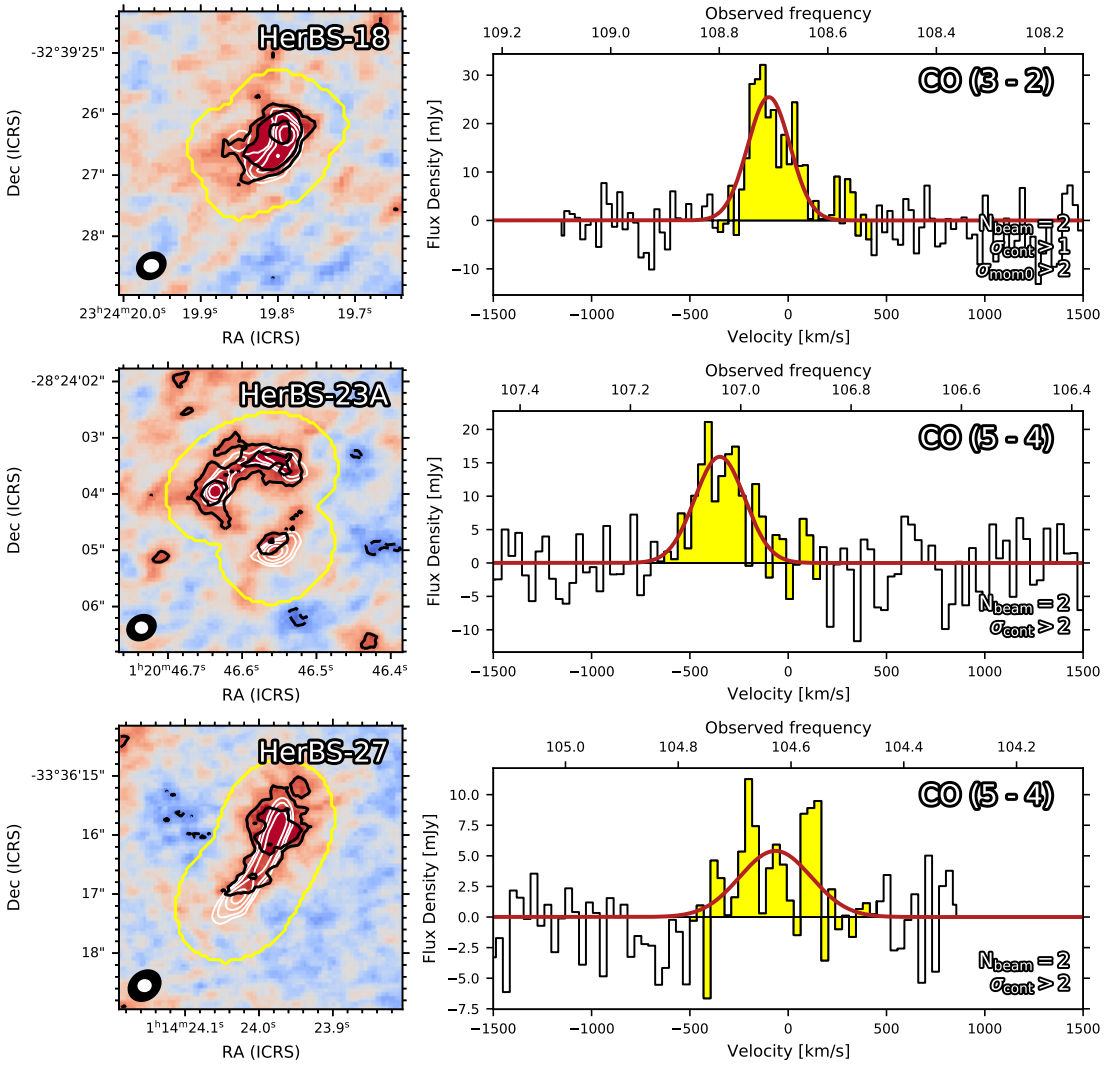

Figure 4.2: The next three galaxies used for the SK analysis: HerBS-18, HerBS-23A and HerBS-27. These plots are analogous to Figure 3.11 (moment 0 on the left and spectrum on the right), where the first two galaxies were presented (HerBS-11 and HerBS-17).

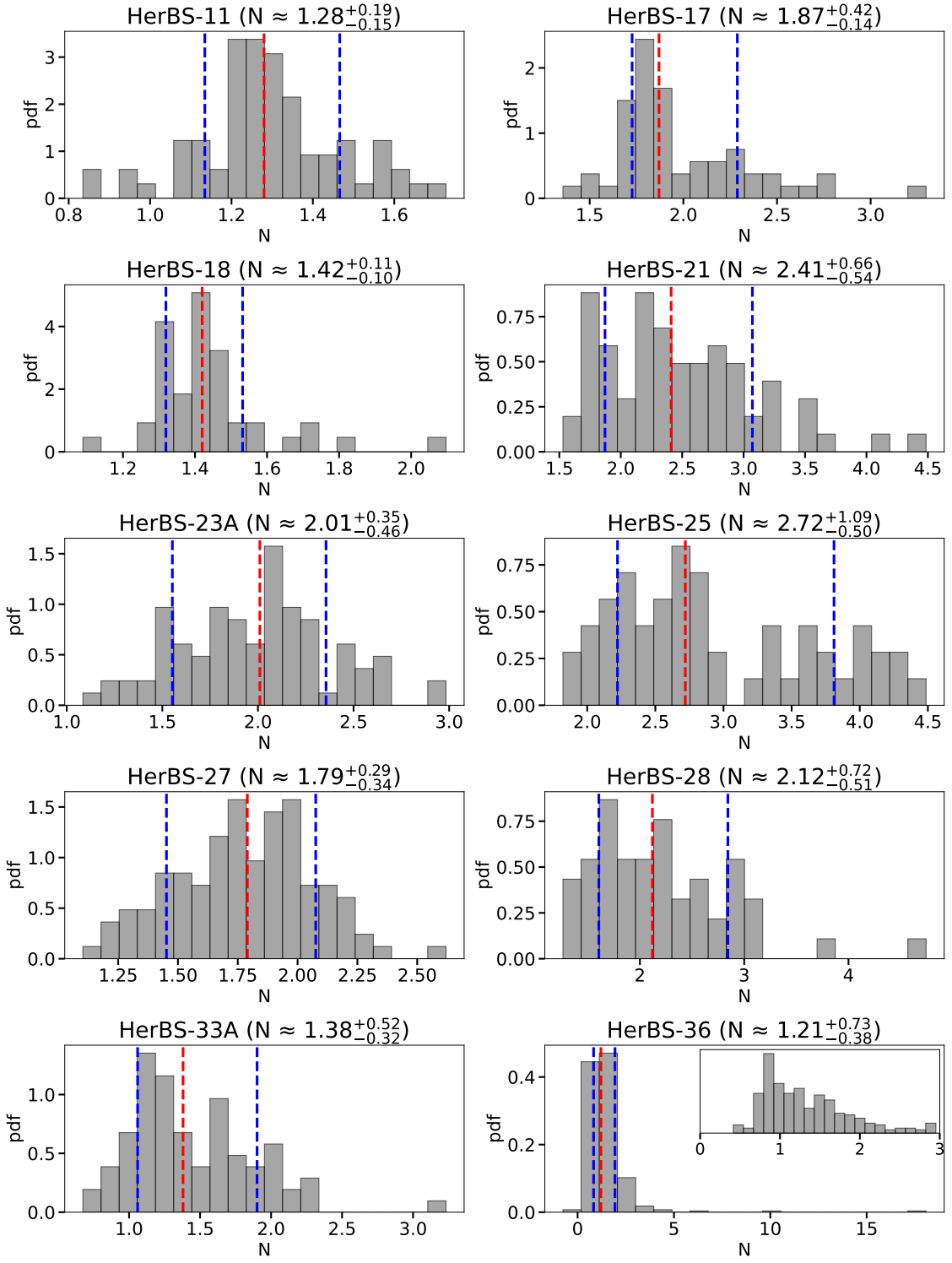

Figure 4.3: Probability density function of the slope N of the resolved Schmidt-Kennicutt relation, for each galaxy. These histograms summarize the slopes from all *direct fits* (as explained in Section 3.7.1), including all cases (the three examples in Appendix G, and beyond). The best N is the median (red dashed line), and the error-bars are percentiles 16 and 84 (blue dashed lines). An inset in the range [0,3] is included in galaxies where the distribution is too spread.

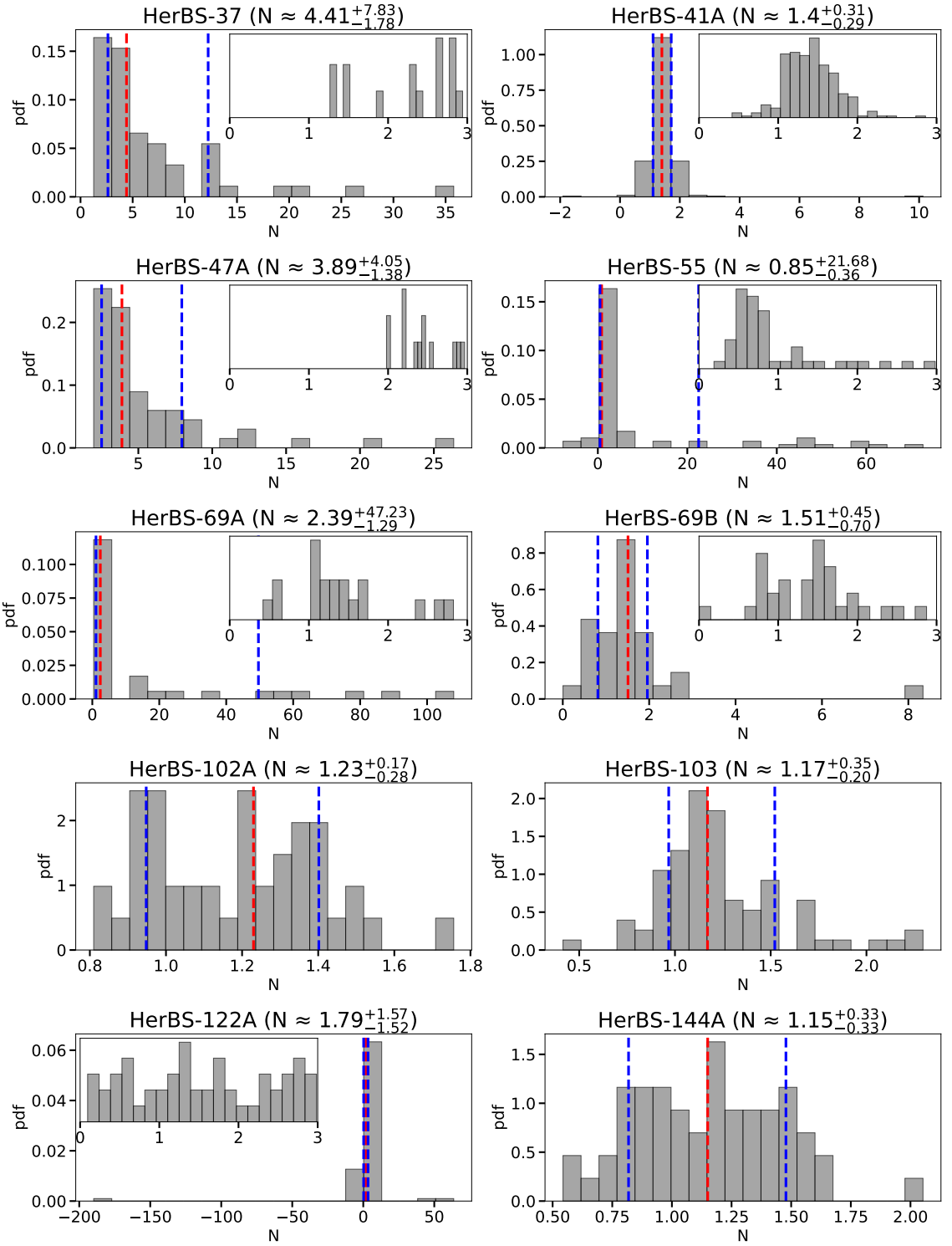

Figure 4.3: (continuation).

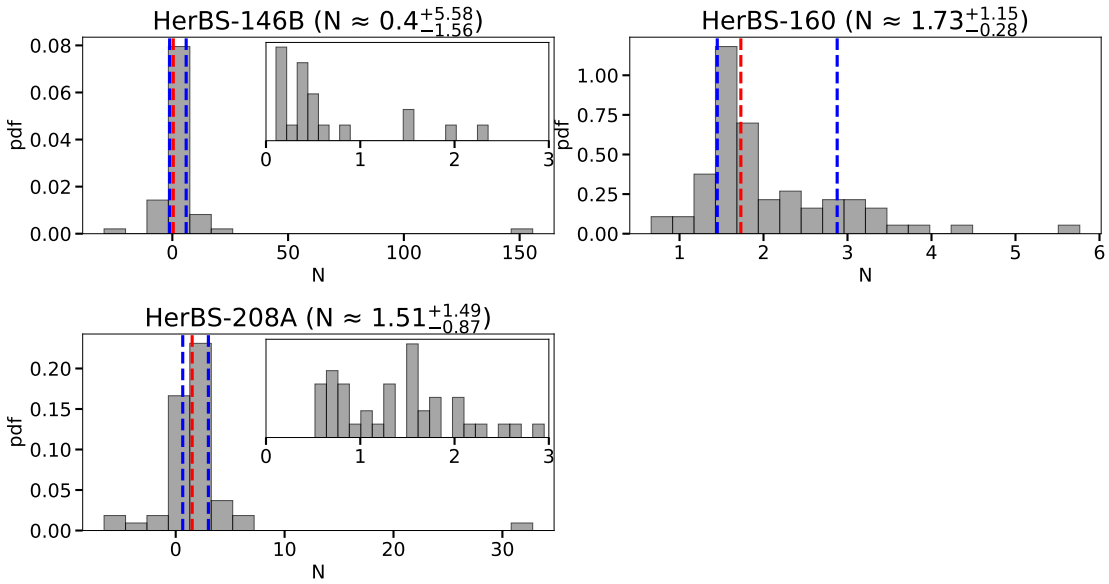

Figure 4.3: (continuation).

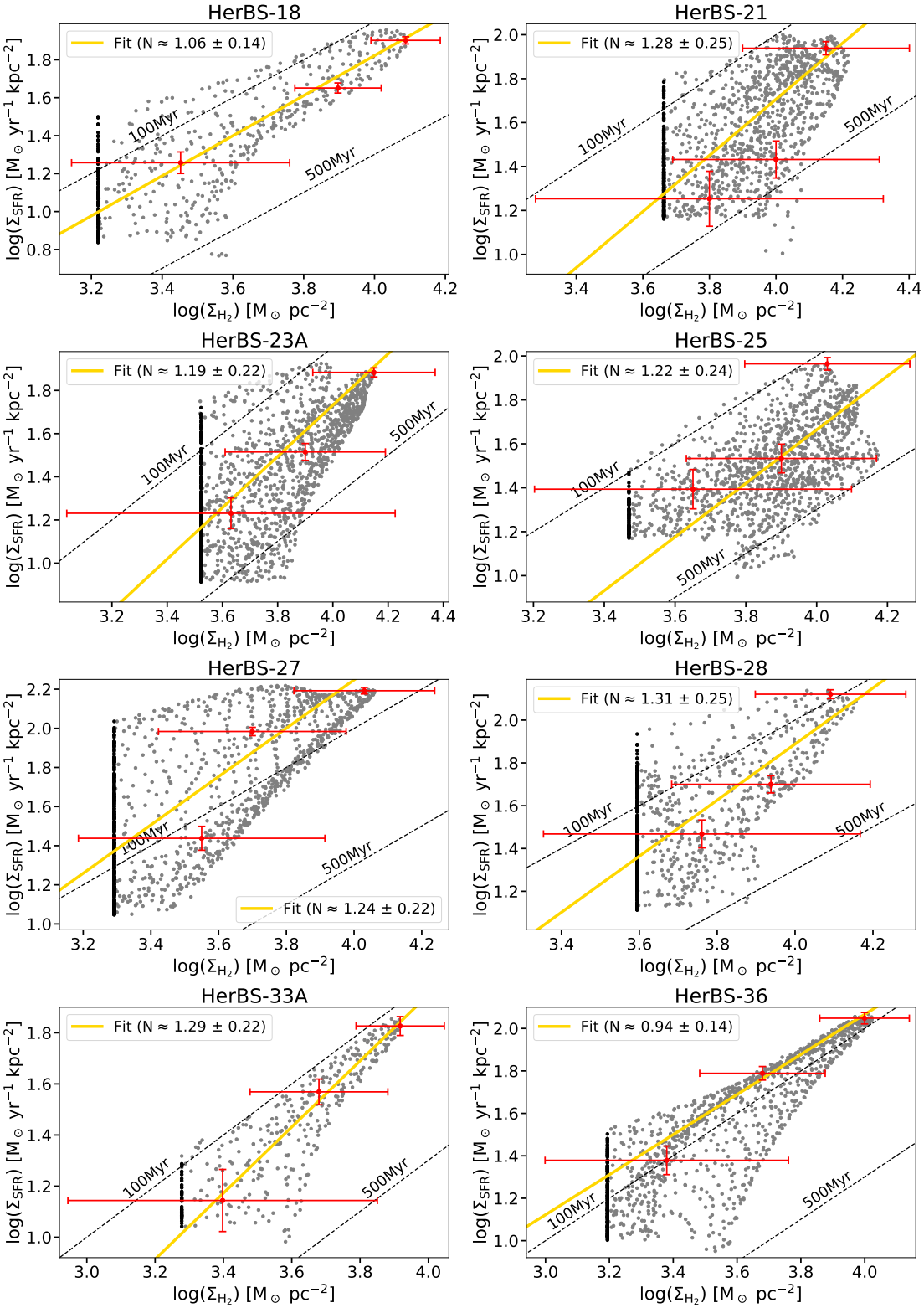

Figure 4.4: Resolved SK diagrams with all measurements. Figure like 3.23, where HerBS-11 and HerBS-17 are shown. Fitted slope N is shown in the legend, chosen as the median$\pm 1\sigma$ of the values sampled by the walkers.

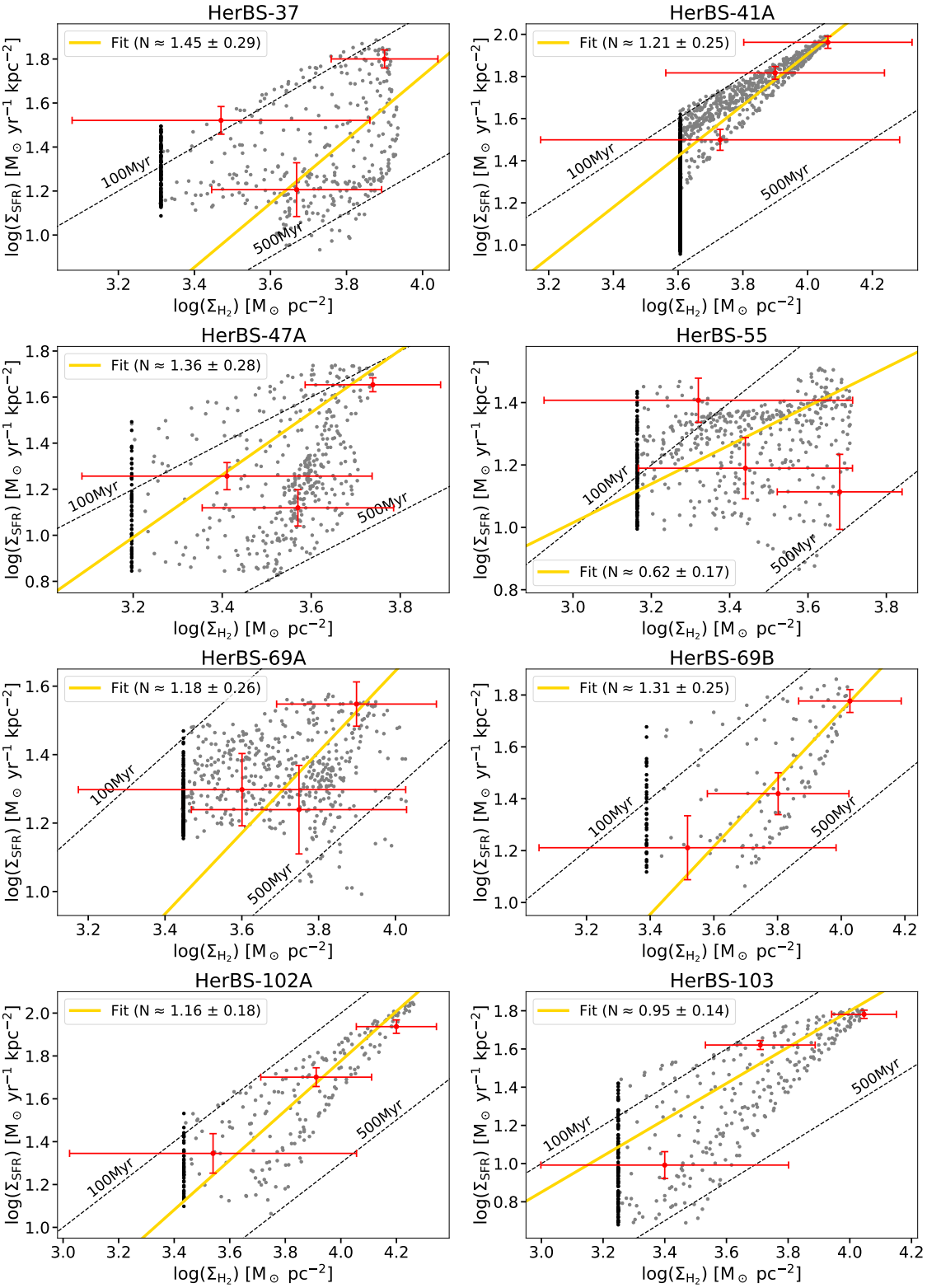

Figure 4.4: (continuation).

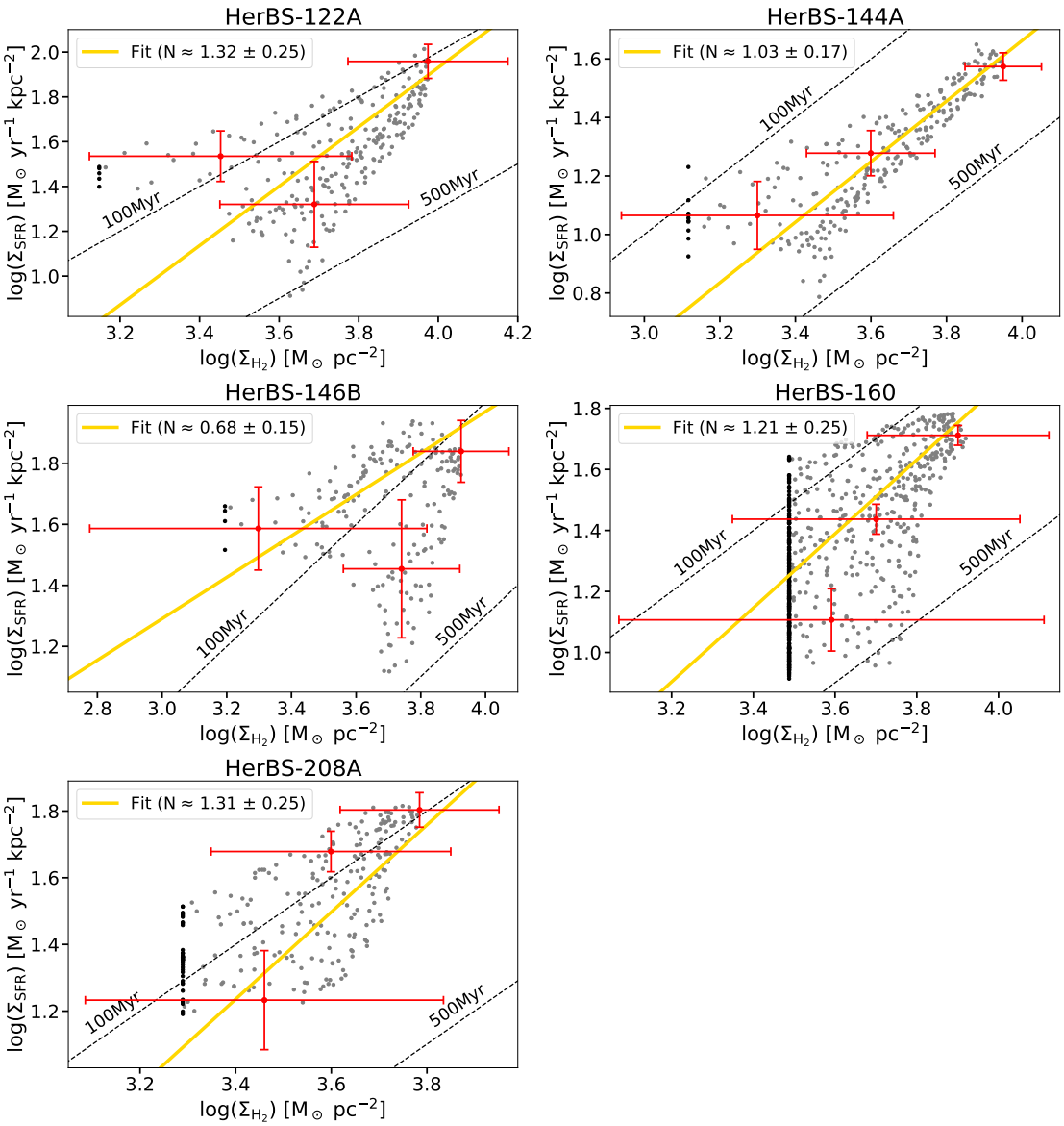

Figure 4.4: (continuation).

5

Discussion

In this chapter, the main results and implications of this work are summarized and compared against the literature in Section 5.1. A number of caveats are discussed in Section 5.2.

5.1 Results in context

Figure 5.1 presents a summary of the slopes N of the resolved Schmidt-Kennicutt relation, obtained for each galaxy. Amongst the 23 Dusty Star-Forming Galaxies (DSFGs) studied in this work, the slopes obtained via ODR and MCMC are

$$N_{\rm ODR} = 1.51^{+0.89}_{-0.32} \ , \tag{5.1}$$

$$N_{\rm MCMC} = 1.21^{+0.10}_{-0.22} \ . \tag{5.2}$$

These correspond to the median galaxy, with error-bars in percentiles 16 and 84 ($\sim \pm 1\sigma$). These error-bars exclude mainly outlier galaxies (orange in Figure 5.1), which will be discussed in Section 5.2.4. Figure 5.1 also shows a comparison of all ODR fits together (1895 in total, from all galaxies). The value obtained is (median and percentiles 16, 84)

$$N_{\rm all} = 1.53^{+1.09}_{-0.55} \ . \tag{5.3}$$

All three constrains on N are consistent within their error-bars. There clearly exists a diversity amongst the galaxies of the sample, noted in the error-bars of these results. Regardless, in all cases the constraints are consistent with $N > 1$, a scenario of efficient star formation with different depletion times within a galaxy. This notion is in agreement with previous findings in individual DSFGs (Hodge et al., 2015; Thomson et al., 2015; Hatsukade et al., 2015; Chen et al., 2017); now extended to a large sample studied with a consistent methodology.

Figure 5.1 also compares N in my sample against constraints in nearby galaxies, where the consensus is a universal star formation at $N \sim 1$. This comparison shows key differences in the star formation between the present time and cosmic noon. The results suggest that DSFGs do not form more stars (i.e. higher $\Sigma_{\rm SFR}$) only because they have more gas available (i.e. higher $\Sigma_{\rm H_2}$), or because the star formation is more efficient (i.e. higher A in equation 2.17, equivalently shorter $\tau_{\rm dep}$), but also because the physical properties of their Giant Molecular Clouds (GMCs) at ∼kpc scales are different from present-time galaxies.

A slope $N > 1$ indicates that GMCs in high-density regions of DSFGs form stars more efficiently than low star-forming regions. The results close to $N \approx 1.5$

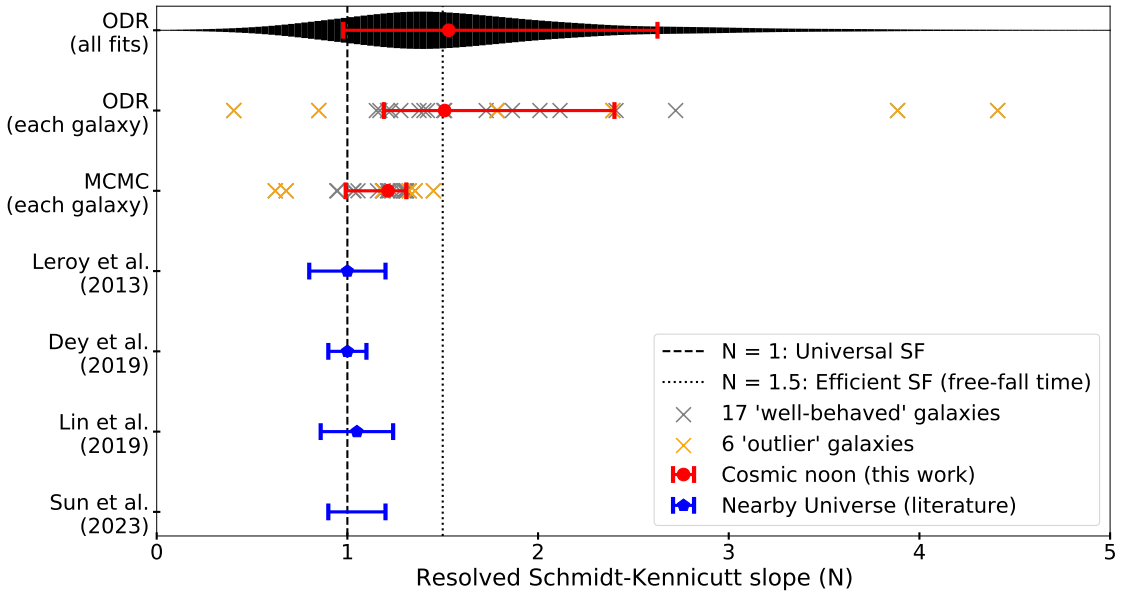

Figure 5.1: Constraints on the Schmidt-Kennicutt slope N in galaxies at resolved scale (∼few kpc). Row 1: density plot with the slopes of all resolved SK diagrams (1895 in total), fitted via orthogonal distance regression (ODR; in Appendix G three examples per galaxies are shown). Median and percentiles 16 and 84 ($\sim \pm 1\sigma$) are shown in red. Row 2: Crosses show the median slope of each of the 23 galaxies, obtained via ODR (i.e., from Figure 4.3). *Well-behaved* and *outlier* galaxies are separated in grey and orange (outliers are HerBS-37, -47A, -55, -69A, -122A, and -146B; see Section 5.2.4). Median galaxy and percentiles 16 and 84 ($\sim \pm 1\sigma$) are shown in red. Row 3: same as row 2, but from total fits via Markov chain Monte Carlo (MCMC; from Figures 3.23 and 4.4). Row 4: 30 local galaxies by Leroy et al. (2013), error-bars come from uncertainties in statistical noise, calibrations, removing data points or galaxies, and changing fitting parameters. Row 5: 39 local galaxies by Dey et al. (2019), error-bars obtained by identifying (and excluding) outliers. Row 6: 14 local galaxies by Lin et al. (2019), error-bar is $\pm 1\sigma$ in their fit. Row 7: 80 local galaxies by Sun et al. (2023), range given by results from six different methods.

even suggest that these clouds in high-density regions are collapsing at a speed similar to their free-fall time, with weak opposition to gravity. Since star formation is intrinsically very inefficient, there must be a mechanism in high-density regions which facilitates this efficient collapse of molecular clouds. As explained in Section 2.3.1, a key factor that prevents molecular clouds from cooling down is feedback effects from massive stars, strong in ultraviolet (UV) and optical emission.

A proposed explanation for the high efficiency in DSFGs comes from the presence of dust. Dust is prominent in these galaxies, and commonly distributed over more compact regions than molecular gas. This is reflected in the majority of moment 0 maps of galaxies, where the white contours (continuum) are more compact than the black contours (CO; e.g. Figure 3.22). In this scenario, dust in DSFGs absorbs the UV and optical radiation and re-emits it at infrared (IR), as explained in Section

2.5. IR radiation is less energetic, it does not interact in the same way with matter, and cannot suppress star formation the same way UV and optical radiation do (e.g. Menon et al., 2022).

This can also be understood with the mean free path of photons ($\lambda_{\rm mfp}$), i.e. the average distance they can travel before interacting. $\lambda_{\rm mfp}$ is commonly short for UV photons, which means they are easily trapped inside molecular clouds. On the contrary. at lower energies (e.g. IR), the cross sections of dust absorption and scattering decrease dramatically, which means $\lambda_{\rm mfp}$ becomes much longer (e.g. Habing et al., 1994; Reissl et al., 2018). As a consequence, the IR photons can escape molecular clouds more easily, which is crucial for them to cool down and, consequently, stars to form.

This cooling mechanism is a common feature of dust across many types of galaxies (e.g. Draine, 2011). The difference in DSFGs is likely due to a combination of factors, such as how compact these galaxies are, even more so the dust, and their intrinsic star formation efficiency. The combination makes it so that molecular gas is used up more quickly in high-density regions (i.e. the depletion time is shorter). This property of DSFGs is in sharp contrast with local galaxies, where GMCs are similar in terms of their star formation output ($N \sim 1$ as shown in Figure 5.1).

The result $N_{\rm ODR} = 1.51^{+0.89}_{-0.32}$ is consistent with clouds collapsing at free-fall time, i.e. $N = 1.5$. This occurs in the theoretical case that no forces oppose gravity in the collapse. Mathematically, this can be seen as follows. Star formation rate is, by definition, the rate at which stellar mass grows. Assuming that stellar mass comes directly from H_2 mass, SFR can be written as

$$\mathrm{SFR} = \frac{\mathrm{d}M(\mathrm{H_2})}{dt} \ . \tag{5.4}$$

The free-fall time is related to the volume density of H_2 (ρ), as

$$t_{\rm ff} = \sqrt{\frac{3\pi}{32G\rho}} \propto \rho^{-1/2} \tag{5.5}$$

(Spitzer, 1978), where G is the gravitational constant. If SFR is consistent with free-fall time ($t = t_{\rm ff}$), the following approximation can be made for equation 5.4

$$\mathrm{SFR} \approx \frac{M(\mathrm{H_2})}{t_{\rm ff}} \propto M(\mathrm{H_2})\rho^{1/2} \ , \tag{5.6}$$

where equation 5.5 was used. Dividing by an area in the sky A, surface densities are introduced

$$\underbrace{\frac{\mathrm{SFR}}{A}}_{\equiv\Sigma_{\rm SFR}} \propto \underbrace{\frac{M(\mathrm{H_2})}{A}}_{\equiv\Sigma_{\rm H_2}} \rho^{1/2} \ . \tag{5.7}$$

Also, the volume density is simply

$$\rho = \frac{M(\mathrm{H_2})}{V} = \frac{M(\mathrm{H_2})}{Ah} = \Sigma_{\rm H_2} h^{-1} \ , \tag{5.8}$$

where A is the area and h a linear thickness. Introducing in equation 5.7,

$$\Sigma_{\rm SFR} \propto \Sigma_{\rm H_2} \left(\Sigma_{\rm H_2} h^{-1}\right)^{1/2} \tag{5.9}$$

$$\Sigma_{\rm SFR} \propto h^{-1/2} \Sigma_{\rm H_2}^{3/2} \ . \tag{5.10}$$

This corresponds to equation 2.17, with a proportionality constant proportional to $h^{-1/2}$. In log-log,

$$\log\left(\Sigma_{\rm SFR}\right) = \frac{3}{2}\log\left(\Sigma_{\rm H_2}\right) - \frac{1}{2}\log(h) + C \ , \tag{5.11}$$

where C is some constant. Then, in a $\log(\Sigma_{\rm SFR}) - \log(\Sigma_{\rm H_2})$ plot (i.e. SK diagram), a slope $N = 3/2 = 1.5$ comes from clouds collapsing at free-fall time.

The efficient star formation in high-density regions of DSFGs found in this thesis (N close to 1.5), could explain why the gas is depleted so quickly in these galaxies. Tracing that back to $z = 0$ (i.e. present-time), such scenario is consistent with the little to no star formation observed in elliptical galaxies today. Regardless, the mechanisms driving the evolution of DSFGs are far more complex than what this thesis can cover, and further studies are needed fully assess the relation between DSFGs and modern ellipticals.

In order to further characterize the 23 galaxies in the Schmidt-Kennicutt relation, Figure 5.2 shows their average position in the SK diagram. They are compared against a wealth of galaxies from the literature, both at high- and low-redshift. The results from this thesis are fully consistent with previous works studying DSFGs. The galaxies are found at the right end of the relation, with more massive H_2 reservoirs than local galaxies, which correlate to higher SFRs.

The HerBS galaxies studied in this thesis have depletion times in the range $\tau_{\rm dep} \approx 100 - 200$ Myr. This is one whole order of magnitude shorter than the usual depletion time of local galaxies, $\tau_{\rm dep} \approx 2$ Gyr (e.g. Sun et al., 2023), and also from high-redshift star-forming galaxies. This is consistent with DSFGs being intrinsically more efficient in their star formation. Nevertheless, the depletion time in my sample is longer than other estimations on DSFGs (see blue squares in Figure 5.2; Hatsukade et al. 2015; Chen et al. 2017).

The parent sample (BEARS; Hagimoto et al. 2023) shows consistent depletion times with my results, but commonly further up in the diagonal. As mentioned in Section 3.1, they employed observations at a resolution of $\sim 2 - 3$ arcsec (some 10 times lower than this thesis). The CO emission of the galaxies in the sample is commonly extended $1 - 2$ arcsec across the sky (see moment 0 maps presented in Appendix G), which means that their observations are only moderately resolved.

As a consequence, their estimations of CO luminosity and SFR are likely biased high. In fact, their $M(H_2)$ calculations are consistently larger than the ones is this work (though always within the error-bars). Since their observations do not fully resolve the emission, their estimates are more sensitive to peak central regions. In this thesis, the peak values in those central regions are averaged down by fainter regions, which likely bring the estimations down the diagonal.

Another factor contributing to the discrepancy may be that they estimate galaxy sizes with the task `IMFIT` of CASA, instead of using resolved values of $\Sigma_{\rm SFR}$ and $\Sigma_{\rm H_2}$

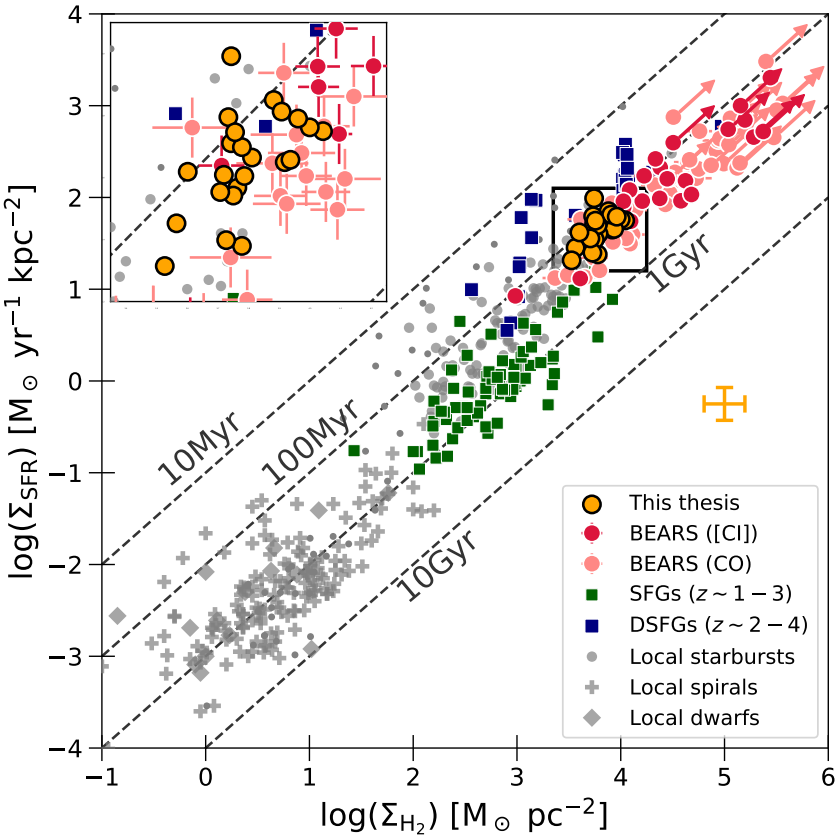

Figure 5.2: Schmidt-Kennicutt star formation relation of the 23 Dusty Star-Forming Galaxies studied in this thesis, compared against results from the literature. For each galaxy, the average position from all resolved SK diagrams is selected. The orange cross shows their average error-bar. BEARS: parent sample from Hagimoto et al. (2023). They employ both CO and [CI] to trace Σ_{H_2}, as discussed in Section 5.2.8. They mark with an arrow the galaxies whose size estimation is only an upper limit. Green squares: star-forming galaxies from Tacconi et al. (2013). Blue squares: DSFGs from Hatsukade et al. (2015), Chen et al. (2017), and references therein. Grey points: nearby starburst from original work by Kennicutt (1989). Grey plus points: nearby spirals from de los Reyes & Kennicutt (2019a,b). Grey diamonds: nearby dwarfs from Kennicutt & De Los Reyes (2021).

directly. The size estimations they report in their Table C.1 appear to be biased small. Regardless, since the morphologies of the galaxies are complex, is it unclear what biases this can introduce.

Another major difference between this thesis and the marginally resolved study of Hagimoto et al. (2023), is the slope in the Schmidt-Kennicutt diagram. They find their galaxies to follow $N \sim 1$, a universal star formation. This is consistent with the idea that DSFGs, as a whole, have a star formation similar to each other (hence $N \sim 1$). As has been discussed in this section, my results suggests that this changes at smaller scales (∼kpc), where the star formation is more efficient in high-density regions of galaxies.

As mentioned before, $N > 1$ is consistent with DSFGs having shorter depletion times in high-density regions, compared to the total average estimated depletion time. In this scenario, there may be galaxy evolutionary mechanisms acting in DSFGs, such as mergers (e.g. Duncan et al., 2019), compaction events (e.g. Zolotov et al., 2015), or efficient accretion (e.g. Dekel et al., 2009; Overzier, 2016). These might efficiently funnel gas onto the higher-density regions, allowing them to sustain the high star-formation rates for longer periods, as the molecular gas continues to be supplied. In particular, mergers are more common at cosmic noon than the present-time (e.g. Duncan et al., 2019), and their consequent bursts of star formation could be the reason why these DSFGs can be detected in our surveys.

Compared to $N \approx 1$ in the marginally resolved study by Hagimoto et al. (2023), the implications in our understanding of DSFGs can be significant. Previous unresolved studies can only calculate an average depletion time, which means they are likely overestimating the depletion time. The combined effect of mechanisms funneling molecular gas to the higher-density regions of galaxies, and the efficient cooling of dust, may drive the high star formation. As shown in this thesis, only resolved studies are able to discern the difference.

In order to further compare the results against the literature, Figure 5.3 shows the resolved slope N of each of the 23 galaxies, against their position in the Schmidt-Kennicutt relation (the x-axis, $\Sigma_{\mathrm{H_2}}$). These are compared to different constraints in the literature obtained at unresolved scales (shaded regions, including the parent sample by Hagimoto et al. 2023). In a smaller panel, a comparison with local resolved studies is included.

From Figure 5.3, it follows that this thesis is probing properties of galaxies unexplored in the literature. Even amongst some of the most recent works (Tacconi et al., 2020; Wang et al., 2022; Hagimoto et al., 2023), unresolved studies have been unable to find galaxies in the high end of the SK relation ($\Sigma_{\mathrm{H_2}} \gtrsim 10^{3.6}$ $\mathrm{M_\odot\ pc^{-2}}$) with such efficient star formation ($N \gtrsim 1.2$). Such efficiencies have only been found further down the SK relation (Gao & Solomon, 2004). Outliers aside, I have found ~ 10 galaxies in this new range.

Figure 5.3 also shows a tentative bimodal distribution: besides the ten galaxies at $N \gtrsim 1.2$, five lie at $N \sim 1$. This is not only a quantitative difference but also a qualitative one: at $N \sim 1$ star formation is no longer *efficient*, but rather the universal case ($\Sigma_{\mathrm{SFR}} \propto \Sigma_{\mathrm{H_2}}$). A proposed follow-up work is to test whether these two groups have more fundamental differences, e.g. in their morphology or stellar mass. This can help disentangle the extent and reasons of the diversity in the sample. The two galaxies at $N \sim 0.6 - 0.7$ are clearly outliers; they are further discussed in Section 5.2.4.

On the right panel of Figure 5.3, my results are compared against Leroy et al. (2013) and Pessa et al. (2022). These studies are qualitatively similar to the one in this thesis, only at the local Universe. They also constrain N with resolved measurements, either in different galaxies (Leroy et al. 2013, as in this thesis) or different environments (Pessa et al., 2022).

Outliers aside, the DSFGs of this thesis lie at larger N than the local Universe, as was already seen in Figure 5.1. In particular, the work by Pessa et al. (2022) constrains the pdfs (solid lines) to distributions significantly more narrow than this

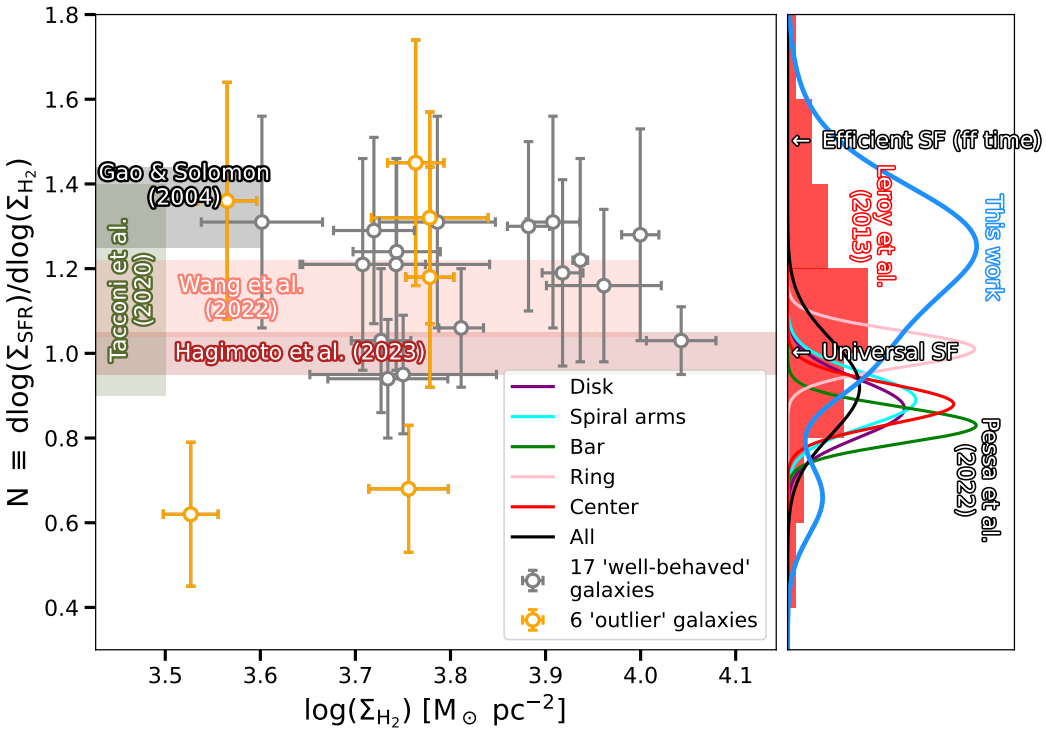

Figure 5.3: Left panel: slopes of the 23 galaxies studied in this work against their average position in the SK diagram (Σ_{H_2}). Only the results obtained with MCMC are included. Well-behaved and outlier galaxies are separated in grey and orange (see Section 5.2.4). These results are compared against constraints from unresolved measurements in the literature (Gao & Solomon 2004 in local Universe; Tacconi et al. 2020 across $z \sim 1-3$; Wang et al. 2022 across $z \sim 0.4-3.6$; and the parent sample Hagimoto et al. 2023 at cosmic noon). These are shown as shaded regions, which also reflect how far up the Σ_{H_2} axis they probed. Right panel: In blue, an approximate pdf of my results, compared against pdfs of resolved measurements in the local Universe by Leroy et al. 2013 (red histogram, they also calculate a separate slope for each galaxy), and by Pessa et al. 2022 (in solid lines, they compared different environments of galaxies).

thesis (solid blue line). They conduct a comprehensive work with almost 50,000 resolved measurements at scales $\sim$ 150 pc. Such level of details is inaccessible at high-redshift, which partly explains why the pdf of this thesis is significantly less constrained.

As mentioned earlier in this section, the results of this thesis ($N > 1$ in a large sample of DSFGs) are fully consistent with resolved studies of individual DSFGs in the literature (e.g. Hodge et al., 2015; Thomson et al., 2015; Hatsukade et al., 2015; Chen et al., 2017). All these authors find different depletion times within their galaxies, with a more efficient star formation in high-density regions. The only study that quantifies the slope is Hodge et al. (2015), who report $N = 2.1 \pm 1.0$ (in agreement with my results).

Based on these studies on individual galaxies, and others on larger samples

(e.g. Bakx et al., 2024), it can be said that the notion of having an efficient star formation scenario in DSFGs, with shorter depletion times in high-density regions, was already present in the literature. This thesis finds $N > 1$ in a systematic search in a large sample of DSFGs, which provides unprecedented statistical significance to this claim.

Some authors have argued that observational studies of star formation relations (such as SK) are greatly biased by the physical models that are assumed. Sun et al. (2023) reflect that only changing the SFR tracer can alter the slope N up to $\sim 15\%$. Furthermore, the choice of $\alpha_{\rm CO}$ can have an impact as big as $\sim 25\%$. They argue that such biases remain the dominant source of uncertainties in the conclusions that authors draw from their results. All of these factors together, often make galaxies from different studies difficult to compare against each other. The results presented in this thesis are free from this bias. The 23 galaxies were compared fairly under the same models, using as few assumptions as possible.

Other types of galaxies at high-redshift have also shown $N > 1$. Studies on individual main-sequence star-forming galaxies (MS SFGs) have found $N = 1.14 \pm 0.1$ (Genzel et al., 2013), and more recently $N = 1.27 \pm 0.1$ (Arriagada-Neira et al., 2025). As shown in Figure 5.2, star-forming galaxies (in green) commonly have longer depletion times than DSFGs, and smaller gas reservoirs. However, their N values are consistent with the scenario found for DSFGs in this thesis.

Considering this, a proposed work is to conduct a similar study as done in this thesis, only on a sample of less extreme galaxies such as MS SFGs. This can point at DSFGs simply being a more extreme version of galaxies with lower star-formation rates and dust masses. Such comparison, at the same cosmic epoch, can help assess the role of dust or funneling mechanisms (e.g. mergers, compaction, or accretion) in making the SFR in DSFGs so efficient.

A similar work proposed for the future, is not to compare DSFGs against a different population at cosmic noon, but rather against sample of local (ultra) luminous infrared galaxies ((U)LIRGs) starbursts. (U)LIRGs can be considered the DSFG equivalent at the present-time. An analogous work to the one conducted in this thesis, may help to assess the role of the large reservoirs of molecular gas available at cosmic noon, which were significantly larger than they are now (e.g. Inami et al., 2020).

5.2 Caveats

5.2.1 Beam-by-beam approach

The resolved Schmidt-Kennicutt diagrams were built following the algorithm described at length in Section 3.6. The overarching goal was to make measurements only in regions that are statistically independent from each other, down to the smallest size allowed by the resolution. For this reason, an aperture resembling the beam of the CO data cube was created, resulting in physical scales of a few kpc. A much easier approach is to build the resolved SK relation pixel-by-pixel, which has been done previously in the literature at high-redshift (e.g. Béthermin et al. 2023; Bakx et al. 2024; the latter in the HerBS sample).

There are many statistical advantages to the method developed in this thesis. Beam-by-beam measurements yields fewer points in the SK diagram than pixel-by-pixel, but each of them is statistically independent (approximately). The different regions within a galaxy are therefore separated from each other in a meaningful way, i.e. probing the finest details possible allowed by the data, without artificially improving the statistics (i.e. not assuming a better resolution than reality).

With this approach, the detailed study of each region (i.e. measuring CO $S\mathrm{d}V$ and continuum, in order to place one point in the SK diagram) captures the statistics robustly, less sensitive to outliers, with minimized correlation. Properties at smaller scales might be missed in this process, but it is a fair compromise in order to gain the statistical advantage. The noise is measured in large emission-free regions, in order to get the best possible statistics of the background sky, and maximize the signal-to-noise ratio. Thanks to all these considerations, the estimations of N provided by the algorithm can be considered reliable.

Bakx et al. (2024) studied the resolved SK relation of 16 DSFGs of the HerBS sample, calculating pixel-by-pixel. A significant drawback of this method is that the majority of the calculations are not statistically independent. Many pixels lie in the same ALMA beam, and quantifying their correlation is not trivial. This would make estimations of N less confident that the method employed in this thesis (the authors did not estimate N). They can still describe the star formation of the galaxies, as they obtain an average position of each galaxy in the SK diagram, and see the spread of the relation. However, the statistical weight of outlier pixels with extreme values is more likely to offset their analysis than in the beam-by-beam description.

In reality, there are no truly independent measurements in radioastronomy. This is because the beam is not a unit rectangle or *top-hat*, it rather has the distribution presented in Figure 3.3 (nearly Gaussian). It can decrease close to zero at large angles, but it never quite reaches zero. This means that in radio astronomical observations, one can not draw two circles next to each other in the sky and claim that they give *independent* measurements.

Under this constraint, the beam size was modeled by the solid angle of the beam, following equations 3.2 and 3.42. This is related to how an antenna responds to a source at different angles from the center of the beam. Measuring after the solid angle is therefore a scientifically motivated decision, given the limitations. Furthermore, the aperture was carefully designed so that it would tessellate perfectly and all the emission is captured. Such approach is relatively novel in the study of the Schmidt-Kennicutt relation. One example on large samples where such feature is addressed explicitly is the very recent work by Leroy et al. (2025), who employ hexagonal apertures on local galaxies.

There have been a number of studies at high-redshift which build resolved SK diagrams aligned with the resolution of the observations (e.g. Thomson et al. 2015; Hatsukade et al. 2015; Chen et al. 2017). They place apertures based on the aspect of the integrated emission of the CO line (its moment 0 map), considering clumps or regions with peak emission. Other works (e.g. Hodge et al., 2015) smooth down the CO map to match the beam resolution, but it is unclear if the specific way this smoothing is done can affect the diagram, since different regions might get smoothed together with others arbitrarily. Other attempts (e.g. Arriagada-Neira et al., 2025)

employ circular apertures, where it is unclear if there was any flux loss, or by which criteria the apertures were placed.

All these authors focus on specific galaxies, which means that there is no consistent approach by which all DSFGs can be compared fairly. In this thesis, one single algorithm was used on a large number of galaxies systematically (23 in total). For this reason, the conclusions following the calculation of N can be considered statistically more robust. Furthermore, the method did as few assumptions as possible, not relying on any morphologies, H_2 distribution, or one specific way of smoothing or placing of apertures.

5.2.2 Selection biases

Amongst the galaxies where ALMA covered the frequency of a CO line, only the brightest and most extended were used for the SK analysis (19 out of 40, and four extra from Bakx et al. 2024). This is due to observational constraints: molecular gas is undetected in faint galaxies, and unresolved in galaxies that are too compact, where dust emission is also unresolved. Other galaxies which were included in the analysis can be considered as *barely* resolved (e.g. HerBS-36, -41A, -69B, -103).

This is an important selection bias. The efficient star formation scenario ($N > 1$) found for DSFGs does not necessarily extend to the other sources. In particular, the dust being more compact than the molecular gas has been proposed as potential reason why GMCs use up their gas faster in high-density regions of DSFGs. If the molecular gas is similarly compact, a slope closer to $N \sim 1$ might be expected. Further studies are needed to determine the properties of more faint and compact galaxies.

The issue with fainter galaxies can potentially be solved by employing deeper observations, i.e. having ALMA observe those galaxies for longer than only ~ 2 minutes. This solution *seems* simple, but ALMA time is expensive and usually compromises are made when observing such a large sample of galaxies (in section 5.2.6 this is discussed at more detail). Another way of accessing faint sources is by stacking. This is averaging the emission of a large number of galaxies, to achieve a statistical detection (e.g. Knudsen et al., 2015). This requires having many undetected galaxies observed at the same CO transition.

The issue with compact sources is due to the limited resolution that can be achieved. ALMA is state-of-the-art when it comes to spatial resolution in radioastronomy; it hardly gets any better with the current technology. Longer baselines could be achieved by operating antennas from completely different observatories, in a technique known as Very Long Baseline Interferometry (VLBI). This allows astronomers to create baselines as long as the distances between continents. Such projects are commonly large collaborations aimed at specific sources, such as the first black hole ever imaged (Event Horizon Telescope Collaboration et al., 2019). Therefore, it is unlikely to be used for observing large samples.

Gravitational lensing can be a way to access the properties of fainter sources. Amongst the 23 galaxies tested, several are at least partially lensed (HerBS-23A, -25, -28, -47A, -69A). It is unclear if the continuum emission and CO emission are lensed with the same magnification, as this can change across different frequencies

(e.g. Gururajan et al., 2022).

Since the SK diagram is built with surface densities, it is not so severely affected by gravitational lensing. When uncorrected by magnifications, data points may move along constant times diagonal ($N = 1$) in the worst case. A more important issue about lensing is that sources may be multiply imaged (see schematic of Figure 2.10). As a consequence, when the algorithm detects an extended emission where many apertures can be placed, these may not truly be statistically independent. As seen in Appendix G, strongly lensed galaxies like HerBS-25 or HerBS-69 have many more data points in their resolved SK diagrams than a typical galaxy. These are likely oversampled, with many measurements coming from the same part of the galaxy.

Since the lensing magnification is unknown, it is difficult to quantify the extent of this effect. The potentially strong correlation therefore is not accounted for. Future work modeling the lensing on both the dust continuum and CO emission would provide a more complete picture of the resolved star formation in the galaxies. Such work has been done is large samples of DSFGs in the literature (e.g. Vieira et al., 2013; Spilker et al., 2016). This type of modeling is far from being trivial, and is commonly done in the visibility space of the data (i.e. in the Fourier domain, see Section 3.2.1).

Another proposed work, to further test the algorithm, is using it on galaxies with known properties. For this, simulated observations are commonly employed. In particular, ALMA offers the `SIMALMA` task in CASA[1], which allows astronomers to simulate their own data as if they were real ALMA observations.

Several galaxies could be simulated under different parameters, and test if the algorithm can retrieve the properties of the galaxies. This could also show how the results may be affected by the morphology of the galaxy, brightness, noise level, lensing, or the angular resolution. This can provide insights on how the algorithm would perform in galaxies excluded from the SK analysis conducted in this work.

5.2.3 CO Spectral Line Energy Distribution

As explained in Section 3.3, the molecule CO is used in this work to trace the molecular gas. This is by far the most used tracer by astronomers, mainly because its abundance and low excitation energy make it fairly ubiquitous in Giant Molecular Clouds (GMCs), and because its emission lines can be observed in the mm range by ALMA or other radio telescopes (e.g. Hodge & da Cunha, 2020). Much of what is known about the molecular gas in DSFGs, or any other galaxies, comes from the study of CO (e.g. Glover & Mac Low, 2011; Bolatto et al., 2013).

The single most problematic aspect of using CO, and of the entire physical model assumed in this thesis, is that the ground state transition CO($1-0$) can not be studied directly. A ratio between the luminosity of a higher transition and CO($1-0$) must be estimated, following a CO spectral line energy distribution (SLED).

I considered the same SLED for all galaxies (see Table 3.2). This may be an oversimplification of the properties of the galaxies, but when no further information is available, one single carefully-chosen SLED is considered the best way to introduce

[1] `https://casaguides.nrao.edu/index.php/Simalma_(CASA_6.1.1)`

as few assumptions and biases as possible into the methodology. By doing this, all galaxies can be compared fairly against each other.

The SLED employed in this thesis comes from the work by Harrington et al. (2021). They conducted a comprehensive study on DSFGs at high-redshift (see Section 3.3), similar to the HerBS sample. Hagimoto et al. (2023) showed that the HerBS sample, when stacked together, follows the CO SLED proposed by Harrington et al. (2021) consistently.

Constraining the CO SLED is an ongoing effort in the scientific community. At least for now, in the study of the high-redshift, it is likely that any SLED available in the literature would introduce uncertainties, as was the case in this work. Several galaxies included in this thesis have multiple CO lines observed by ALMA (see Appendix D). A future work comparing the total fluxes across all CO transitions could further constrain the SLED of the HerBS samples.

This issue could be bypassed by directly observing the ground state transition CO(1−0). This transitions is commonly fainter than higher transitions, which makes it more difficult to detect. Furthermore, at redshift $z \gtrsim 2.3$, the rest wavelength $\lambda_{\rm rest} = 2.6$ mm is redshifted beyond $\lambda_{\rm obs} \approx 8.6$ mm (following equation 2.6), which falls outside the range ALMA can observe. Other radio telescopes would be needed. Even so, due to the larger wavelength, the resolution of such observations would decrease significantly (see equation 3.1), which makes it questionable whether it would be suitable for a resolved study like done in this thesis.

5.2.4 Outlier galaxies

In Figures 5.1 and 5.3, six galaxies were shown in orange as *outliers*: HerBS-37, -47A, -55, -69A, -122A, and -146B. These galaxies represent the most extreme cases in both figures, which do not seem to follow a similar trend in N as the other 17 galaxies.

As explained in Section 2.4, a key assumption of the SK relation is that the star formation (from dust emission) and the molecular gas are co-spatial. Considering the tracers I am employing, this corresponds to the continuum and the CO moment 0 maps overlapping. A close look at the plots in Appendix G shows that this assumption is partially violated in several galaxies. Comparing the black and white contours (CO and continuum, respectively), some interesting cases are

- Strongly lensed sources where a significant part of the Einstein ring has no molecular gas (HerBS-28, -69A),
- Compact sources where gas and dust are slightly offset from each other (HerBS-33A, -69B, -122A, -146B).
- Sources where both dust and gas follow complicated morphologies, which do not resemble each other, and overlap only partially (HerBS-37, -55, -160). This could be indicator of a galaxy in a merger state, which may drive molecular gas and dust components to differ this much.
- One source seems slightly lensed (HerBS-47A), as an Einstein ring shape is hinted. Gas extends to regions closer to the center, with no dust.

In many of these galaxies (e.g. HerBS-37, -47A, -55, -69A, -160; see Appendix G), the resolved SK diagrams show several points in y ($\Sigma_{\rm SFR}$) which are only an

upper limit in x (Σ_{H_2}). These reflect regions of the galaxies with strong continuum emission (i.e. star formation detected), where the CO line has low signal-to-noise ratio (SNR < 1, i.e. no H_2 detected).

These regions could be key to show that star formation and molecular gas are not co-spatial. Such complex morphologies in DSFGs have been reported in the literature (e.g. Calistro Rivera et al., 2018). This scenario raises the question, is the Schmidt-Kennicutt relation even adequate to describe the star formation in these galaxies?

In some cases the slope N can still be constrained relatively well, whereas in HerBS-37, -47A, -55, -69A, -122A, and -146B, the SK relation likely does not provide a proper description of the star formation (this is discussed in Section 5.2.5). For this reason, the results from these galaxies were included with a warning in Figures 5.1 and 5.3.

5.2.5 Linear fits

Figure 5.4 summarizes the slopes N of each galaxy as constrained by both methods: the individual fits via orthogonal distance regression (ODR), and the combined fits via Markov chain Monte Carlo (MCMC). The first striking feature is how differently the slopes are constrained. The results in blue come from directly comparing the different individual resolved SK diagrams (as shown in Appendix G). The error-bars ($\sim \pm 1\sigma$) are significantly larger than when fitting all measurements together (in red). This is likely because the MCMC routines underestimate the spread in the data.

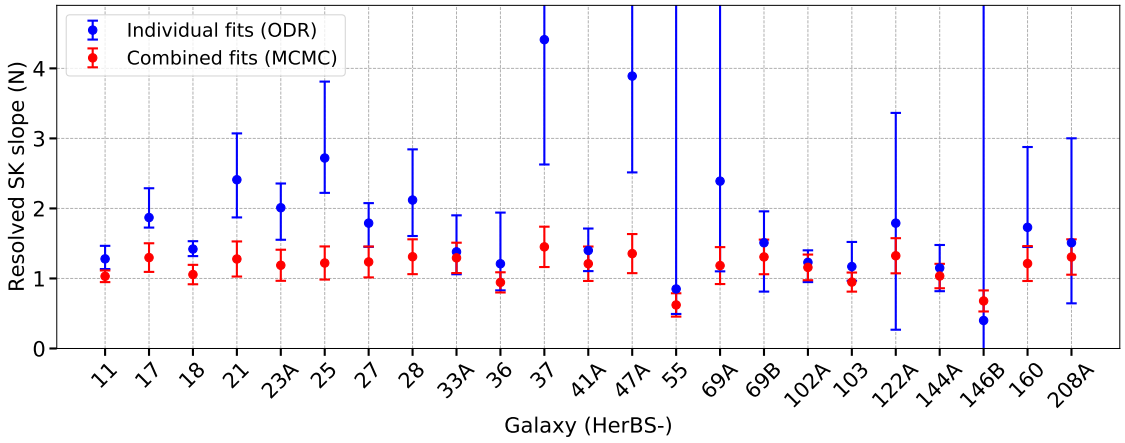

Figure 5.4: Slope N of the resolved Schmidt-Kennicutt star formation relation, obtained for each of the 23 galaxies. Both methods are compared; from the separate fits via ODR (blue), and the total fit via MCMC (red). Median and error-bars ($\sim \pm 1\sigma$) are the same as presented in Figures 4.3 and 4.4. The error-bars of HerBS-37, 47A, 55, 69A and 146B are cut out for better visualization.

As mentioned in Section 3.7.2, when using MCMC it is common to add a small term of intrinsic scatter ϵ to the model (e.g. Pessa et al., 2022), of the sort

$$y = Nx + b + \epsilon \ , \tag{5.12}$$

where ϵ may be drawn randomly from a normal distribution centered in 0. This term is added because galaxies are complex, there are physical mechanisms that create a scatter around the line. Even with *perfect* measurements there would be a scatter, so a small ϵ accounts fo this.

The model $y = Nx + b$ assumes that the straight line has no dispersion (no ϵ term). For this reason, the fitting routine assumes that all the scatter of the data points comes from the error measurements. This makes it so that the walkers do not *need* to sample a wide posterior for N. By introducing ϵ they are expected to sample a wider posterior, since the model is showing that the correlation is actually not so tight (e.g. Hogg et al., 2010).

Introducing ϵ requires calculating and inverting the covariance matrix in every step of every walker, which can be computationally expensive. It also introduces one more parameter to the model, which may diminish the statistical power of the methodology. A future work testing the effects of a small ϵ, may show if the more realistic representation of reality is worth the extra complexity of the model.

One consequence of omitting ϵ is that the $\pm 1\sigma$ red error-bars in Figure 5.4 are likely artificially small. This makes it so that the two methods often yield results which do not agree within their uncertainties, as is the case in HerBS-17, 18, 21, 23A, 25, 27, 28, 37, and 47A. Regardless, a simple inspection of Figures 3.23 and 4.4 shows that the median N sampled via MCMC is still good representation of the data for *well-behaved* galaxies (e.g. HerBS-11, -17, -18, -33A, -41A, -102A, or -144A).

These well-behaved galaxies are the ones that comply with the basic assumption of the SK relation: SFR (dust) and H_2 (CO) are co-spatial. Some outlier galaxies discussed in Section 5.2.4 (where dust and CO not co-spatial) proved difficult to constrain with the fitting routines. In the individual fits (blue in Figure 5.4), N for the galaxies HerBS-37, -47A, -55, -69A, -122A, or -146B are remarkably unconstrained; their large error-bars go beyond the range shown in Figure 5.4 (except 122A).

In these six galaxies, the regions where gas and dust are not co-spatial, result in SK diagrams that clearly do not follow a straight line. For this reason, the individual fits attempted (see three examples per galaxy in Appendix G) yield such inconsistent slopes. Furthermore, these six galaxies clearly represent outliers in the total distributions of Figures 5.1 and 5.3.

In Figure 4.4, SK diagrams including all measurements were presented. For these six galaxies (HerBS-37, -47A, -55, -69A, -122A, or -146B), a straight line is not obtained (e.g. compare HerBS-55 and HerBS-41A). As explained before, the inability to properly describe a linear relation is not reflected in a large error-bar for N, because the MCMC walkers are sampling posterior distributions that are too narrow. Performing χ^2 tests can be a future way of quantifying the goodness of the fits.

Also from Figure 5.4, it is seen that the median N prediction from the individual fits are consistently larger than those by MCMC. For several galaxies, these individual fits reach medians of $N \gtrsim 2$ and even $N \gtrsim 3$. This potentially indicates a correlation between $\Sigma_{\rm SFR}$ and $\Sigma_{\rm H_2}$ remarkably stronger than in the local Universe, where $N \sim 1$.

A possible explanation for the high N value is the different way in which the

upper limit data points are accounted for. The MCMC fit includes all of them at once. They can often be a significant fraction of all the data points, particularly in fainter galaxies (e.g. they are more than half of the data points in HerBS-160). As a consequence, they might weigh more in the fitting, lowering the slope N.

In the individual fits (see Appendix G), this is likely to have less of an impact because there are many more fits being done. This means that specific SK diagrams containing many upper limits, are likely outnumbered by other SK diagrams where there are just one or two. These outlier cases might yield a very different slope, but the median slope is still not so affected. In Figure 4.3 is shown how there are always outliers for N, across all galaxies. Choosing the median value with a $\sim \pm 1\sigma$ uncertainty intends to counter these effects.

In both methods, the upper limits in $\Sigma_{\mathrm{H_2}}$ are treated as a 0.75σ detection, a simplification easy to implement. There are more sophisticated approaches proposed in the literature. These include using a cumulative Gaussian distribution to the likelihood (e.g. Appendix A2 of Sawicki 2012). This was attempted but resulted in instabilities in the fitting routine.

The fitting routines (both ODR and MCMC) can be further tested in future work. Understanding the impact of the upper limit can be considered the top priority in this regard. Leroy et al. (2013) have shown that a having many upper limits in the x-axis ($\Sigma_{\mathrm{H_2}}$) can bias slopes high (up to $\sim 40\%$ in their example of Figure 17). A fit comparison on data with full measurements, against data clipped at some $\Sigma_{\mathrm{H_2}}$ threshold, can show whether the upper limits are being accounted for successfully or not.

An important sanity check suggested for the future is to attempt the fit with the same data, under the same assumptions, only inverting the x and y axes. This can show if there are some systematic errors affecting the fits. This can be particularly useful in *extreme* fits where N is very large. A fit where $N = 10$ or $N = 40$ are qualitatively just as *bad* (i.e. they are clearly not a realistic representations of the star formation), so it is unclear what can be driving the fits to such values.

More specifically about the MCMC fitting routine, there are also ideas for future work. Introducing a more rigorous likelihood distribution for the upper limits, powered with a small term for intrinsic scatter ϵ, could potentially yield more realistic posterior distributions for N, with better median values and dispersion. There are also different ways of processing the error-bars (e.g. Akritas & Bershady, 1996; Kelly, 2007), instead of the covariance matrix described in Section 3.7.2.

5.2.6 Sensitivity

In Appendix H the SNR of all apertures in all tessellations are presented. In all galaxies the SNR of the continuum is better than the CO line. There are galaxies with many apertures that exceed comfortably SNR > 3 in the continuum, while having few or no measurements of the CO line at SNR > 3 (e.g. HerBS-21, -28, -41A, -47A, -69A, -160, -208A).

This has to do with the sensitivity of the CO data cubes. ALMA spent ~ 2 minutes per source during the observations. The statistics provided are good enough for the work presented in this thesis. However, longer exposure times on source can

yield more precise measurements of velocity integrated fluxes $S\mathrm{d}V$ of the CO line.

ALMA time is expensive. As shown in Table 4.1, ALMA observed 122 galaxies located in 67 different fields. The remaining sources in the South Galactic Pole were also observed (Bakx et al., 2024). In order to study such a large sample, the observation depth of each galaxy is necessarily limited. As an example of a single-source approach at high-redshift, Arriagada-Neira et al. (2025) observed one galaxy for ~ 20 hours with ALMA. The ability to target individual sources, possibly stand out ones, allows for deep complements to studies on larger samples as in this thesis.

In Section 5.2.4 it was mentioned that some galaxies show distributions of dust and H_2 that are significantly offset from each other. This may be related to regions with star formation but no molecular gas. Such physical scenario can make the SK relation inadequate. Further observations of these galaxies at greater depth in CO can determine whether this is an intrinsic feature, or an artifact caused by limited sensitivity. Studying the effects of different exposure times in simulated galaxies of `SIMALMA`, can also be helpful in this regard.

As mentioned in Section 5.2.5, data that is clipped in one axis can bias the estimation of the slope significantly (e.g. Leroy et al., 2013). This is a common issue in resolved SK studies, where there are often sensitivity limitations in the CO observations (not so much in the dust). In this regard, `SIMALMA` can also help compare how N varies when a galaxy is observed at different depth levels. This is similar to the suggestion of clipping Σ_{H_2} presented in Section 5.2.5, only traced further back to the potential root of the issue.

5.2.7 α_{CO} factor

Tracing H_2 with CO involves choosing an α_{CO} factor to convert directly from CO(1−0) luminosity to H_2 mass. There are entire reviews written about this factor alone (e.g. Bolatto et al., 2013). Other authors describe α_{CO} as an *infamous* parameter (e.g. Casey et al., 2014). Calibrating an adequate α_{CO} can get very tricky, since there are many physical mechanisms involved in the relation between CO and H_2. This factor can vary significantly depending on density, temperature or type of galaxy.

Similarly to the CO SLED, I chose on single value for α_{CO}, at $\alpha_{CO} = (4.0 \pm 0.1)$ $M_\odot(\mathrm{K\ km\ s^{-1}pc^2})^{-1}$. Using one single value for α_{CO} introduces as few assumption as possible, providing the methodology with more statistical power. As mentioned in Section 3.3.3, this value calibrated by Dunne et al. (2022) comes from a comprehensive study on 400 galaxies, testing three different H_2 tracers. This value has already been employed in the HerBS sample by Hagimoto et al. (2023) and Bakx et al. (2024).

In high-redshift studies in the literature, some authors also consider one single value for α_{CO} (e.g. Hodge et al., 2015; Hatsukade et al., 2015). Other authors choose to calibrate α_{CO} values specific to their galaxies. For instance, Chen et al. (2017) separate the star, gas and dark-matter component of their galaxy, and estimate the velocity dispersion. From their analysis they derived $\alpha_{CO} = 1.8 \pm 1.1$ $M_\odot(\mathrm{K\ km\ s^{-1}pc^2})^{-1}$. The larger error-bars reflect how uncertain the calibration of α_{CO} can become when trying to include as much physics as possible.

Calibrating a specific α_{CO} is largely possible because studies at high-redshift

commonly focus on individual galaxies. The aim of the thesis is precisely the opposite; to test the Schmidt-Kennicutt relation in large samples of DSFGs and compare them fairly, with the same methodology. Therefore, choosing one single $\alpha_{\rm CO}$ is the best practical decision.

In the local Universe, where galaxies can be studied at greater detail, authors more commonly introduce more physics to the $\alpha_{\rm CO}$ factor. Sun et al. (2023) tried four different prescriptions for $\alpha_{\rm CO}$, considering metallicity, gas+star mass surface density, CO integrated intensity, and CO resolution. Leroy et al. (2013) chose $\alpha_{\rm CO}$ considering dust shielding at low metallicity, variations in line width, optical depth, and CO temperature in galaxy centers. Considering this many processes would certainly be a better description of reality, but could detriment the statistical power of the method. It is also more difficult to describe high-redshift galaxies at such fine details.

5.2.8 A different H_2 tracer: [CI]

An alternative H_2 tracer is [CI], i.e. the fine structure lines of neutral carbon. In (U)LIRGs, this has been proven to correlate well with CO, and therefore H_2. This has been shown both on detailed studies of a few galaxies (e.g. Papadopoulos & Greve, 2004), and in large samples (e.g. Jiao et al., 2017). In DSFGs at high-redshift, there is ongoing research trying to assess the usefulness of [CI] as an alternative to CO. A promising recent study by Frias Castillo et al. (2024) showed a strong correlation between [CI]$(1-0)$ and CO$(1-0)$ transitions, in a sample of ten DSFGs. Such correlation is strong all the way to $z = 5$.

Hagimoto et al. (2023) build an (unresolved) SK relation for the parent sample using both CO and [CI] lines (see BEARS in Figure 5.2). The H_2 masses they estimate from both tracers are consistent. Where both lines are available, they rather use [CI]$(1-0)$, because the ground state can be studied directly; there is no need to convert from a higher J transition to [CI]$(1-0)$, which is an issue in CO. Regardless, the relation between CO and H_2 is far more studied in the literature than between [CI] and H_2 (it is the most widely used tracer). This wealth of information is naturally also something to consider when choosing the tracer.

In this thesis, a [CI] line is potentially found in 23 galaxies (see Table D.1 of Appendix D, where [CI]$(1-0)$ is labeled [CI]609μm as and [CI]$(2-1)$ as [CI]370μm). This is a significant number, the same as the number of galaxies where the SK relation was tested in this thesis. The rest wavelengths of these [CI] transitions are similar to those of CO, if anything slightly lower, which could allow for a similar or better resolution. For some galaxies, ALMA observed both the frequency of a low CO line, and a [CI] line (HerBS-18, -23, -39, -49A, -49B, -103, -114, -123, -135A, -144A, -192, -208A, -208B).

A reason why [CI] is not as widely used as CO is that it can also trace phases of the ISM that are not H_2, such as atomic gas (e.g. Miyamoto et al., 2021). Atomic gas can also fuel star formation, only at a much deeper level (i.e. going far down the left-hand side of the SK relation; e.g. Bigiel et al. 2008), since it needs to become cold H_2 first. A proposed future work is to build the resolved SK relations with [CI], and compare to the work done in CO. This could shed light on just how much the

results (i.e. N estimations) are affected when choosing a different tracer. Also, new galaxies where CO was not detected could potentially be studied (e.g. HerBS-49B and HerBS-114).

5.2.9 Infrared luminosity as SFR tracer

In this thesis the SFR is traced with the IR luminosity ($L_{\rm IR} = L_{(8-1000)\,\mu{\rm m}}$), emitted by the dust shrouding the starlight. As mentioned in Section 3.4, there are several ways of tracing SFR in galaxies. For instance, in other types of galaxies (main-sequence) it is common to consider both the dust-obscured and un-obscured contributions, by adding the UV luminosity (e.g. Wang et al., 2022).

In DSFGs, using only the dust-obscured component is by far the most accepted approach, as the dust can be safely assumed to absorb and re-radiate the entire continuum emission. This has been employed by authors to estimate SFR both in the HerBS sample (Hagimoto et al., 2023; Bakx et al., 2024), and other dusty samples (e.g. Reuter et al., 2020; Traina et al., 2024).

A proposed future work is to better-constrain the IR luminosity of each galaxy. As explained in Section 3.4, the current estimations were done by Bakx et al. (2018) and Bakx et al. (2020a). The authors fitted a spectral energy distribution (SED) to density flux measurements of the HerBS sample at 0.250-, 0.350-, 0.500- and 0.850 mm. They employed the 22 galaxies whose spectroscopic redshifts were known.

In the years since, the HerBS sample has been observed by ALMA in several cycles, which has allowed for a deeper description of the sample. Urquhart et al. (2022) have calculated the spectroscopic redshift ($z_{\rm spec}$) of 71 more galaxies. This thesis includes $z_{\rm spec}$ for 10 more galaxies, and 5 to be confirmed. All together, these are significantly more $z_{\rm spec}$ measurements than the 22 used by Bakx et al. (2018). Furthermore, ALMA has provided flux density measurements at more wavelengths than the four available initially.

As shown by the $k-$correction in Figure 2.9, the spectrum of a (U)LIRG is expected to peak at some wavelength. This peak shifts to longer wavelengths (lower frequencies) for increasingly higher redshift. Since the radio window spans roughly $\lambda \approx 0.3$ mm $-$ 30 m, a peak at $\lambda \lesssim 0.3$ mm can not be observed by a radio telescope. This is the case in galaxies at $z \lesssim 2.5$, whose redshift is simply not high enough to *move* the peak inside the window.

A key aspect of an accurate SED fitting is having measurements of the density flux at both sides of this peak. If there are only measurements of one side of the peak, it becomes way more difficult to determine where the peak is; consequently, to fit a SED. Obtaining density flux measurements at the long$-\lambda$ side of the peak, at $\sim$mm wavelengths, is relatively easy since that is well inside the radio window. The difficulty often lies in the measurements at short-λ, close to the ~ 0.3 mm limit. ALMA observes closer to 0.3 mm with increasingly higher bands.

In the HerBS sample, Bendo et al. (2023) have already used new measurements, at 101 GHz and 151 GHz, to fit a SEDs in a dozen of HerBS galaxies. The more recent work by Bendo et al. (2025) followed up on this, with measurements at Bands 3 through 8 (same bands as available for this thesis; these are frequencies 106 GHz, 140 GHz, 199 GHz, 232 GHz, 287 GHz, and 412 GHz). By employing measurements

of high ALMA bands, the authors are able to probe both sides of the peak.

A proposed work for the future is combining these measurements with the ones studied originally (Bakx et al., 2018, 2020a). This may produce a more robust SED fit of the HerBS sample, where both sides of the peak are probed. If the HerBS sample was observed at even higher frequencies, with ALMA Bands 9 and 10, the *difficult* side of the SED can be probed deeper, for an even better fit. These potential improvements may yield more accurate estimations of $L_{\rm IR}$ of each galaxy.

It must be noted that fitting the entire HerBS sample together with one single SED, assumes that all galaxies can be described by a common spectrum and dust temperature ($T_{\rm dust}$). $T_{\rm dust}$ has been shown to be diverse amongst samples of DSFGs (e.g. da Cunha et al., 2015; Reuter et al., 2020). For this reason, fitting individual SEDs to each galaxy may be a more accurate way to measure their specific $T_{\rm dust}$ (e.g. the SED fits by Bendo et al. 2023, 2025).

The diversity of dust temperatures provides valuable insights about the properties of DSFGs. However, these are fine differences when it comes to the fitted SED. Since $L_{\rm IR}$ is not calculated from $T_{\rm dust}$ via an equation, but rather from the area under the curve of the fitted SED, the differences in the estimations of $L_{\rm IR}$ would likely not be significant. In order to study a large sample as done in this thesis, considering one single fit is the preferred way in order to introduce as few extra choices as possible, that many diminish the statistical power of the methodology.

6
Conclusion

This thesis constitutes the first work in the literature to constrain the slope N of the Schmidt-Kennicutt (SK) relation in a large sample of dusty star-forming galaxies (DSFGs) at cosmic noon, at a resolved scale of a few kpc. This was done in a total of 23 galaxies, using high-resolution ALMA observations of Band 6 dust emission and CO transitions. By performing linear fits with two different methods, the constraints obtained are $N_1 = 1.51^{+0.89}_{-0.32}$ and $N_2 = 1.21^{+0.10}_{-0.22}$ (both results are median galaxy and 16%, 84% percentiles).

These results are consistent with a scenario of efficient star formation ($N > 1$), where giant molecular clouds collapse faster into stars in high-density regions of DSFGs, at time scales possibly close to free-fall time. The notion of $N > 1$ was already present in the literature, mostly from studies of individual DSFGs. This thesis provides unprecedented statistical significance to this claim. This result differs significantly from the local Universe, where a universal star formation law is commonly found at resolved scales ($N \approx 1$).

Efficient cooling by compact dust may be the reason why star formation is so efficient in high-density regions of DSFGs. The implications of having $N > 1$ at kpc scales in a DSFG remain an open question. If molecular gas can be funneled efficiently into high-density regions, the galaxy might become dominated by this higher star formation rate, depleting the gas faster than what unresolved observations would predict. Further comparisons of the resolved SK relation between DSFGs and other populations of galaxies are needed to assess this scenario, and what has been the evolutionary path of DSFGs from cosmic noon until today.

Observational constraints made it so that only the brightest and most extended galaxies could be studied. Gravitational lensing may be a way to access the properties of fainter objects, so a future work modeling their magnification can be an important improvement to the completeness of the sample. Furthermore, a future revision of the fitting routines can provide more refined estimations of N in each galaxy.

The evolution of galaxies across cosmic time is one of the most fascinating puzzles in modern astronomy. The quest of studying different galaxies across different cosmic epochs has captivated astronomers for decades, and will undoubtedly continue to do so for many more. This thesis has provided the reader with insights into a very special population of galaxies found at a very special time in our Universe. It serves as a contribution to our understanding of how things came to be the way they are today.

AI usage declaration

The author declares the use of Artificial Intelligence (AI; OpenAI 2023) tools. This was limited to

1. Debug of coding.
2. Visualization aspects of Matplotlib and APLpy.
3. Overleaf formatting.

Bibliography

Agertz O., et al., 2020, MNRAS, 491, 1656

Akritas M. G., Bershady M. A., 1996, ApJ, 470, 706

Algera H. S. B., et al., 2023, MNRAS, 518, 6142

Alpher R. A., Bethe H., Gamow G., 1948, Physical Review, 73, 803

Arriagada-Neira S., et al., 2025, A&A, 696, A83

Astropy Collaboration et al., 2013, A&A, 558, A33

Atek H., Richard J., Kneib J.-P., Schaerer D., 2018, MNRAS, 479, 5184

Bakx T. J. L. C., et al., 2018, MNRAS, 473, 1751

Bakx T. J. L. C., et al., 2020a, MNRAS, 494, 10

Bakx T. J. L. C., et al., 2020b, MNRAS, 496, 2372

Bakx T. J. L. C., et al., 2024, MNRAS, 535, 1533

Barger A. J., et al., 2014, ApJ, 784, 9

Barron A. R., 1986, The Annals of Probability, 14, 336

Becker R. H., et al., 2001, AJ, 122, 2850

Bell E. F., McIntosh D. H., Katz N., Weinberg M. D., 2003, ApJS, 149, 289

Bendo G. J., et al., 2023, MNRAS, 522, 2995

Bendo G. J., et al., 2025, arXiv e-prints, p. arXiv:2505.12141

Béthermin M., et al., 2023, A&A, 680, L8

Bevington P. R., Robinson D. K., 2003, Data reduction and error analysis for the physical sciences

Bigiel F., Leroy A., Walter F., Brinks E., de Blok W. J. G., Madore B., Thornley M. D., 2008, AJ, 136, 2846

Bigiel F., et al., 2011, ApJL, 730, L13

Blain A. W., 1999, arXiv e-prints, pp astro–ph/9911449

Boggs P. T., Byrd R. H., Schnabel R. B., 1987, SIAM Journal on Scientific and Statistical Computing, 8, 1052

Bolatto A. D., Wolfire M., Leroy A. K., 2013, ARA&A, 51, 207

Bolatto A. D., et al., 2017, ApJ, 846, 159

Bournaud F., Jog C. J., Combes F., 2007, A&A, 476, 1179

CASA Team et al., 2022, PASP, 134, 114501

Cañameras R., et al., 2015, A&A, 581, A105

Calistro Rivera G., et al., 2018, ApJ, 863, 56

Calzetti D., 2013, in XXIII Canary Islands Winter School of Astrophysics ed., , Secular Evolution of Galaxies. p. 419, doi:10.48550/arXiv.1208.2997

Carilli C. L., Walter F., 2013, ARA&A, 51, 105

Carniani S., et al., 2024, Nature, 633, 318

Casey C. M., Narayanan D., Cooray A., 2014, Phys. Rep., 541, 45

Chapman S. C., Blain A. W., Ivison R. J., Smail I. R., 2003, Nature, 422, 695

Chen C.-C., et al., 2017, ApJ, 846, 108

Chevance M., et al., 2020, Space Sci. Rev., 216, 50

Chevance M., Krumholz M. R., McLeod A. F., Ostriker E. C., Rosolowsky E. W., Sternberg A., 2023, in Inutsuka S., Aikawa Y., Muto T., Tomida K., Tamura M., eds, Astronomical Society of the Pacific Conference Series Vol. 534, Protostars and Planets VII. p. 1 (arXiv:2203.09570), doi:10.48550/arXiv.2203.09570

Chomiuk L., Povich M. S., 2011, AJ, 142, 197

Comrie A., et al., 2021, CARTA: The Cube Analysis and Rendering Tool for Astronomy, doi:10.5281/zenodo.4905459

Condon J. J., Ransom S. M., 2016, Essential Radio Astronomy

Conselice C. J., 2014, ARA&A, 52, 291

Cornwell T. J., Uson J. M., Haddad N., 1992, A&A, 258, 583

Cunningham C. R., Gear W. K., Duncan W. D., Hastings P. R., Holland W. S., 1994, in Crawford D. L., Craine E. R., eds, Society of Photo-Optical Instrumentation Engineers (SPIE) Conference Series Vol. 2198, Instrumentation in Astronomy VIII. pp 638–649, doi:10.1117/12.176772

Daddi E., et al., 2010, ApJL, 714, L118

Dekel A., et al., 2009, Nature, 457, 451

Dey B., et al., 2019, MNRAS, 488, 1926

Di Valentino E., et al., 2021, Classical and Quantum Gravity, 38, 153001

Draine B. T., 2011, Physics of the Interstellar and Intergalactic Medium

Driver S. P., Popescu C. C., Tuffs R. J., Graham A. W., Liske J., Baldry I., 2008, ApJL, 678, L101

Driver S. P., et al., 2009, Astronomy and Geophysics, 50, 5.12

Dudzevičiūtė U., et al., 2020, MNRAS, 494, 3828

Duncan K., et al., 2019, ApJ, 876, 110

Dunne L., Maddox S. J., Papadopoulos P. P., Ivison R. J., Gomez H. L., 2022, MNRAS, 517, 962

Eales S., et al., 2010, PASP, 122, 499

Einstein A., 1936, Science, 84, 506

Evans II N. J., et al., 2009, ApJS, 181, 321

Event Horizon Telescope Collaboration et al., 2019, ApJL, 875, L1

Faber S. M., Jackson R. E., 1976, ApJ, 204, 668

Fan X., Narayanan V. K., Strauss M. A., White R. L., Becker R. H., Pentericci L., Rix H.-W., 2002, AJ, 123, 1247

Finkelstein S. L., et al., 2023, ApJL, 946, L13

Fixsen D. J., Mather J. C., 2002, ApJ, 581, 817

Foreman-Mackey D., Hogg D. W., Lang D., Goodman J., 2013, PASP, 125, 306

Förster Schreiber N. M., Wuyts S., 2020, ARA&A, 58, 661

Frias Castillo M., et al., 2024, arXiv e-prints, p. arXiv:2404.05596

Friedmann A., 1922, Zeitschrift fur Physik, 10, 377

Frieman J. A., Turner M. S., Huterer D., 2008, ARA&A, 46, 385

Gao Y., Solomon P. M., 2004, ApJ, 606, 271

Genzel R., et al., 2010, MNRAS, 407, 2091

Genzel R., et al., 2013, ApJ, 773, 68

Glover S. C. O., Mac Low M. M., 2011, MNRAS, 412, 337

Goldstein H., Poole C., Safko J., 2002, Classical mechanics

Golub G. H., Van Loan C. F., 2013, Matrix Computations, 4th edn. Johns Hopkins University Press

Griffin M., Swinyard B., Vigroux L., 2005, in Wilson A., ed., ESA Special Publication Vol. 577, ESA Special Publication. pp 17–22

Gunn J. E., Peterson B. A., 1965, ApJ, 142, 1633

Gururajan G., et al., 2022, A&A, 663, A22

Guth A. H., 1981, Phys. Rev. D, 23, 347

Habart E., Walmsley M., Verstraete L., Cazaux S., Maiolino R., Cox P., Boulanger F., Pineau des Forêts G., 2005, Space Sci Rev, 119, 71

Habing H. J., Tignon J., Tielens A. G. G. M., 1994, A&A, 286, 523

Hagimoto M., et al., 2023, MNRAS, 521, 5508

Harrington K. C., et al., 2021, ApJ, 908, 95

Harris C. R., et al., 2020, Nature, 585, 357

Harrison C., 2014, PhD thesis, Durham University, UK

Hatsukade B., Tamura Y., Iono D., Matsuda Y., Hayashi M., Oguri M., 2015, PASJ, 67, 93

Hayward C. C., Narayanan D., Kereš D., Jonsson P., Hopkins P. F., Cox T. J., Hernquist L., 2013, MNRAS, 428, 2529

Hewitt J. N., Turner E. L., Schneider D. P., Burke B. F., Langston G. I., 1988, Nature, 333, 537

Heyer M., Krawczyk C., Duval J., Jackson J. M., 2009, ApJ, 699, 1092

Hickox R. C., et al., 2012, MNRAS, 421, 284

Hilton J. L., Hohenkerk C. Y., 2004, A&A, 413, 765

Hodge J. A., da Cunha E., 2020, Royal Society Open Science, 7, 200556

Hodge J. A., Riechers D., Decarli R., Walter F., Carilli C. L., Daddi E., Dannerbauer H., 2015, ApJL, 798, L18

Hodge J. A., et al., 2016, ApJ, 833, 103

Högbom J. A., 1974, A&AS, 15, 417

Hogg D. W., Foreman-Mackey D., 2018, ApJS, 236, 11

Hogg D. W., Bovy J., Lang D., 2010, arXiv e-prints, p. arXiv:1008.4686

Holland W. S., et al., 2013, MNRAS, 430, 2513

Hubble E. P., 1926, ApJ, 64, 321

Hubble E., 1929, Proceedings of the National Academy of Science, 15, 168

Hunter J. D., 2007, Computing in Science and Engineering, 9, 90

Inami H., et al., 2020, ApJ, 902, 113

Ishiyama T., et al., 2021, MNRAS, 506, 4210

Ives H. E., Stilwell G. R., 1938, Journal of the Optical Society of America (1917-1983), 28, 215

Jansky K. G., 1933, Nature, 132, 66

Jáquez-Domínguez J. M., et al., 2023, ApJ, 950, 88

Jarugula S., et al., 2021, ApJ, 921, 97

Jiao Q., Zhao Y., Zhu M., Lu N., Gao Y., Zhang Z.-Y., 2017, ApJL, 840, L18

Jolly J.-B., 2021, PhD thesis, Chalmers University of Technology, Sweden

Kannan R., Garaldi E., Smith A., Pakmor R., Springel V., Vogelsberger M., Hernquist L., 2022, MNRAS, 511, 4005

Kaur K. P., Joshi P. S., 2021, Bulgarian Astronomical Journal, 35, 60

Kelly B. C., 2007, ApJ, 665, 1489

Kennicutt Jr. R. C., 1989, ApJ, 344, 685

Kennicutt Jr. R. C., 1998, ApJ, 498, 541

Kennicutt Jr. R. C., De Los Reyes M. A. C., 2021, ApJ, 908, 61

Kennicutt R. C., Evans N. J., 2012, ARA&A, 50, 531

Kirkpatrick A., Sharon C., Keller E., Pope A., 2019, ApJ, 879, 41

Knudsen K. K., Lindroos L., Vlemmings W. H. T., Conway J. E., Marti-Vidal I., 2015, in Advancing Astrophysics with the Square Kilometre Array (AASKA14). p. 168 (arXiv:1501.05643), doi:10.22323/1.215.0168

Koopmans L., et al., 2015, in Advancing Astrophysics with the Square Kilometre Array (AASKA14). p. 1 (arXiv:1505.07568), doi:10.22323/1.215.0001

Kroupa P., 2001, MNRAS, 322, 231

Krumholz M. R., Tan J. C., 2007, ApJ, 654, 304

Laher R. R., Gorjian V., Rebull L. M., Masci F. J., Fowler J. W., Helou G., Kulkarni S. R., Law N. M., 2012, PASP, 124, 737

Leitherer C., et al., 1999, ApJS, 123, 3

Lemaître G., 1931, MNRAS, 91, 483

Leroy A. K., et al., 2013, AJ, 146, 19

Leroy A. K., et al., 2025, ApJ, 985, 14

Li G.-X., 2024, MNRAS, 528, L52

Lilly S. J., Eales S. A., Gear W. K. P., Hammer F., Le Fèvre O., Crampton D., Bond J. R., Dunne L., 1999, ApJ, 518, 641

Lin L., et al., 2019, ApJL, 884, L33

Ma C. J., et al., 2015, ApJ, 806, 257

MacLaren I., Richardson K. M., Wolfendale A. W., 1988, ApJ, 333, 821

Madau P., Dickinson M., 2014, ARA&A, 52, 415

Marr J. M., Snell R. L., Kurtz S. E., 2015, Fundamentals of Radio Astronomy: Observational Methods (Series in Astronomy and Astrophysics)

Martí-Vidal I., 2015-2016, Interferometry lecture notes

McKee C. F., Ostriker E. C., 2007, ARA&A, 45, 565

Menon S. H., Federrath C., Krumholz M. R., 2022, MNRAS, 517, 1313

Merlin E., Pilo S., Fontana A., Castellano M., Paris D., Roscani V., Santini P., Torelli M., 2019, A&A, 622, A169

Miyamoto Y., et al., 2021, PASJ, 73, 552

Murphy E. J., et al., 2011, ApJ, 737, 67

Newville M., et al., 2025, LMFIT: Non-Linear Least-Squares Minimization and Curve-Fitting for Python, doi:10.5281/zenodo.598352

OpenAI 2023, ChatGPT: Optimizing Language Models for Dialogue, `https://openai.com/chatgpt`

Overzier R. A., 2016, A&ARv, 24, 14

Pan H.-A., et al., 2022, ApJ, 927, 9

Papadopoulos P. P., Greve T. R., 2004, ApJL, 615, L29

Pearson E. A., et al., 2013, MNRAS, 435, 2753

Peebles P. J. E., 1968, ApJ, 153, 1

Penzias A. A., Wilson R. W., 1965, ApJ, 142, 419

Perlmutter S., et al., 1999, ApJ, 517, 565

Pessa I., et al., 2022, A&A, 663, A61

Planck Collaboration et al., 2020, A&A, 641, A6

Popesso P., et al., 2023, MNRAS, 519, 1526

Pound R. V., Rebka G. A., 1959, Phys. Rev. Lett., 3, 439

Ragone-Figueroa C., Granato G. L., Parente M., Murante G., Valentini M., Borgani S., Maio U., 2024, A&A, 691, A200

Rangwala N., et al., 2011, ApJ, 743, 94

Reissl S., Klessen R. S., Mac Low M.-M., Pellegrini E. W., 2018, A&A, 611, A70

Remijan A. J., Markwick-Kemper A., ALMA Working Group on Spectral Line Frequencies 2007, in American Astronomical Society Meeting Abstracts. p. 132.11

Reuter C., et al., 2020, ApJ, 902, 78

Riess A. G., et al., 1998, AJ, 116, 1009

Riess A. G., et al., 2022, ApJL, 934, L7

Robertson B., Bullock J. S., Cox T. J., Di Matteo T., Hernquist L., Springel V., Yoshida N., 2006, ApJ, 645, 986

Robitaille T., Bressert E., 2012, APLpy: Astronomical Plotting Library in Python, Astrophysics Source Code Library, record ascl:1208.017

Robitaille T., Ginsburg A., Beaumont C., Leroy A., Rosolowsky E., 2016, spectral-cube: Read and analyze astrophysical spectral data cubes, Astrophysics Source Code Library, record ascl:1609.017

Rosenberg M. J. F., et al., 2015, ApJ, 801, 72

Salpeter E. E., 1955, ApJ, 121, 161

Sancisi R., Fraternali F., Oosterloo T., van der Hulst T., 2008, A&ARv, 15, 189

Sanders D. B., Mirabel I. F., 1996, ARA&A, 34, 749

Sawicki M., 2012, PASP, 124, 1208

Schmidt M., 1959, ApJ, 129, 243

Schmidt M., 1963, ApJ, 137, 758

Schneider P., 2006, Extragalactic Astronomy and Cosmology

Shetty R., Clark P. C., Klessen R. S., 2014, MNRAS, 442, 2208

Shu F. H., Adams F. C., Lizano S., 1987, ARA&A, 25, 23

Smail I., Ivison R. J., Blain A. W., 1997, ApJL, 490, L5

Snell R. L., Kurtz S. E., 2019, Fundamentals of Radio Astronomy: Astrophysics (Series in Astronomy and Astrophysics)

Solomon P. M., Vanden Bout P. A., 2005, ARA&A, 43, 677

Solomon P. M., Downes D., Radford S. J. E., 1992, ApJL, 398, L29

Spilker J. S., et al., 2016, ApJ, 826, 112

Spitzer L., 1978, Physical processes in the interstellar medium, doi:10.1002/9783527617722.

Stanley F., et al., 2023, ApJ, 945, 24

Strandet M. L., et al., 2017, ApJL, 842, L15

Sun J., et al., 2023, ApJL, 945, L19

Tacconi L. J., et al., 2013, ApJ, 768, 74

Tacconi L. J., Genzel R., Sternberg A., 2020, ARA&A, 58, 157

Taranu D., Dubinski J., Yee H. K. C., 2015, in IAU General Assembly. p. 2256542

Taylor D. J., et al., 2025, MNRAS, 536, 1149

Thomson A. P., Ivison R. J., Owen F. N., Danielson A. L. R., Swinbank A. M., Smail I., 2015, MNRAS, 448, 1874

Traina A., et al., 2024, A&A, 681, A118

Tsai C.-W., et al., 2015, ApJ, 805, 90

Tully R. B., Fisher J. R., 1977, A&A, 54, 661

Urquhart S. A., et al., 2022, MNRAS, 511, 3017

Valiante E., et al., 2016, MNRAS, 462, 3146

Vallini L., et al., 2023, Monthly Notices of the Royal Astronomical Society, 527, 10

Vieira J. D., et al., 2013, Nature, 495, 344

Virtanen P., et al., 2020, Nature Methods, 17, 261

Vulcani B., et al., 2011, MNRAS, 412, 246

Wang T.-M., et al., 2022, A&A, 660, A142

Wise J. H., 2019, Contemporary Physics, 60, 145

Wong T., Blitz L., 2002, ApJ, 569, 157

Yang C., et al., 2017, A&A, 608, A144

Yang D., et al., 2023, ApJ, 953, 40

Zavala J. A., et al., 2021, ApJ, 909, 165

Zhou S., Aragón-Salamanca A., Merrifield M., Andrews B. H., Drory N., Lane R. R., 2023, MNRAS, 521, 5810

Zolotov A., et al., 2015, MNRAS, 450, 2327

da Cunha E., et al., 2015, ApJ, 806, 110

de los Reyes M. A. C., Kennicutt Jr. R. C., 2019a, ApJ, 872, 16

de los Reyes M. A. C., Kennicutt Jr. R. C., 2019b, ApJ, 878, 74

A

Celestial coordinates

Objects in space have a unique position in the celestial sphere, defined by the celestial coordinates[1]. These allow astronomers to easily communicate where in the sky an object is. The coordinates are defined by the right ascension (R.A.[2]) and declination (Dec.[3]). These are analogous to latitude and longitude coordinates that locations have on Earth.

Due to the precession and nutation of Earth, these coordinates change over time, although very slowly. For full accuracy, celestial coordinates must always be reported with a context clarifying a reference point. A popular standard convention is Julian epoch 2000 (J2000). Under this convention, the coordinates of an object are reported as they would appear on January 1, 2000, noon of Terrestial Time.

A new system adopted by the International Astronomical Union is the International Celestial Reference System (ICRS[4]). This is a system that sets its origin in the solar system barycenter, and is intended to show no global rotation with respect to a set of distant extragalactic objects.

In practice, both systems are very similar to each other. In order to convert from one to the other, only minor corrections are needed (e.g. Hilton & Hohenkerk, 2004), and astronomers commonly use both system interchangeably. In this thesis, all positions in the sky are set according to ICRS, as reported by ALMA.

[1]For the interested reader: `https://en.wikipedia.org/wiki/Equinox_(celestial_coordinates)`

[2]For the interested reader: `https://en.wikipedia.org/wiki/Right_ascension`

[3]For the interested reader: `https://en.wikipedia.org/wiki/Declination`

[4]For the interested reader: `https://en.wikipedia.org/wiki/International_Celestial_Reference_System_and_its_realizations`

B

Corner plots

In Figure B.1 I present the MCMC-sampled posterior distribution of the slope N and intercept b, for two example galaxies (HerBS-11 and HerBS-17). The two parameters are clearly anti-correlated. This is expected since at $x > 0$, the steeper the line (large N), the further down it will intercept the y axis (small b). The individual posterior distributions of the parameters are fairly symmetric in both galaxies. Furthermore, the cornerplots are qualitatively the same in all galaxies, so these two are enough to illustrate the point. The most crucial aspect of these plots is the value and error-bar extracted for the slope, which are shown and discussed in Chapter 5 for all galaxies.

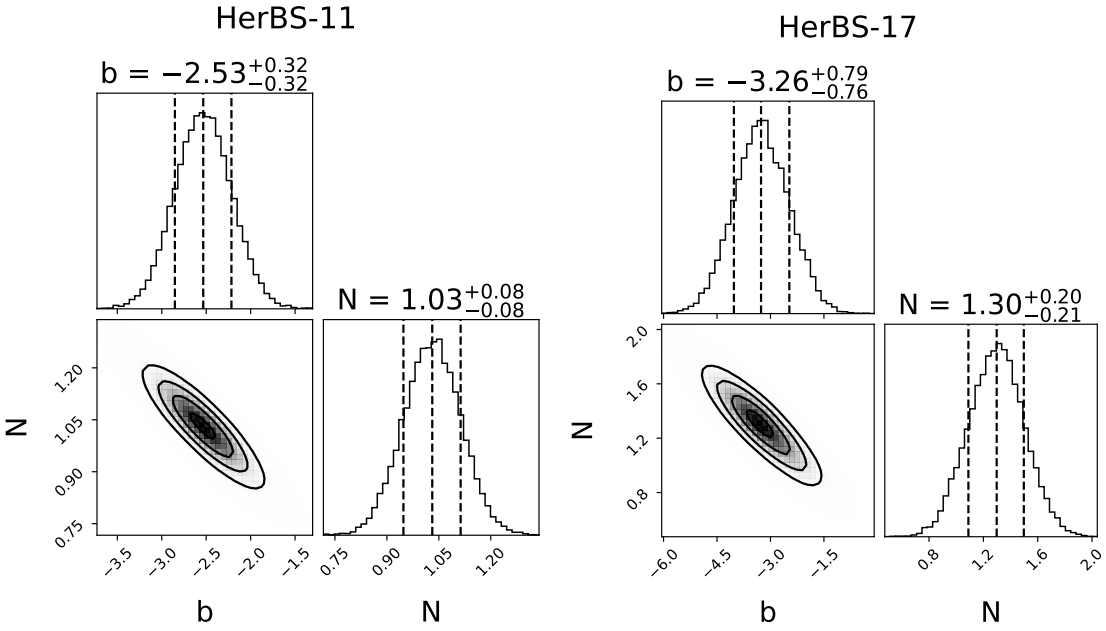

Figure B.1: Posterior distribution of the intercept and slope for two galaxies, obtained with MCMC sampling.

C

Dust continuum emission

In Figure C.1 I present the dust continuum emission of all galaxies included in this work (a sample of 122 in total), across ALMA Bands 3 through 8. The exact (R.A., Dec.) coordinate of each galaxy were determine by visual inspection with the software CARTA.

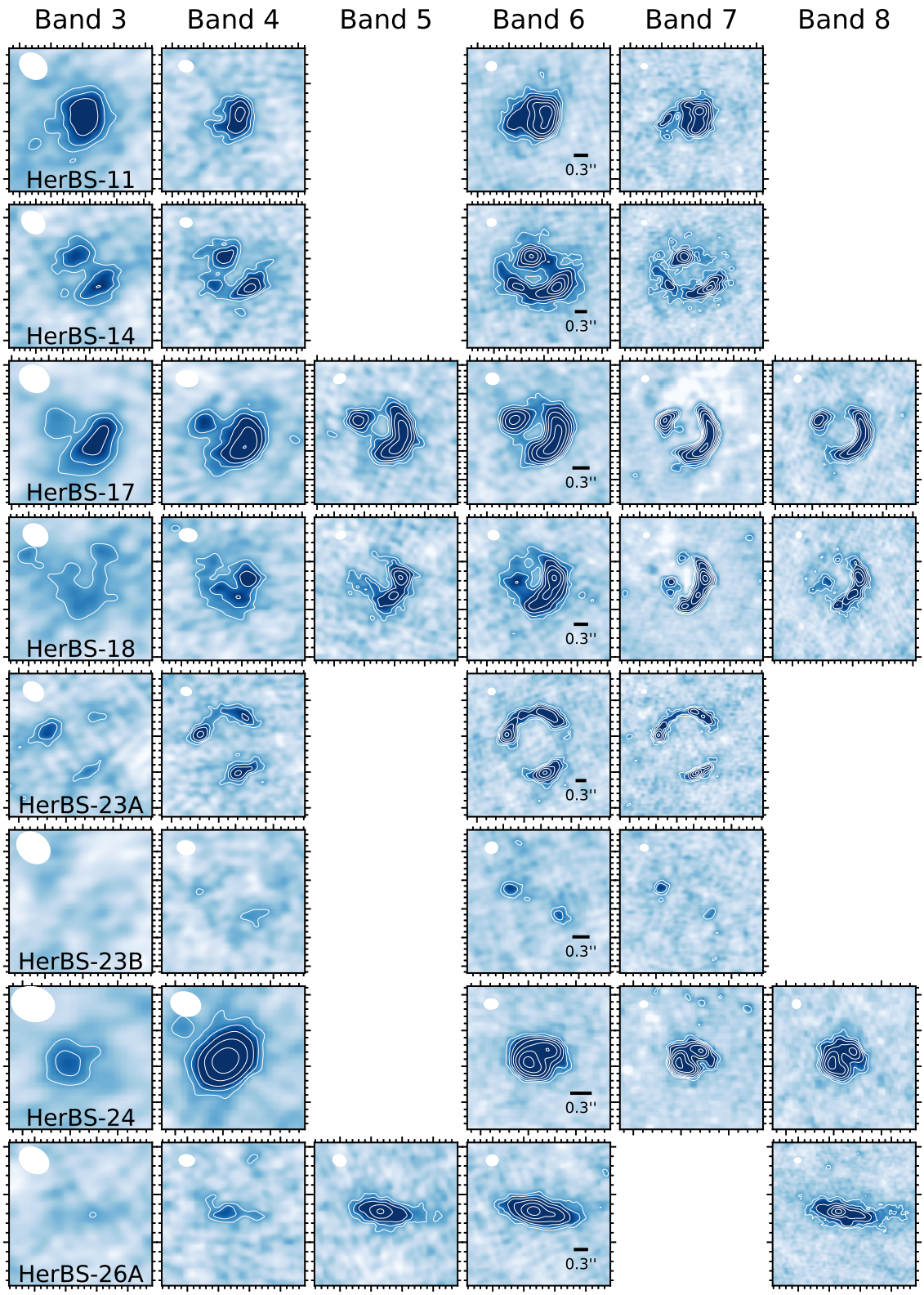

Figure C.1: Dust continua of eight galaxies across ALMA bands 3-8 (where available). White contours are included at SNR levels of 3, 5, 8 and beyond, following the Fibonacci sequence. A scale-bar at 0.3" is included in Band 6 to reflect the angular size of the respective galaxy (this scale-bar applies to all bands). In the top left, the ALMA beam size is shown as a white ellipse.

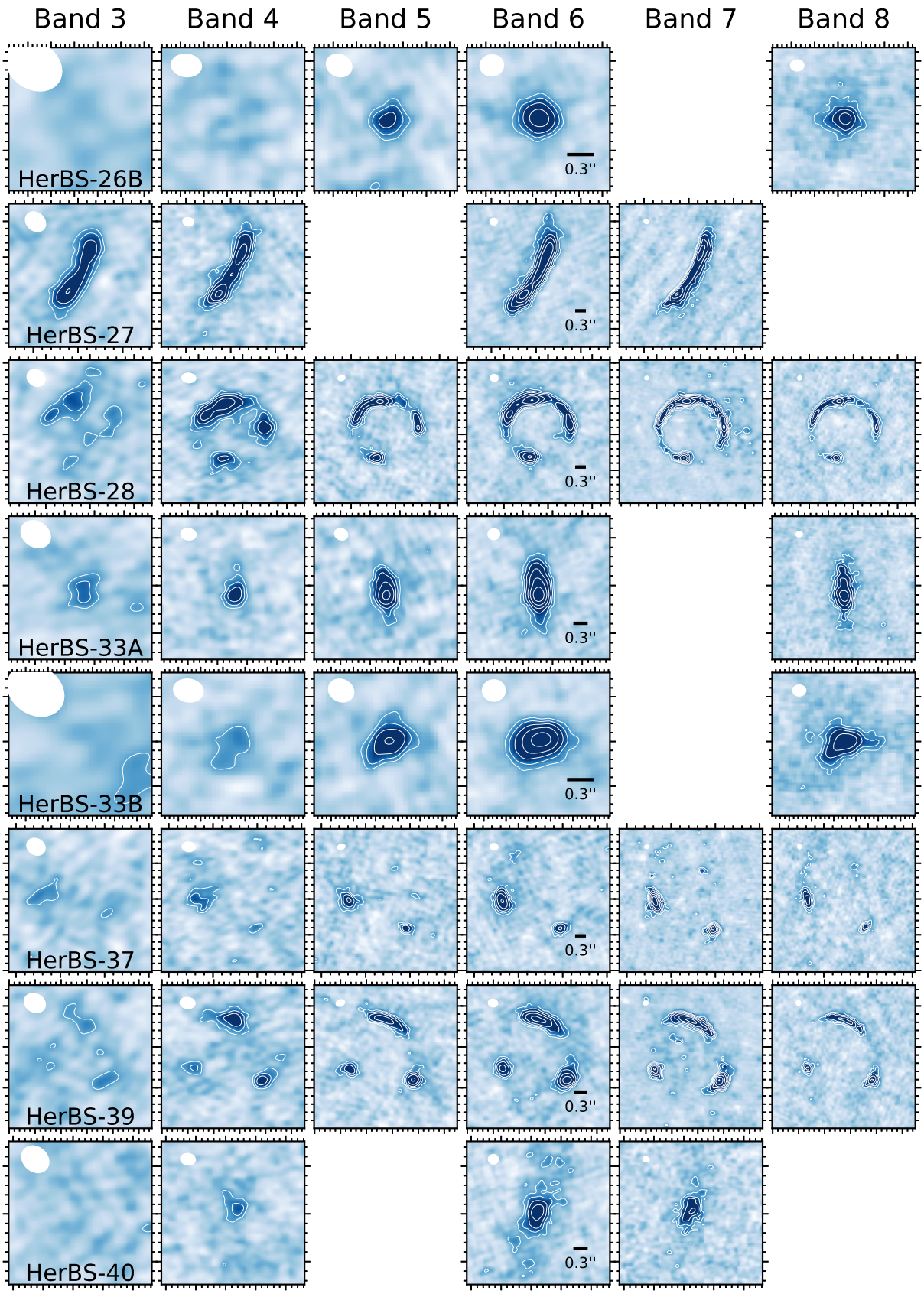

Figure C.1: (continuation).

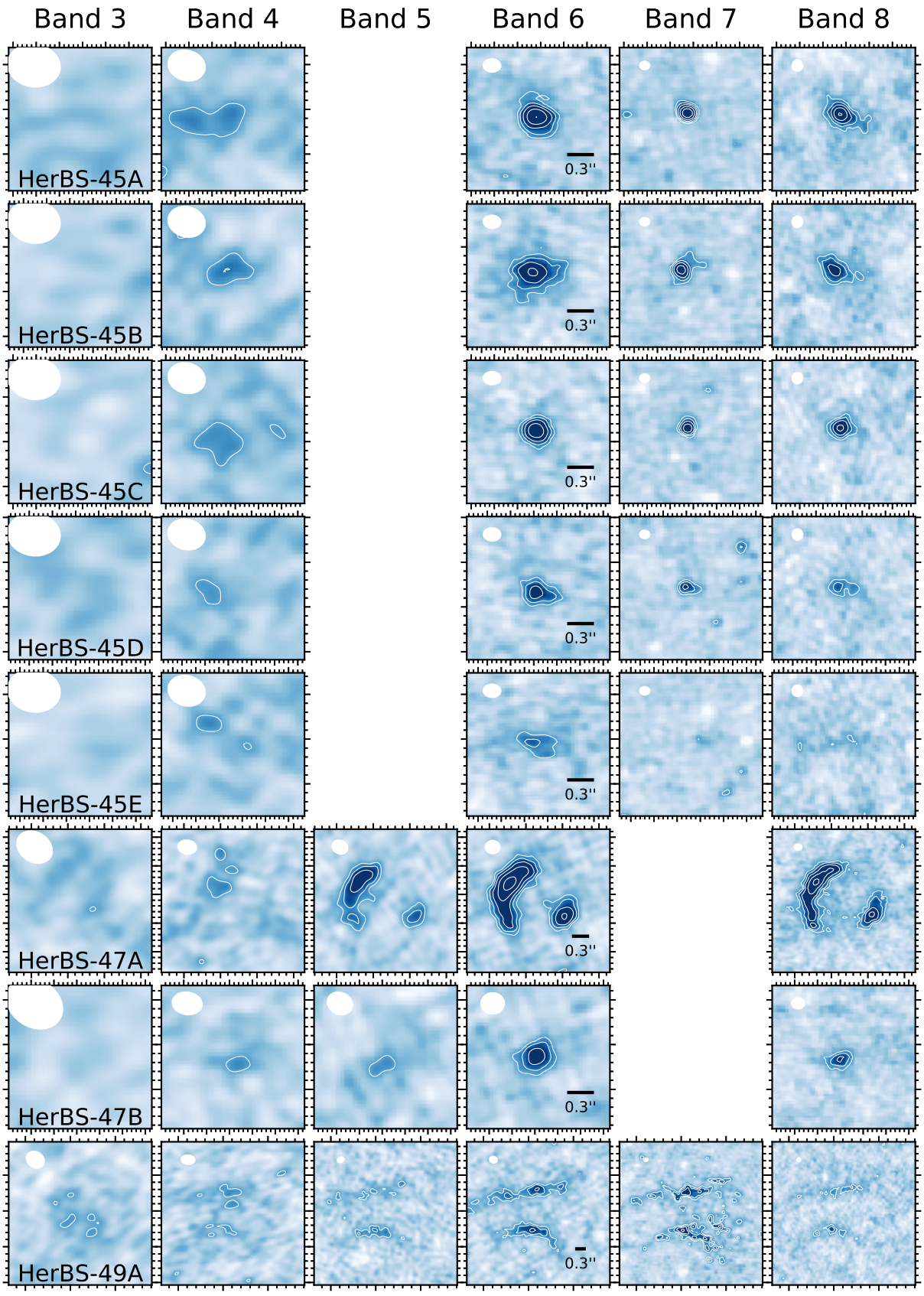

Figure C.1: (continuation).

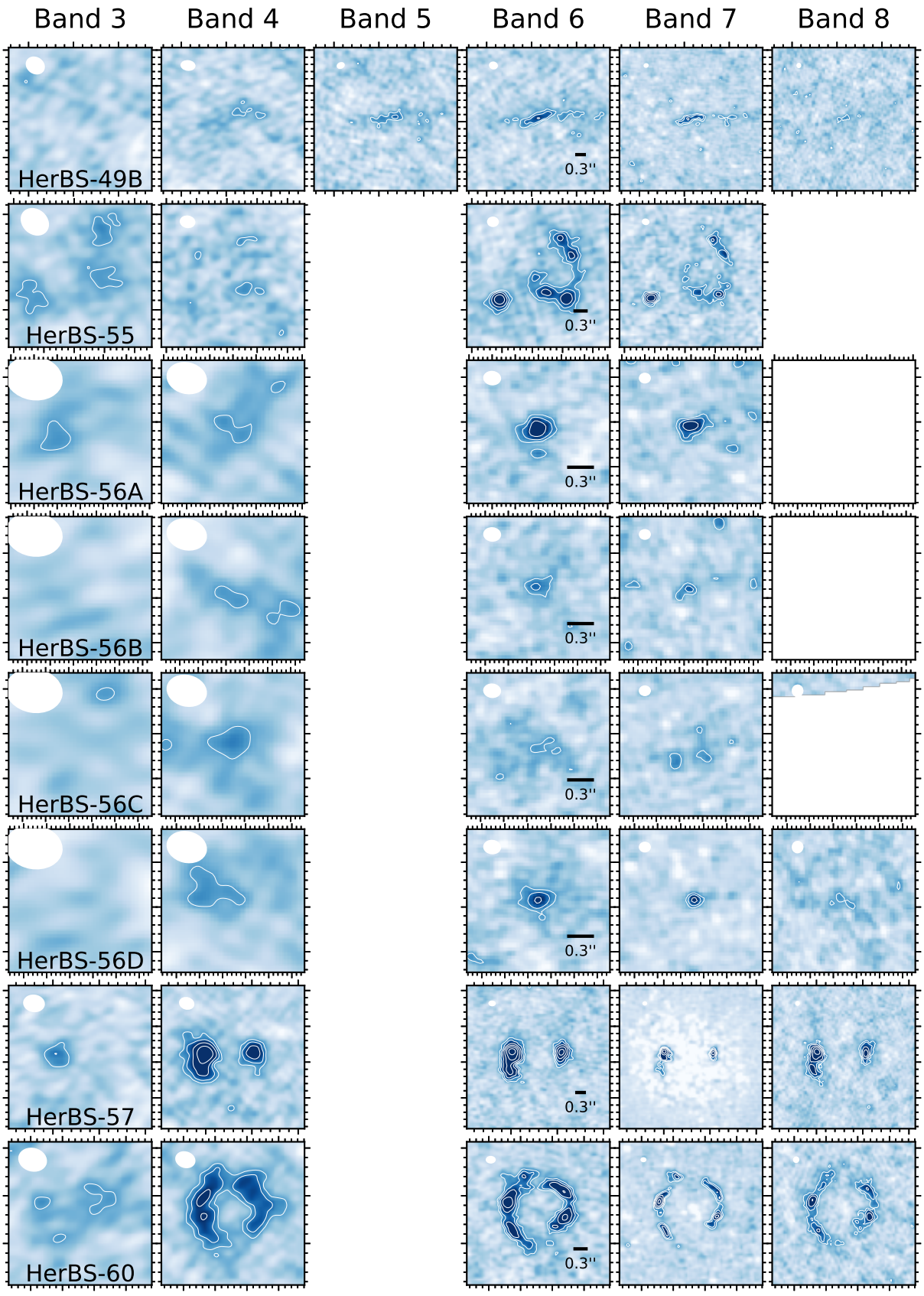

Figure C.1: (continuation).

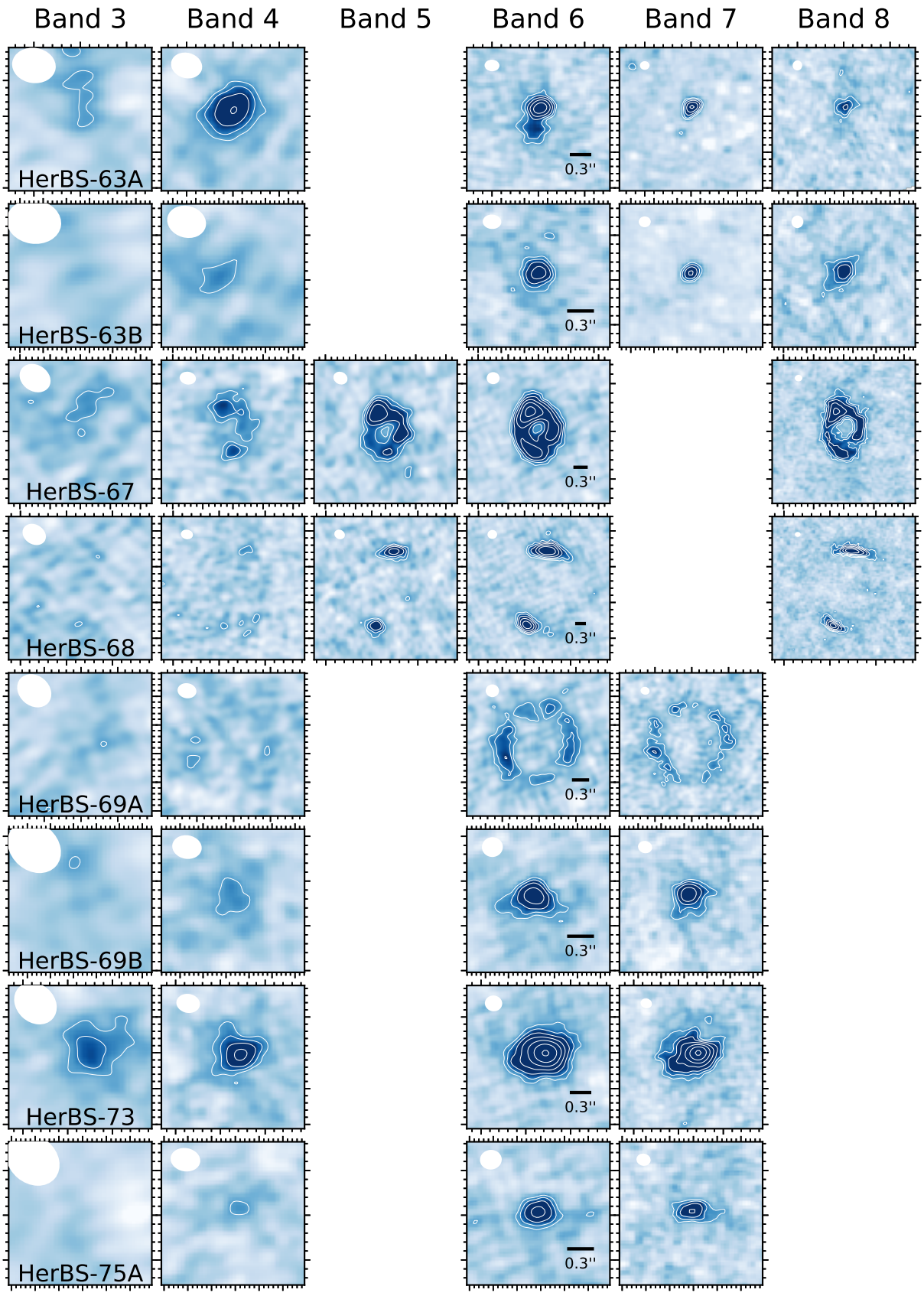

Figure C.1: (continuation).

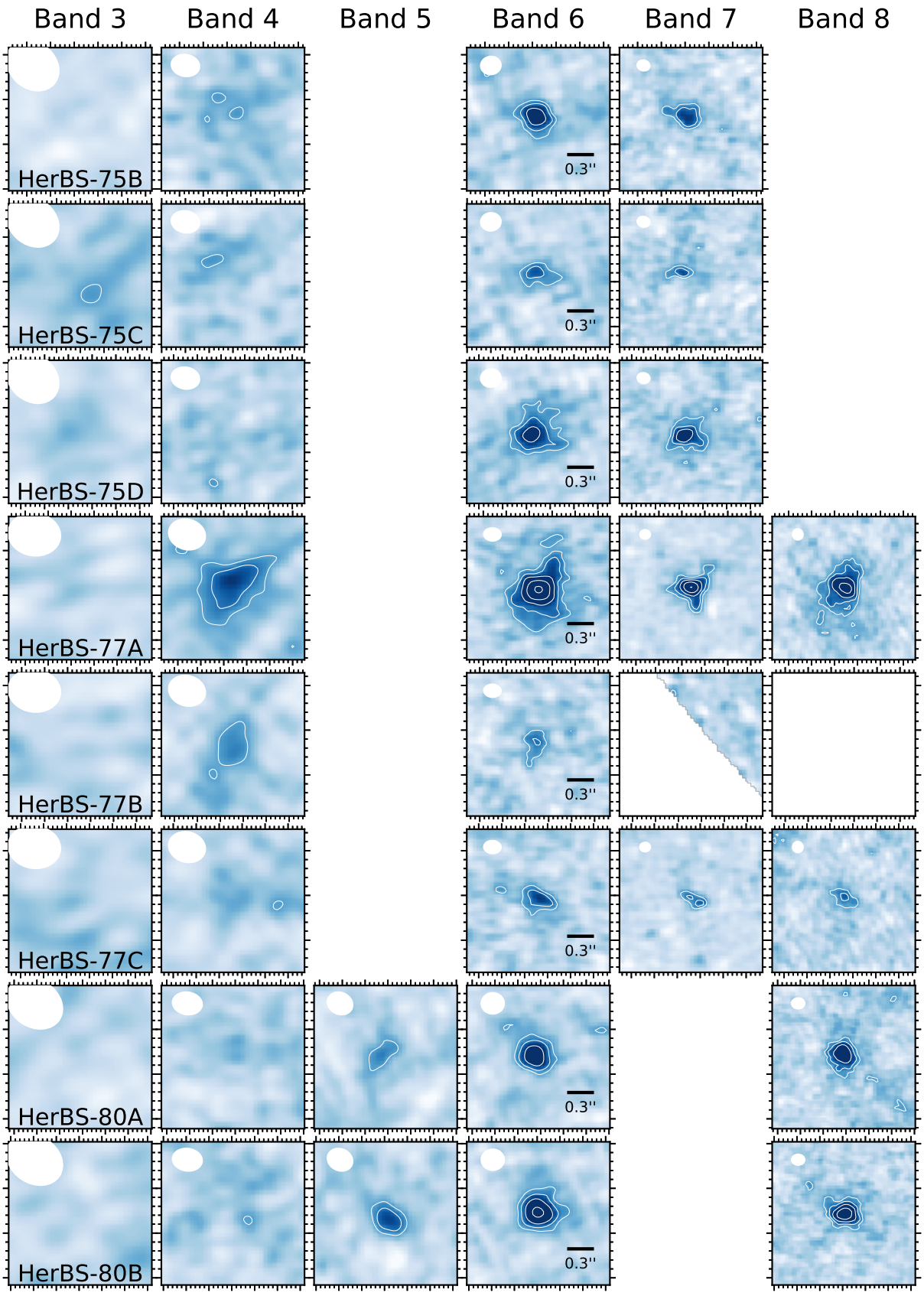

Figure C.1: (continuation).

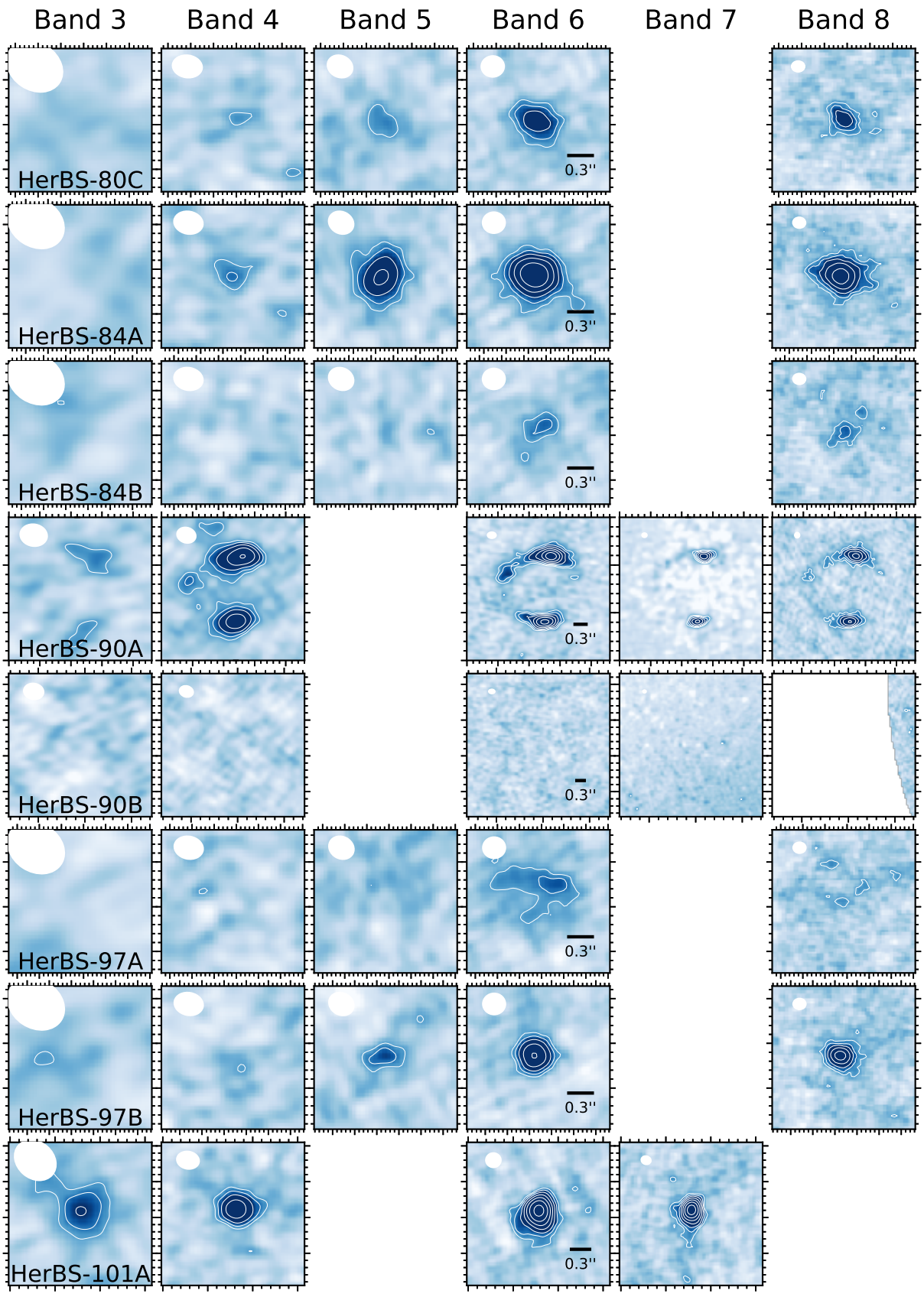

Figure C.1: (continuation). Source 90B is clearly undetected but included for completeness, since it is reported by Bendo et al. (2023).

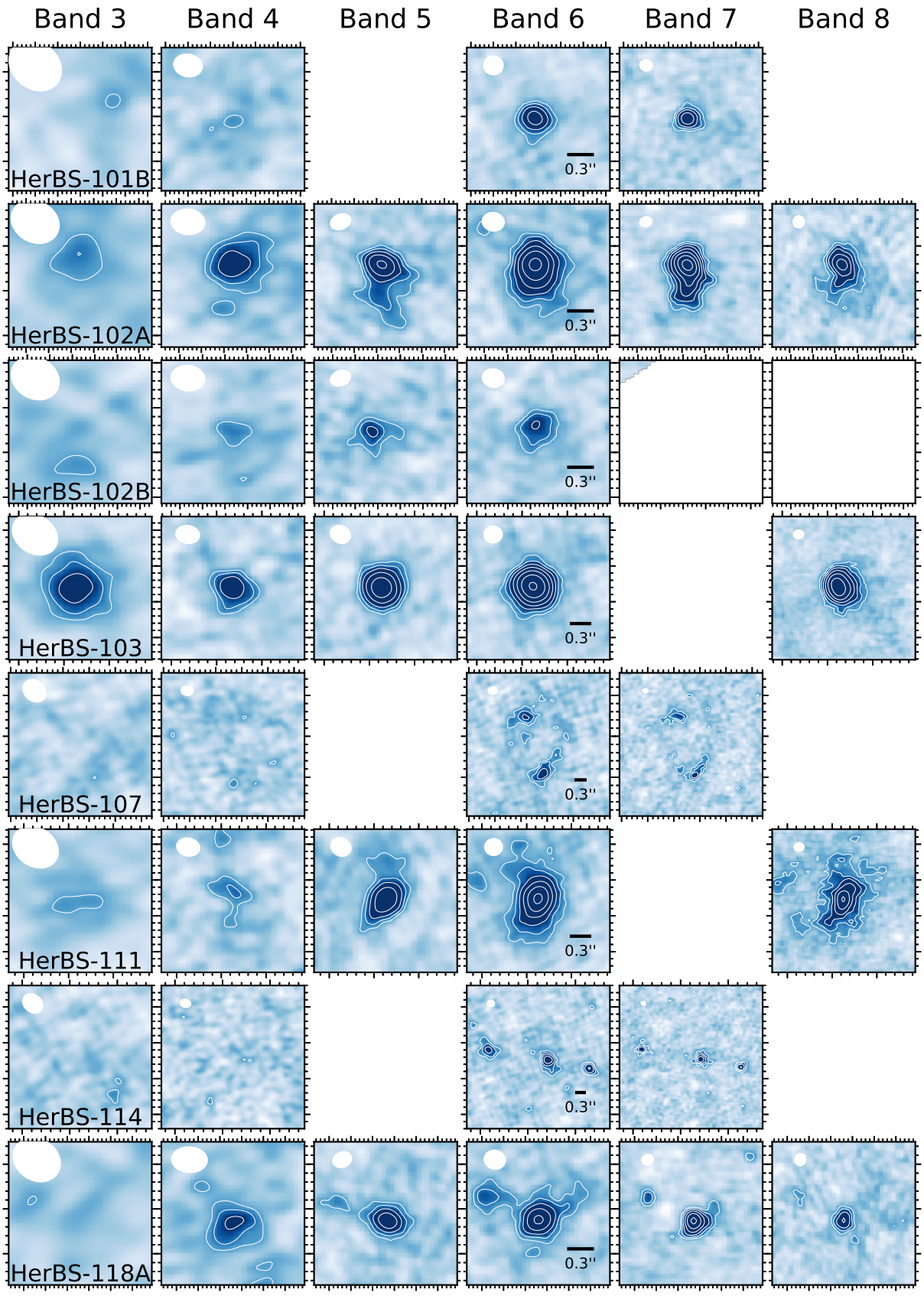

Figure C.1: (continuation).

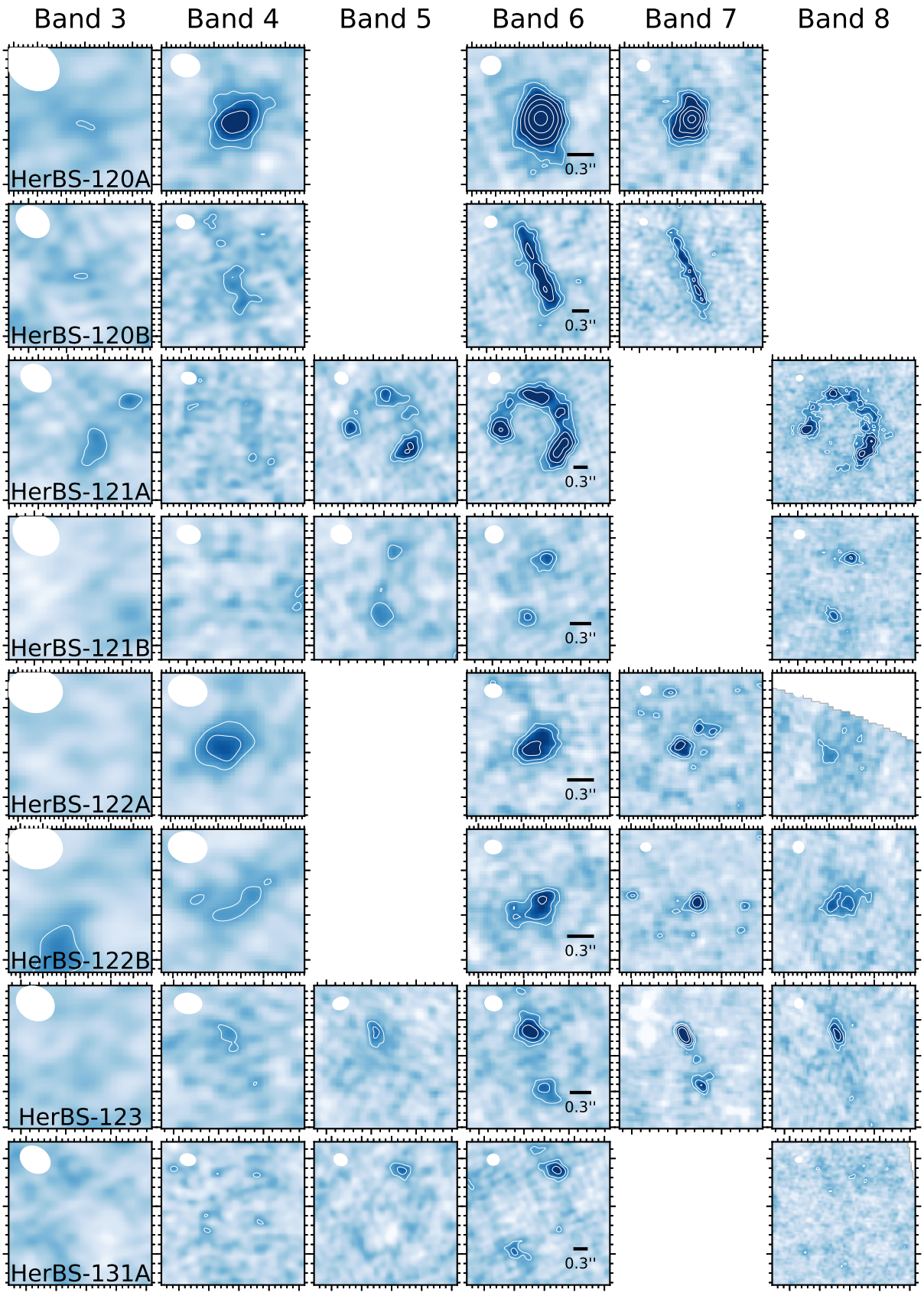

Figure C.1: (continuation).

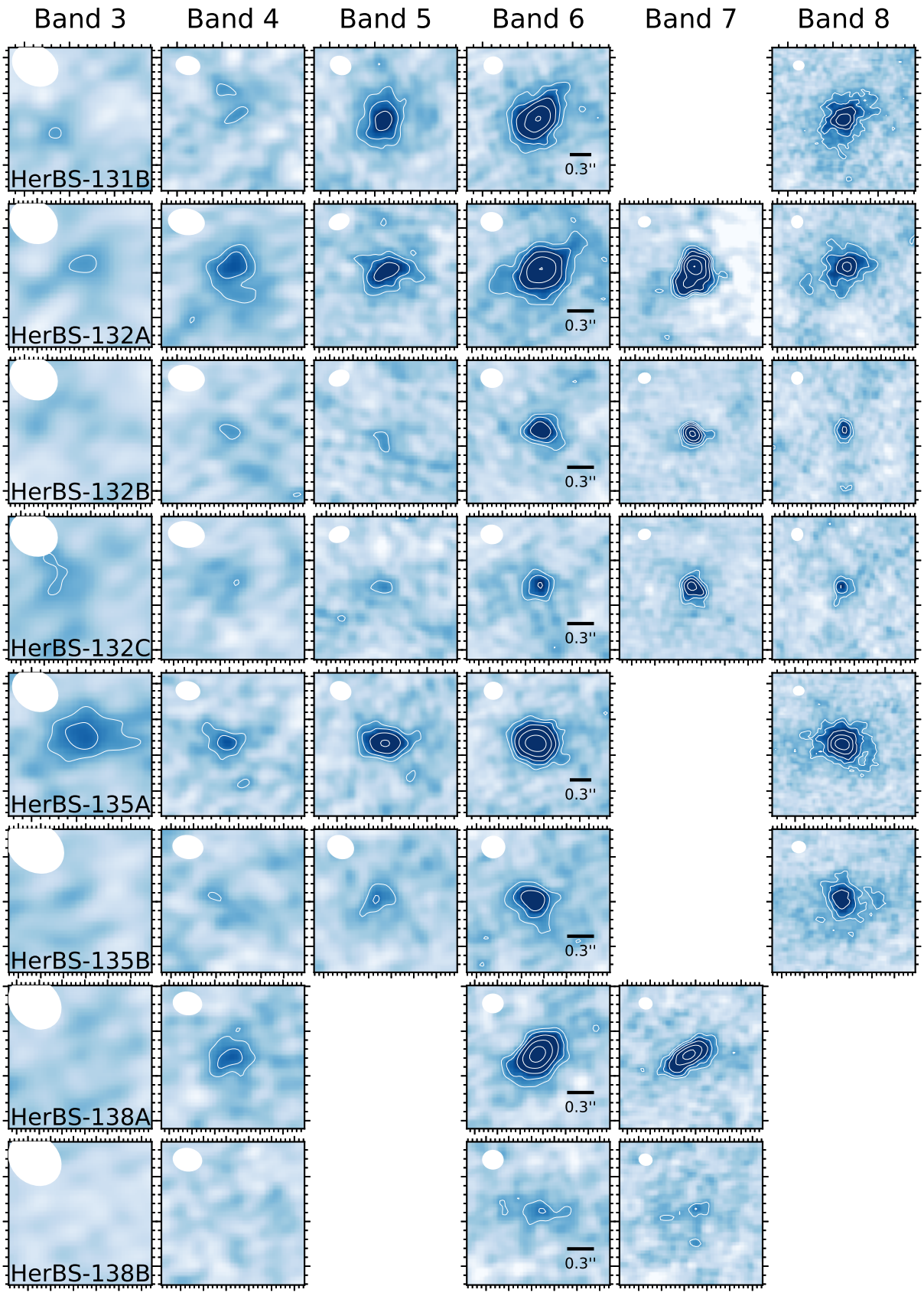

Figure C.1: (continuation).

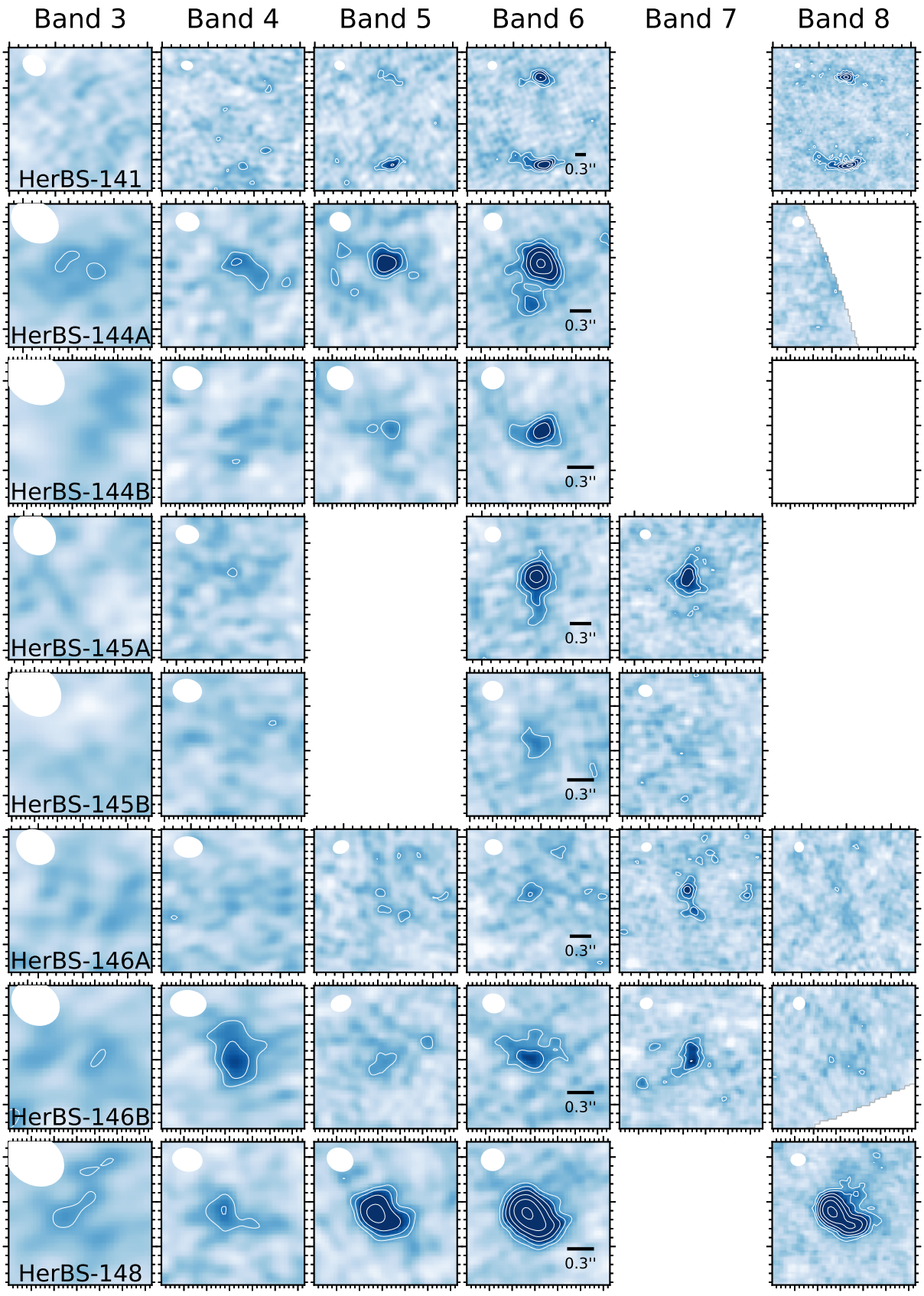

Figure C.1: (continuation).

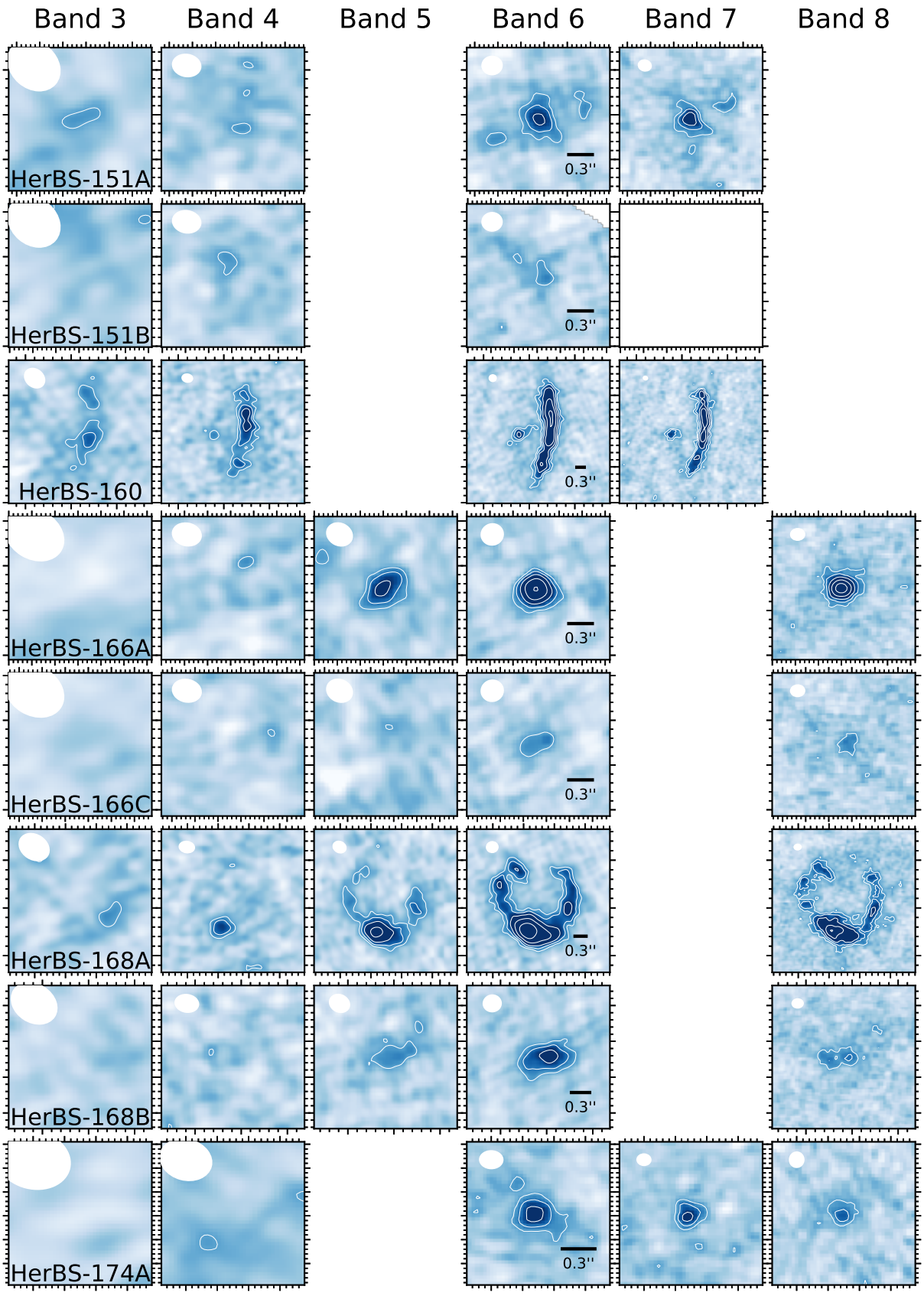

Figure C.1: (continuation).

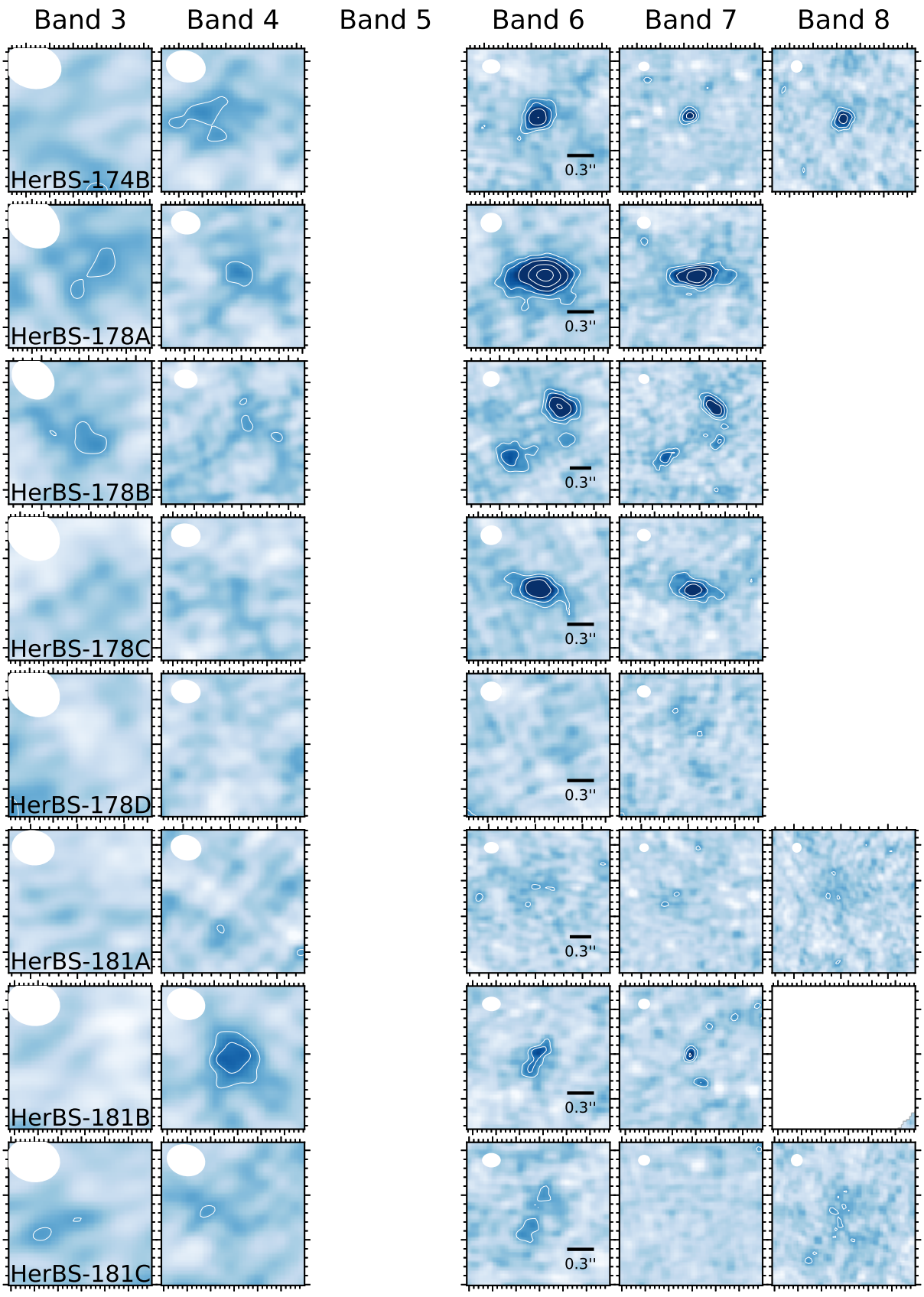

Figure C.1: (continuation). Sources 178D and 181A are clearly undetected but included for completeness, since they are reported by Bendo et al. (2023).

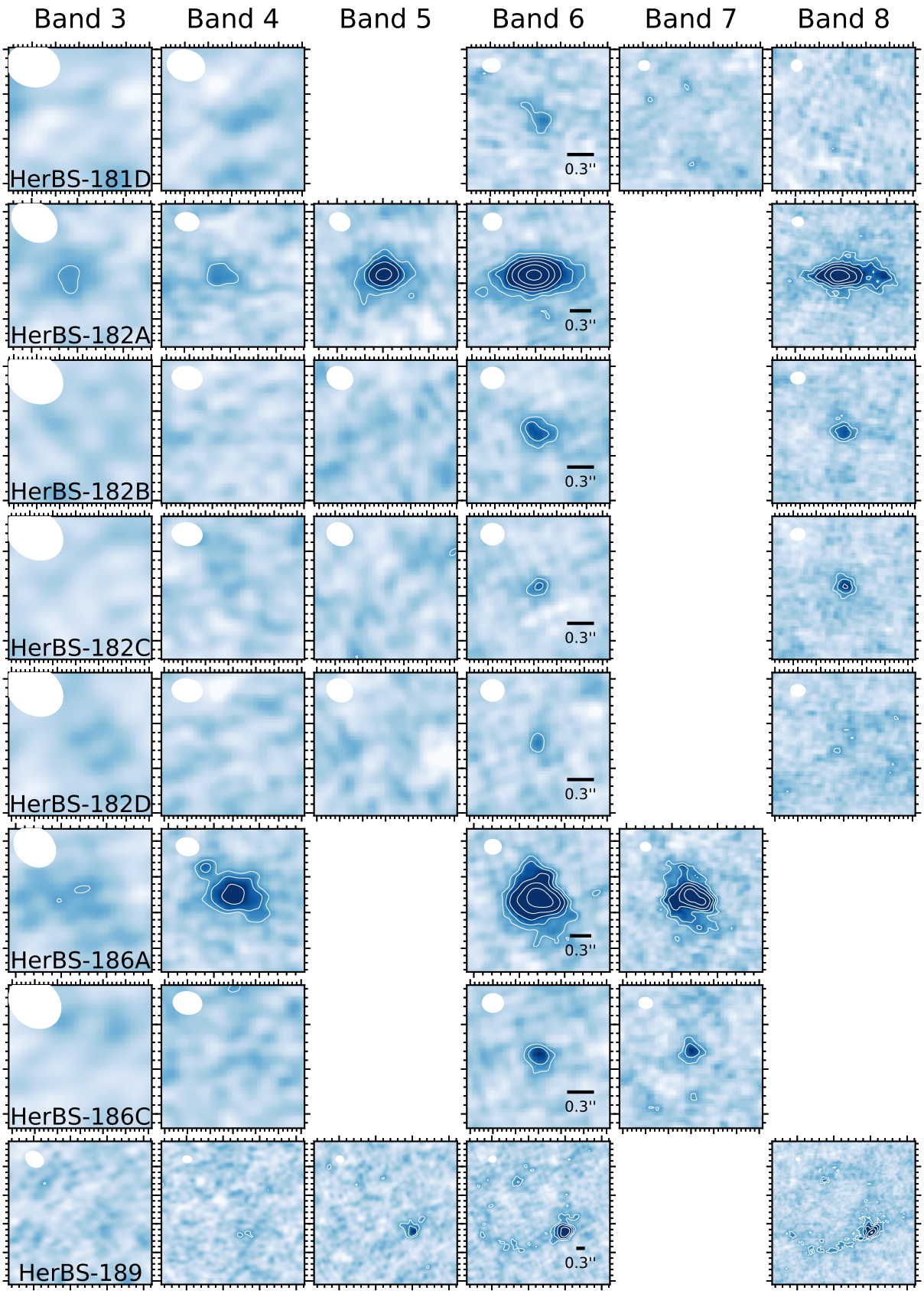

Figure C.1: (continuation).

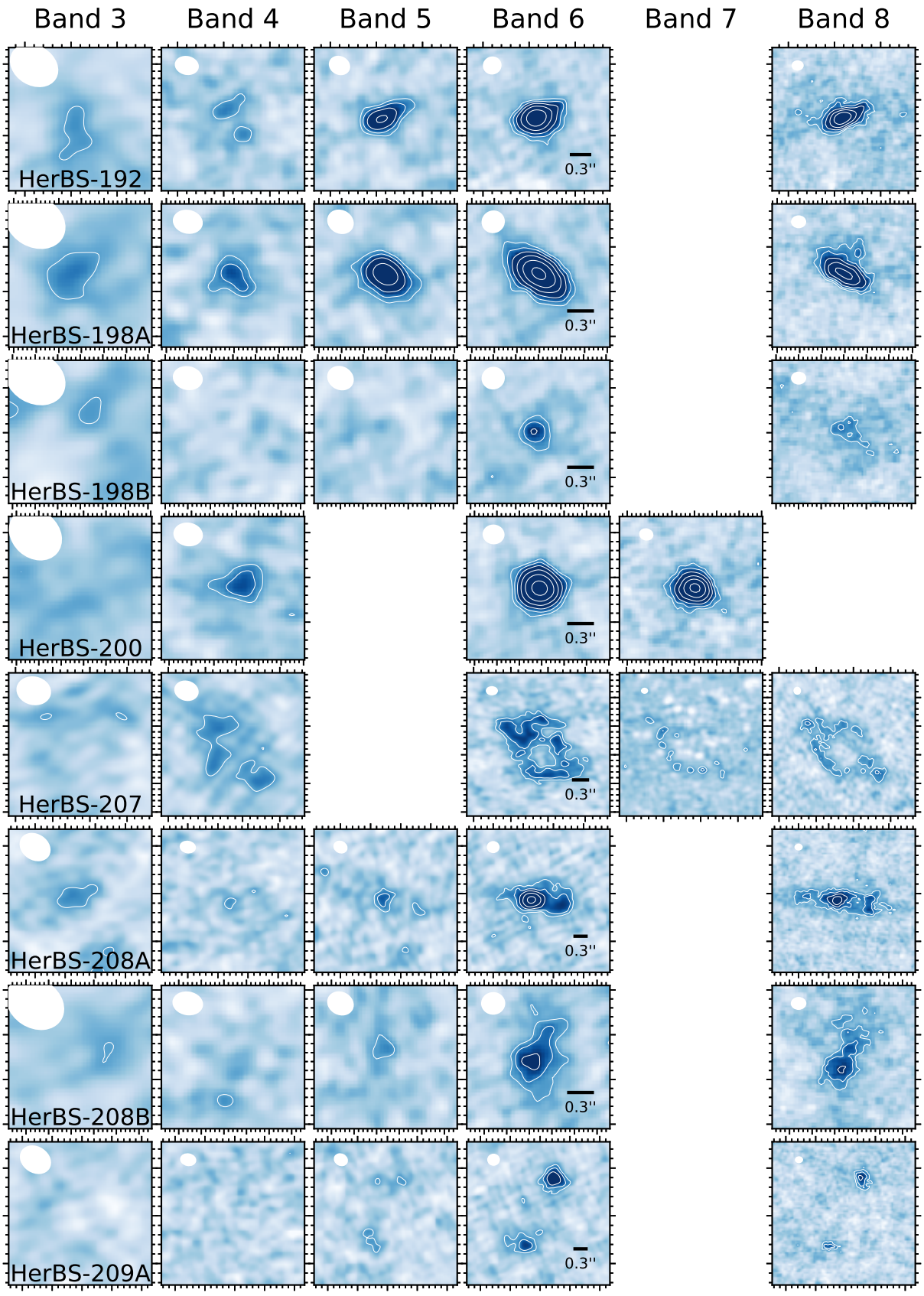

Figure C.1: (continuation).

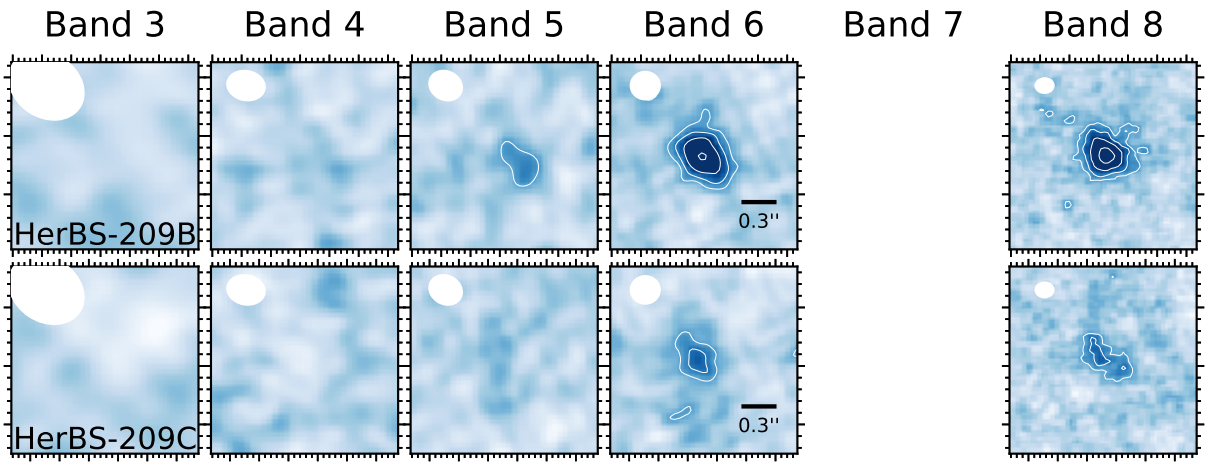

Figure C.1: (continuation).

D

Lines covered by ALMA

In Table D.1 I present all potential emission and absorption lines observed in each galaxy, based on their redshifts and the frequency ranges covered by the ALMA data across Bands 3-8. Naturally, only the 69 galaxies whose spectroscopic redshift is known are included in the table.

The search was done amongst the lines shown in Figure 2.8. Other lines that were considered are [NII]122μm, OH 119μm a, OH 119μm b, [OIII]88μm, and [OI]63μm. The specific frequency of each transition was taken from the database *Splatalogue* [1] (Remijan et al., 2007).

For some lines (mostly the low CO transitions relevant to this work), the total velocity-integrated flux, width and position are included, obtained as explained in Section 3.5.3 (Gaussian fit). In cases where no line is detected, an upper limit is estimated as follows. The area under a Gaussian curve can be calculated from its height h and Full Width at Half Maximum (FWHM) as

$$S\mathrm{d}V \approx 1.067 \times h \times \mathrm{FWHM}. \tag{D.1}$$

(Bevington & Robinson, 2003). For a 3σ detection, h can be estimated as

$$h = \frac{3\sigma}{\sqrt{N_{\mathrm{ch}}}}, \tag{D.2}$$

so that the upper limit is

$$S\mathrm{d}V < 1.067 \times \frac{3\sigma}{\sqrt{N_{\mathrm{ch}}}} \times \mathrm{FWHM}. \tag{D.3}$$

σ is the standard deviation of the spectrum, and N_{ch} is the number of velocity channels needed to cover the FWHM, i.e. $N_{\mathrm{ch}} = \mathrm{FWHM}/dv$ (dv is the channel width). The standard deviation is computed in the velocity range $-600 < v/(\mathrm{km\ s^{-1}}) < 600$. The FWHM of each galaxy are reported by Urquhart et al. (2022) (if not available, FWHM = 400 km s^{-1} is assumed).

[1] `https://splatalogue.online`

Table D.1: Potential spectral lines in the sample.

Line	Frequency [GHz]	Band	$S\mathrm{d}V$ [Jy km s^{-1}]	$\mathrm{d}V$ [km s^{-1}]	$V - V_{\mathrm{CO}}$ [km s^{-1}]
		HerBS-11 $z = 2.631$			
$\mathrm{CO}(3-2)$	95.234	Band 3	10.01 ± 0.85	382 ± 24	-44 ± 10
$\mathrm{OH^+}(1_0-0_1)$	250.357	Band 6			
$\mathrm{CO}(8-7)$	253.869	Band 6			
$\mathrm{OH^+}(1_2-0_1)$	267.641	Band 6			
$\mathrm{H_2O}(1_{1,1}-0_{0,0})$	306.622	Band 7			
$\mathrm{H_2O^+}$	307.119	Band 7			
		HerBS-14 $z = 3.782$			
$\mathrm{CO}(11-10)$	264.955	Band 6			
[NII]205μm	305.548	Band 7			
		HerBS-17 $z = 2.6101$			
$\mathrm{CO}(3-2)$	95.786	Band 3	7.32 ± 1.44	540 ± 80	56 ± 34
$\mathrm{CO}(6-5)$	191.538	Band 5			
$\mathrm{CH^+}(1-0)$	231.317	Band 6			
[NII]205μm	404.734	Band 8			
		HerBS-18 $z = 2.182$			
$\mathrm{CO}(3-2)$	108.673	Band 3	6.87 ± 0.9	253 ± 25	-98 ± 10
[CI]609μm	154.670	Band 4			
$\mathrm{CO}(6-5)$	217.308	Band 6			
		HerBS-23A $z = 4.39$			
$\mathrm{CO}(5-4)$	106.914	Band 3	5.07 ± 1.0	299 ± 44	-347 ± 19
$\mathrm{H_2O}(2_{1,1}-2_{0,2})$	139.524	Band 4			
$\mathrm{CO}(7-6)$	149.657	Band 4			
[CI]370μm	150.156	Band 4			
		HerBS-24 $z = 2.198$			
[CI]370μm	253.078	Band 6			
$\mathrm{CO}(8-7)$	288.243	Band 7			
		HerBS-26A $z = 3.157$			
$\mathrm{CO}(7-6)$	194.047	Band 5	4.66 ± 1.36	365 ± 80	343 ± 34
[CI]370μm	194.694	Band 5			
$\mathrm{OH^+}(1_2-0_1)$	233.775	Band 6			
$\mathrm{OH^+}(1_1-0_1)$	248.496	Band 6			
		HerBS-27 $z = 4.509$			
$\mathrm{CO}(5-4)$	104.605	Band 3	2.46 ± 0.82	428 ± 107	-64 ± 45
$\mathrm{H_2O}(2_{1,1}-2_{0,2})$	136.510	Band 4			
$\mathrm{CH^+}(1-0)$	151.584	Band 4			
$\mathrm{CO}(12-11)$	250.861	Band 6			
[NII]205μm	265.226	Band 6			
$\mathrm{CO}(14-13)$	292.575	Band 7			
		HerBS-28 $z = 3.925$			
$\mathrm{CO}(4-3)$	93.612	Band 3	5.66 ± 1.96	607 ± 158	-199 ± 469
$\mathrm{CO}(6-5)$	140.401	Band 4			

Table B.1: (continuation).

Line	Frequency [GHz]	Band	$S\mathrm{d}V$ [Jy km s^{-1}]	$\mathrm{d}V$ [km s^{-1}]	$V - V_{\mathrm{CO}}$ [km s^{-1}]
$H_2O(2_{1,1} - 2_{0,2})$	152.697	Band 4			
H_2O^+	231.379	Band 6			
		HerBS-33A $z = 2.9951$			
$CO(3 - 2)$	86.555	Band 3	2.85 ± 1.15	713 ± 217	405 ± 92
$CO(5 - 4)$	144.244	Band 4			
$CO(8 - 7)$	230.733	Band 6			
$H_2O(2_{0,2} - 1_{1,1})$	247.285	Band 6			
$CH^+(2 - 1)$	417.805	Band 8			
$CO(15 - 14)$	432.180	Band 8			
		HerBS-37 $z = 2.619$			
$CO(3 - 2)$	95.550	Band 3	6.41 ± 1.98	681 ± 156	137 ± 68
$CO(6 - 5)$	191.067	Band 5			
$CH^+(1 - 0)$	230.749	Band 6			
		HerBS-39 $z = 3.229$			
$CO(4 - 3)$	109.019	Band 3	4.97 ± 1.36	288 ± 62	-14 ± 24
$CO(7 - 6)$	190.743	Band 5			
[CI]370μm	191.379	Band 5			
$OH^+(1_0 - 0_1)$	214.955	Band 6			
$CO(8 - 7)$	217.971	Band 6			
$OH^+(1_2 - 0_1)$	229.795	Band 6			
$CH^+(2 - 1)$	394.697	Band 8			
		HerBS-40 $z = 1.971$			
$H_2O(2_{1,1} - 2_{0,2})$	253.125	Band 6			
$OH^+(1_0 - 0_1)$	305.973	Band 7			
		HerBS-45A $z = 2.434$			
$CO(8 - 7)$	268.433	Band 6			
$H_2O(2_{0,2} - 1_{1,1})$	287.690	Band 7			
$OH^+(1_1 - 0_1)$	300.815	Band 7			
$CO(9 - 8)$	301.955	Band 7			
$CO(12 - 11)$	402.445	Band 8			
		HerBS-47A $z = 2.433$			
$CO(3 - 2)$	100.727	Band 3	3.99 ± 0.95	282 ± 50	-40 ± 21
$CO(4 - 3)$	134.297	Band 4			
		HerBS-49A $z = 2.724$			
$CO(5 - 4)$	154.744	Band 4	4.67 ± 1.12	141 ± 25	5 ± 10
$CO(7 - 6)$	216.609	Band 6			
[CI]370μm	217.331	Band 6			
[NII]205μm	392.355	Band 8			
		HerBS-49B $z = 2.730$			
$CO(5 - 4)$	154.495	Band 4	< 4.53		
$CO(7 - 6)$	216.261	Band 6			
[CI]370μm	216.982	Band 6			
		HerBS-55 $z = 2.656$			

Table B.1: (continuation).

Line	Frequency [GHz]	Band	$S\mathrm{d}V$ [Jy km s^{-1}]	dV [km s^{-1}]	$V - V_{\mathrm{CO}}$ [km s^{-1}]
$\mathrm{CO}(3-2)$	94.583	Band 3	4.22 ± 1.13	521 ± 105	30 ± 44
$\mathrm{CO}(8-7)$	252.133	Band 6			
$\mathrm{OH^+}(1_2 - 0_1)$	265.811	Band 6			
$\mathrm{H_2O}(1_{1,1} - 0_{0,0})$	304.525	Band 7			
$\mathrm{H_2O^+}$	305.019	Band 7			
		HerBS-56C $z = 2.561$			
$\mathrm{CO}(3-2)$	97.106	Band 3	1.42 ± 0.58	312 ± 96	-137 ± 41
$\mathrm{CO}(5-4)$	161.828	Band 4			
$\mathrm{OH^+}(1_0 - 0_1)$	255.278	Band 6			
$\mathrm{OH^+}(1_1 - 0_1)$	290.087	Band 7			
		HerBS-57 $z = 3.265$			
$\mathrm{CO}(6-5)$	162.127	Band 4			
$\mathrm{H_2O^+}$	267.184	Band 6			
$\mathrm{CO}(10-9)$	270.102	Band 6			
$\mathrm{HF}(1-0)$	288.974	Band 7			
$\mathrm{CO}(15-14)$	404.831	Band 8			
		HerBS-60 $z = 3.261$			
$\mathrm{CO}(6-5)$	162.280	Band 4			
$\mathrm{H_2O^+}$	267.435	Band 6			
$\mathrm{CO}(10-9)$	270.356	Band 6			
$\mathrm{HF}(1-0)$	289.246	Band 7			
$\mathrm{CO}(15-14)$	405.211	Band 8			
		HerBS-63A $z = 2.432$			
$\mathrm{CO}(8-7)$	268.590	Band 6			
$\mathrm{H_2O}(2_{0,2} - 1_{1,1})$	287.857	Band 7			
$\mathrm{OH^+}(1_1 - 0_1)$	300.990	Band 7			
$\mathrm{CO}(9-8)$	302.131	Band 7			
$\mathrm{CO}(12-11)$	402.679	Band 8			
		HerBS-67 $z = 3.71$			
$\mathrm{CO}(6-5)$	146.810	Band 4			
$\mathrm{OH^+}(1_0 - 0_1)$	193.003	Band 5			
$\mathrm{OH^+}(1_2 - 0_1)$	206.328	Band 5			
$\mathrm{H_2O}(3_{1,2} - 3_{0,3})$	232.986	Band 6			
$\mathrm{H_2O}(3_{2,1} - 3_{1,2})$	246.903	Band 6			
		HerBS-68 $z = 2.719$			
[CI]609μm	132.337	Band 4			
$\mathrm{CO}(8-7)$	247.862	Band 6			
		HerBS-69A $z = 2.075$			
$\mathrm{CO}(4-3)$	149.932	Band 4	5.65 ± 5.74	472 ± 467	-24 ± 59
		HerBS-69B $z = 2.073$			
$\mathrm{CO}(4-3)$	150.030	Band 4	1.75 ± 0.86	313 ± 116	13 ± 50
		HerBS-73 $z = 3.026$			
$\mathrm{HF}(1-0)$	306.129	Band 7			

Table B.1: (continuation).

Line	Frequency [GHz]	Band	$S\mathrm{d}V$ [Jy km s^{-1}]	$\mathrm{d}V$ [km s^{-1}]	$V - V_{\mathrm{CO}}$ [km s^{-1}]
		HerBS-77A $z = 2.228$			
$OH^+(1_2 - 0_1)$	301.054	Band 7			
		HerBS-80A $z = 2.231$			
$H_2O(2_{1,1} - 2_{0,2})$	232.756	Band 6			
		HerBS-80B $z = 1.968$			
$CO(5 - 4)$	194.160	Band 5	1.84 ± 1.04	471 ± 225	-127 ± 70
$CO(6 - 5)$	232.976	Band 6			
		HerBS-84A $z = 2.5178$			
$CO(3 - 2)$	98.299	Band 3	2.14 ± 0.97	642 ± 221	-157 ± 92
		HerBS-90A $z = 3.992$			
[CI]609μm	98.590	Band 3			
$H_2O(2_{1,1} - 2_{0,2})$	150.648	Band 4			
$CO(7 - 6)$	161.589	Band 4			
[CI]370μm	162.128	Band 4			
$CO(11 - 10)$	253.809	Band 6			
$CO(13 - 12)$	299.864	Band 7			
$CO(18 - 17)$	414.787	Band 8			
		HerBS-101A or HerBS-101B $z = 2.0269$			
$CO(7 - 6)$	266.494	Band 6			
[CI]370μm	267.383	Band 6			
$CO(8 - 7)$	304.536	Band 7			
		HerBS-102A $z = 3.287$			
$CO(4 - 3)$	107.544	Band 3	3.65 ± 1.02	375 ± 79	-43 ± 33
$CO(8 - 7)$	215.022	Band 6			
$H_2O(2_{0,2} - 1_{1,1})$	230.447	Band 6			
		HerBS-103 $z = 2.942$			
$CO(3 - 2)$	87.721	Band 3	2.70 ± 0.92	550 ± 142	212 ± 60
$CO(5 - 4)$	146.187	Band 4			
$CO(7 - 6)$	204.630	Band 5			
[CI]370μm	205.313	Band 5			
$OH^+(1_0 - 0_1)$	230.605	Band 6			
$CO(8 - 7)$	233.841	Band 6			
$OH^+(1_2 - 0_1)$	246.526	Band 6			
		HerBS-107 $z = 2.553$			
[CI]609μm	138.520	Band 4			
		HerBS-111 $z = 2.371$			
[CI]609μm	145.998	Band 4			
$CO(6 - 5)$	205.124	Band 5			
$CH^+(1 - 0)$	247.724	Band 6			
		HerBS-114 $z = 2.3017$			
$CO(3 - 2)$	104.733	Band 3	< 2.00		
$CO(4 - 3)$	139.637	Band 4			
[CI]609μm	149.063	Band 4			

Table B.1: (continuation).

Line	Frequency [GHz]	Band	$S\mathrm{d}V$ [Jy km s^{-1}]	$\mathrm{d}V$ [km s^{-1}]	$V - V_{\mathrm{CO}}$ [km s^{-1}]
$CH^+(1-0)$	252.924	Band 6			
$OH^+(1_2-0_1)$	294.334	Band 7			
HerBS-118A or HerBS-118B $z = 4.0923$					
[CI]609μm	96.648	Band 3			
$OH^+(1_2-0_1)$	190.838	Band 5			
$H_2O(2_{0,2}-1_{1,1})$	194.004	Band 5			
$OH^+(1_1-0_1)$	202.855	Band 5			
$CO(9-8)$	203.624	Band 5			
$H_2O(3_{1,2}-3_{0,3})$	215.495	Band 6			
[OI]145μm	404.546	Band 8			
$CO(18-17)$	406.617	Band 8			
HerBS-120A $z = 3.125$					
$CO(5-4)$	139.701	Band 4	0.98 ± 0.56	336 ± 146	258 ± 62
$OH^+(1_1-0_1)$	250.424	Band 6			
$CO(9-8)$	251.373	Band 6			
$H_2O(3_{1,2}-3_{0,3})$	266.028	Band 6			
$CO(11-10)$	307.155	Band 7			
HerBS-120B $z = 3.124$					
$CO(5-4)$	139.735	Band 4	3.26 ± 1.35	500 ± 157	0 ± 66
$OH^+(1_1-0_1)$	250.485	Band 6			
$CO(9-8)$	251.434	Band 6			
$H_2O(3_{1,2}-3_{0,3})$	266.092	Band 6			
$CO(11-10)$	307.230	Band 7			
HerBS-121A $z = 3.741$					
$CO(6-5)$	145.850	Band 4			
$OH^+(1_0-0_1)$	191.741	Band 5			
$CO(8-7)$	194.431	Band 5			
$OH^+(1_2-0_1)$	204.979	Band 5			
$H_2O(3_{1,2}-3_{0,3})$	231.463	Band 6			
$H_2O(3_{2,1}-3_{1,2})$	245.288	Band 6			
HerBS-122A $z = 2.883$					
$CO(5-4)$	148.408	Band 4	1.73 ± 0.49	259 ± 55	-17 ± 23
$H_2O(2_{0,2}-1_{1,1})$	254.424	Band 6			
$CO(9-8)$	267.039	Band 6			
$H_2O(1_{1,1}-0_{0,0})$	286.722	Band 7			
H_2O^+	287.188	Band 7			
$H_2O(3_{2,1}-3_{1,2})$	299.488	Band 7			
$CO(14-13)$	415.090	Band 8			
HerBS-123 $z = 2.17$					
$CO(3-2)$	109.084	Band 3	1.44 ± 0.64	148 ± 53	54 ± 20
[CI]609μm	155.256	Band 4			
$CO(6-5)$	218.130	Band 6			
HerBS-131B $z = 2.197$					

Table B.1: (continuation).

Line	Frequency [GHz]	Band	$S\mathrm{d}V$ [Jy km s^{-1}]	$\mathrm{d}V$ [km s^{-1}]	$V - V_{\mathrm{CO}}$ [km s^{-1}]
$\mathrm{CO}(4-3)$	144.210	Band 4	< 3.34		
$\mathrm{CO}(12-11)$	432.279	Band 8			
		HerBS-132A $z = 2.473$			
[CI]609μm	141.711	Band 4			
$\mathrm{H_2O}(2_{1,1}-2_{0,2})$	216.537	Band 6			
$\mathrm{CO}(7-6)$	232.264	Band 6			
[CI]370μm	233.038	Band 6			
		HerBS-135A $z = 2.401$			
$\mathrm{CO}(3-2)$	101.675	Band 3	2.92 ± 1.07	504 ± 139	395 ± 59
[CI]609μm	144.711	Band 4			
$\mathrm{CO}(6-5)$	203.315	Band 5			
$\mathrm{CH^+}(1-0)$	245.539	Band 6			
[NII]205μm	429.618	Band 8			
		HerBS-138B $z = 1.407$			
$\mathrm{CO}(2-1)$	95.778	Band 3	1.53 ± 0.50	168 ± 41	58 ± 17
		HerBS-141 $z = 2.085$			
-					
		HerBS-144A $z = 2.42$			
$\mathrm{CO}(3-2)$	101.110	Band 3	3.19 ± 0.75	248 ± 44	80 ± 18
$\mathrm{CO}(4-3)$	134.807	Band 4			
[CI]609μm	143.907	Band 4			
		HerBS-145A $z = 2.730$			
$\mathrm{CO}(3-2)$	92.707	Band 3	1.58 ± 1.19	941 ± 589	74 ± 191
$\mathrm{H_2O}(2_{0,2}-1_{1,1})$	264.860	Band 6			
$\mathrm{H_2O}(3_{1,2}-3_{0,3})$	294.200	Band 7			
$\mathrm{H_2O^+}$	305.507	Band 7			
		HerBS-146B $z = 2.003$			
$\mathrm{CO}(4-3)$	153.527	Band 4	2.93 ± 0.92	374 ± 89	27 ± 37
$\mathrm{CO}(5-4)$	191.897	Band 5			
$\mathrm{CO}(6-5)$	230.261	Band 6			
		HerBS-148 $z = 3.0876$			
$\mathrm{CH^+}(1-0)$	204.296	Band 5			
		HerBS-160 $z = 3.955$			
$\mathrm{CO}(4-3)$	93.046	Band 3	3.15 ± 1.12	429 ± 115	91 ± 49
$\mathrm{CO}(6-5)$	139.551	Band 4			
$\mathrm{H_2O}(2_{1,1}-2_{0,2})$	151.773	Band 4			
[NII]205μm	294.880	Band 7			
		HerBS-168A $z = 2.583$			
$\mathrm{CO}(6-5)$	192.987	Band 5			
$\mathrm{CH^+}(1-0)$	233.067	Band 6			
$\mathrm{CO}(13-12)$	417.785	Band 8			
		HerBS-174A or HerBS-174B $z = 1.6669$			
$\mathrm{H_2O}(1_{1,1}-0_{0,0})$	417.467	Band 8			

Table B.1: (continuation).

Line	Frequency [GHz]	Band	$S\mathrm{d}V$ [Jy km s^{-1}]	$\mathrm{d}V$ [km s^{-1}]	$V - V_{\mathrm{CO}}$ [km s^{-1}]
		HerBS-178A $z = 2.658$			
$\mathrm{CO}(3-2)$	94.531	Band 3	1.31 ± 0.67	456 ± 175	-166 ± 74
$\mathrm{CO}(8-7)$	251.996	Band 6			
$\mathrm{OH^+}(1_2 - 0_1)$	265.665	Band 6			
$\mathrm{H_2O}(1_{1,1} - 0_{0,0})$	304.358	Band 7			
$\mathrm{H_2O^+}$	304.853	Band 7			
		HerBS-178B $z = 2.655$			
$\mathrm{CO}(3-2)$	94.609	Band 3	1.19 ± 0.54	247 ± 84	249 ± 8063
$\mathrm{CO}(8-7)$	252.202	Band 6			
$\mathrm{OH^+}(1_2 - 0_1)$	265.883	Band 6			
$\mathrm{H_2O}(1_{1,1} - 0_{0,0})$	304.608	Band 7			
$\mathrm{H_2O^+}$	305.103	Band 7			
		HerBS-178C $z = 2.656$			
$\mathrm{CO}(3-2)$	94.583	Band 3	1.16 ± 1.04	855 ± 580	-212 ± 246
$\mathrm{CO}(8-7)$	252.133	Band 6			
$\mathrm{OH^+}(1_2 - 0_1)$	265.811	Band 6			
$\mathrm{H_2O}(1_{1,1} - 0_{0,0})$	304.525	Band 7			
$\mathrm{H_2O^+}$	305.019	Band 7			
	HerBS-181A, HerBS-181B, HerBS-181C or HerBS-181D $z = 1.524$				
-					
		HerBS-182A $z = 2.227$			
$\mathrm{H_2O}(2_{1,1} - 2_{0,2})$	233.044	Band 6			
	HerBS-186A, HerBS-186B or HerBS-186C $z = 3.1701$				
$\mathrm{CO}(5-4)$	138.190	Band 4			
$\mathrm{H_2O}(1_{1,1} - 0_{0,0})$	266.982	Band 6			
$\mathrm{H_2O^+}$	267.416	Band 6			
$\mathrm{HF}(1-0)$	295.551	Band 7			
		HerBS-189 $z = 3.300$			
$\mathrm{CO}(5-4)$	134.016	Band 4	7.45 ± 2.67	236 ± 64	-94 ± 27
$\mathrm{CH^+}(1-0)$	194.204	Band 5			
		HerBS-192 $z = 2.4037$			
$\mathrm{CO}(3-2)$	101.594	Band 3	1.69 ± 1.31	805 ± 475	160 ± 196
$\mathrm{CO}(4-3)$	135.453	Band 4			
[CI]609μm	144.596	Band 4			
$\mathrm{CH^+}(1-0)$	245.344	Band 6			
[NII]205μm	429.277	Band 8			
		HerBS-200 $z = 2.151$			
$\mathrm{CH^+}(1-0)$	265.020	Band 6			
$\mathrm{CO}(8-7)$	292.542	Band 7			
		HerBS-207 $z = 1.569$			
$\mathrm{CO}(6-5)$	269.160	Band 6			
$\mathrm{CO}(9-8)$	403.625	Band 8			
		HerBS-208A $z = 2.478$			

Table B.1: (continuation).

Line	Frequency [GHz]	Band	$S\mathrm{d}V$ [Jy km s^{-1}]	$\mathrm{d}V$ [km s^{-1}]	$V - V_{\mathrm{CO}}$ [km s^{-1}]
CO$(3-2)$	99.424	Band 3	2.64 ± 1.54	835 ± 366	-41 ± 155
CO$(4-3)$	132.559	Band 4			
CO$(7-6)$	231.930	Band 6			
[CI]370μm	232.703	Band 6			
[NII]205μm	420.107	Band 8			
CO$(13-12)$	430.398	Band 8			
		HerBS-208B $z = 2.483$			
CO$(3-2)$	99.281	Band 3	0.86 ± 0.69	303 ± 183	0 ± 77
CO$(4-3)$	132.369	Band 4			
CO$(7-6)$	231.597	Band 6			
[CI]370μm	232.369	Band 6			
[NII]205μm	419.504	Band 8			
CO$(13-12)$	429.780	Band 8			
		HerBS-209A $z = 2.272$			
CO$(7-6)$	246.532	Band 6			
[CI]370μm	247.354	Band 6			

E

All galaxies for SK analysis

In Figure E.1 I present the remaining galaxies used for the SK analysis (the first five are shown in Figures 3.11 and 4.2), with the moment 0 (left) and the total spectrum (right) of the corresponding CO line. The last four galaxies (HerBS-21, HerBS-25, HerBS-36 and HerBS-41A) were not a part of my original sample, therefore they are not included in Section 4.1. They are presented by Bakx et al. (2024), and were facilitated by the authors for the SK analysis of this thesis.

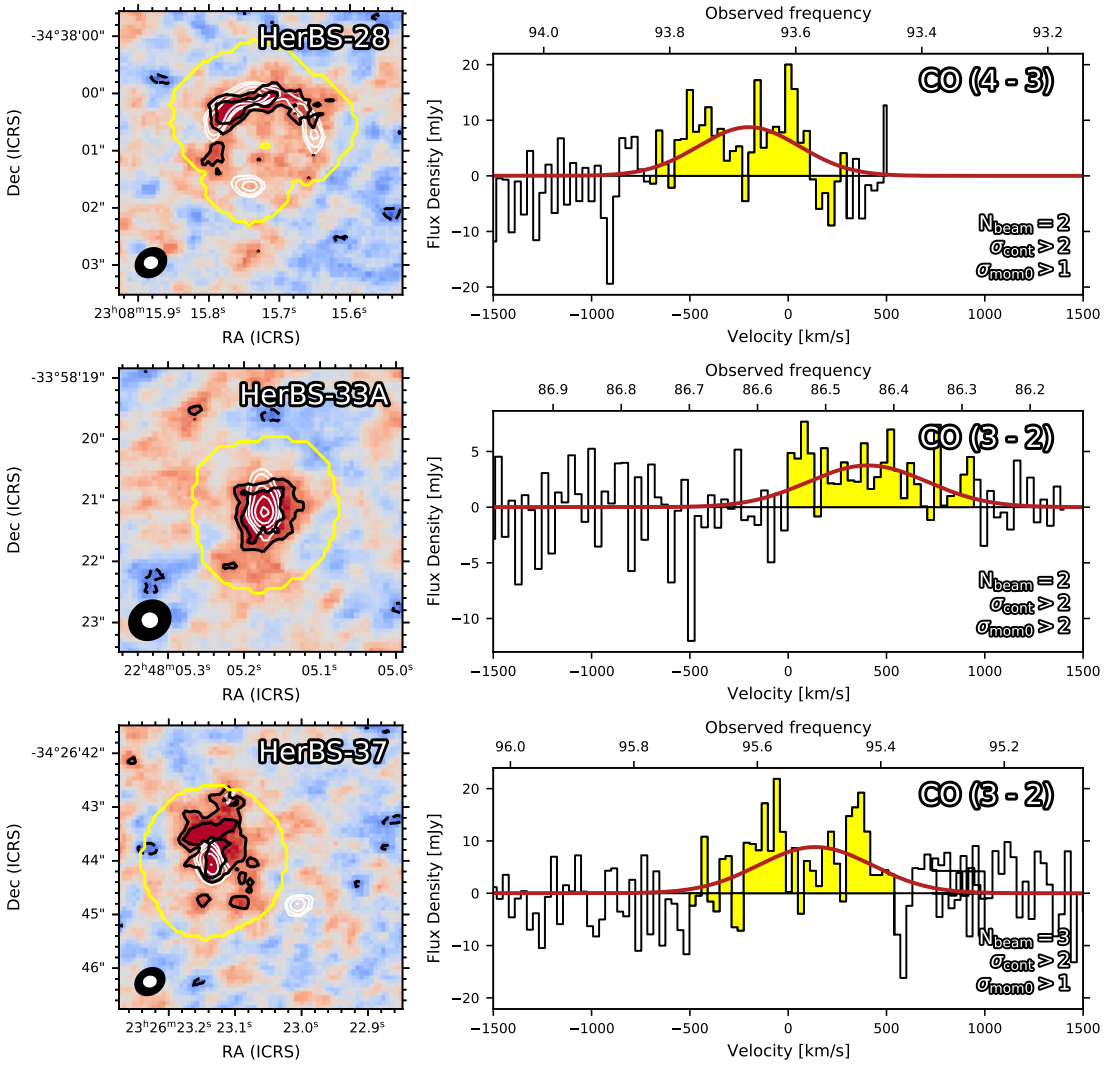

Figure E.1: Remaining galaxies used for the SK analysis. Plots like Figure 3.11.

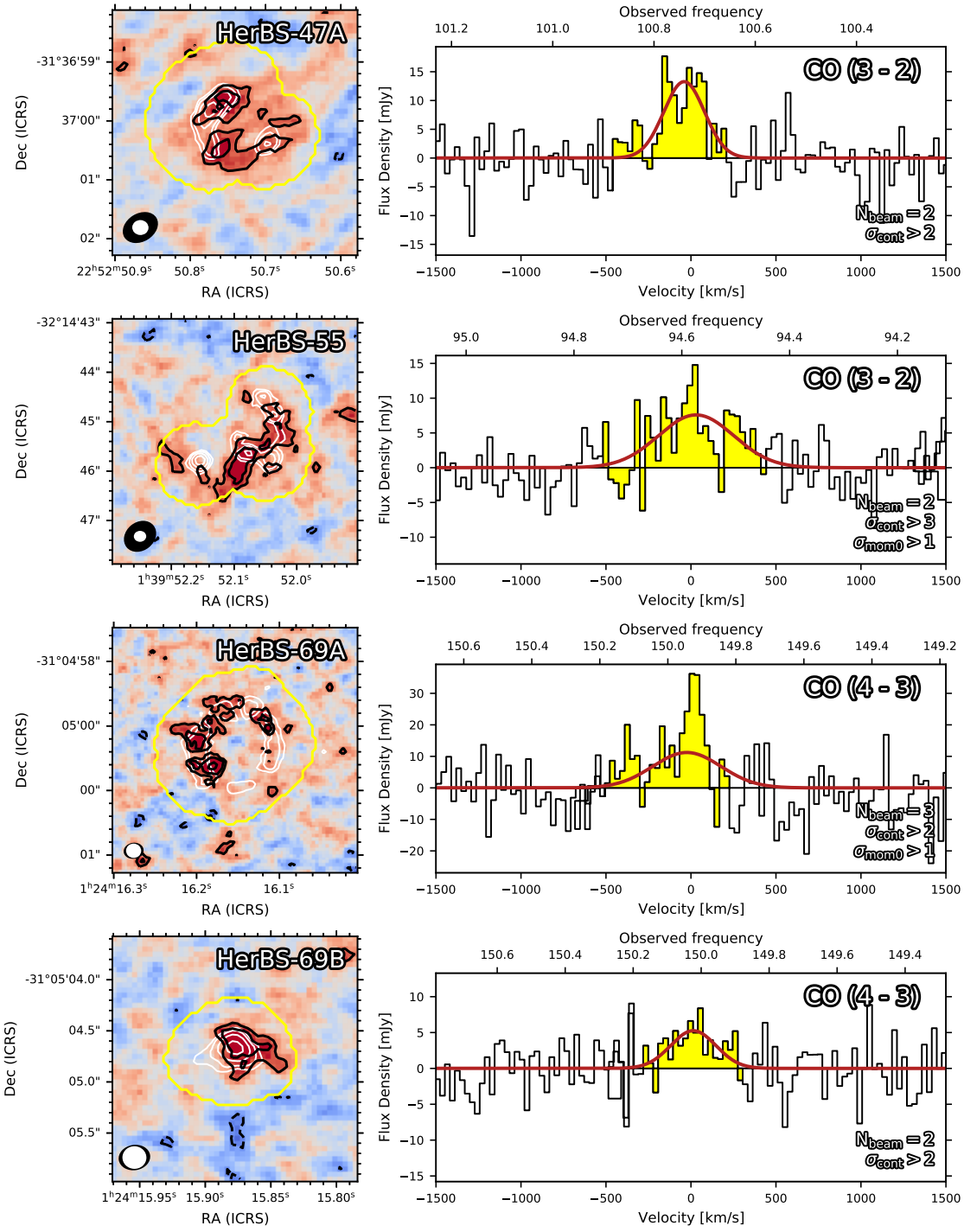

Figure E.1: (continuation).

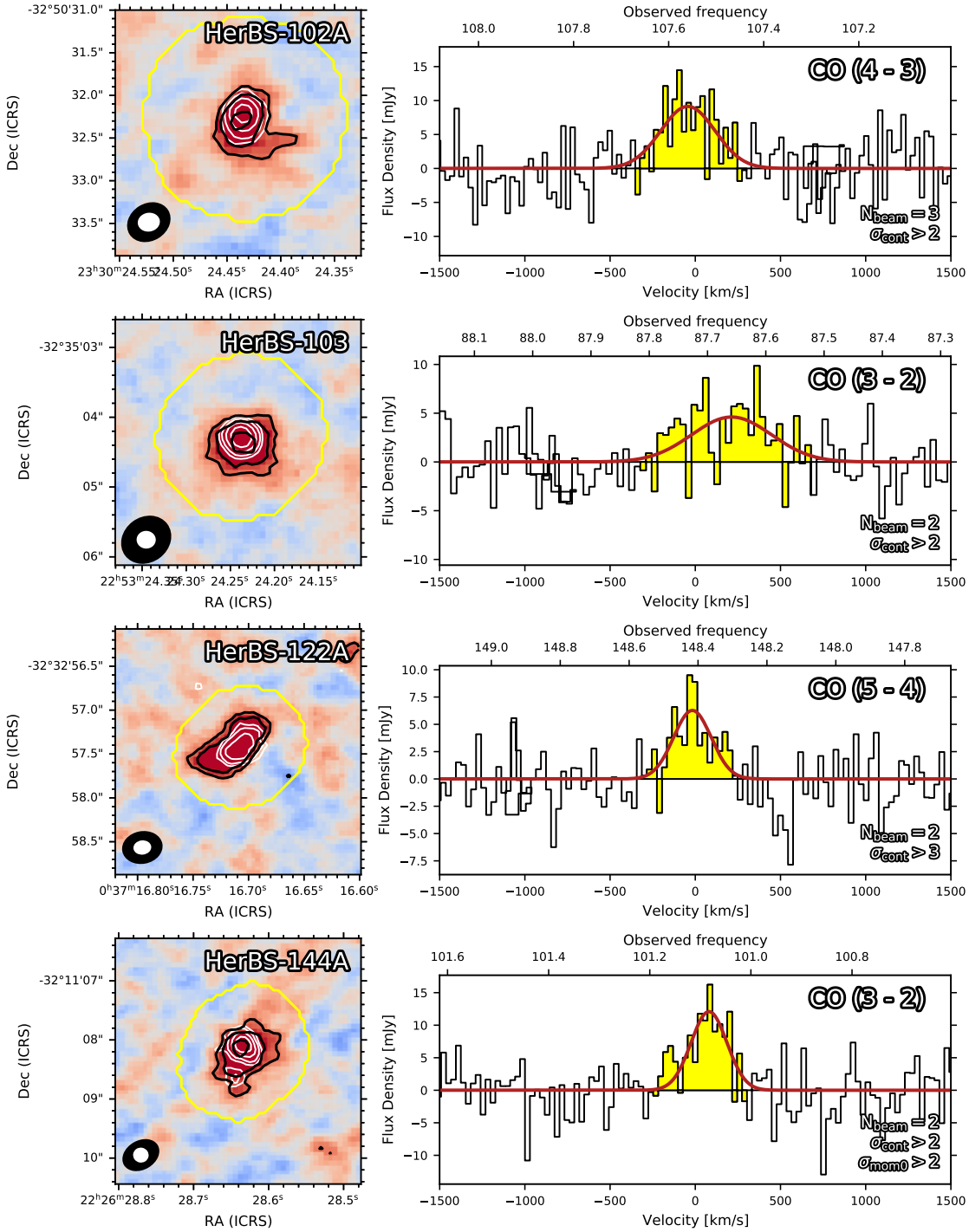

Figure E.1: (continuation).

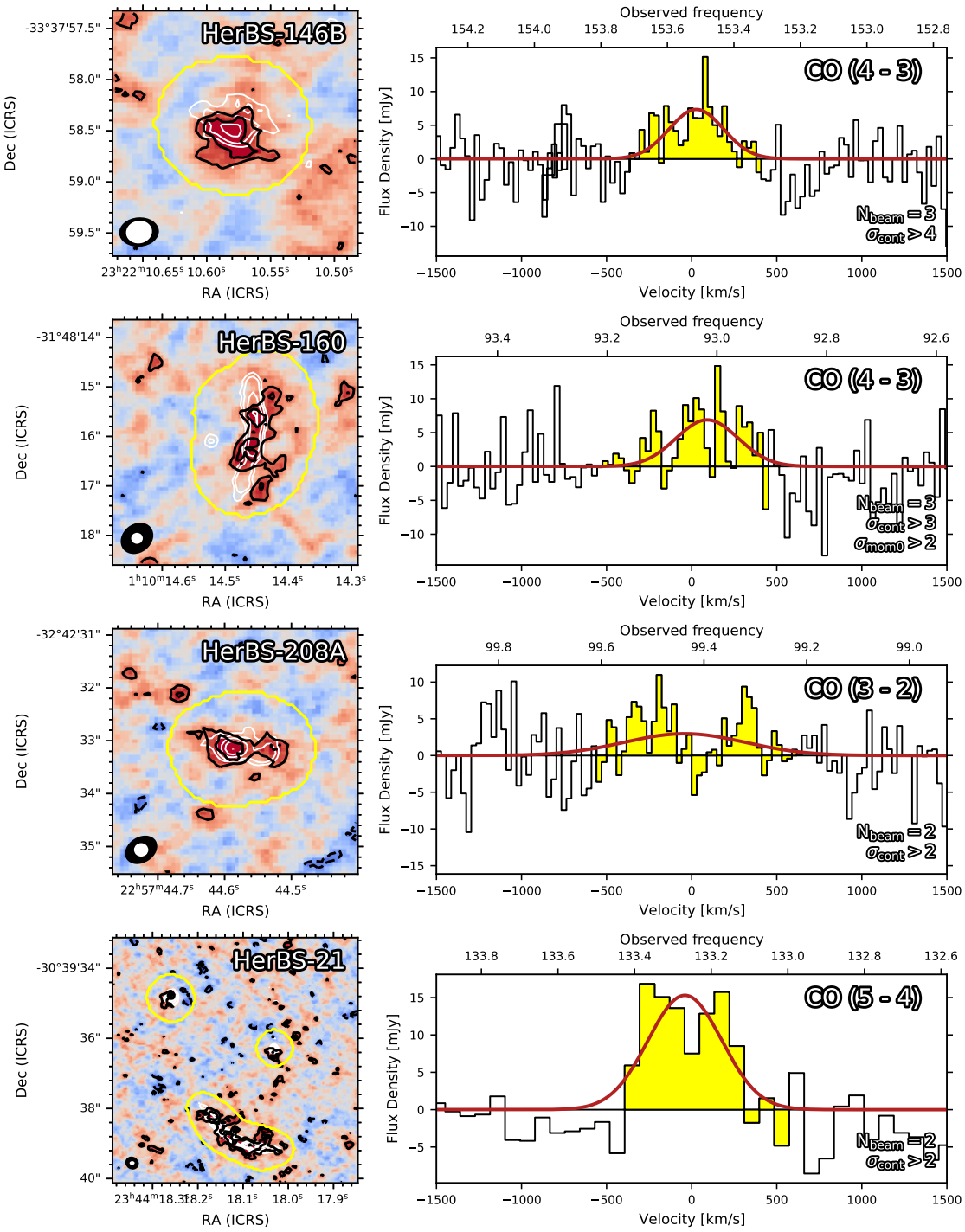

Figure E.1: (continuation). In HerBS-21; the white contours correspond to ALMA Band 7, not Band 6.

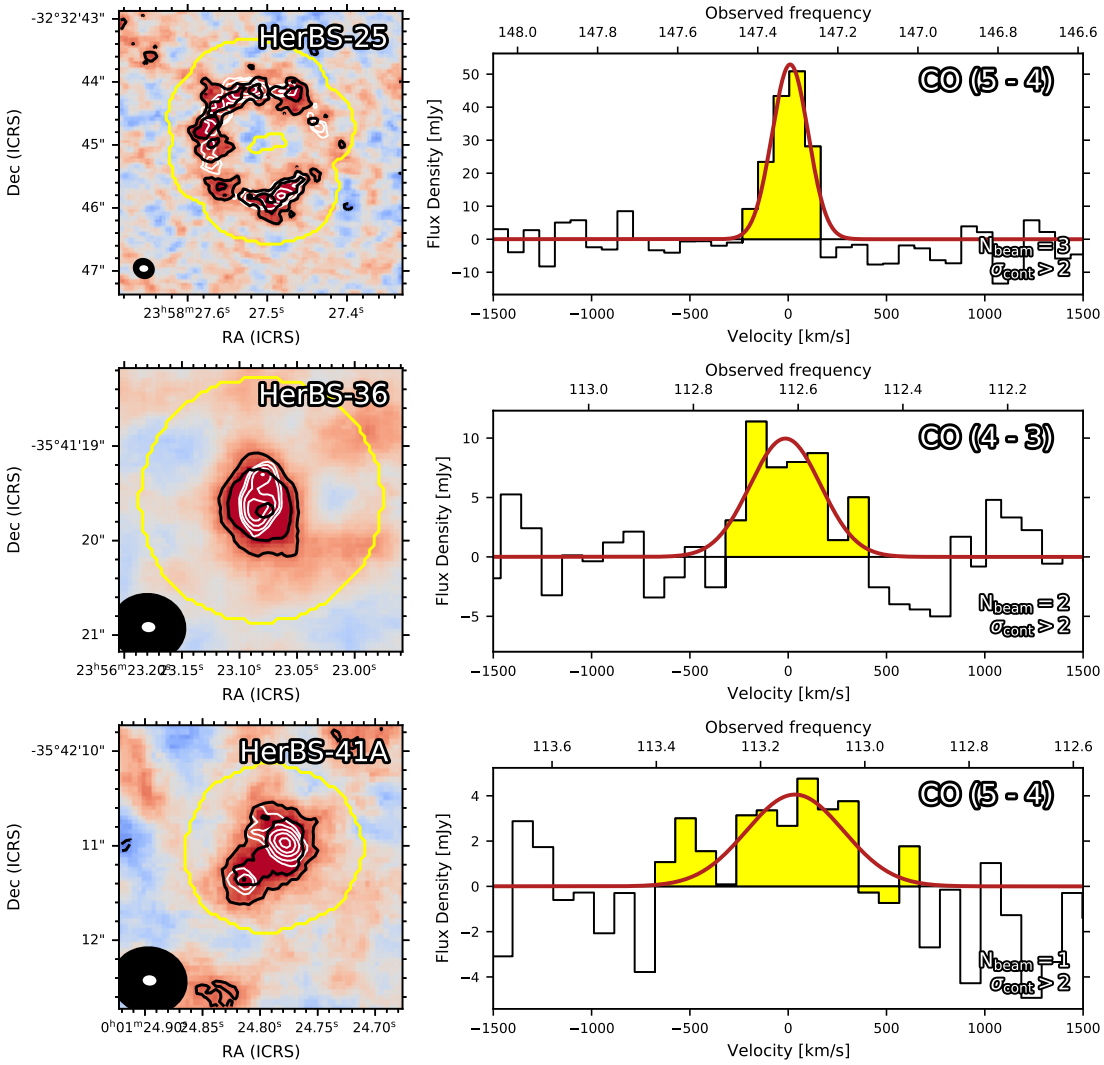

Figure E.1: (continuation). In these three galaxies, the white contours correspond to ALMA Band 7, not Band 6.

F

Galaxies excluded from SK

In Figure F.1 I present three galaxies whose CO frequency was observed but which were excluded from the SK analysis.

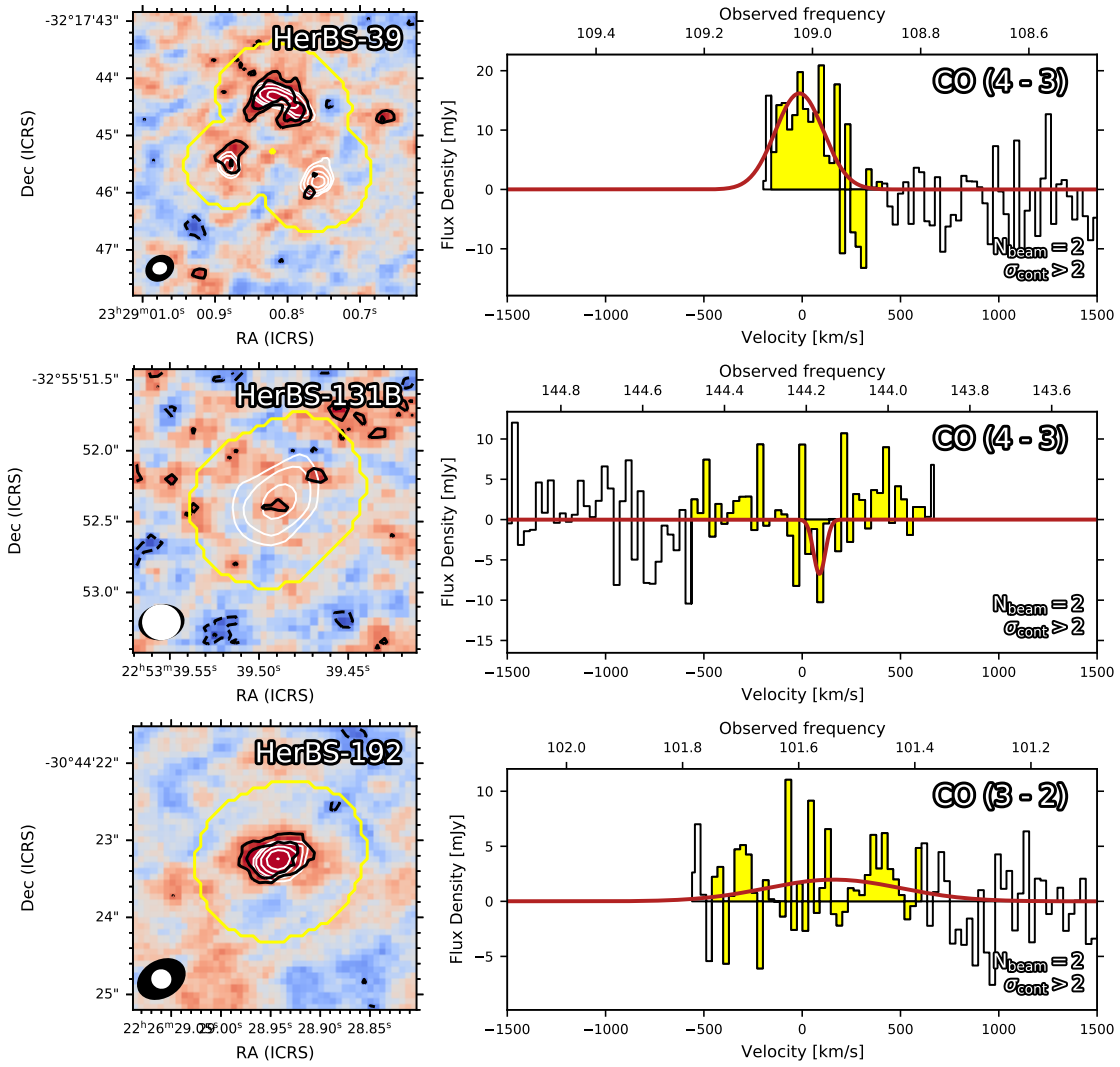

Figure F.1: Three examples of galaxies of the sample which were excluded from the SK analysis. These plots are analogous to Figure 3.11 (moment 0 on the left and spectrum on the right). HerBS-39: line is only partially covered by the ALMA range, i.e. there is flux missing. HerBS-131B: line is undetected. HerBS-192: emission is too compact to be well resolved, i.e. is it of the same size of the beam.

G

Resolved SK diagrams

In Figure G.1, three resolved SK diagrams are presented for each galaxy. The first diagram has the tessellation of apertures centered around the respective celestial coordinates shown in Table 4.1, i.e. around the *center* of the galaxy. The second diagram has the apertures at the most offset position as possible compared to the first one.

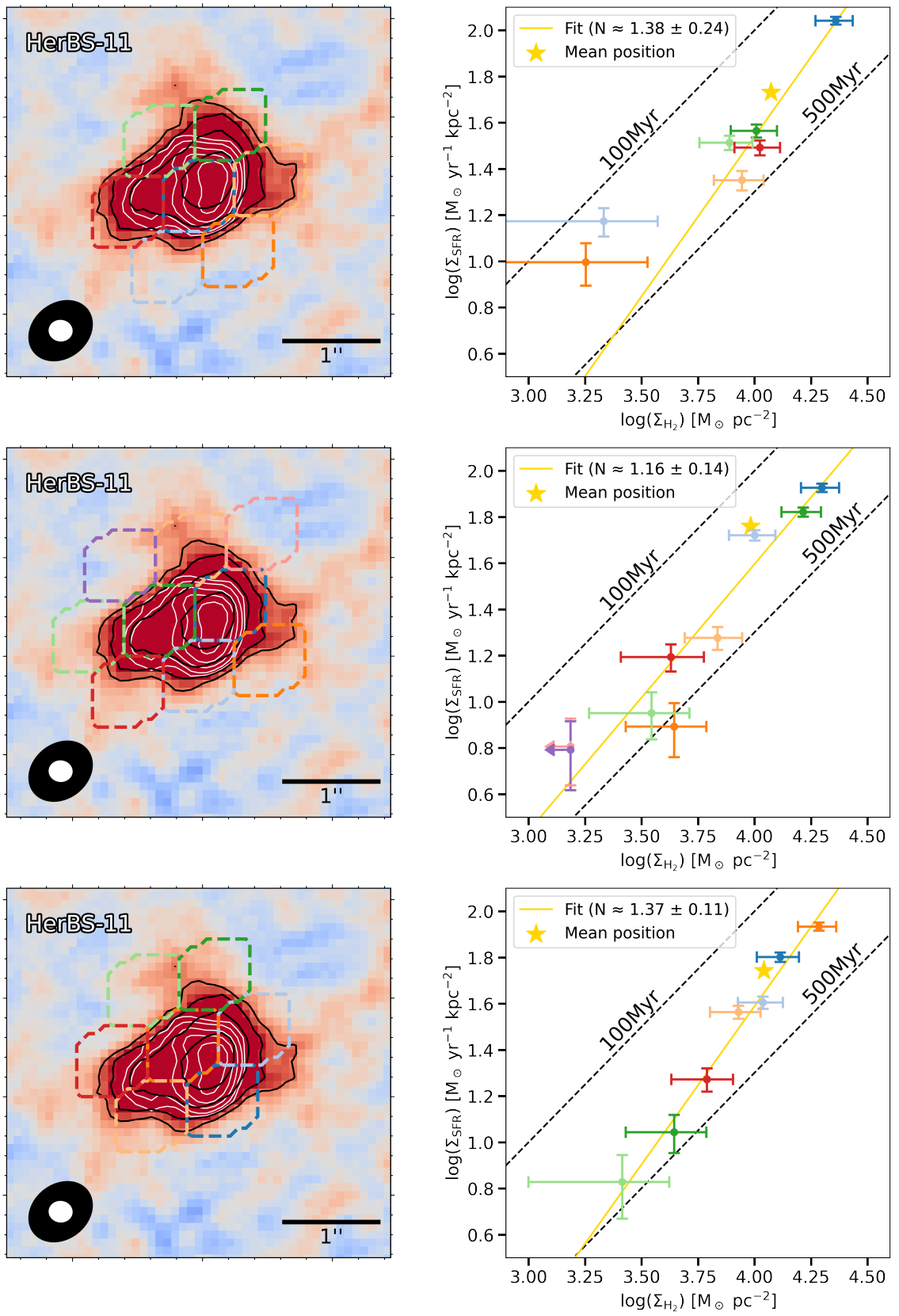

Figure G.1: Three example resolved SK diagrams for each galaxy. Plots like Figure 3.22 (i.e. color map and black contours are moment 0 map, while white contours are continuum map). In this page: HerBS-11, where 73 SK diagrams like these were built in total.

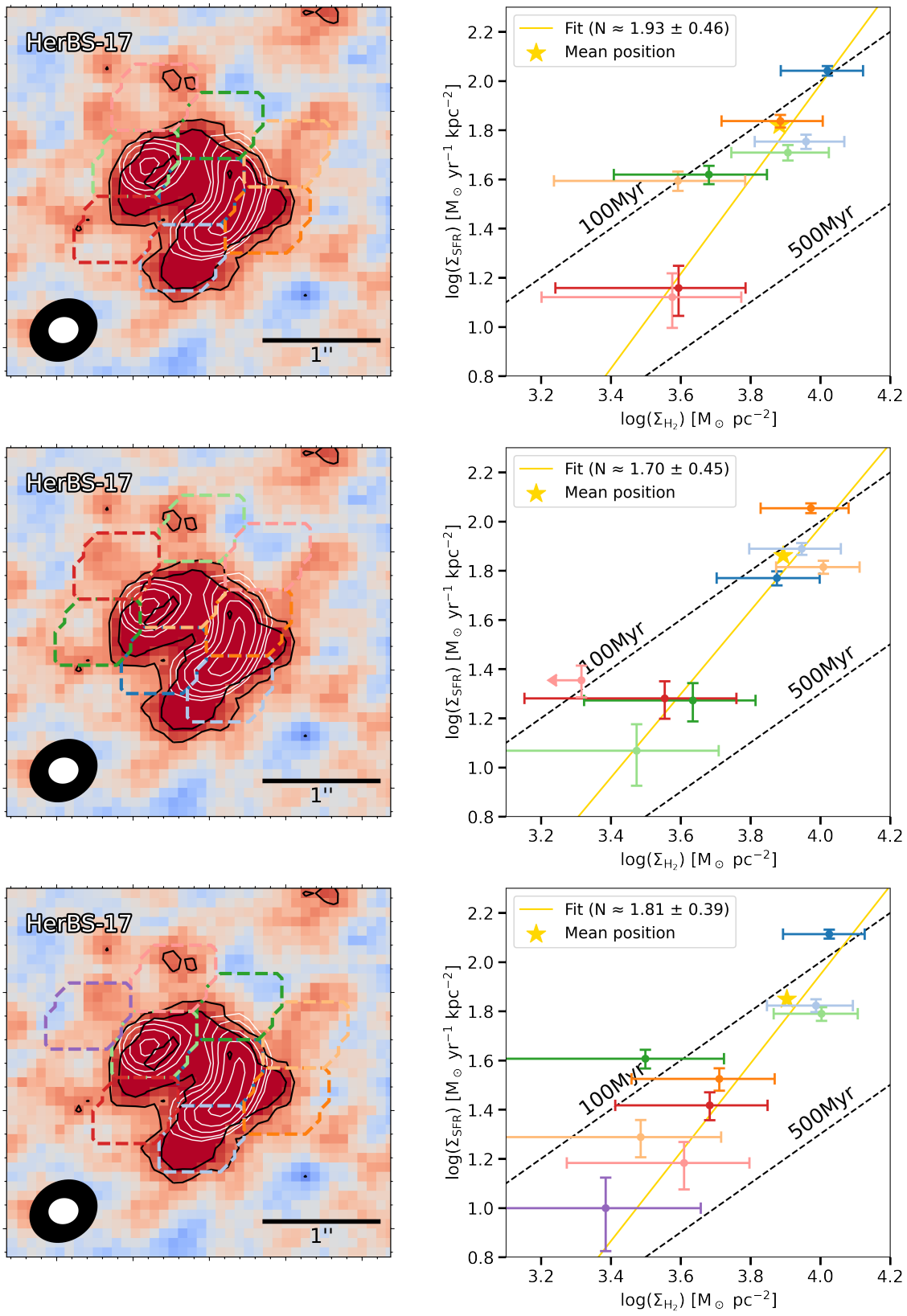

Figure G.1: (continuation). In this page: HerBS-17, where 55 SK diagrams like these were built in total.

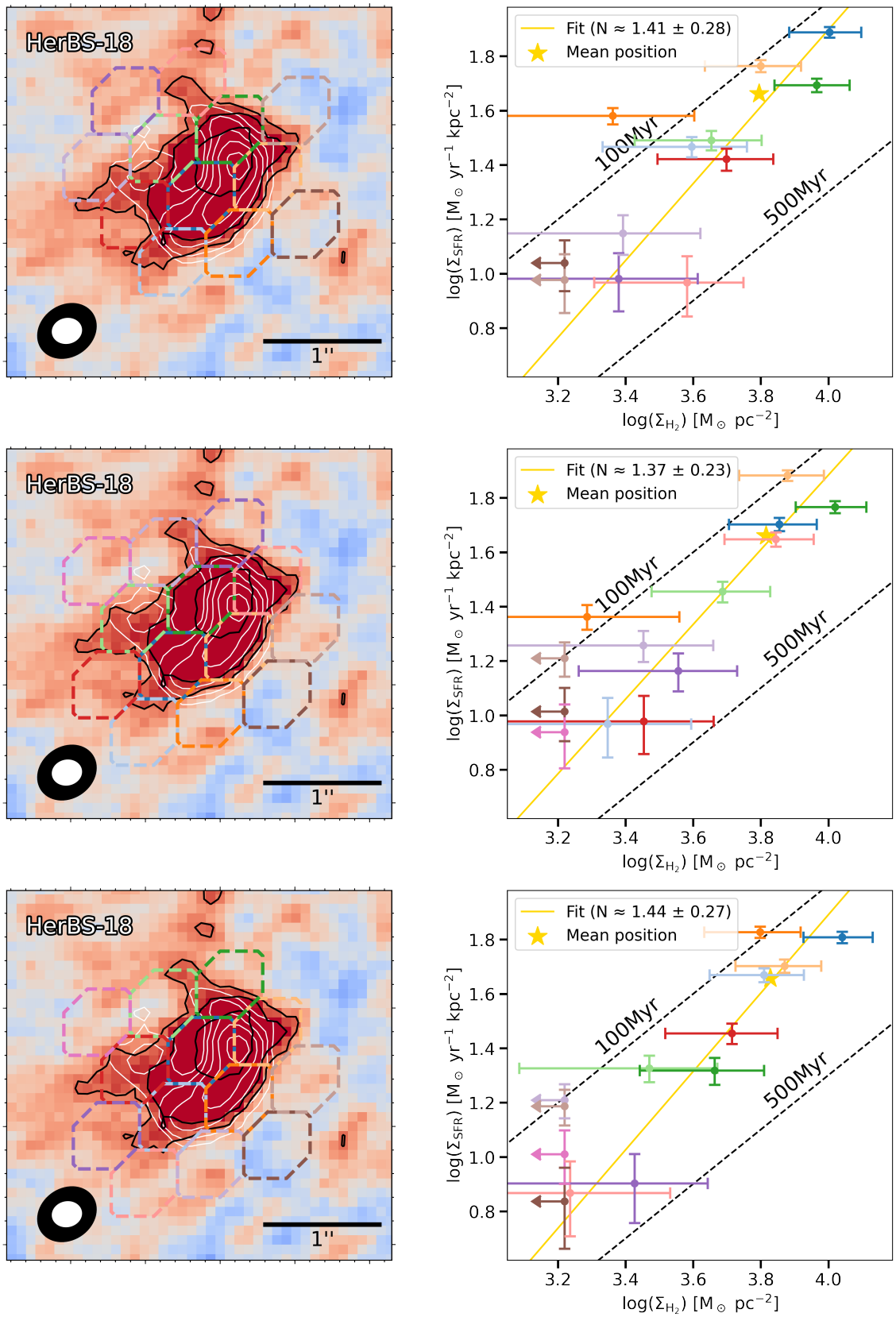

Figure G.1: (continuation). In this page: HerBS-18, where 43 SK diagrams like these were built in total.

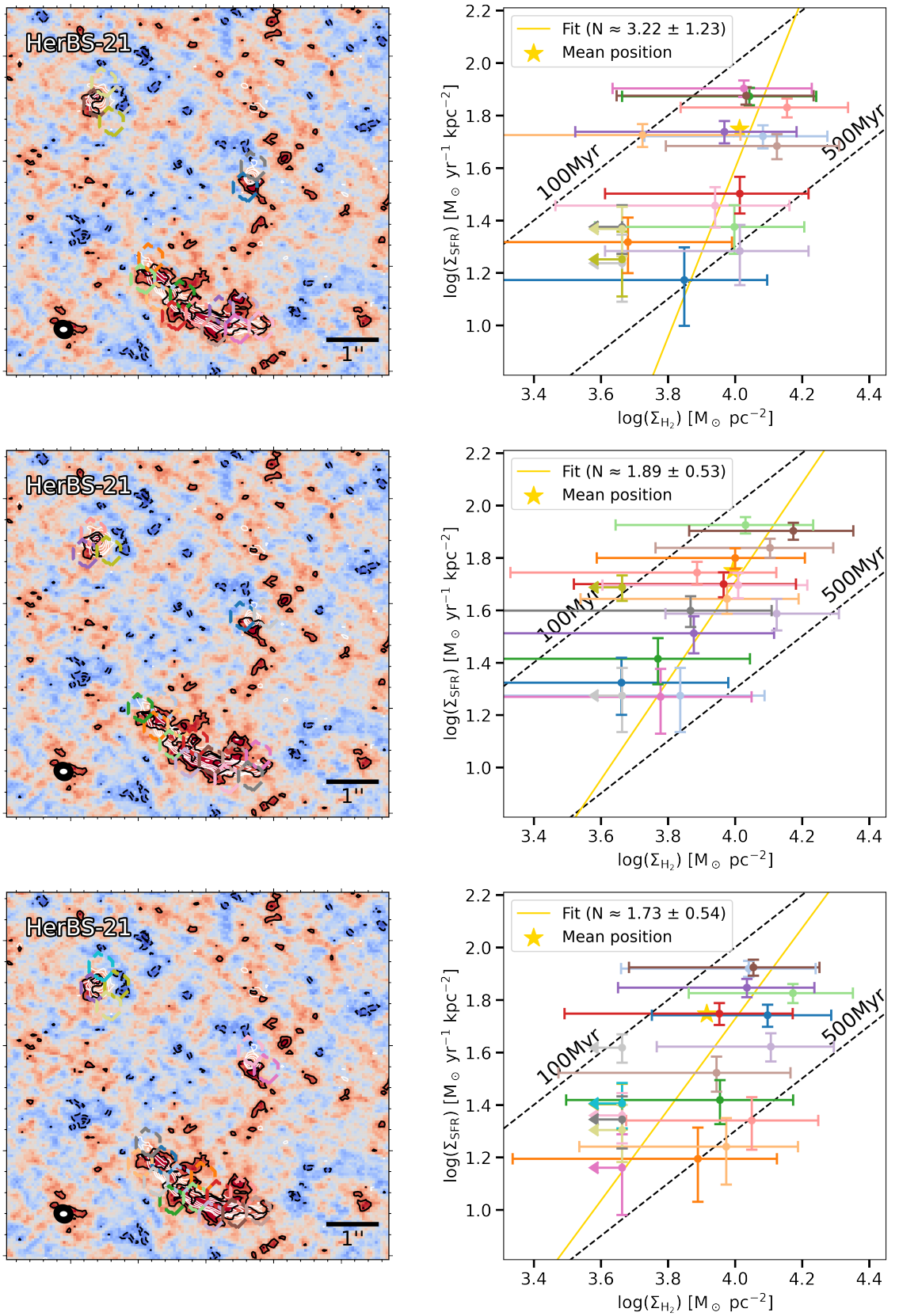

Figure G.1: (continuation). In this page: HerBS-21, where 69 SK diagrams like these were built in total.

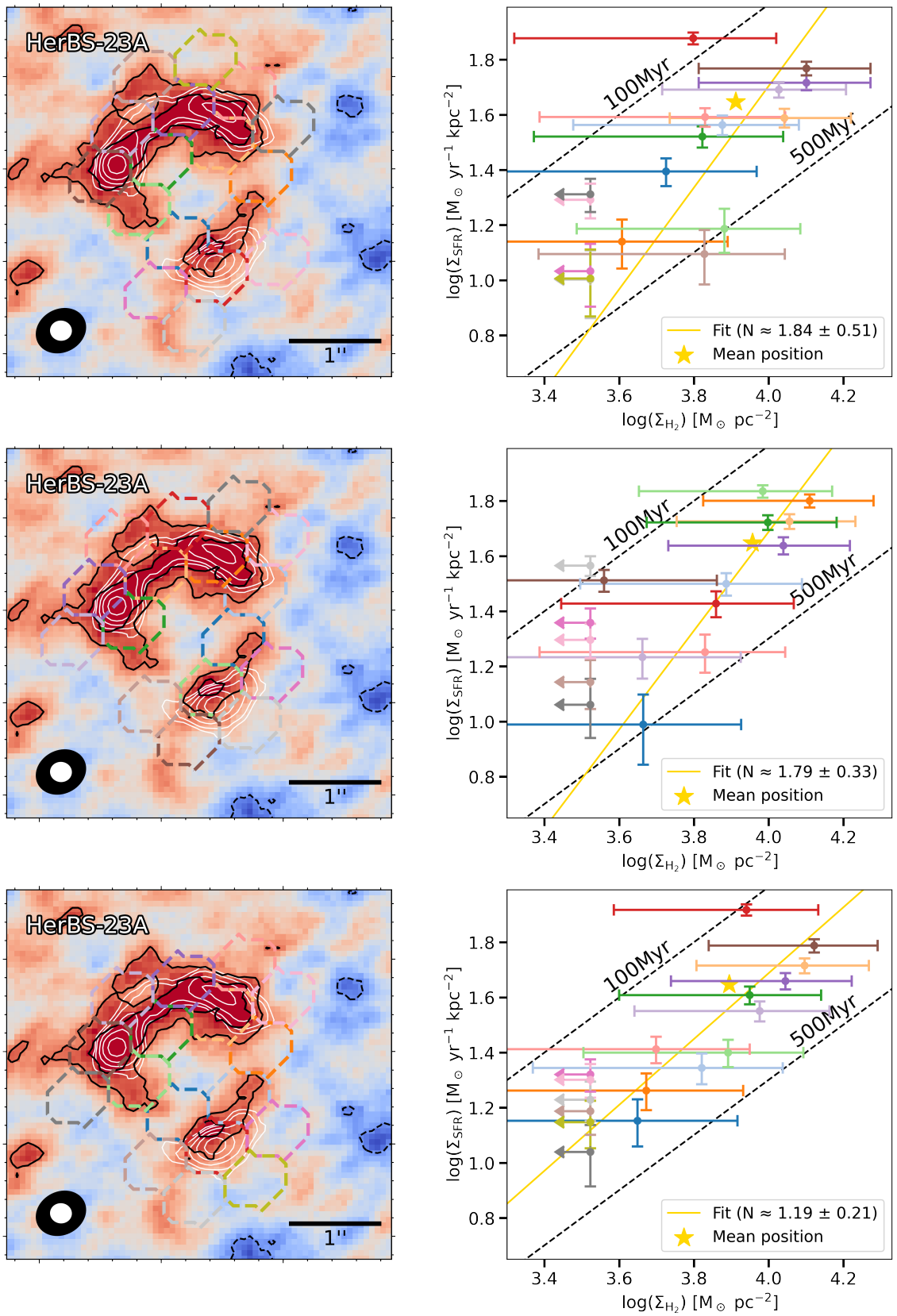

Figure G.1: (continuation). In this page: HerBS-23A, where 87 SK diagrams like these were built in total.

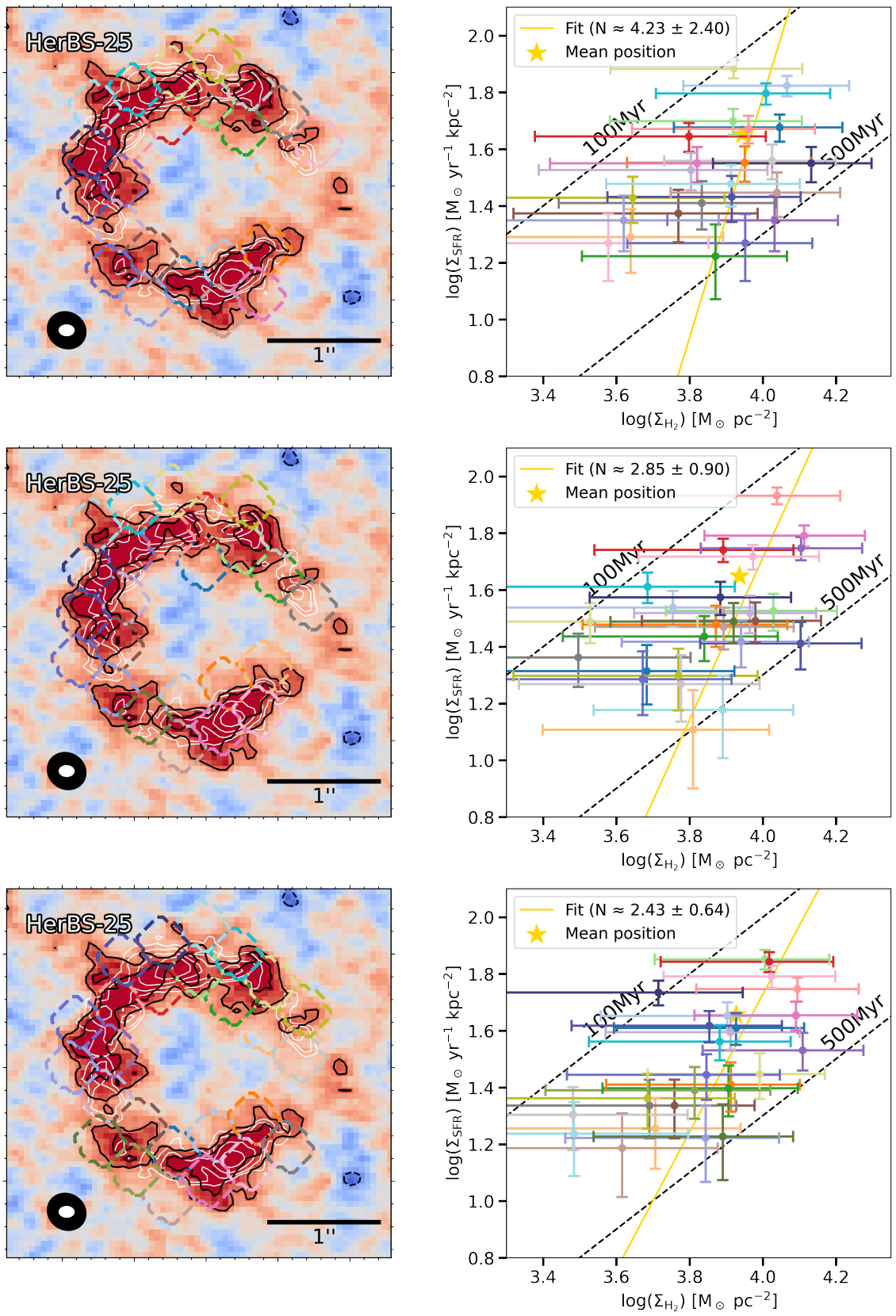

Figure G.1: (continuation). In this page: HerBS-25, where 53 SK diagrams like these were built in total.

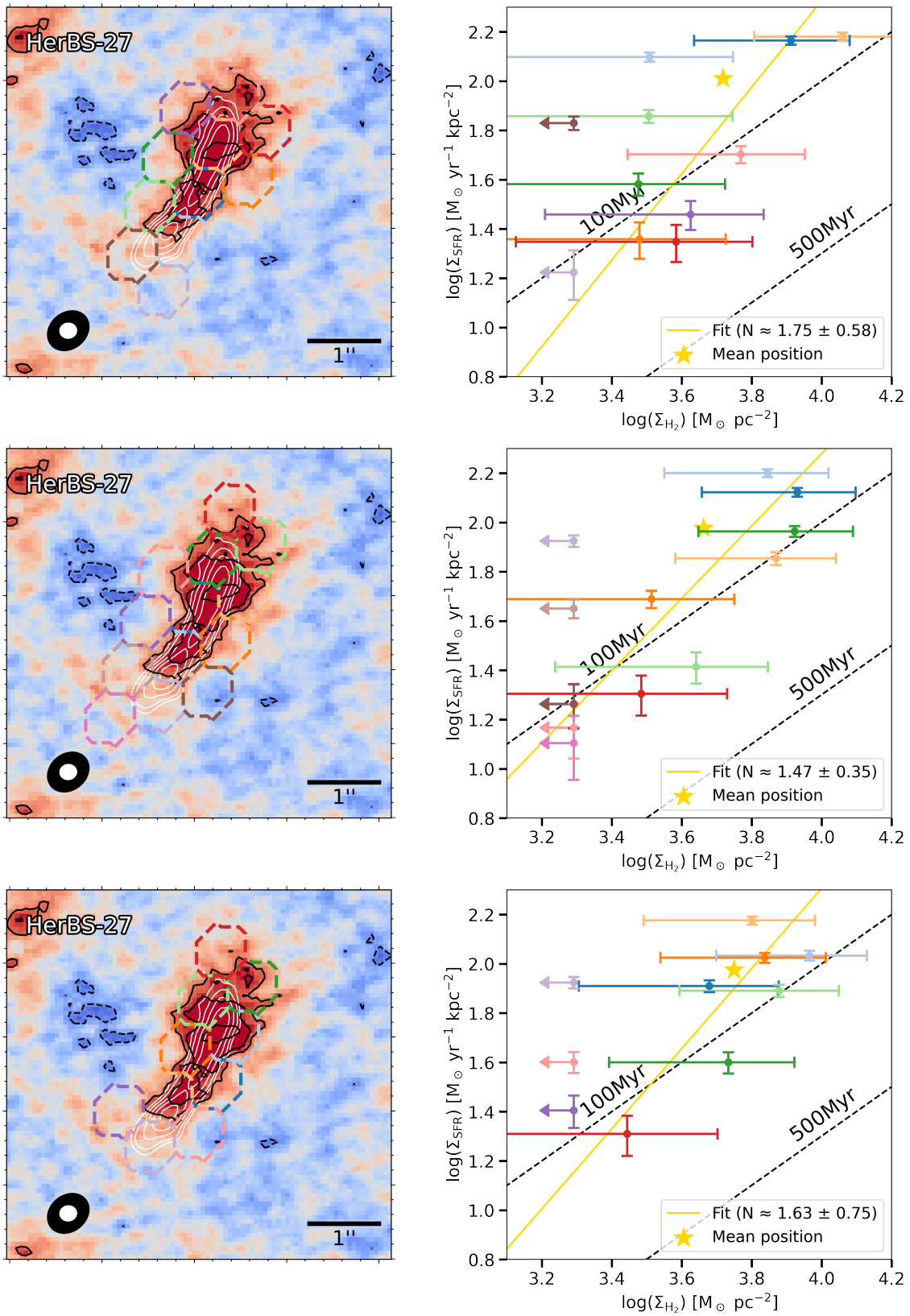

Figure G.1: (continuation). In this page: HerBS-27, where 109 SK diagrams like these were built in total.

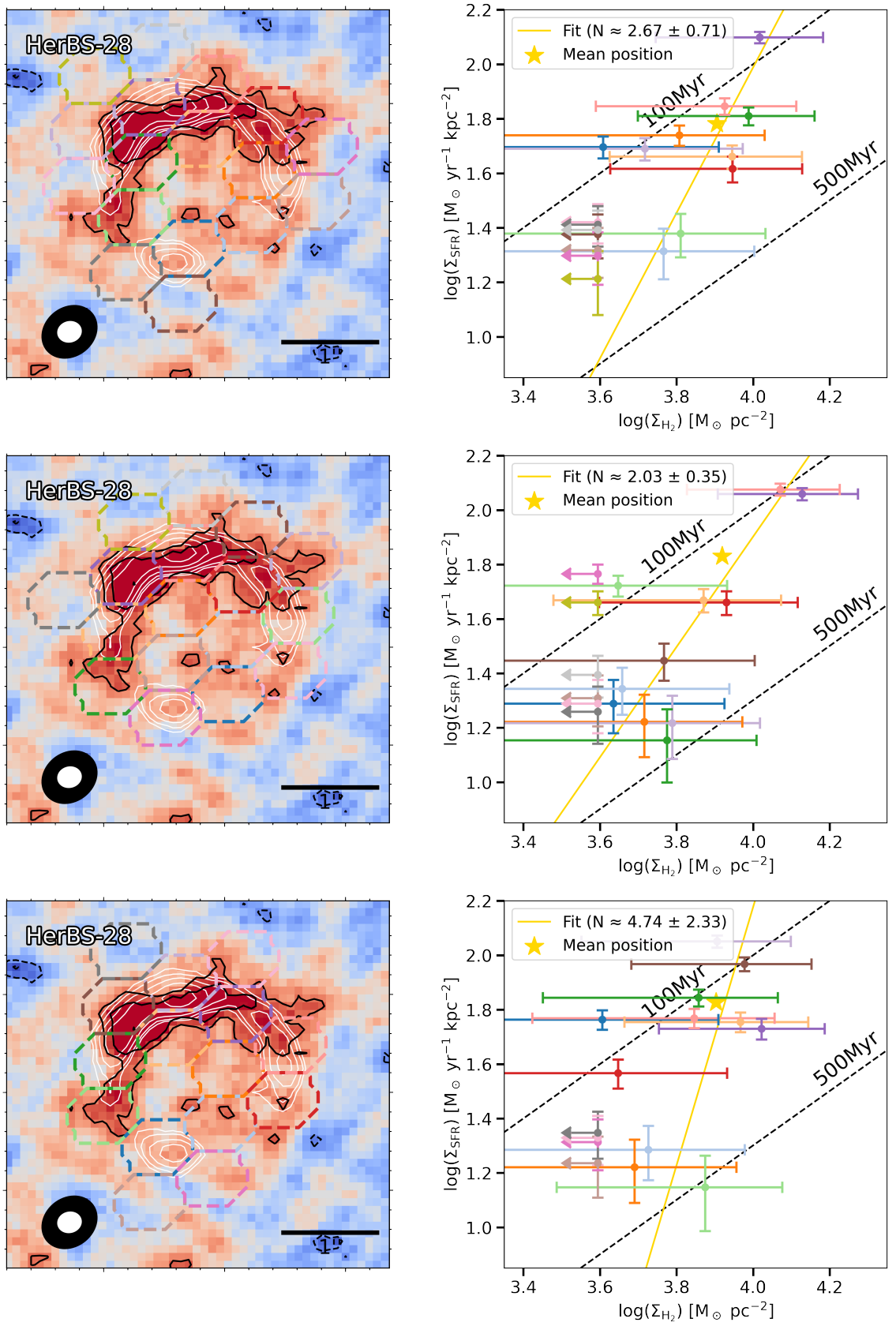

Figure G.1: (continuation). In this page: HerBS-28, where 53 SK diagrams like these were built in total.

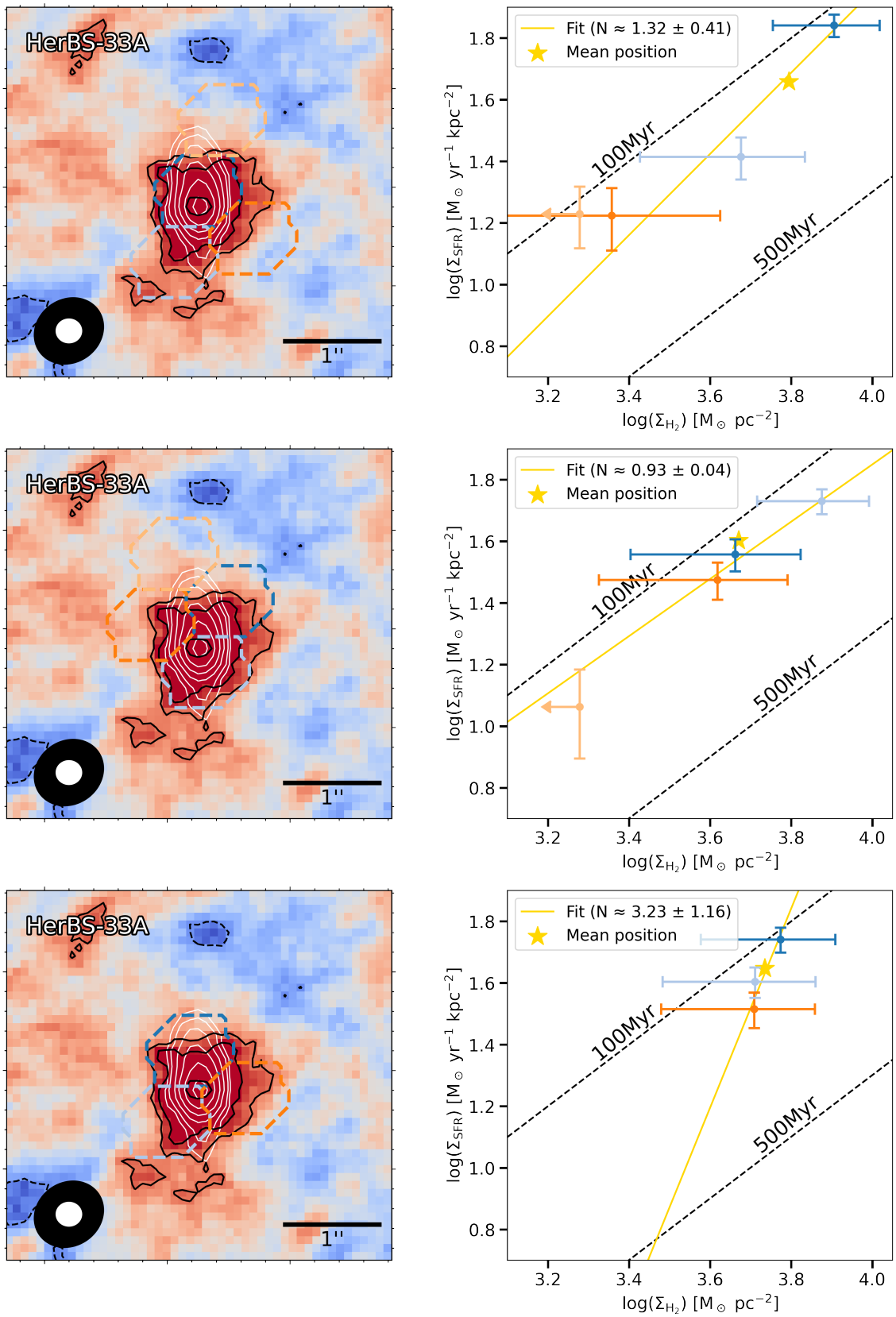

Figure G.1: (continuation). In this page: HerBS-33A, where 81 SK diagrams like these were built in total.

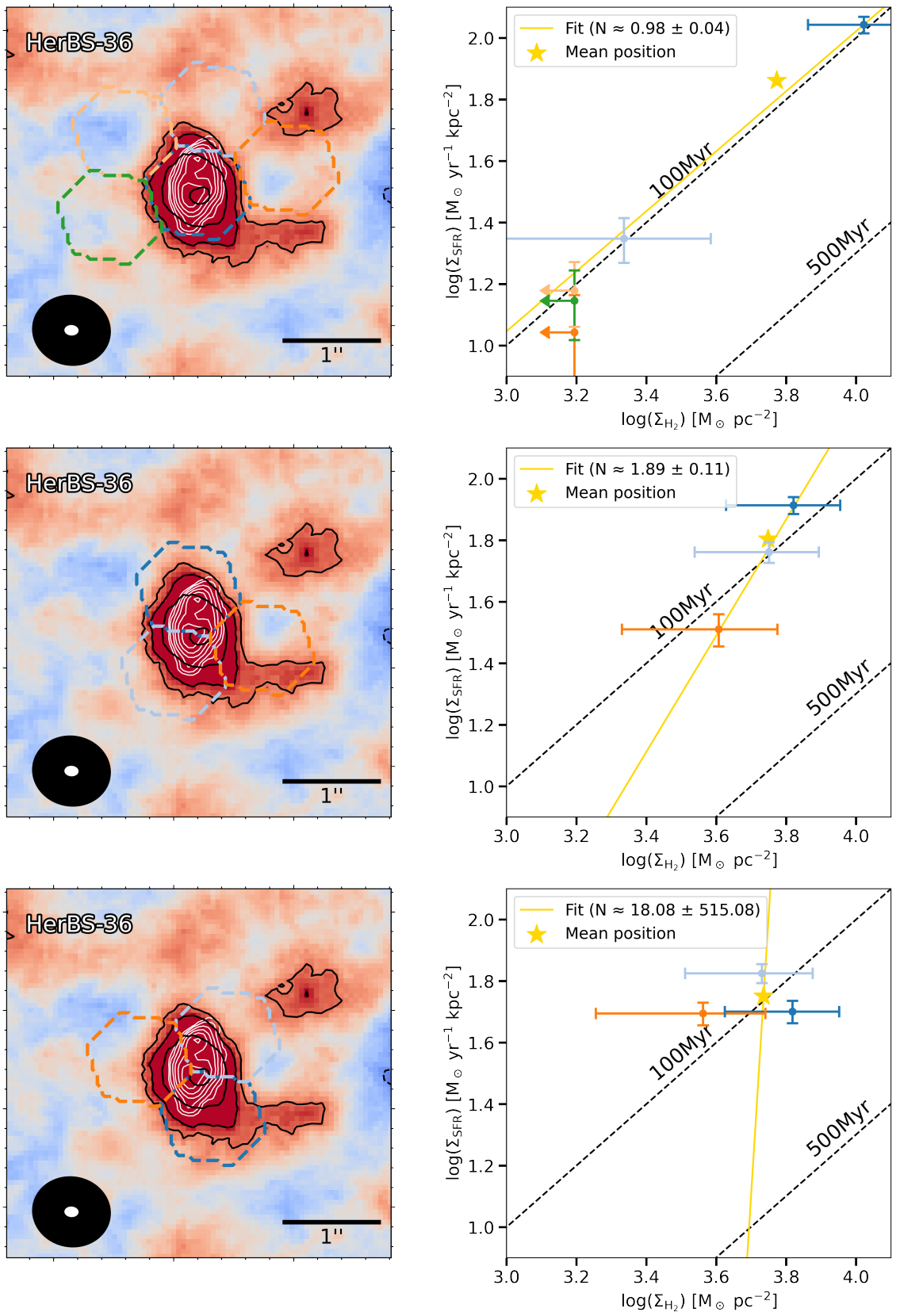

Figure G.1: (continuation). In this page: HerBS-36, where 291 SK diagrams like these were built in total.

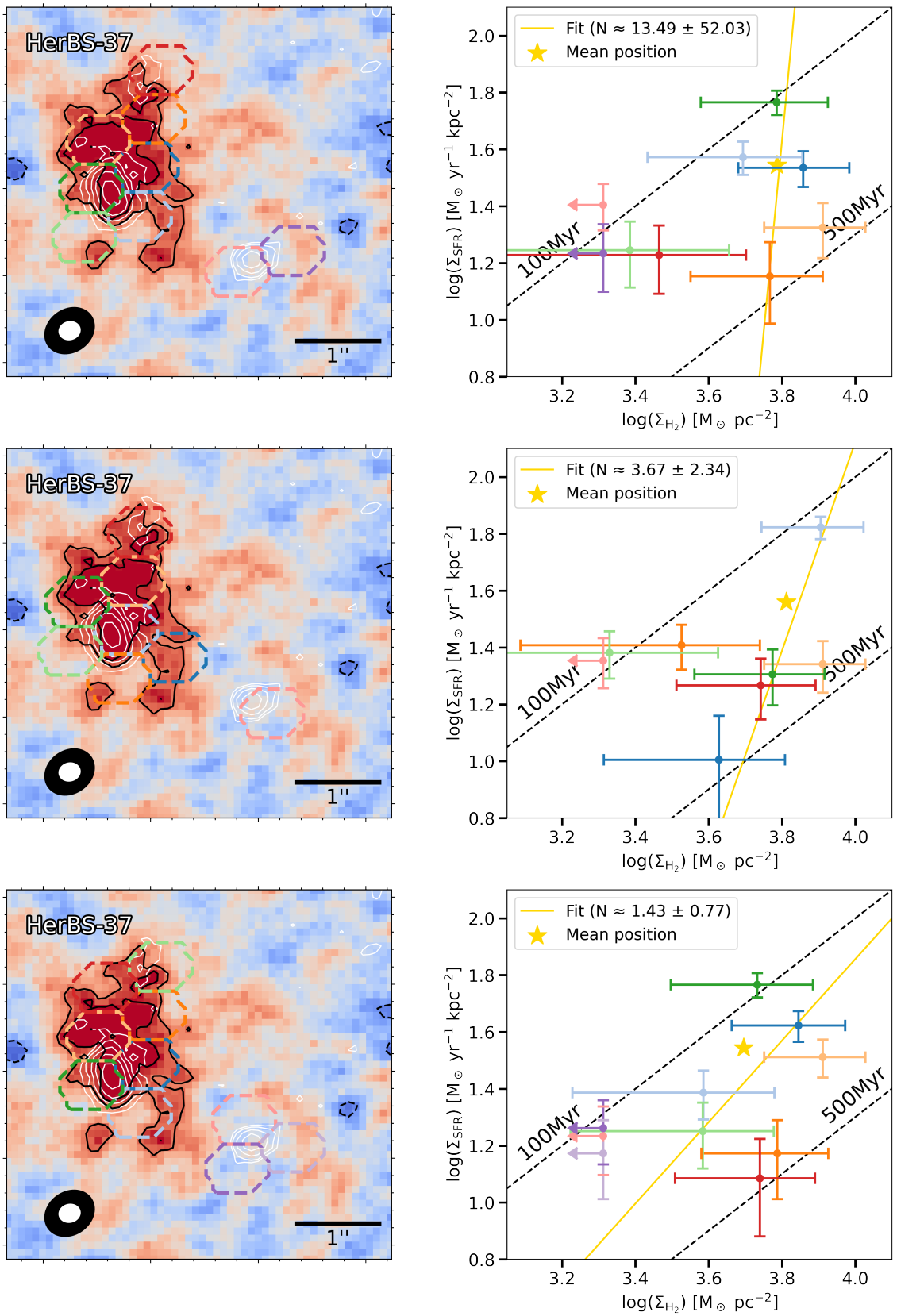

Figure G.1: (continuation). In this page: HerBS-37, where 53 SK diagrams like these were built in total.

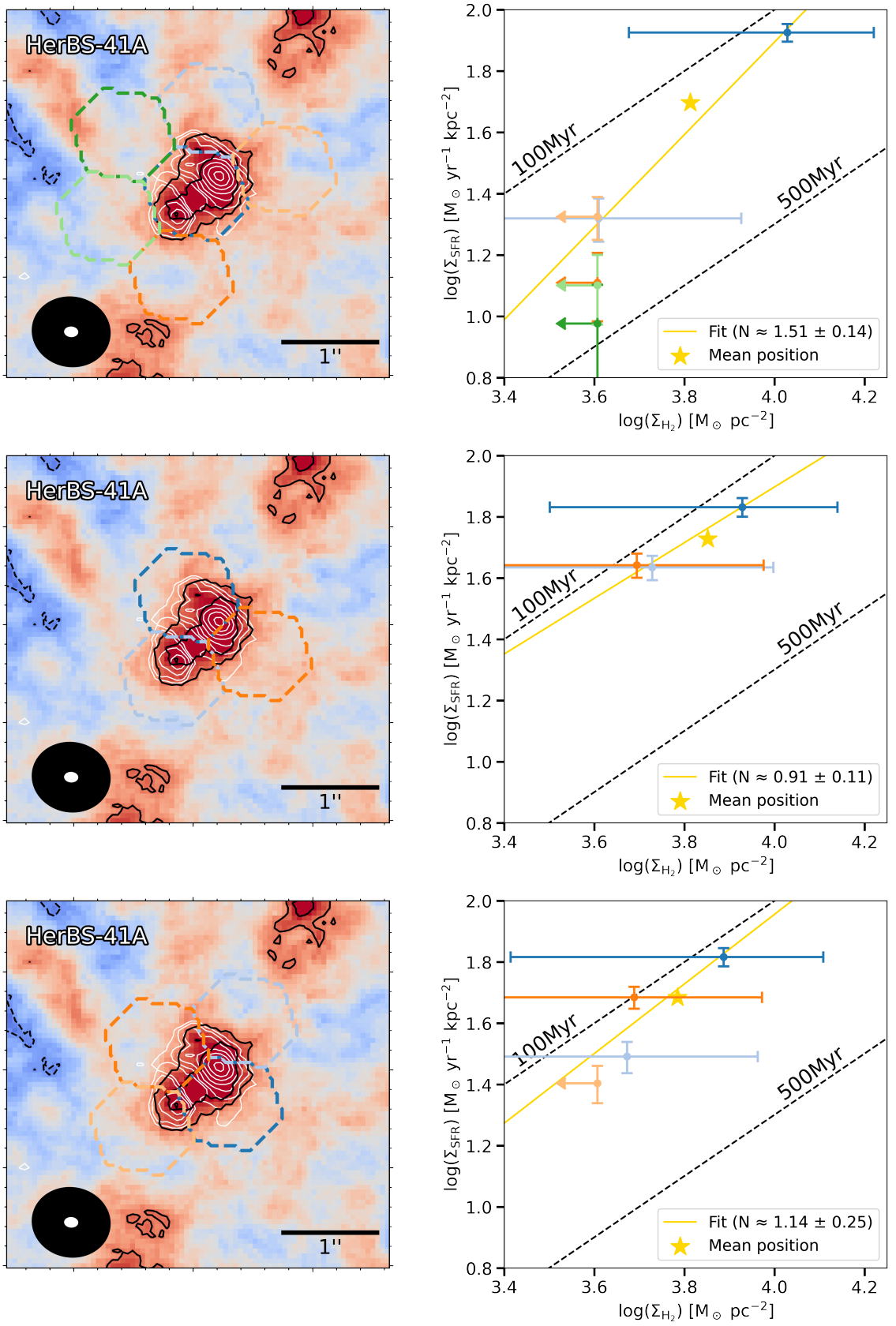

Figure G.1: (continuation). In this page: HerBS-41A, where 291 SK diagrams like these were built in total.

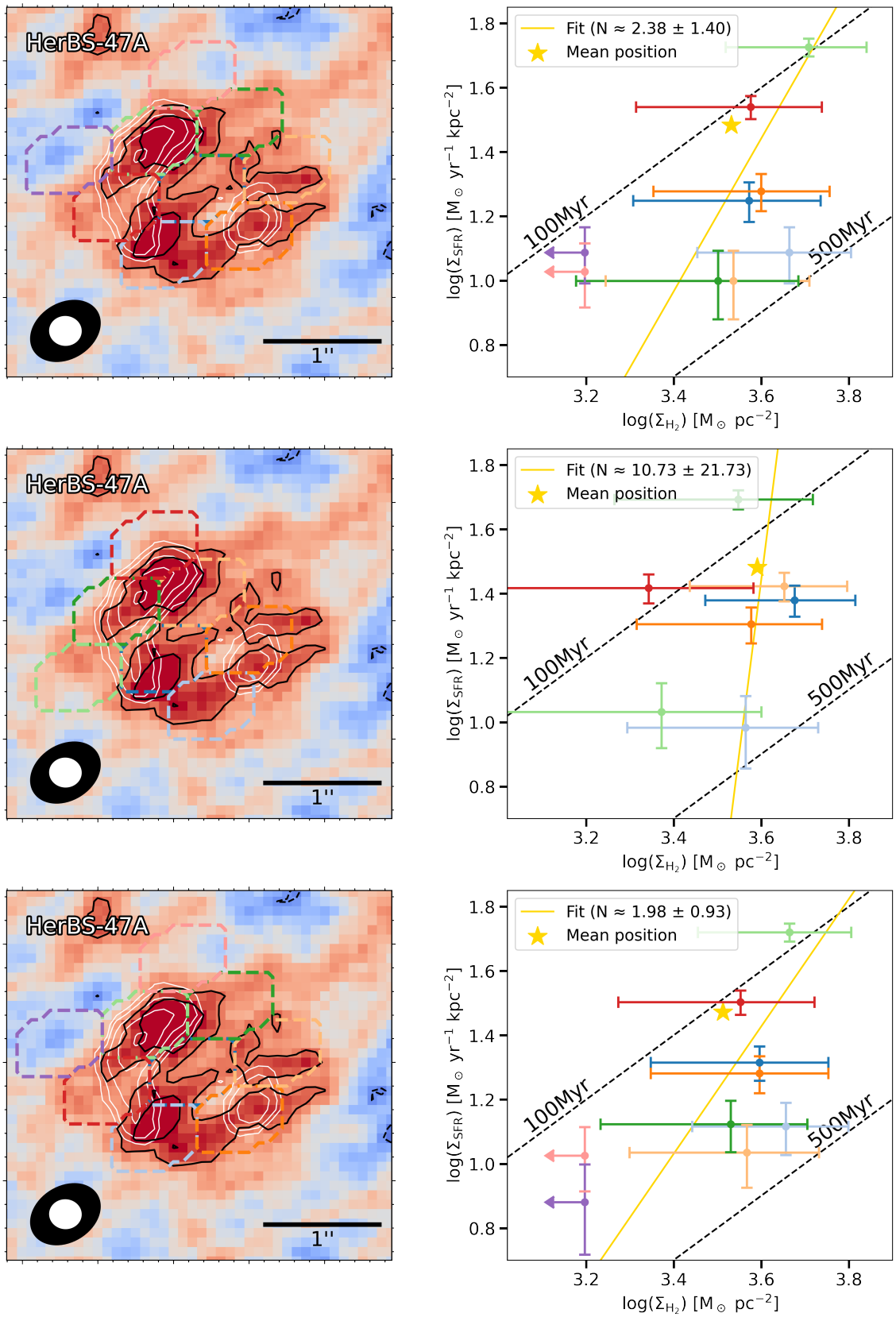

Figure G.1: (continuation). In this page: HerBS-47A, where 55 SK diagrams like these were built in total.

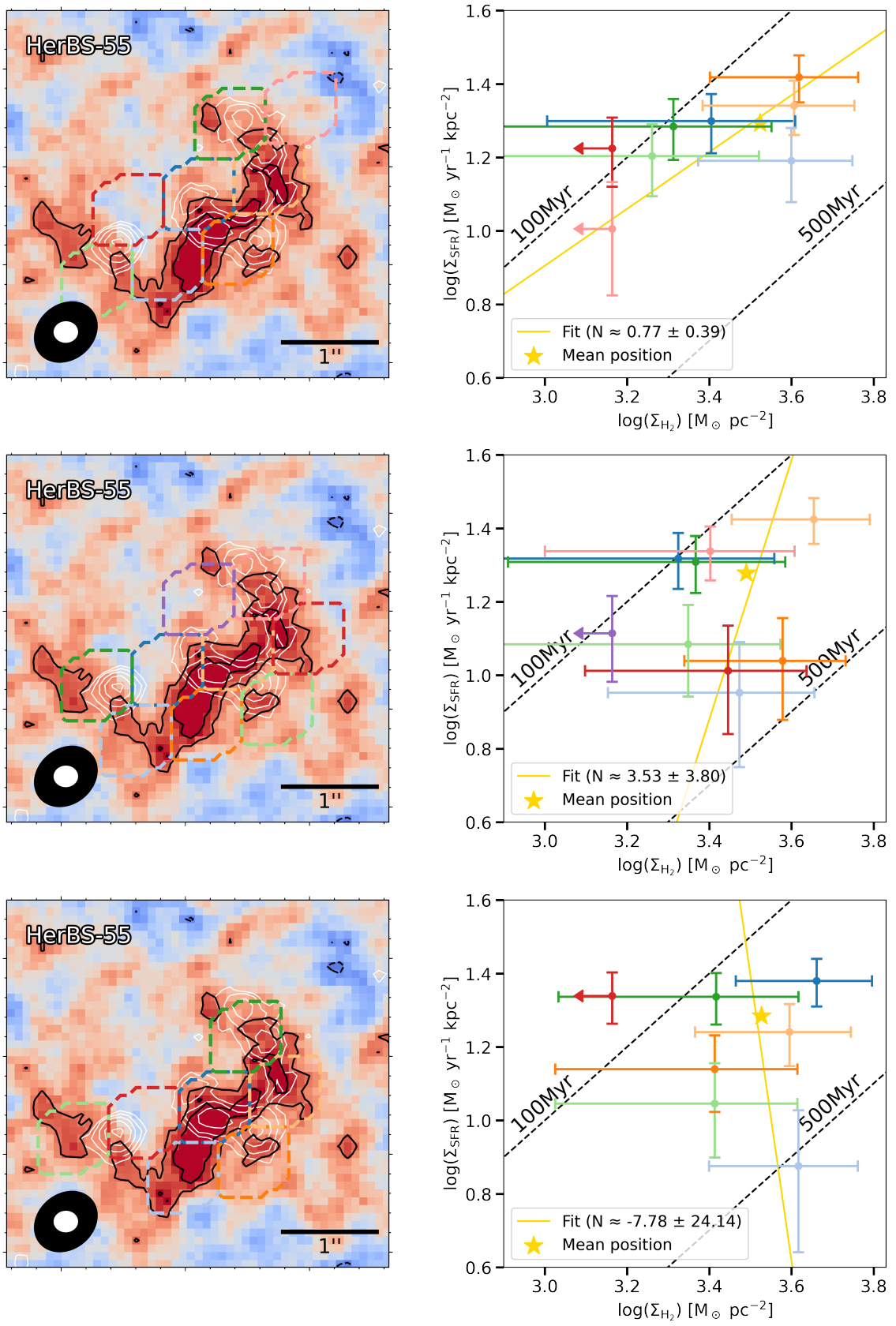

Figure G.1: (continuation). In this page: HerBS-55, where 73 SK diagrams like these were built in total.

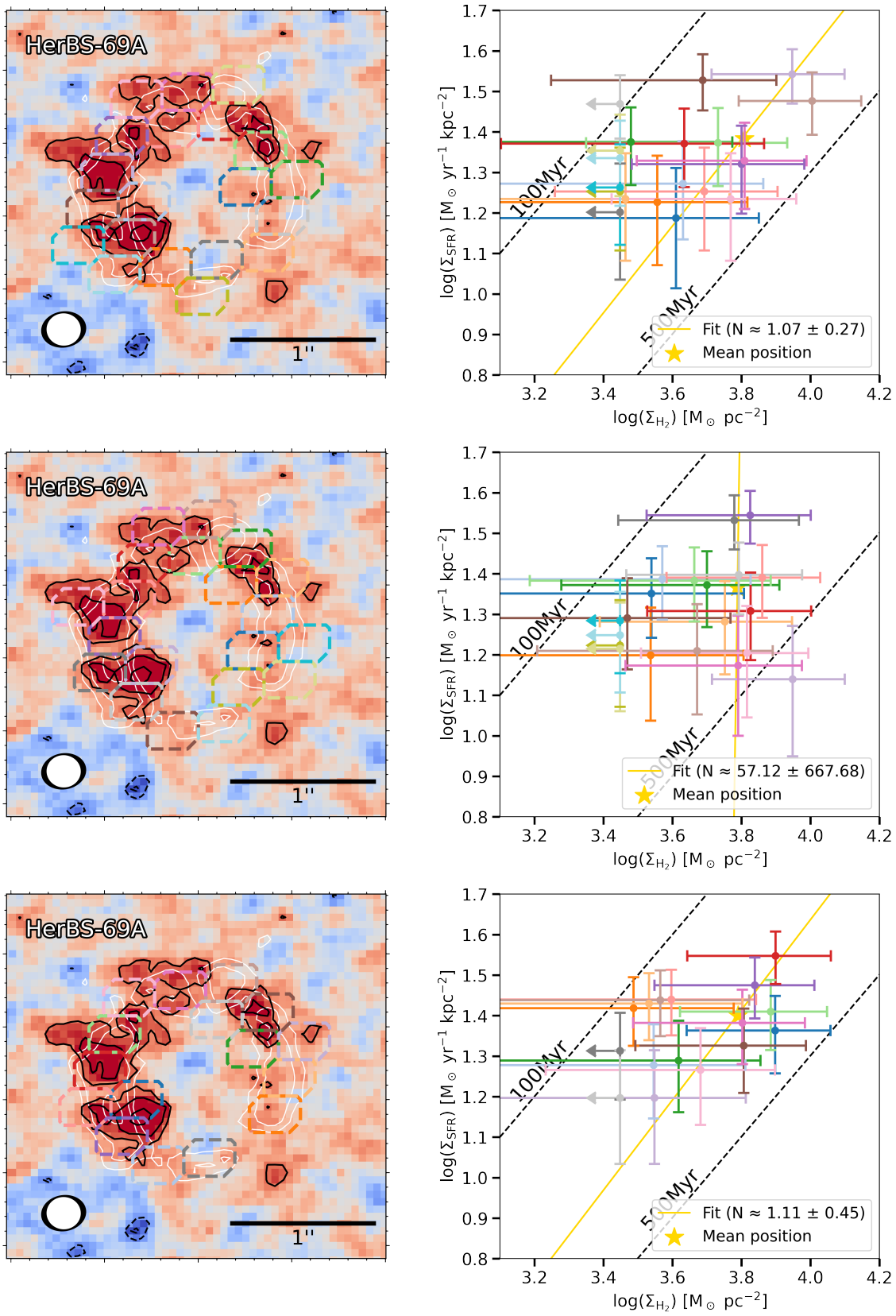

Figure G.1: (continuation). In this page: HerBS-69A, where 33 SK diagrams like these were built in total.

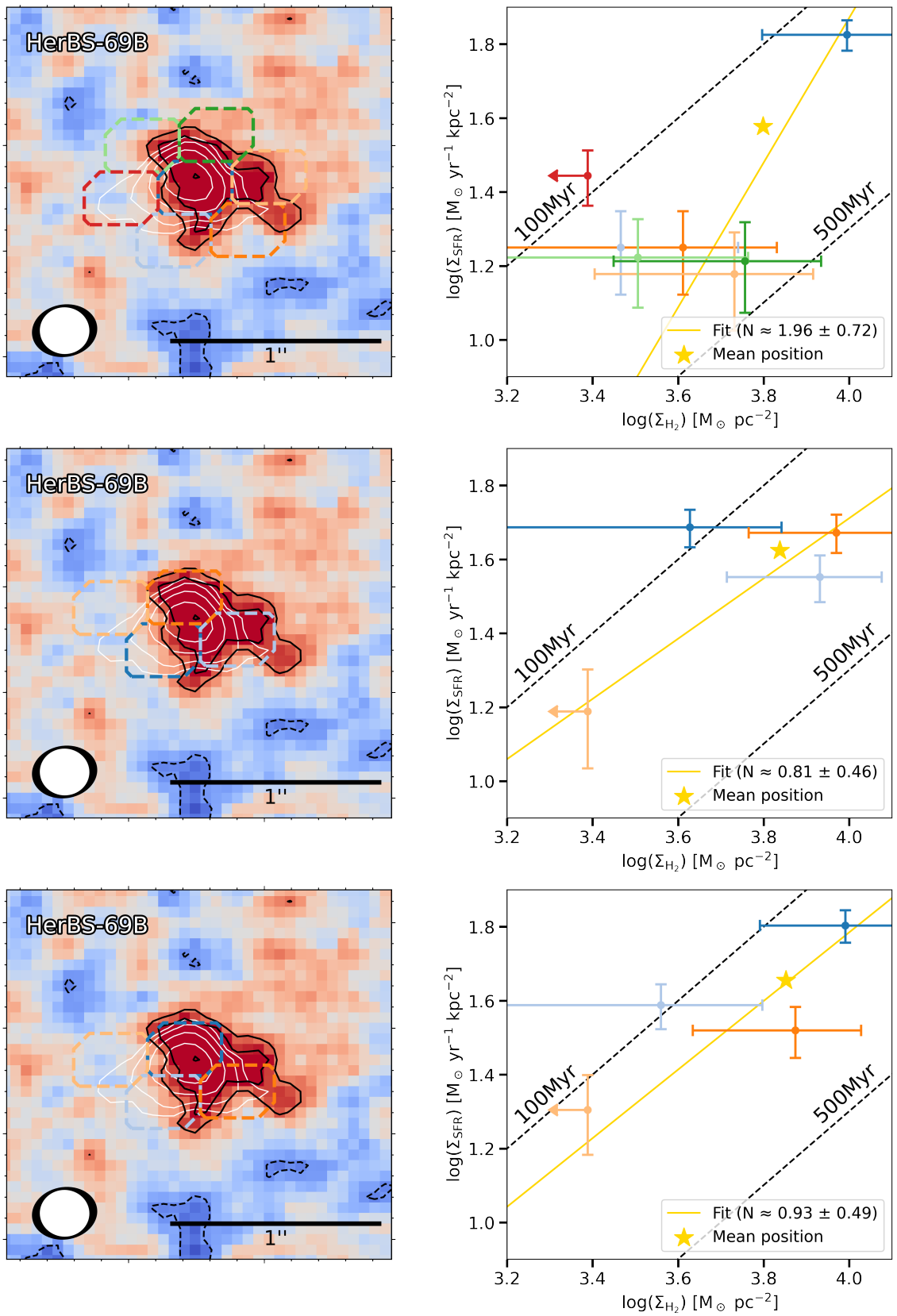

Figure G.1: (continuation). In this page: HerBS-69B, where 33 SK diagrams like these were built in total.

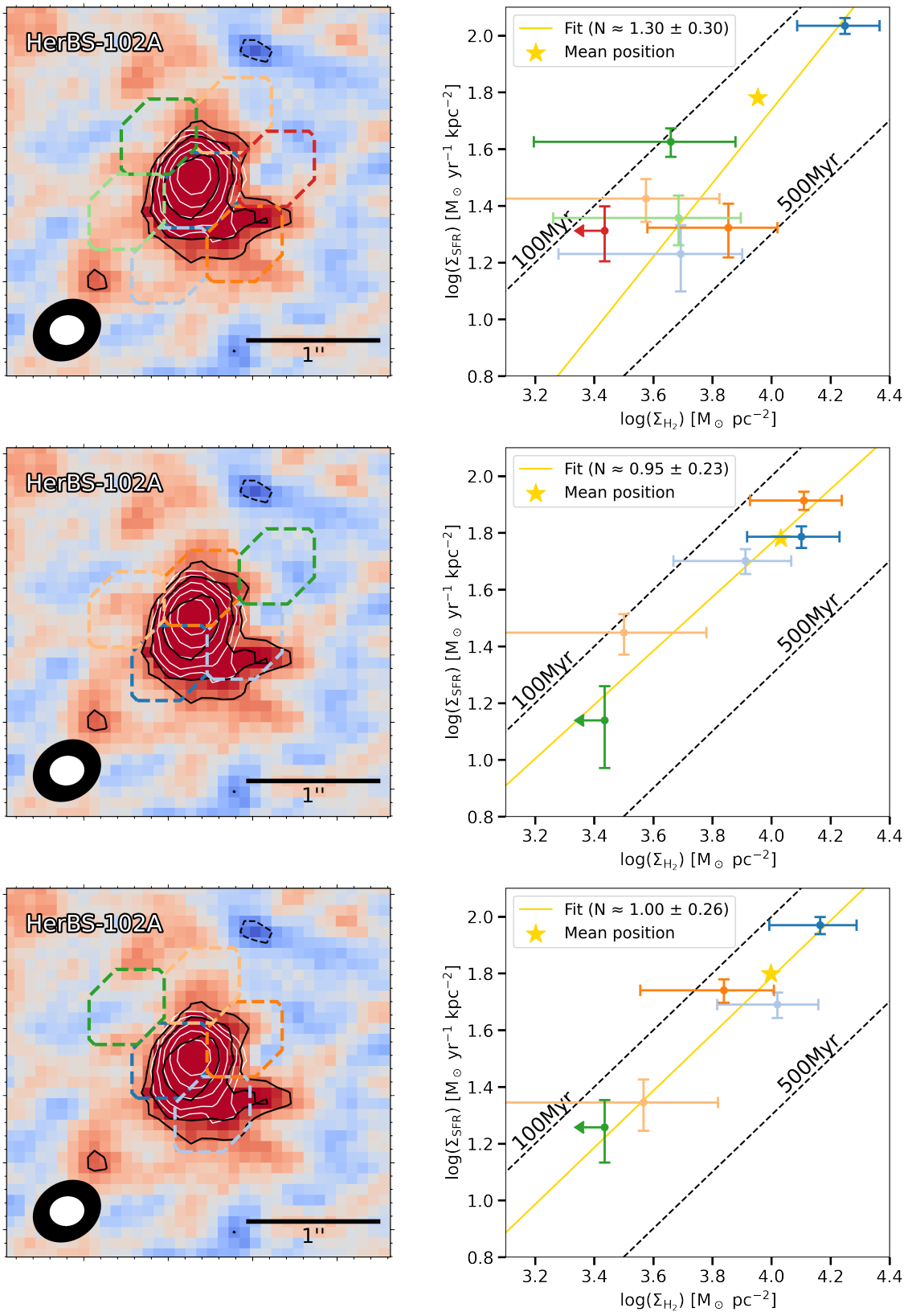

Figure G.1: (continuation). In this page: HerBS-102A, where 43 SK diagrams like these were built in total.

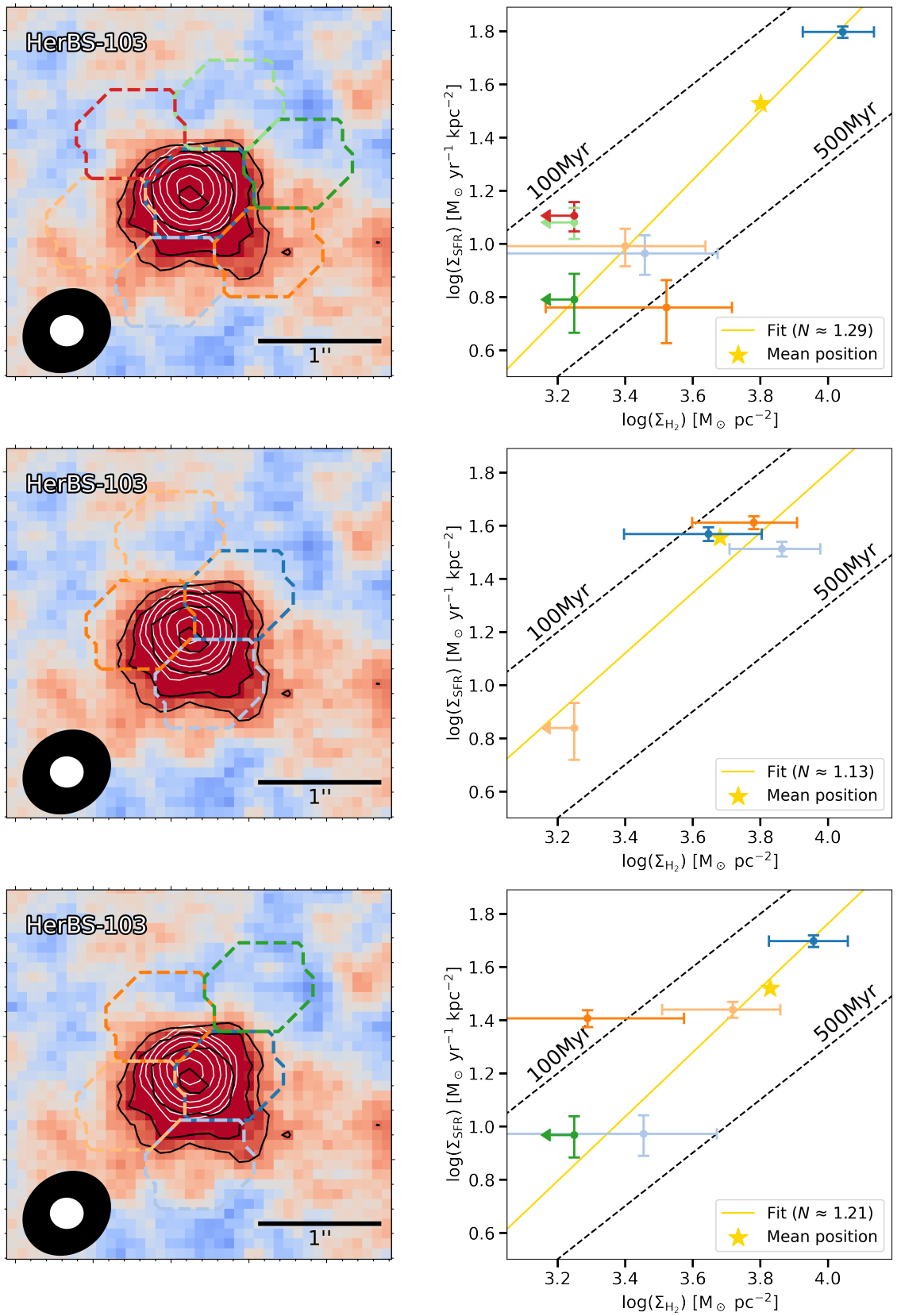

Figure G.1: (continuation). In this page: HerBS-103, where 81 SK diagrams like these were built in total.

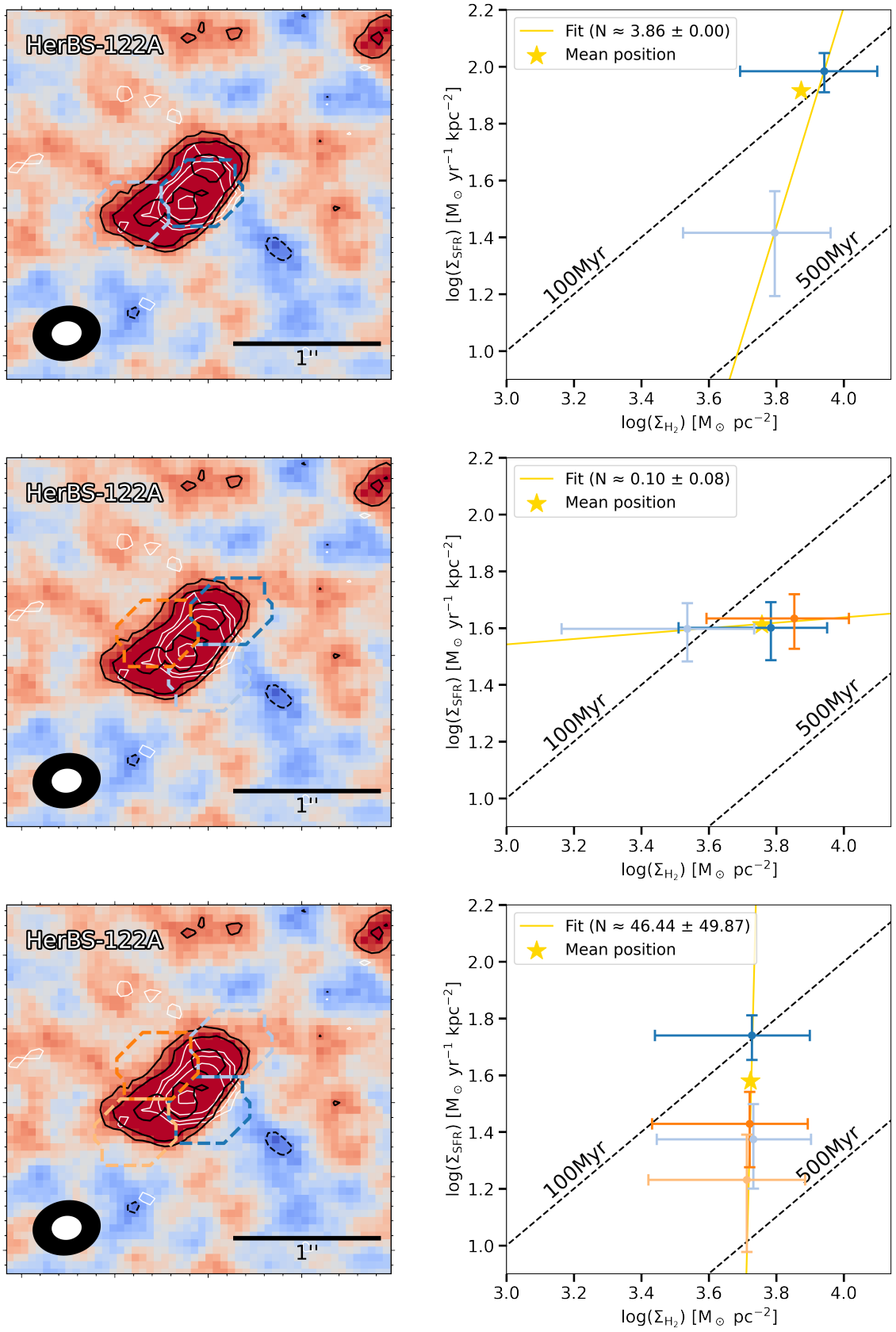

Figure G.1: (continuation). In this page: HerBS-122A, where 81 SK diagrams like these were built in total.

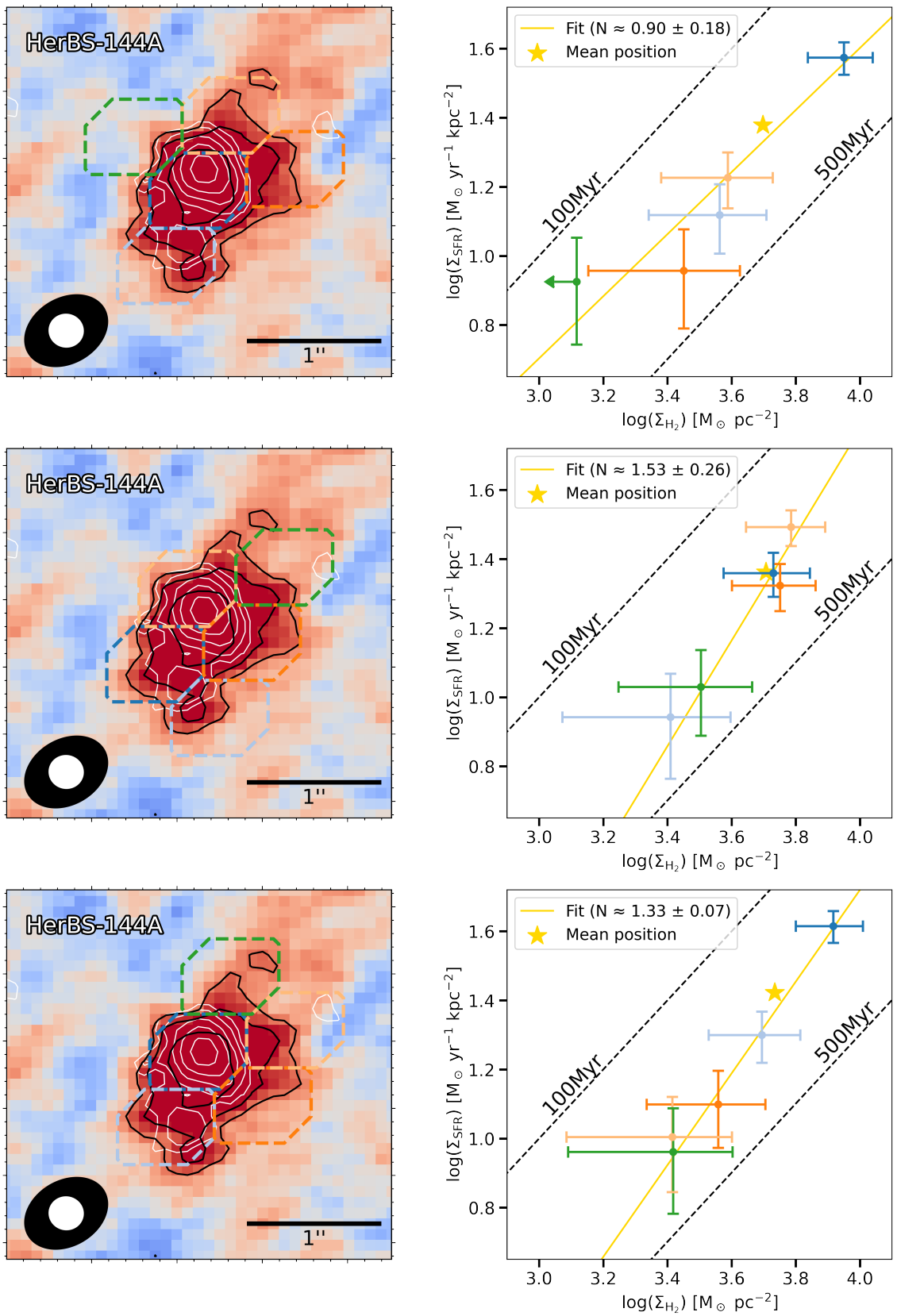

Figure G.1: (continuation). In this page: HerBS-144A, where 57 SK diagrams like these were built in total.

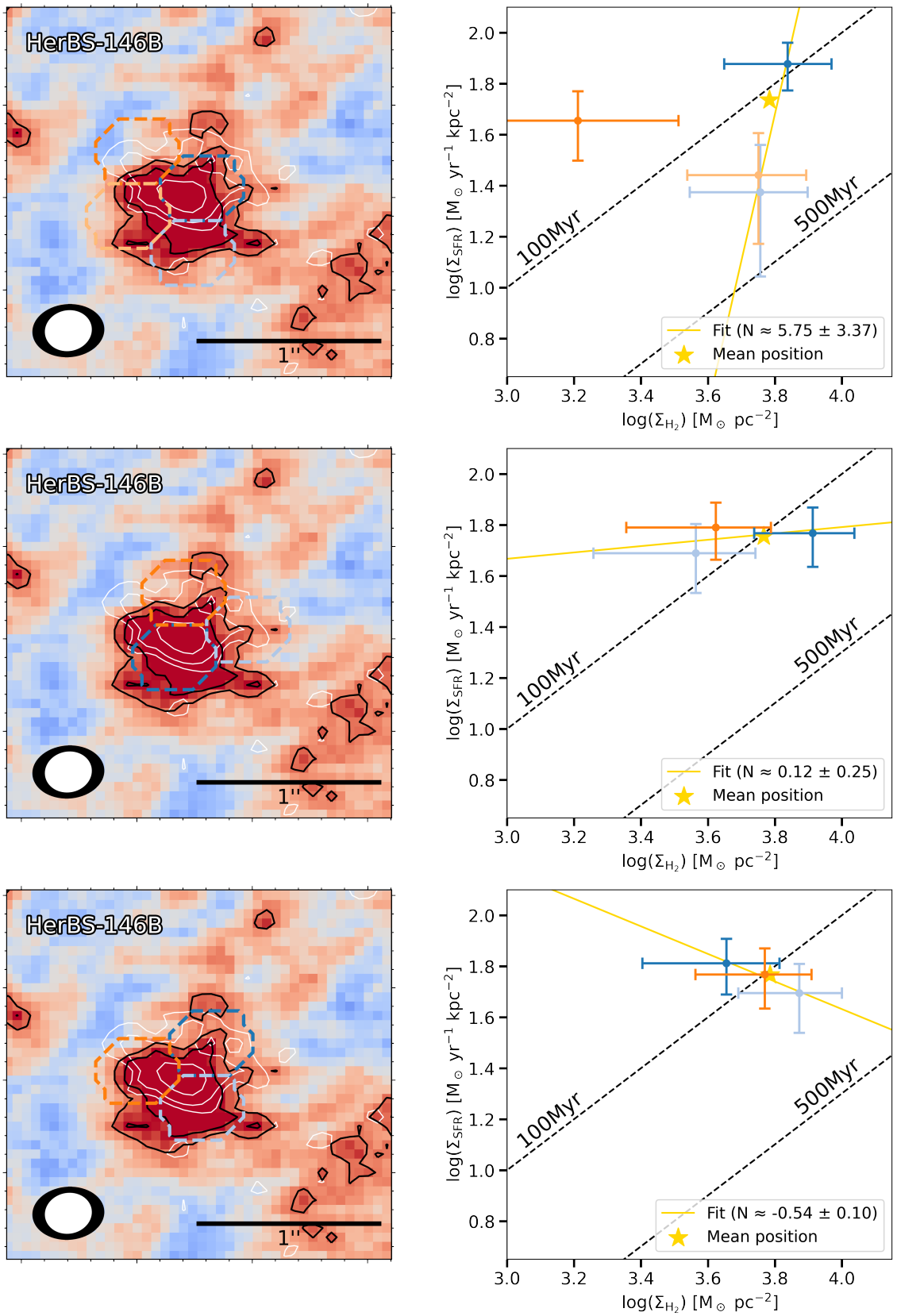

Figure G.1: (continuation). In this page: HerBS-146B, where 53 SK diagrams like these were built in total.

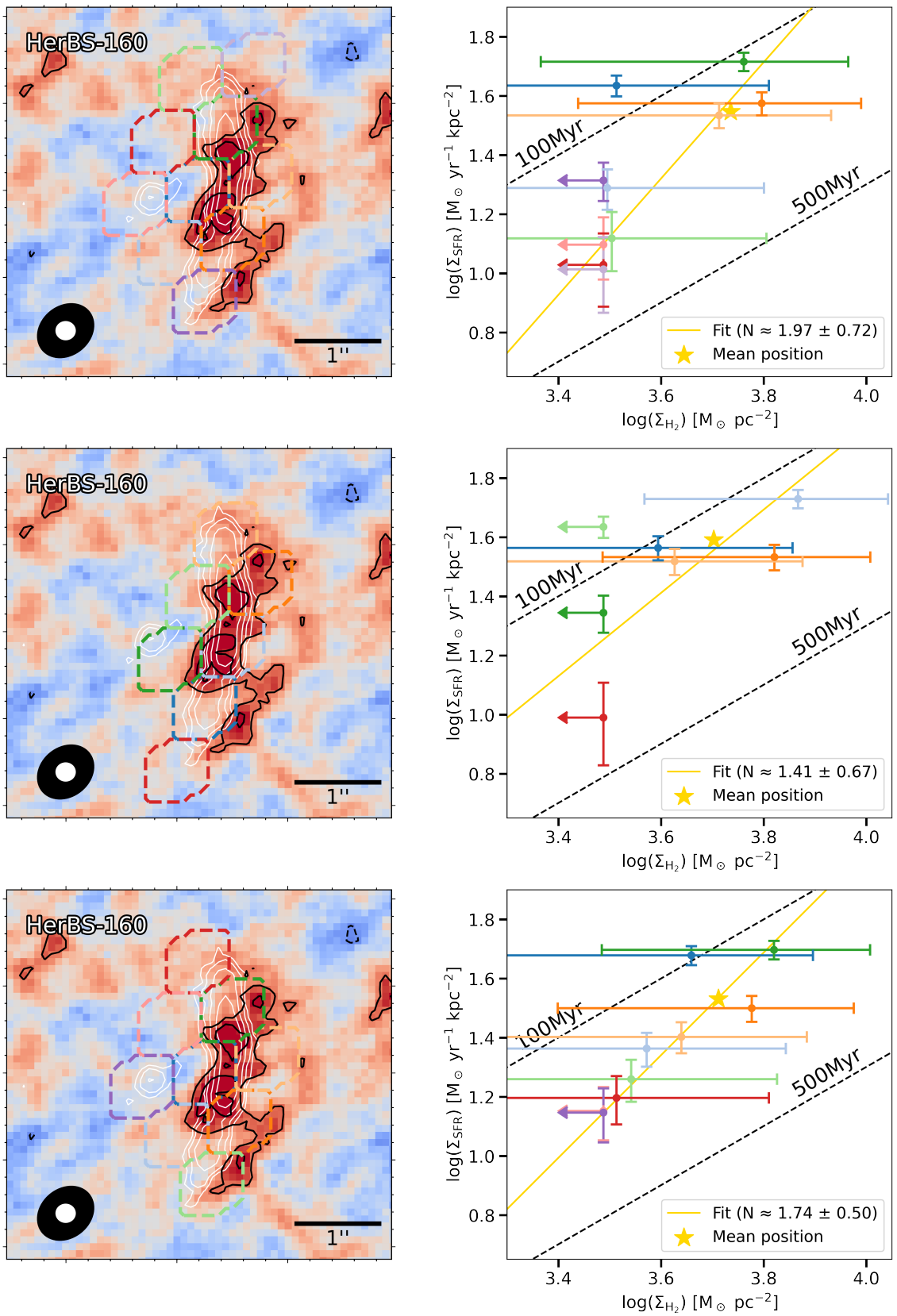

Figure G.1: (continuation). In this page: HerBS-160, where 73 SK diagrams like these were built in total.

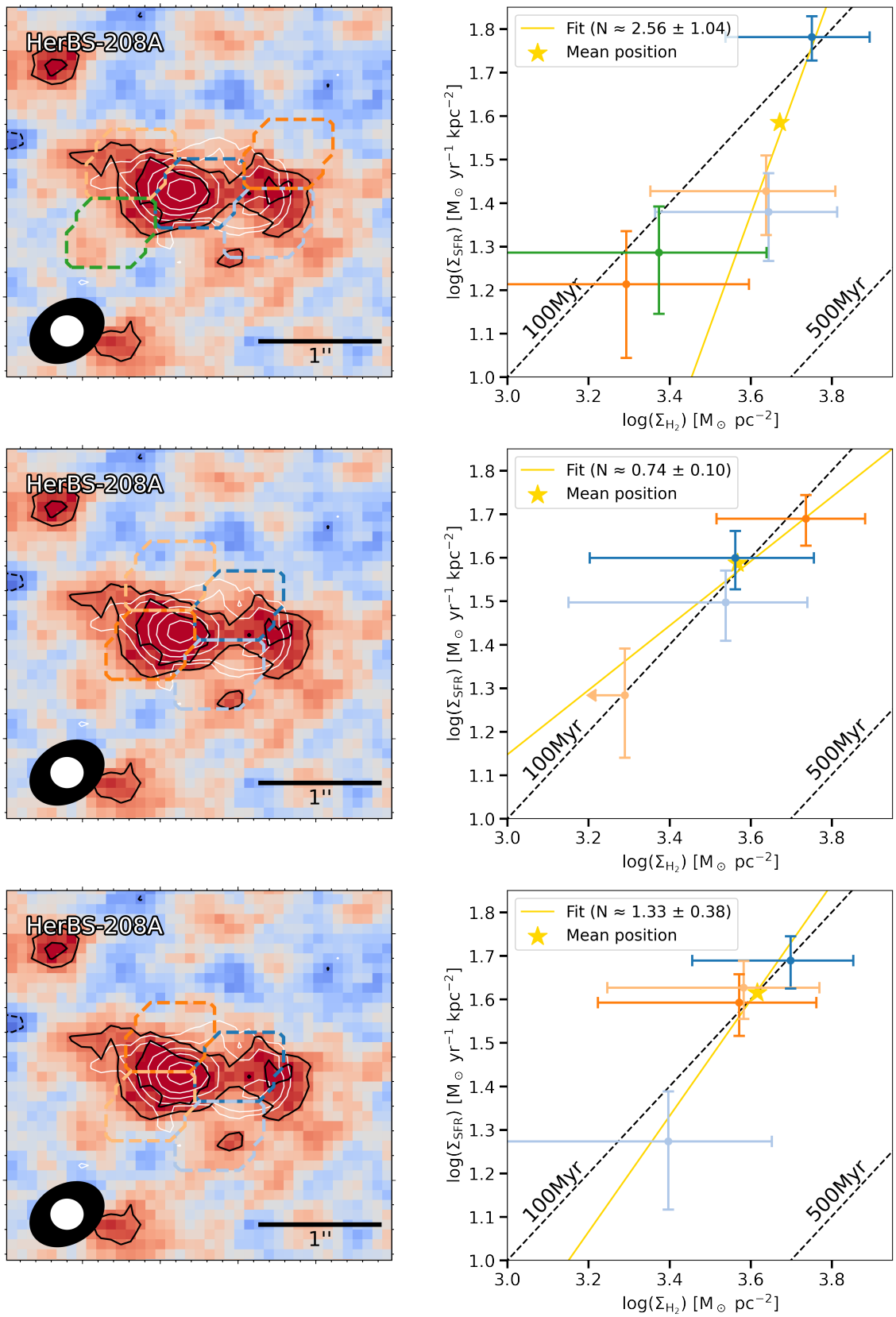

Figure G.1: (continuation). In this page: HerBS-208A, where 55 SK diagrams like these were built in total.

H

SNR

Figure H.1 presents the Signal-to-noise ratio (SNR) of all apertures from all tessellations. All 23 galaxies employed for the Schmidt-Kennicutt analysis are included.

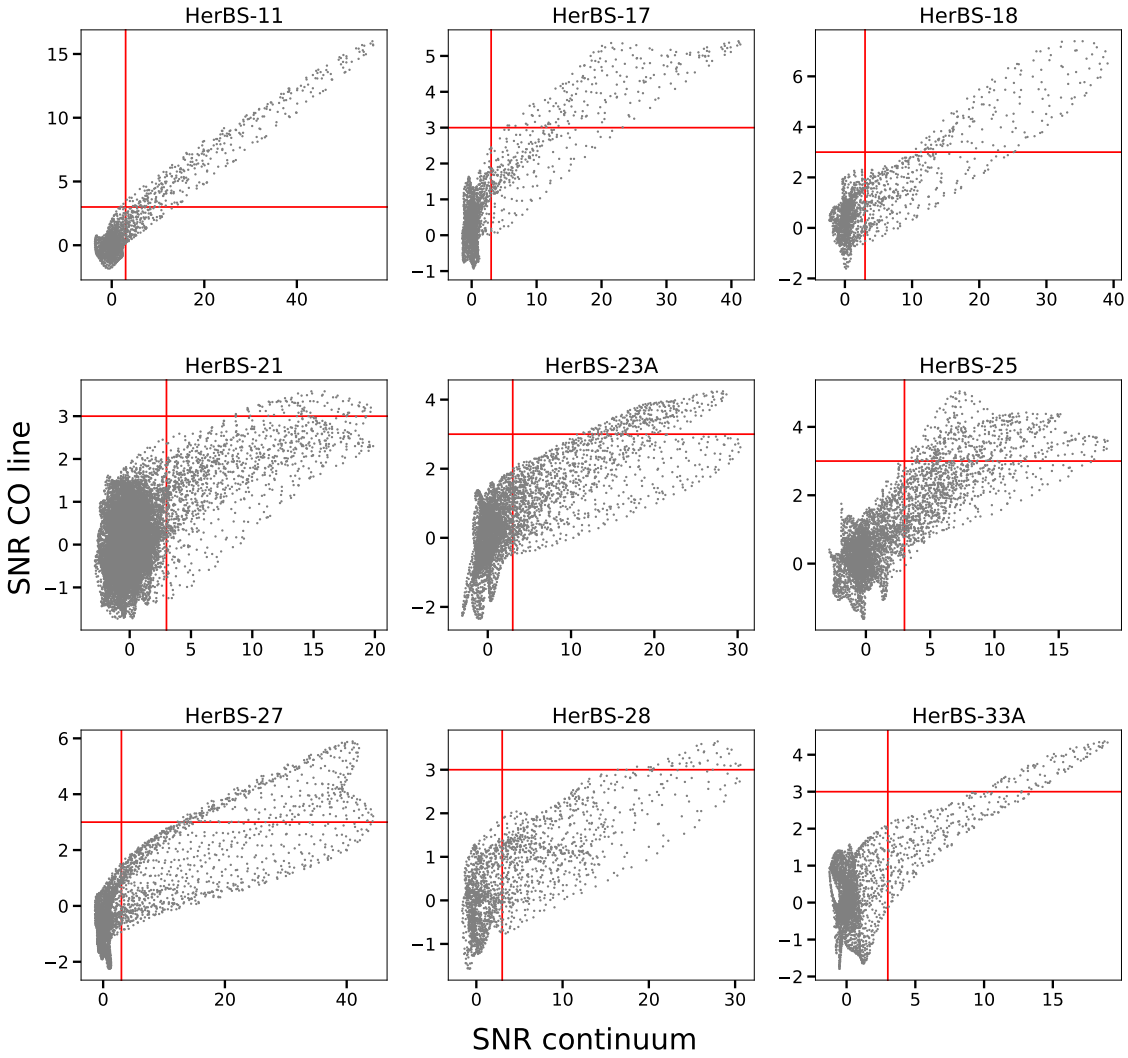

Figure H.1: Signal-to-noise ratio of all apertures in all galaxies. These include the apertures that were not used in the SK resolved, i.e. those with low SNR in the line and continuum. In all galaxies the continuum is in Band 6, with the exception of HerBS-21, -25, -36 and -41A, where it corresponds to Band 7. Each plot has red lines indicating SNR = 3, the threshold used for a detection (see Section 3.6.6).

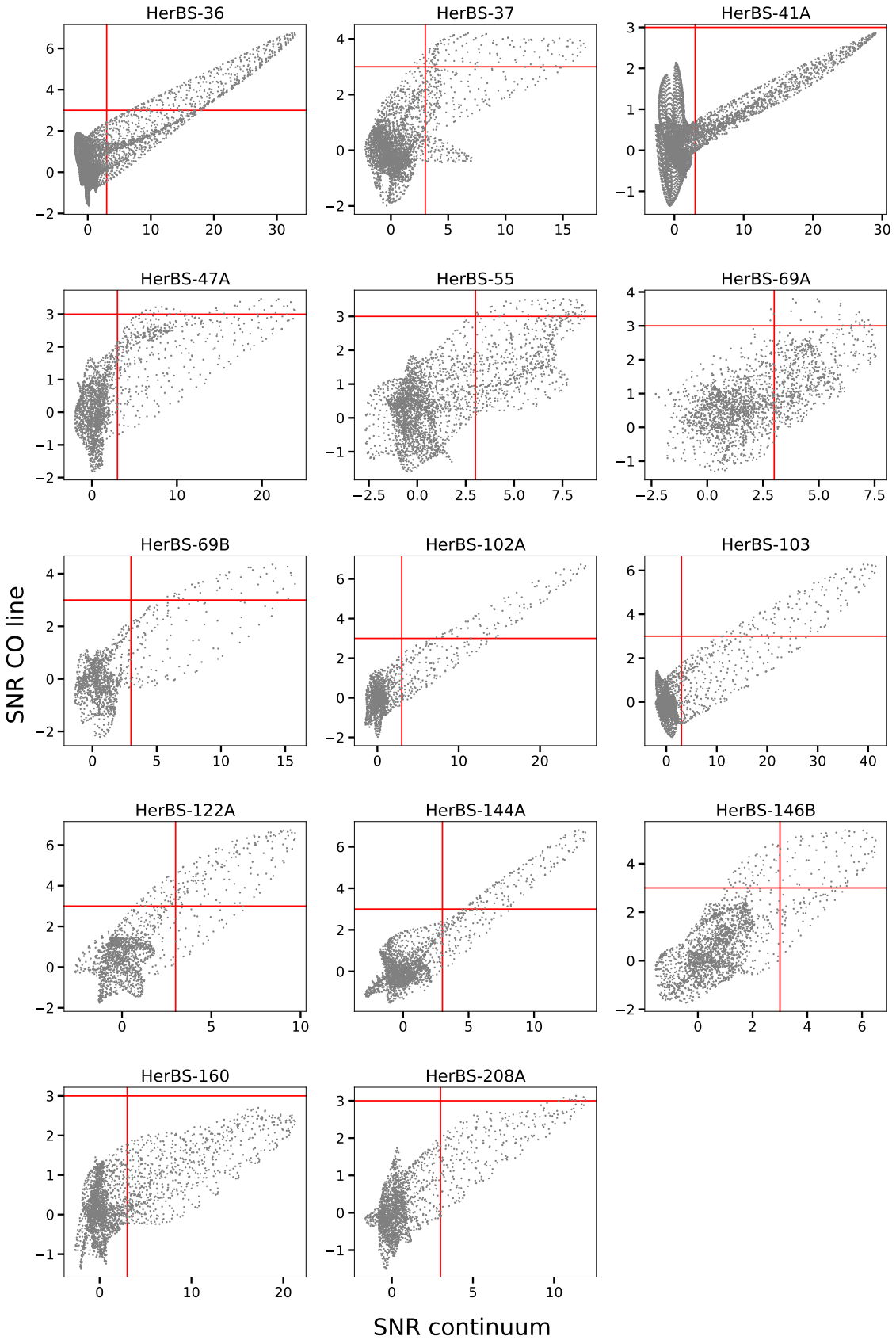

Figure H.1: (continuation).

DEPARTMENT OF SPACE, EARTH AND ENVIRONMENT
CHALMERS UNIVERSITY OF TECHNOLOGY
Gothenburg, Sweden
www.chalmers.se

CHALMERS
UNIVERSITY OF TECHNOLOGY